APPLICATIONS OF

HEAT AND MASS TRANSFER ANALYSIS

IN BIO-MEDICINE AND MATERIALS

by

Rajeev Hatwar

A dissertation submitted to Johns Hopkins University in conformity with the requirements for the degree of Doctor of Philosophy

Baltimore, Maryland

July 2017

Abstract

Heat and mass transfer analysis has its application in various fields including automobile, steam-electric power generation, energy systems, HVAC, electronic device cooling and in characterizing and diagnosing diseases. Here we have focused on applying the principles of heat and mass transfer to biological tissue and materials.

In the first part we introduce a computational method to simultaneously estimate size, location and blood perfusion of model cancerous breast lesions from surface temperature data. A 2-dimensional computational phantom of axisymmetric tumorous breast with six tissue layers, epidermis, papillary dermis, reticular dermis, fat, gland, muscle layer and spherical tumor was used to generate surface temperature distributions and estimate tumor characteristics iteratively using an inverse algorithm based on the Levenberg-Marquardt method. However, similar steady state temperature profiles for different tumors are insufficient to simultaneously estimate blood perfusion, size and location of tumor. This becomes possible when transient temperature data are used along with steady state data. Thus, in addition to the steady state temperature data, we modified and expanded the inverse algorithm to include transient data that can be captured by dynamic infrared imaging. Blood perfusion is an indicator of the growth rate of the tumor and therefore its evaluation can lead to assessment of tumor malignancy.

In the second part we treat X-ray computed tomography (CT) perfusion. The goal was to reduce the total radiation exposure by reducing the number of scans without compromising information integrity. CT scan images obtained from a rabbit model of liver and tumors were processed using the maximum slope (MS) method to estimate blood perfusion in the liver. Limitations of MS method are also discussed. The MS

method makes use of key time points, forming the basis of the rationale to explore optimization strategies that utilize variable time intervals, rather than the more common approach of fixed time intervals. Results show that this leads to significant improvement, without compromising diagnostic information.

In the last section we explore the magnetic shielding efficacy of superconducting materials and methods to mitigate the effect of necessary discontinuities in superconducting shield.

Acknowledgement

This work was made possible only through generous help of time and attention from numerous people.

Firstly I would like to thank my primary advisor, Dr. Ivkov, for his guidance and support. It was an honor to work with him. It was not an easy task to train an engineering student the subtleties of medical research, but under his able guidance it became possible. I would like to thank him for being so patient and helpful. I not only gained technical knowledge in his guidance, but also time/resource management and leadership.

It was a great honor to have the guidance of Dr. Meneveau, as a co-advisor, for the PhD and I am grateful for his guidance. The ease with which he could grasp difficult concepts and give insightful comments was a treat to watch and good learning experience.

I would also like to thank Dr. Liapi for patiently teaching an engineering student the subtleties of CT scanners and analyzing the images. It was a challenging task to grasp new concepts in a short amount of time, but with her guidance and encouragement it became possible.

I am very grateful to Dr. Whitcomb for his support and guidance.. I express my gratitude to the department for mechanical engineering for providing partial financial support during my PhD. I also appreciate the support of Kamal, Hangjian, Nitin, Kaushik and many friends who made the stay in Baltimore memorable.

Lastly I would like to thank my parents for always supporting me. And heartfelt gratitude to my wife, Niranjana, who came into my life in the later part of my PhD and was extremely caring and patient throughout. Without her support this last phase of my PhD would not have been possible. Here I would also like to express my gratitude to Sahaja Yoga, the meditation which I have been practicing since my high school, and its founder Shree Mataji. It helped me stay calm, balanced and give my best during the most difficult of the situations.

This PhD has been challenging and it would not have been possible without the help of all the people mentioned above. It would not be an exaggeration to say that all of them were like God sent angels at crucial moments of this work.

Table of Content

LIST OF TABLES

LIST OF FIGURES

Chapter 1

Introduction

The present work deals with heat and mass transfer and its application to biological tissue. We begin by giving basic definitions of temperature, heat transfer and relevant laws (thermodynamic) governing energy transfer.

Matter consists of atoms and molecules which are in constant motion. This motion is in the form of random translational motion, internal vibrations and rotations. The energy associated with these motions is referred to as thermal energy or heat. The particles possess kinetic energy by virtue of their motion and temperature is a measure of average kinetic energy. When molecules with higher kinetic energy collide with molecules of lower energy a transfer of energy takes place. This leads to an increase in the kinetic energy of the molecules with lower energy. By definition higher kinetic energy represents a higher temperature and therefore energy is being transferred from higher temperature to lower temperature. This transfer of energy from higher temperature to lower temperature is known as heat transfer and is described in detail below.

1.1. HEAT TRANSFER

In this section the basic concepts of heat transfer, relevant to the present work are explained. First the different modes of heat transfer are described followed by the concepts of thermodynamics (Incropera *et.al.*).

1.1.1 Modes of heat transfer

Heat transfer occurs via conduction, convection and radiation. When heat transfer occurs within a stationary medium, whether a solid or fluid, it is known as conduction. Convection occurs when heat is transferred between a surface and a moving fluid. The third form of heat transfer, radiation, occurs when surfaces emit electromagnetic waves as thermal radiation.

Conduction

In order to explain conduction it is best to start by considering a gas which is devoid of any bulk, macroscopic motion and has a temperature gradient. Molecules at higher temperature have higher kinetic energy and when they collide with molecules of lower energy they transfer energy. In this way there is a net transfer of energy from higher temperature to lower temperatures. This is also known as diffusion of energy. The case can be easily extended to fluids, the only difference being that the molecules in a fluid are closer to each other than in gas and consequently stronger and more frequent molecular interactions occur.

The case of solids is similar to that of gases and liquids but with important differences. In a solid, the atoms are arranged in fixed periodic spatial relation known as lattice. Here the microscopic motion which is responsible for thermal energy has two components. First, due to movements of free electrons and second due to the lattice vibrations also referred to as phonons when considering it as a particle like behavior. The contribution from electrons is dominant for the case of pure metals, whereas for the case of non-conductors and semiconductors it is the heat transfer through phonons which

dominates. A special case of conduction occurs in solids with very low electrical resistivity and is known as ballistic conduction. It is generally observed when the mean free path of electrons is much longer as compared to the dimensions of the material for example in metal nano wires.

When a metal rod is heated at one end the temperature of the other end also rises gradually. The heat transfers from one end to the other by conduction.

The rate equation used for describing this is known as Fourier's law and is given in one dimension as

$$q_x^{"} = -k\frac{dT}{dx} \tag{1.1}$$

where $q_x^{"}$ is the heat flux (W/m^2) or heat transferred per unit area, heat flux, in the x - direction, k is the thermal conductivity and T is the temperature.

Convection

Convective heat transfer takes place when a surface comes into contact with a moving fluid and there is a temperature difference between the fluid and surface. Although convective heat transfer occurs at the boundary of the two materials, it is also important to understand the heat transfer within the fluid, away from the surface for a complete understanding of convection. We have seen in the previous section the heat transfer through random molecular motion, diffusion. In convection there is an additional component to this by the virtue of the motion of the fluid. Due to this bulk motion of the fluid, the random molecular motion is also transferred. Heat transfer by this mechanism is referred to as advection. Convective heat transfer occurs by both diffusion and advection.

So, in addition to the heat diffusing into the fluid at the solid liquid interface, there is also heat transfer taking place through advection due to upstream fluid, which has already come into contact with the surface and exchanged heat.

Convection in single-phase fluids can be classified into three forms:

1. Forced convection: This form of convection is driven by an external stimulus. An example of this is cooling of a microprocessor in a computer by a fan. The fan directs external air towards the microprocessor. The microprocessor transfers heat to the air and cools. The amount of heat transfer achieved can depend on various factors including, temperature difference between the incoming air and the microprocessor surface, velocity and density of air.
2. Natural/free convection: Here the fluid flow is driven by buoyancy forces. An example of natural convection can be a heated vertical plate. The plate will heat the air in its vicinity, the heated air being less dense than the surrounding air will rise. The incoming cold air will again get heated up due to the plate and will rise, hence continuing the cycle.
3. Mixed/combined convection: As the name suggests this form of convection is a mixture of forced and natural convection. If we have a heated vertical plate, which is an example of natural convection and if we add a fan at the bottom, blowing air along the walls, this will be the case of mixed convection.

The rate equation which is used to describe convection is given by Newton's law of cooling.

$$q'' = h(T_\infty - T_s) \tag{1.2}$$

where q'' (W/m^2) is the heat transfer from the ambient air to the surface, h (W/(m^{2}K)) is the convective heat transfer coefficient, T_∞ (K) is the ambient temperature and T_s (K) is the surface temperature.

Radiation

The third form of heat transfer is radiation (thermal radiation). It requires no medium and energy is transferred in the form of electromagnetic waves, with wavelengths ranging from 0.1 to 100 μm approximately. Any surface which has a temperature above 0 K emits thermal radiation. It is the vibrations of the constituent molecules or electron transitions, sustained by its internal energy, which are responsible for these radiations. As the internal energy is related to temperature this form of radiation is associated with thermal energy of the matter. Thermal radiation comprises of infrared and visible radiation and a portion of ultraviolet. As high energy electrons transitions to a lower state an object emits radiation and a lower energy electron jumps to a higher state as it absorbs radiations. Similarly, changes in the vibrational energy of molecules are also associated with the absorption and emission of radiations although at much lower energies as compared to electron transition. An object emits and absorbs radiations continuously, if radiation emission equals absorption the temperature of the object remains constant. The temperature of the object increases if absorption dominates and it decreases when emission is dominant.

An example of heat transfer through radiation is the heating of satellites orbiting the earth. There is no atmosphere present in space, so there is no possibility of heat transfer from conduction and convection. But when the satellite is between the earth and the sun, therefore outside the shadow of the sun, it receives radiation from the sun and

heats. In fact it is a challenging problem to remove this heat as there is no possibility of convection and conduction. Multilayer insulation material is employed for this purpose, it reflects most of the radiation.

The maximum radiation which can be emitted by a surface is given by the Stefan-Boltzmann law

$$E_b = \sigma T_s^4 \tag{1.3}$$

where E is the emissive power (W/m^2), σ (5.67 $\times 10^{-8}$ W/m^2. K^4) is the Stefan-Boltzmann constant, T_s is the surface temperature (K). This is an idealized case, where the surface is considered as a blackbody. Real surfaces emit less radiation than a blackbody at same temperature, depending on various factors, including material and surface. To incorporate this loss in emissive power, emissivity (ε) is defined, which ranges from 0 to 1. After including this the emissive power is given by

$$E = \varepsilon \sigma T_s^4 \tag{1.4}$$

where ε is the surface emissivity.

The radiation incident on a surface is absorbed, and the extent of absorption is governed by the absorptivity, α, which ranges from 0 to 1. Surfaces with equal emissivity and absorptivity are known as grey surfaces. For grey surfaces the rate equation is given as

$$q''_{rad} = \varepsilon \sigma (T_s^4 - T_{sur}^4) \tag{1.5}$$

where q''_{rad} is heat transfer occurring from the surface to the surrounding, T_{sur} is the ambient temperature (K).

1.1.2 Thermodynamics

In the last section (1.1.1) different modes of heat transfer were discussed. There is a need for additional set of laws, known as laws of thermodynamics, to conduct heat transfer analysis.

The first law of thermodynamics relates to the conservation of energy. It states that the change in the total amount of energy stored in a control volume is equal to the net energy input into the volume and the energy generated in the volume. This is given by the following equation

$$\Delta E_{stored} = E_{in} - E_{out} + E_{generated} \tag{1.6}$$

where ΔE_{stored} is the energy stored in the control volume, E_{in} is the energy entering the volume, E_{out} is the energy leaving the body and $E_{generated}$ is the energy generated in the body.

Using the conduction rate equation (Eq. 1.1) and the first law of thermodynamics (Eq. 1.6) on a control volume gives us the heat diffusion equation

$$\rho c \frac{\partial T}{\partial t} = k\nabla^2 T + Q \tag{1.7}$$

where ρ is the density (kg/m^3), c is the specific heat capacity(J/(kg.K)), k is the thermal conductivity (W/(m. K)) and Q is the heat generation rate (W/m^3).

First law of thermodynamics (Eq. 1.6) along with the knowledge of different modes of heat transfer is sufficient for conducting heat transfer analysis on wide range of

engineering problems. Some of them are designing fan for cooling microprocessor, radiators in automobiles, dewar to store cryogenic liquids, HVAC and solar cookers.

Second law of thermodynamics deals with the direction of heat transfer. It states that the entropy of an isolated system cannot decrease over time, where entropy, on a microscopic level, is a measure of disorder. Clausius gave mathematical form to change in entropy [J/K]

$$\partial S = \partial Q/T \tag{1.8}$$

In a system with objects at two different temperatures, if the heat flows from the hot to the cold object the entropy increases, therefore this is the only plausible direction of heat flow. Thus the second law of thermodynamics makes it possible to know the direction of heat transfer.

1.1.3 Finite element method

The principles discussed in this section can be applied to solve heat transfer related problems for simple geometries. However, in the real world, the problem domains are complex and have no simple analytical solutions for the underlying partial differential equations. Some examples of partial differential equation are heat diffusion equation for heat transfer analysis, Navier-Stokes equation for fluid dynamics analysis and bio-heat transfer equation for heat transfer analysis in biological tissue.

To solve this problem finite element method (FEM) is employed, which is one of the numerical methods available based on Galerkin method. FEM divides the domain into smaller parts, referred as elements, which have common points referred to as nodal

points. A polynomial is used to interpolate values within the element. This leads to a set of simultaneous equations which can be solved to obtain unknown variables. FEM was used by commercial software COMSOL Multyphysics v 4.2 (2011) in the present work to solve for the temperature distribution.

1.2. Bio Heat Transfer

Body tissue is a complex system with blood flow and metabolic activity. Apart from supplying nutrients the blood flow also affects the temperature of the body tissue. The metabolic activity also leads to heat generation, referred as metabolic heat generation rate. Understanding the contribution of these two factors in the heat transfer within body can be very useful in estimating the temperature distribution within the body. Several models have been suggested to describe bio heat transfer (Pennes 1998). Pennes bio heat transfer equation has been experimentally validated and used extensively in the literature (Pennes 1998).

Bio heat transfer as described in Pennes bio-heat equation is very similar to the standard heat transfer equation. The heat generation term has two components, metabolic heat generation rate and heat transfer through blood perfusion.

$$\rho c \frac{\partial T}{\partial t} = k\nabla^2 T + \rho_b c_b \omega_b (T_b - T) + Q \tag{1.9}$$

where ρ_b [kg/m^3], c_b [J/kg.K], T_b [K] and ω_b [m^3/s/m^3] represent density, specific heat of blood, arterial temperature and blood perfusion rate respectively. Q [W/m^3] is the metabolic heat generation rate.

To solve the heat diffusion equation, analytically or numerically, domain boundary conditions and initial conditions need to be specified. In the present case boundary conditions are specified at the inner body and at the outer surface. The outer boundary is given a convection boundary condition, which will be explained in detail in the second section. The inner body surface is assumed to be at a core body temperature of 37° C, which is maintained at this temperature due to thermoregulation.

Human body cannot function properly if the core temperature falls below 35° C or goes above 42° C. Temperatures beyond this range could lead to brain injury and is fatal. The function of thermoregulation in human body is performed by hypothalamus, which sends signals to the body to perform the appropriate function. If the body requires cooling it undergoes sweating and vasodilation. As the sweat evaporates it cools down the skin in the process and as the blood vessels become wider near the skin surface it leads cooling of the blood and thereby body. On the other hand if the body requires heating, it leads to vasoconstriction (narrowing of blood vessels) and shivering. Vasoconstriction decreases the blood flow to extremities and thereby reduces the heat flow from the extremities of the body to the surrounding. Shivering, on the other hand generates heat in the body because of the rapid movements of the muscles. All these process allows hypothalamus to control internal body temperature at 37° C.

There are certain conditions which dysregulate temperature control, some of them are staying in cold or hot conditions, exercise and digestion. It can also be an indication of some abnormal functioning of the body, as fever, under functioning thyroid gland, inflammation and tumor can also lead to an increase or decrease of temperature. Tumor is dealt in more detail later.

There are certain parameters which are more influential in the temperature distribution within the body, as compared to other parameters. Based on analysis conducted by Çetingül and Herman (Çetingül and Herman, (2010)) blood perfusion rate and metabolic heat generation rate were found to be the most dominant parameters affecting the heat transfer distribution within the tissue.

1.3. Thermography

There are various instruments available to measure temperature, including thermocouples, thermistors, resistance thermal detectors and infrared cameras. Of these only infrared cameras (thermography) can provide a spatial temperature distribution and the rest can give temperatures only of a single point at a time. The knowledge of spatial variation is critical in a clinical setting while diagnosing a disease, based on surface temperature distribution. The basic concepts involved in thermography are described below.

A blackbody at any given temperature emits radiation across a wide range of wavelengths. The intensity of radiation at each wavelength is dependent on the temperature of the blackbody and can be obtained by the Stefan-Boltzman law. It is interesting to note that sun (5800 K) emits radiations of maximum intensity within the visible spectral region. Eyes of human beings have evolved to maximize the utilization of that part of the solar radiations which has maximum intensity. Similarly infrared cameras also utilize that part of the radiation which has maximum intensity. For human applications the working temperature range is around room temperature. At room temperature the intensity peaks around 10 μm, therefore the sensors in infrared camera

are designed to measure radiation around this wavelength. The images obtained from infrared cameras, showing the temperature distribution, are referred as thermograms.

Infrared cameras were first used around 1950s and have undergone tremendous improvements, from bulky units to hand held cameras. They have various applications including night vision cameras, which detects the heat signature left by humans and other animals to detect their activity during night, when visibility is low or absent. The earliest infrared cameras had spatial and temporal resolution of 5 mm and 0.3 - 1 K respectively. Over the years, with technological advancement, spatial and temporal resolution has improved to 0.003 mm and 5 mK, respectively. (Cetingul M. P. 2010)

Among other uses it can also be used on humans and other animals for diagnosing purposes. Abnormalities in the human tissue, caused by diseases, lead to local temperature variations (Barnes 1963). This is a common observation in the case of skin cancer (Herman 2012), breast cancer (Ng 2009), hemangioma (Saxena and Willital 2008) and deep tissue injury (Bhargava *et al.* 2014). Infrared cameras can be used to detect these temperature variations and therefore can aid in diagnosing diseases (Ng 2009).

A significant amount of work has been done in qualitative analysis of breast cancer infrared images (Ng, E. Y. -K., 2009). The asymmetry in temperature distribution is used as an indicator of abnormalities. Researchers have also shown interest in extracting quantitative thermograms. The heat transfer within the human tissue is modeled and then the surface temperature data are used to determine internal features. This aspect is dealt with in great detail in chapters 2, 3 and 4 of the present work.

Other applications of thermography are in skin hemodynamics (Anbar *et al.* 1997), plaque (Bahtia *et al.* 2003), food allergies (Clark *et al.* 2007), Cataract (Corvi *et al.* 2006) and extracranial-intracranial bypass surgery (Okada Y. 2007).

1.4. Tumors

Tumors can be categorized into cancerous, or 'malignant', and non-cancerous, or 'benign'. Malignant tumors are highly heterogeneous in nature and variations are found even within the same cancer types. Not all tumors are solid, sometimes they have cysts or liquid areas. Some regions of tumors are characterized by necrotic regions, which are deprived from blood supply. The periphery of the tumor is where all the activity is concentrated and is highly perfused.

Malignant tumors have a high growth rate and therefore a high metabolic rate due to which it generates more heat as compared to the normal tissue. Due to fast growth rate it also needs higher supply of nutrients, which leads to angiogenesis, and therefore these regions are highly perfused. Both these factor leads to elevated temperature in its vicinity (Lawson 1956, Kennedy *et al.* 2009) This elevated temperature can also be observed on the surface and can be recorded using infrared camera.

The severity of cancer can be seen from the fact that in 2012, the total number of new cancer cases, all over the world, was 14 million, and around 8 million deaths were reported (NIH-NCI). Within the US it is estimated that 1.7 million new cases and 0.8 million deaths will be observed in 2016. According to an estimate, based on 2010-12 data, around 40 % of men and women in US will develop some form of cancer in their lifetime. Breast cancer, lung and bronchus cancer and prostate cancer are the most

prevalent forms of cancer. Large amounts of money have been spent in US to fight cancer. $125 billion was spent in 2010 and an estimated $156 billion will be spent in 2020. Still, there were 14.5 million people in 2014 that were not able to get cancer diagnosis.

In the present work the focus has been on the second most common forms of cancer in women, breast cancer and the cancer with one of the highest 5 year mortality rate, liver cancer. Based on breast cancer statistics, the lifetime probability of developing breast cancer is 12.3 % (1 in 8) for women in the U.S. (Siegel *et al.* 2016). In 2016, around 246,660 new cases and around 40,450 deaths are expected to be reported in the U.S. alone (National Cancer Institute, 2016). Early detection of breast cancer is currently the most effective way to fight the disease.

The spread of tumor cells from the place of formation to another part of the body is known as metastasis. In this process tumor cells break away from primary tumor, travel through the blood and lymph system and form a new tumor in other organs or tissue of the body. Cancer diagnosis at an early stage can prevent metastatic growth of the tumor. It becomes extremely difficult to treat someone with tumor metastasis, therefore the role of early diagnosis becomes extremely important. Any progress in this direction can prove very fruitful in terms of saving lives. Therefore in the present we have focused on cancer diagnosis and tumor characterization.

1.5. Inverse Heat Transfer

The problem of estimating the underlying parameters from the observable data is called “inverse problem”. It can be as simple as calculating gravity by measuring the rate of descent of a falling body and as complex as estimating tumor characteristics using

surface temperature distribution. Inverse problems are encountered in various fields of science and engineering, such as non-destructive testing, medicine, geology, archaeology, oceanography, material science and astrophysics. Inverse problems in heat transfer are referred to as inverse heat transfer (Ozisik M N and Orlande H 2000). An example of inverse heat transfer is to estimate the intensity of an internal heat source from the surface temperature distribution.

Inverse heat transfer has application in aerospace, mechanical, chemical and nuclear engineering. An example of its application in aerospace engineering is in designing the insulation tiles of the space shuttle. Due to extreme conditions it is impossible to measure the heat flux of the tiles directly. So the temperature within the tile is measured and from this the heat flux at the outer surface is estimated. It has also been applied in cancer diagnostics and characterization.

Different methods are used to solve the inverse problems, including genetic algorithm, neural networks, Levenberg-Marquardt method and various gradient descent algorithms. Inverse heat transfer problems are inherently ill-posed (Ozisik M N and Orlande H 2000), as a small change in the observed data can have significant effect on the estimation of underlying parameters. In order to tackle this problem regularization methods are used. One such widely used method is the Levenberg-Marquardt method. The Levenberg-Marquardt method is a common method for solving non-linear optimization problems. It is a combination of gradient descent method and Gauss Newton algorithm. The gradient descent part dominates when the solution is far and Gauss Newton approach dominates when the solution is close. An advantage of this method over other methods such as genetic algorithm and neural network, is that it does not

require test cases to run. This can prove helpful in clinical settings where test cases will be required for each and every case, while for LM method there will not be such requirement.

1.6. Superconductivity

Superconductivity is a phenomenon where the electrical conductivity of a material becomes zero below certain characteristic temperature known as critical temperature. Critical temperatures are generally below 100 K and therefore it is important to ensure proper insulation for the superconducting material (cables, wires). Without proper insulation, large temperature gradients develop which can lead to the heating of the system, which in turn can lead to temperature rise of superconducting material above its critical temperature and destroy it. Therefore heat transfer analysis is an important aspect for superconductivity applications.

1.7. Overview

In the first part of this thesis (Chapter 2-4) heat transfer is modeled within the body to relate the tumor parameters, such as tumor size, depth and blood perfusion, with the surface temperature distribution. Chapter 2 starts with a description of diagnostic modalities for breast cancer, mammography and infrared thermography. It is followed by the computational model for breast cancer. This model is used in chapter 3 to analyze the effect of various geometrical and thermophysical properties on steady state temperature profile. This is followed by the analysis of the effect of application of cooling load on temperature distribution. With this background, Chapter 4 estimate tumor parameters, size, location and blood perfusion rate, based on the surface temperature distribution in

steady and transient state, which is easily available, thus providing a non-invasive method of tumor diagnosis and characterization.

Heat transfer within the body is very sensitive to blood flow (perfusion). Therefore it becomes important to study it in detail. The next part of this thesis deals with measurement of blood perfusion within the body tissue using computer tomography (CT) perfusion (Chapter 5-6). Different methods used in literature for CT perfusion are discussed here. CT perfusion in itself is a diagnostic tool for liver cancer. In liver the ratio of the portal vein and hepatic artery, two blood vessels supplying blood to the liver, is used to ascertain the possibility of a tumorous region. As an extension to the analysis of CT perfusion, an optimized protocol of CT perfusion is developed to reduce the radiation dose. A critique of a widely used method for CT perfusion is also included in that section.

Towards the end of this work, an application of heat transfer in the extreme environment of cryogenic temperatures, superconducting materials, is examined (Chapter 7). Superconducting materials are capable of shielding magnetic fields. In this section the shielding efficacy of superconducting materials, under different circumstances, is tested. The use of superconducting materials is only possible when very low temperatures (below 100 K) can be obtained and maintained. There are commercially available cryogenic vessels, dewars, which are vacuum insulated and used for storing cryogenic liquids. Special materials are designed to sustain the fatigue of large temperature changes.

Chapter 2

Breast Cancer: Diagnosis and Characterization

2.1 INTRODUCTION

Human breast comprises multiple tissue layers but the most common regions for the breast cancer are the mammary glands (ductal tissue), although it also sometimes occur in the stromal tissue. Ductal carcinoma, invasive and in situ, is the most common form of breast cancer. Tumors have abberant growth with higher metabolic activity and angiogenesis/neovascularization. Depending on biology, stage and growth it can be present with unusual and extensive necrotic regions.

Staging of the breast cancer is based on the size of the tumor, its presence in the lymph nodes, the extent of its spread in the breast and the rest of the body. Based on the stage and type of breast cancer the treatment path can be decided. Some of the treatments are lumpectomy, mastectomy, lymph node dissection, chemotherapy, radiation therapy, hormonal therapy, targeted therapies and complimentary medicine. With extensive treatment plans available it becomes important to detect and characterize tumors to give the best possible treatment at the right time. Further, tumors are geographicaly, etiologically and pathologically hetrogenous and therefore it becomes much more important to study it on a case by case basis before deciding on a treatment.

Various test methods, such as X-ray mammography, biopsy, ultrasound, magnetic resonance imaging (MRI) and infrared (IR) thermography have been used in the past to detect breast cancer. Although X-ray mammography, ultrasound and MRI are

non-invasive and can accurately measure the location and size of the tumor, they provide insufficient information to determine whether a tumor is benign or malignant. In order to ascertain the diagnosis, a patient has to endure multiple screenings, which can take precious time and lead to further progression of the disease.

Mammography

Among all modalities, X-ray mammography is considered to be the gold standard for breast cancer detection. Since the early 1960s, it has been the most widely used tool for breast cancer detection, but it has some significant limitations including radiation exposure, cost, patient discomfort, and more important, a high false positive rate (Sobti *et al.* 2005). Table 2.1 shows that the sensitivity (true positive rate) for this modality reduces with decreasing age, it is as high as 81 % for women older than 64 years and it drops to 54 % for women younger than 40 years. Further the results are inaccurate for "dense glandular tissue (Osako *et al.* 2007, Jackson *et al.* 1993, Kennedy *et al.* 2009), implants, fibrocystic breasts or for those on hormone replacement therapy" (Harvey *et al.* 1997, Fletcher *et al.* 2003, Hoekstra 2001, Kennedy *et al.* 2009).

It has also been reported that harmful effects of radiation exposure associated with mammography outweighs the benefits for women below a certain age (Berrington de Gonzalez 2005, Law 2007). Finally, due to pressure applied during mammography there are high chances of tumor rupture which may lead to the mixing of the malignant cells with the blood.

Table 2.1: Sensitivity (true positive rate) of mammography (Rosenberg 1998, Bronzino 2006)

	Sensitivity
Less than 40 years	54 %
40-49 years	77 %
50-64 years	78 %
More than 64 years	81 %
Women with dense breast	68 %
Women on estrogen replacement therapy	74 %

As an alternative, it is also possible to detect cancerous lesions using thermal imaging (IR thermography), a technique which is non-invasive and more comfortable for patient. Thermography is based on the fact that malignant tumors generate excess heat because of increased metabolic heat generation and they also require an increased supply of blood to support growth of cancerous cells. The increased heat generation underneath the skin surface causes increased surface temperatures and characteristic thermal signatures, which can be visualized by IR thermography (Kennedy *et al* 2009, Lawson 1956). The technical details on IR thermography are covered in chapter 1 (Introduction). In 1957 Lawson was the first to use thermography for diagnosis of breast cancer (Lawson 1957, 1958, Lawson and Chughtai 1963, *Cross ref*. E. Y. -K. Ng 2009). During the past few decades, IR thermography has been increasingly used for breast cancer detection and has been proven to be a promising adjunct diagnostic tool (Ng 2009, Kennedy *et al* 2009). It is non-invasive in nature and equipments are relatively less

expensive than some other diagnostic modalities, such as MRI. A comparative study of mammography and infrared imaging was done by Head *et al.* 1999 and is shown in Table 2.2.

Table 2.2: Comparison between mammography and infrared imaging (Head *et al.* 1999)

	Mammography	Infrared imaging
Sensitivity	86 %	86 %
Specificity	79 %	89 %
Positive predictive value	28 %	23 %
Negative predictive value	92 %	99.4 %

Thermography as an adjunct technique

Infrared thermography has been approved by FDA in 1982 as an adjunctive technique (Arora *et al.* 2008). In 1998 Keyserlingk *et al.* conducted a study to analyze the effectiveness of thermography as an adjunct technique. For ductal carcinoma detection, the sensitivity for clinical examination, mammography and infrared imaging was 61 %, 66 % and 83 % respectively. When infrared imaging was added with suspicious and equivocal mammograms the sensitivity increased from 85 % to 95 %. This further increased to 98 % with an addition of clinical examination. They observed that thermography and mammography were unable to detect tumors of less than 12.8 mm and 16.6 mm diameter respectively. When infrared imaging (thermography) was used with

clinical examination and mammography they together were able to identify 95 % of the cases (Jiang *et al.* 2005). Ng 2009 in his review of thermography for detection of breast cancer concluded that in last 15 years the thermographic tests on breast cancer have achieved specificity and sensitivity of 90 % on an average provided the tests are done by trained people and the tests are conducted according to the "strict standardized thermogram interpretation protocols".

Thermography: prognostic significance

Thermography also has prognostic significance. "Thermography has the ability to detect breast cancer 10 years prior to mammography" (Dixon 1999). The prognostic significance is highlighted by a study performed by Handley in 1962 in which they discovered that patients with a 1-2^{o} C rise had reduced chances of recurrent cancer than the patients with 3^{o} C rise. (Keyserlingk *et al.* 2000). A longitudinal study conducted by Gautherie and Gros (1980) reported that thermography was able to detect cancer at an earlier stage, compared to other modalities, such as mammography (the gold standard), ultrasonography and biopsy. This study was conducted over 12 years on a group of 1245 women with an abnormal thermogram. Their condition was initially diagnosed as normal or benign, based on conventional diagnostic modalities, including mammography, ultrasonography and biopsy. One-third of the women in this study developed breast cancer within next five years. These results suggest that thermography was better able to detect breast cancer at a very early stage of the disease, when conventional methods failed. Therefore, these researchers concluded that thermography, used in conjunction with other diagnostic modalities, can improve the early detection of breast cancer. (Isard 1984, Bronzino 2006). Combined with other imaging modalities, details about size and

location of the tumor can be obtained in addition to the heat generation rates that IR thermography can address.

"Recent advances in cancer research have determined that the biological activity of a neoplasm is far more significant an indicator of aggressiveness than the size of the tumor" (Bronzino 2006). The amount of heat generated is directly related to the degree of metabolic activity which is measurable in the form of surface temperature distribution.

Dynamic thermography

"Nagasawa and Okada (1973) reported that in order to better differentiate breast cancer from benign breast disease, thermography should be done during thermal recovery," Ohashi and Uchida 2000 used dynamic thermography to diagnose breast cancer. They reported considerable improvement in diagnostic accuracy (82% as compared to 54% in steady state thermography) but there was no improvement in the false positive rate they attributed this to the image processing system.

Quantitative Thermography

As of now thermography practice is subjective and the diagnosis is based on asymmetry, hyperthermic patterns and "complex vascular features" (Kennedy *et al.* 2009). There is a need to quantify the whole process. Theoretically it is possible to determine the size and location of the tumor based on the surface temperature distribution and the current work examines these aspects of thermography. Further the impact of the thermophysical properties on the surface temperature distribution has been analyzed and it is possible to get a fair estimate of the thermophysical properties based on the surface

temperature distribution. It is important to note that all this information can be retrieved based on non-invasive technique thermography.

In the past (Jiang *et al.* 2005, Ng and Fok 2003, Ng *et al.* 2001, Ng and Kee 2008) many computer aided tools have been used to assist doctors to make diagnostic decisions. These include artificial neural network (ANN), bayesian belief networks, linear discriminate analysis, fuzzy logic and fusion of fuzzy logic and ANN. Bayers rule analysis was used by (Ng *et al.* 2001). It had a low total accuracy of 59 % but as high as 74% of the patients had a true positive test (positive predictive value of 74 %). In 2008 Ng and Kee analyzed thermograms using ANN and bio-statistical methods. The method developed by them was able to achieve 80.95 % accuracy rate, 100% sensitivity and 70.6 % specificity.

Gautherie (1980) also observed that the metabolic heat generation rate is higher for tumors with a faster growth rate, and established a relationship between metabolic heat generation and cancer growth rate. Further, he observed that tumors with a higher growth rate had a high probability of dissemination. Thus, estimation of the metabolic activity of the tumor from surface temperature measurements can provide a measure of the malignancy of the tumor. This can prove to be an added advantage of IR thermography over other diagnostic modalities. It should be noted that high vascularization necessary to support accelerated malignant cell growth can be quantified in terms of the local blood perfusion rate. Therefore both increased metabolic activity (heat generation) and increased blood perfusion can serve as markers of malignancy. Prior studies on melanoma (clinical and computational modeling: Pirtini Çetingül and Herman, 2010) and breast cancer (computational modeling: Chanmugam *et al,* 2012)

suggest that the influence of blood perfusion on the thermal signature of the cancerous lesion is more pronounced than metabolic heat generation rate.

Therefore, it can be said that till date, thermography has been a largely qualitative technique, and diagnosis was based on qualitative criteria such as asymmetry, hyperthermic patterns and abnormal vascular patterns (Kennedy *et al* 2009). Usually, the quantitative information extracted was the temperature increase at a location selected by the person interpreting the image, compared to the temperature of a nearby region unaffected by the lesion or the corresponding contralateral location. A need exists to add additional quantitative components to the interpretation of thermal images, so that vital information about the tumor, such as size, location, metabolic activity and, most importantly, stage can be extracted from the thermograms. The problem of extracting the model parameters (location, size, perfusion) from the observable surface temperature data is known as the 'inverse problem' and will be dealt with in chapter 3. In the next section The mathematical model used to model heat transfer within the breast tissue is described in the next section.

2.2 MATHEMATICAL MODEL

The schematic of the investigated geometry is displayed in Figure 2.1. The breast shape can vary, and in this study it is modeled as a hemisphere. In clinical applications the actual shape can be measured by a 3D imager, such as the Kinect, motion sensing input devices. We consider a single tumor, which is spherical in shape and is located at the axis of the hemisphere. Other shapes, such as elliptical, can also be used, which would introduce additional unknowns to be determined in the inverse reconstruction. By selecting the axially symmetrical two-dimensional (2D) problem in this analysis, the

computational effort is kept reasonable in the initial testing stage of the reconstruction algorithm. Also, the interpretation of the results is more intuitive and algorithm progress is easier to track for the two dimensional case. Our previous study shows that the thermal signature of the tumor on the skin surface will be very similar for off axis locations (Chanmugam *et al,* 2012). The approach can easily be generalized to a three-dimensional (3D) problem, such as those discussed by Chanmugam *et al.* (2012), at a later stage and this would require improvements in the meshing of the direct problem. Further, it is assumed in the model that the thermophysical properties of the tissue and tumor are known.

The overall goal of the inverse reconstruction is to non-invasively measure key tumor parameters, the depth and size of the tumor. Since the blood perfusion rate can be related to malignancy, we add blood perfusion as the third parameter in our analysis. The inverse problem is solved for two cases, the first deals with steady state analysis, while the second case deals with a transient situation. For steady state, we reconstruct two unknown tumor parameters, the depth of the tumor measured from the skin surface (D) and the radius of the tumor (R) (Figure 2.1). In transient analysis we reconstruct a third unknown, the blood perfusion rate (ω_b).

Human breast tissue in this analysis comprised six layers: epidermis, papillary dermis, reticular dermis, fat, gland and muscle as well as the tumor, the seventh region, as indicated in Figure 2.1. The Pennes bioheat equation (Pennes (1948)) was used to model heat transfer in the layers of the breast and in the tumor as

$$\rho_n c_n \frac{\partial T_n}{\partial t} = k_n \nabla^2 T_n + \rho_b c_b \omega_{b,n} (T_b - T_n) + Q_n , \qquad \text{n} = 1, 2, 3, 4, 5, 6, 7 . \quad (2.1)$$

In Equation (2.1) ρ_b [kg/m^3], c_b [J/kg.K], T_b[K] and $\omega_{b,n}$ [m^3/s/m^3] represent the density and specific heat of blood, the arterial blood temperature and the blood perfusion rate of the tissue layer n, respectively. ρ_n [kg/m^3], c_n [J/kg.K], T_n[K], k_n[W/m.K] and Q_n[W/m^3], are the corresponding tissue properties: density, specific heat, temperature, thermal conductivity and metabolic heat generation. The thermophysical properties for the seven tissue types are summarized in Table 2.3 along with their thicknesses (th_n), based on data reported by Pirtini Çetingül and Herman (2010), Ng and Sudharsan (2001), Amri et al. (2011) and Jiang et al. (2011). Density (ρ_b) and specific heat (c_b) for blood were 1060 kg/m^3 and 3770 J/(kg.K), respectively (Pirtini Çetingül and Herman (2010)). The radius of the hemi-spherical breast V was taken to be 72 mm (Ng and Sudharsan (2001)) (figure 2.1). Blood perfusion rate and metabolic heat generation rate were tumor specific and also depend on the stage of the tumor. One of the plausible set of values is given in Table 2.3.

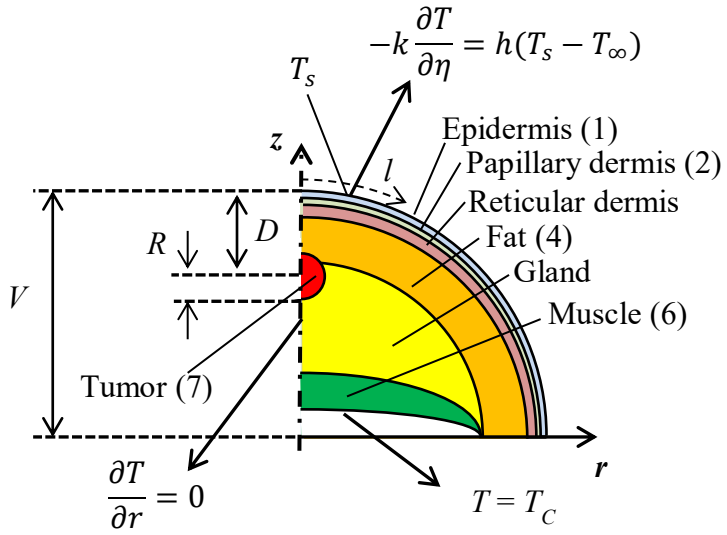

Figure 2.1: Schematic of the biophysical situation: breast cross section, tumor, tissue layers and the thermal boundary conditions.

Table 2.3: Thermophysical properties of the tissue layers in Equation (2.1)

		Thickness	Thermal conductivity	Density	Heat capacity	Blood perfusion rate	Metabolic heat generation
		Th Mm	k W/(m.K)	ρ kg/m^3	c J/(kg.K)	ω_b 10^{-4} m^3/s/m^3	Q W/m^3
1	Epidermis [a]	0.1	0.235	1200	3589	0	0
2	Papillary dermis[a]	0.7	0.445	1200	3300	2	368.1
3	Reticular dermis[a]	0.8	0.445	1200	3300	13	368.1
4	Fat	5[b]	0.21 [b]	930 [c]	2674 [a]	1.8 [b,d]	400 [b]
5	Gland	43.4[b]	0.48 [b,c]	1050 [c]	3770 [c]	5.4 [b,d]	700 [b]
6	Muscle	15[b]	0.48 [b]	1100 [c]	3800 [a]	8.1 [b,d]	700 [b]
7	Tumor	---	0.48 [b,c]	1050 [c]	3770 [c]	108 [b,d]	5000 [b]

[a] Pirtini Çetingül and Her man (2011)

[b] Ng and Sudharsan (2001)

[c] Amri *et al* (2011)

[d] Jiang *et al* (2011)

The system of seven coupled partial differential equations described by Equation (2.1) is solved for the following set of thermal boundary conditions.

Heat flux continuity and the temperature continuity at the interfaces of two tissue layers:

$$k_n \frac{\partial T_n}{\partial \xi} = k_{n+1} \frac{\partial T_{n+1}}{\partial \xi} \quad , \qquad n = 1, \ldots\ldots, 6. \tag{2.2}$$

$$T_n = T_{n+1} \, , \qquad n = 1, \ldots\ldots, 6, \tag{2.3}$$

$$k_7 \frac{\partial T_7}{\partial \xi} = k_{adj} \frac{\partial T_{adj}}{\partial \xi} \tag{2.4}$$

$$T_7 = T_{adj} \tag{2.5}$$

where ξ is the direction perpendicular to the interface between the layers, $k_{adj}$and T_{adj} is the thermal conductivity and temperature of the tissue layer adjacent to the tumor. The inner portion of the muscle layer, the region of the breast which touches the chest wall, is assumed to be at the core body temperature

$$T(z = chest\ wall) = T_C = 37\ ^{\circ}\text{C} \ . \tag{2.6}$$

The skin surface is exposed to ambient air during the exam, which leads to loss of heat to the atmosphere, described by the convective boundary condition as

$$-k_1 \frac{\partial T_1}{\partial \eta} = h\left(T_{1,s} - T_{\infty}\right) \ . \tag{2.7}$$

where h = 10 $\text{Wm}^{-2}\text{K}^{-1}$, k = 0.235 $\text{Wm}^{-1}\text{K}^{-1}$, T_{∞} = 21 ℃

where h is the convective heat transfer coefficient, k_1 is the thermal conductivity of the epidermis, the outermost tissue layer, $T_{1,s}$ is the temperature of the epidermis at the skin surface in contact with air and η is the direction perpendicular to the skin surface.

Dynamic IR imaging involves cooling of the skin surface and analysis of the transient thermal response to the excitation. Initially the skin surface is at steady state under ambient conditions. It is cooled by maintaining the surface at 14 ℃ for time t_c. This is modeled by using constant temperature boundary condition.

$$T_s = 14\,℃ \qquad 0 \leq t < t_c \tag{2.8}$$

The cooling in our analysis is applied for the duration of $t_c = 60$ s (Cheng and Herman (2014)). It should be noted that here computational phantom is being used. Subsequently the surface is again exposed to the ambient conditions in the exam room and hence the convective boundary condition (equation (2.7)) is applied on the surface. This reheating process following the exposure to cooling is called the thermal recovery. Surface temperature data in this study are computed or recorded for 1000 s during the thermal recovery process.

The system of seven partial differential equations (2.1) is solved, subject to boundary conditions (2 - 8) using the commercial software COMSOL Multiphysics v 4.3 (2013). A MATLAB code was developed for solving the inverse problem. While solving the inverse problem in MATLAB, COMSOL was accessed to compute temperature distributions for a given set of input parameters updated by the inverse reconstruction algorithm. For the purpose of communication and control of COMSOL by means of MATLAB, the LiveLink for MATLAB was used. The PC computer system used to run the present model was equipped with an Intel core i-7 processor, with 3.4 GHz frequency and 32 GB RAM. A typical mesh generated for the computational domain contains 8,000 elements (figure 2.2(a)). It takes about 6 seconds to solve the set of equations for steady state analysis and about 16 seconds for the transient analysis. Mesh sensitivity analysis

was carried out to ensure that the change in temperature, due to further refinement of the mesh, was less than 0.1 %. The choice of the time step was governed by two factors, computational speed and accuracy. A smaller time step increases the accuracy but it also leads to increase in computational time. For the present case a time step of 2 seconds was taken as the temperature change was less than 0.1% after decreasing the time step. The steady state temperature distribution in the cancerous breast for the conditions described by equations (2.1-2.8), obtained using COMSOL, is shown in figure 2.2 (b).

This section is divided into two parts. In the first part (Chapter 3) cancerous breast model is analyzed, the effect of various parameters on the surface temperature is studied. Second part (Chapter 4) focuses on solving the inverse problem of detecting tumor parameters based on surface temperature distribution.

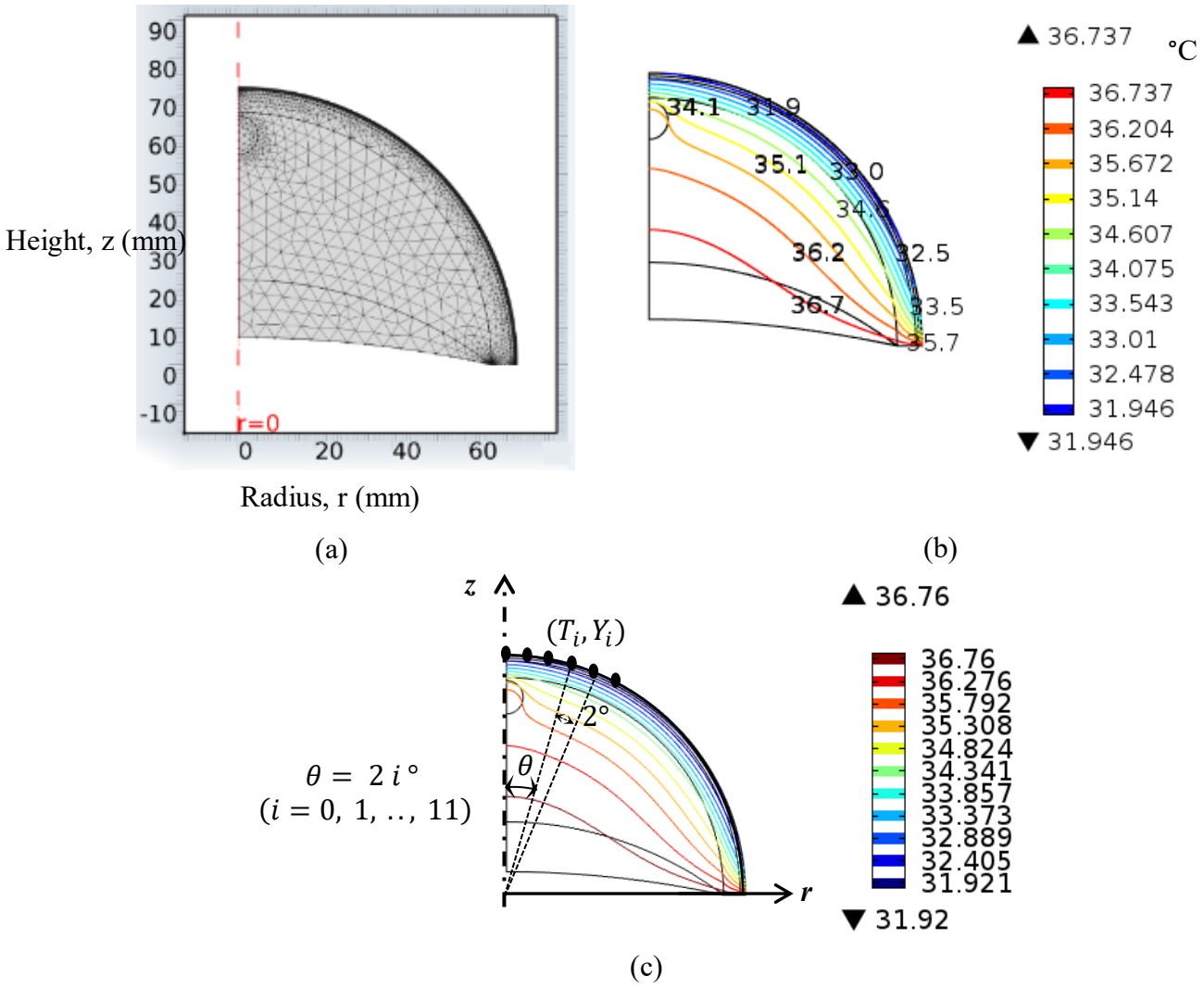

Figure 2.2: (a) Computational mesh, (b) computed temperature distribution in the cancerous breast and (c) coordinate system and surface data points used for the inverse reconstruction

Chapter 3

Thermal Analysis of Cancerous Breast Model

The complete authorship of this work should be read as Dr. Arjun Chanmugam, Rajeev Hatwar and Prof. Cila Herman. The development of computational model and the analysis was performed by Rajeev Hatwar under the guidance of Prof. Cila Herman and Dr. Arjun Chanmugam. This work was published in International Mechanical Engineering Congress Exposition 2012 (Chanmugam, Hatwar and Herman 2012).

3.1 INTRODUCTION

Thermography (Infrared imaging) has been around since the late 1950s, but the mechanisms of heat transfer between diseased and native tissue and the differences between the two have yet to be well described. Previous studies indicate that tumors generate more heat than healthy tissue and this temperature difference can be identified by using steady state thermal imaging (Lawson 1956, Kennedy *et al.* 2009). Despite the technological advances made with infrared imaging, thermographic imaging largely remains qualitative in nature (Kennedy *et al.* 2009) which limits its utility.

Researchers have used computational modeling to relate the skin surface temperature distribution to tumor size and location for breast cancer (Osman and Afify 1984, 1988 , Sudharsan *et.al.*1999, Sudharsan and Ng 2000, Ng and Sudharsan 2001, Jiang *et al.* 2011). Osman and Afify (1984, 1988) were one of the first using a hemispherical model with different tissue layers of uniform thickeness. Later Sudharsan and Ng (2000, 2001) used models which adequately depicted the breast anatomy. Jiang et al (2011) have incorporated elastic deformation in their modeling.

Mital and Pidaparti 2008 and Mitra and Balaji 2010 used evolutionary alogrithms and neural networks respectively to predict tumor size and location using breast thermograms. In their analysis the metabolic heat generation rate was varied with tumor diameter, whereas the blood perfurion rate of the tumor was kept constant.

In this study, we present a quantitative analysis to provide a more accurate description of the thermal characteristics of breast cancer lesions including the dependance of the temperature distribution on size, shape, and depth of the lesion. Specifically we used a parametric analysis of the breast to obtain a set of features that can be used to predict the location and size of the breast cancer lesion from surface temperature measurements, which is essential in diagnostic applications. In order to improve thermal image acquistion procedure and ensure reproducibility and accuracy of the imaging procedure, a cooling load was applied in the analysis to enhance the thermal visibility and allow meaningful measurements of the physical and thermophysical characterisitics of the lesion. This work should allow clinicians a more accurate, noninvasive and cost effective tool in the early diagnosis of one of the most common and dangerous cancers.

3.2 NUMERICAL MODELING

The dimensions of these layers are given in Table 3.1. In order to investigate early stage cancer, the tumor diameter has been kept under 20 mm (Hammer *et al.* 2008). The blood perfusion rate (ω_b) for fat, gland, muscle and tumor is taken as 0.0006 sec^{-1} , 0.0009 sec^{-1} and 0.012 sec^{-1} respectively. These values are close to the values used by Ng and Sudharsan (2001).

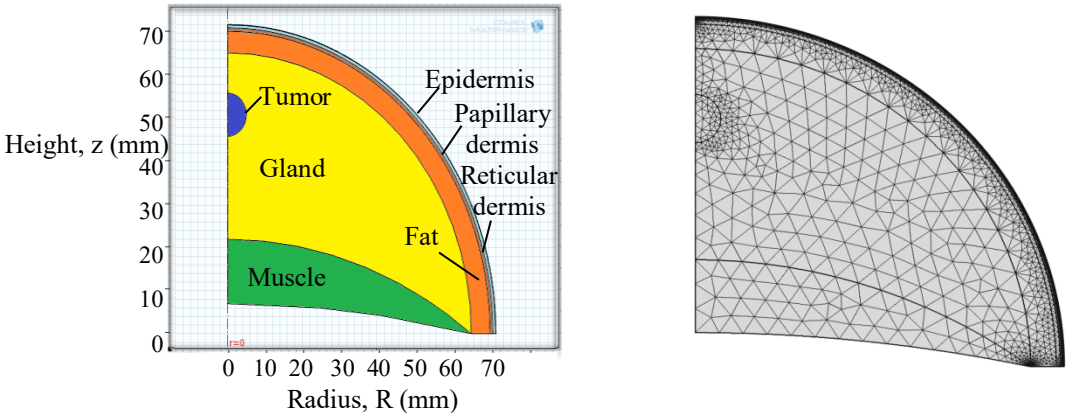

Figure 3.1: (a) Schematic of the breast used in the computational model. The various tissue layers are epidermis, papillary dermis, reticular dermis, fat, gland and muscle layers. It is 2D axisymmetric model and has a spherical tumor centered at the axis. (b) The domain is divided into numerous smaller regions comprising of elements. The computational mesh hence generated is shown here.

The commercial software COMSOL Multiphysics v 4.2 (2011) was used to solve these equations, which uses FEM to solve the underlying equations. The mesh generated in COMSOL is displayed in figure 3.1 (b). The mesh is finer for thin layers (epidermis, papillary dermis and reticular dermis) compared to other layers. In order to ensure the mesh independence we tracked the temperature of a point on the axis located on the surface and the average surface temperature. The grid points were varied from 5000 to 29000 and the temperature difference was less than 0.1 %. To ensure that the transient analysis is independent of the time step, the surface temperature at the axis was tracked. The variation in temperature was less than 0.1% when the time step was varied from 0.1 seconds to 2 seconds. Hence a mesh with 7800 grid points and a time step of 1 s (the time step was 0.1 s for the initial 10 s) were used.

Table 3.1: Thermophysical properties

	Epidermis [a]	Papillary Dermis [a]	Reticular Dermis [a]
h (mm)	0.1	0.7	0.8
k (W/m.K)	0.235	0.445	0.445
ρ (kg/m^3)	1200	1200	1200
c (J/kgK)	3589	3300	3300
Q (W/m^3)	0	368.1	368.1
ω_b (m^3/s/m^3)	0	0.0002	0.0013

	Fat	Gland	Muscle	Tumor
h (mm)	5.0[b]	43.4[b]	15 [b]	--
k (W/mK)	0.21 [c]	0.48 [c]	0.48 [c]	0.48 [c]
ρ (kg/m^3)	930 [d]	1050 [d]	1100 d	1050 [d]
c (J/kgK)	2770[d]	3770 [d]	3800 [a]	3852 [a]
Q (W/m^3)	400 [c]	700 [c]	700 [c]	5000 [e]

[a] Cetingul and Herman 2010

[b] Sudharsan and Ng 2000

[c] Ng and Sudharsan 2001

[d] Amri *et al.* 2011

[e] Jiang *et al.* 2011

3.3 Results and discussion

In this section computational simulation results are presented and discussed. The analysis is divided into two parts, steady state and transient. In steady state analysis the

effect of tumor size and location on the surface temperature is studied. Based on this analysis two key features were identified, which can be used to predict the tumor characteristics. In addition, a parametric study is carried out to investigate the effect of blood perfusion rate and metabolic heat generation rate of the tumor on the surface temperature. The second part of this section focuses on the transient analysis and the propagation of the cooling effect into the tissue. The effect of cooling time and cooling temperature on the thermal contrast on the skin surface, obtained during recovery phase, is analyzed.

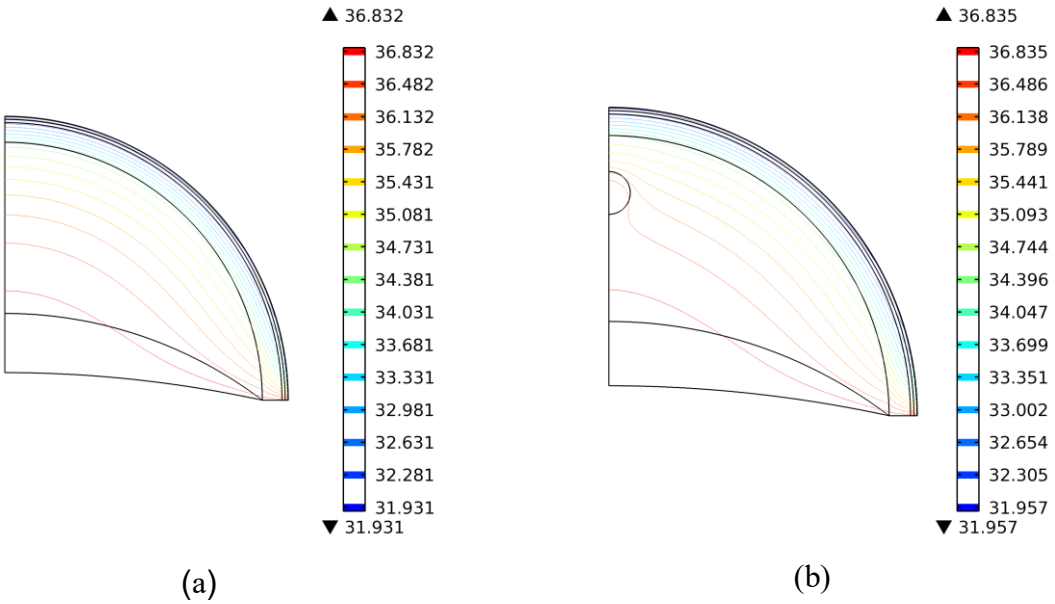

Figure 3.2: (a) Isotherms for normal breast (b) isotherms for cancerous breast

3.3.1 Steady State Analysis

Figure 3.2 (a) shows the isotherms for the half cross section in a model of a normal breast during steady state. The temperature decreases through the tissue towards the skin surface. The isotherms for cancerous breast are shown in figure 3.2 (b). Near the tumor the isotherms become distorted and indicate that the tumor has higher temperature when

compared to the normal tissue. This increase in temperature is also visible on the skin surface.

Effect of tumor size and depth

The surface temperature, T, along the circumference of the breast is displayed in figure 3.3(a). The surface temperature profiles for different sizes (r, tumor radius) and locations of the tumor (d, depth beneath the skin surface) are plotted along with the temperature profile for a normal case. The results suggest there is temperature increase in the range from 0.1°C to 0.8°C, and these increases can be accurately measured by modern infrared cameras, which have temperature and spatial resolution of 10 mK and 0.05 mm respectively. The difference in temperature, ΔT, between the cancerous and normal (without lesion) case (bottom blue line in figure 3.3(a)) is plotted in figure 3.3 (b) to analyze the effect of tumor. As expected, for an axisymmetric tumor, the maximum temperature rise, ΔT_{max}, is detected at the axis. For a fixed tumor radius of 5 mm, the maximum temperature difference increased from 0.08 °C to 0.58 °C as the depth of tumor is decreased from 20 mm to 10 mm. Similarly, for a fixed depth of 15 mm, the maximum temperature difference increased from 0.03 °C to 0.50 °C as the radius of the tumor is increased from 2.5 mm to 7.5 mm. All other properties remained the same.

The dependence of the maximum temperature difference on tumor size and depth is shown in figure 3.4 (a). The result agrees with the observation made by Amri *et al.* 2011 that the presence of tumor is always accompanied with an increase in surface temperature. The temperature rise might be very small but it is always present even for very a small tumor. It is clear from the figure 3.4 (a) that as the tumor size increases for

fixed depth and as the depth of the tumor decreases for fixed diameter, the maximum temperature difference increases.

According to a similar analysis done by Amri *et al.* 2011 and Jiang *et al.* 2011, they obtained negligible variation in maximum temperature difference with varying tumor size. In their analysis they used equation

$$Q = C/(468.6 \ln 200 r + 50) \quad (3.1)$$

to calculate metabolic heat generation from the diameter of the tumor. According to this expression, the metabolic heat generation rate decreases with increasing size. Due to this decrease, the effect of increasing size of tumor is countered by the decreasing metabolic heat generation rate, and therefore there is no significant change in maximum surface temperature as the size of the tumor varies. Therefore, the mismatch between the results obtained here and that given in literature is due to the variation in metabolic heat generation rate. In order to do a comprehensive analysis we assume that the metabolic heat generation rate is independent of the tumor diameter. We treat it as an independent parameter, which is more consistent with clinical observations both large and small tumors can be aggressive and have large metabolic heat generation rates, and vice versa.

While figure 3.4 (a) is helpful to understand the behavior of maximum temperature rise as the depth and size of the tumor are varied, this result alone cannot be used to estimate the location and size of the tumor. The analysis suggests that the same maximum temperature rise can be observed for different combinations of tumor depth and size.

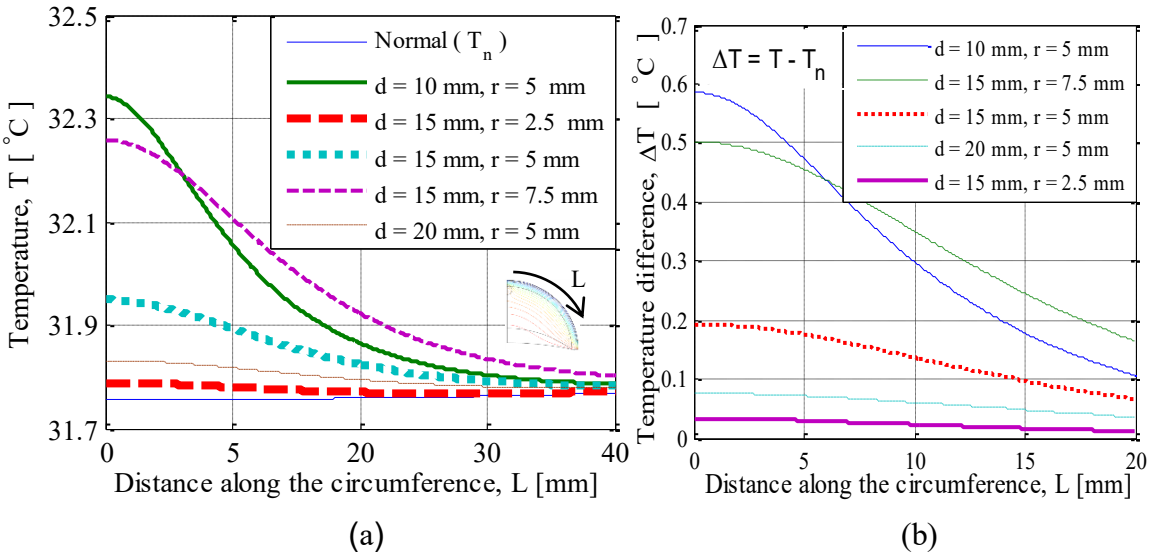

Figure 3.3: (a) Surface temperature along the circumference of the breast, starting from the axis, for tumors radius *r* and tumor depth *d* as parameters.(b) The rise in surface temperature due to the presence of tumor, *ΔT*, has been plotted here. It increases with increasing tumor radius for a fixed tumor depth of 15 mm and with decreasing tumor depth for a fixed tumor radius of 5 mm.

The results in figure 3.3 (b) indicate that the slope of the temperature difference curve increases (it becomes steeper) with decreasing tumor depth. Here 'half temperature difference length' (L_T), is used as a measure of this slope. It is defined as the distance from the axis along the circumference at which the temperature difference drops to half its maximum value. As the slope of the temperature profile increases, the corresponding L_T decreases. Figure 3.4 (b) shows the variation of the half temperature difference with size and depth of the tumor, and the results indicate that L_T decreases with decreasing depth and radius. When L_T is used along with maximum temperature difference, the location and size of the tumor can be estimated. Even though there are different combinations of radius and depth which gives same ΔT_{max} (figure 3.4 (a)), those particular set of combinations will not give the same L_T (figure 3.4 (b)) as can be clearly

seen from figure 3.4. The size and depth of the tumor are the only variables in this analysis, and metabolic heat generation and blood perfusion rate were kept constant.

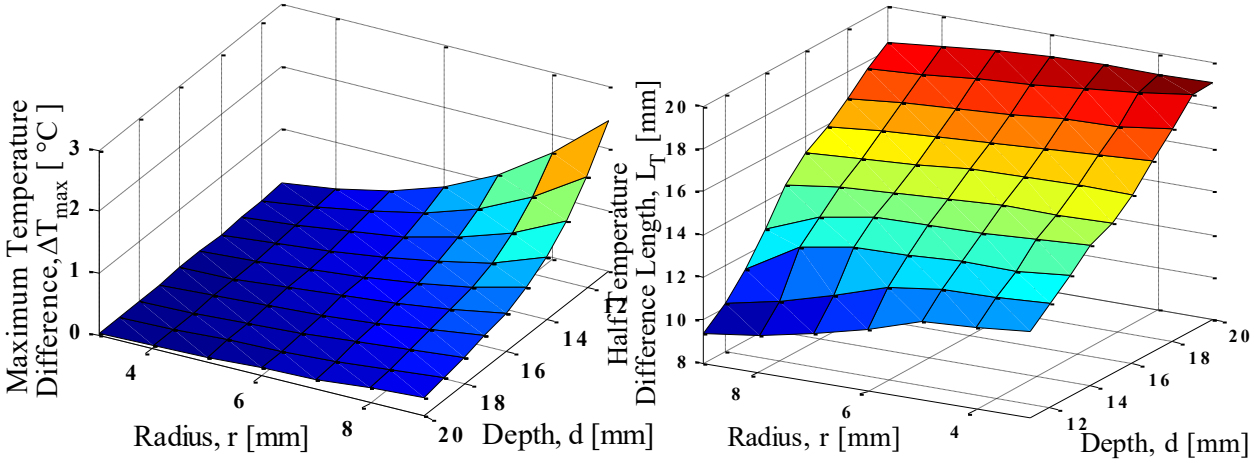

Figure 3.4: (a) Maximum temperature difference, ΔT_{max}, as function of tumor size and depth (b) the half temperature difference length, L_T, (a measure of the slope) as function of tumor size and depth.

Off-axis tumors

In the foregoing analyses, we largely considered tumors that were symmetrical around the axis. In this section off-axis tumors are analyzed by varying the polar angle of the tumor. The computational model is three dimensional. The governing equations and boundary conditions are still given by equations 2.1-2.8. Even though the model has changed from 2D axisymmetric to three dimensional, the equations will remain the same as they are in general form and can be used for any dimensional space/coordinate system. Figure 3.5 shows the surface temperature distribution for tumors with polar angles of 0^o, 30^o and 60^o. It can be seen that the region with maximum temperature moves away from the center as the polar angle of the tumor increases. This can be seen more clearly in figure 3.6, which shows the temperature along the circumference for different positions

of the tumor. The polar angle of the maximum temperature location is equal to that of the tumor.

Parametric variation

The effect of blood perfusion rate and metabolic heat generation on the surface temperature difference (increase in surface temperature due to the presence of tumor) has been analyzed in figure 3.7. With increasing blood perfusion rate and metabolic heat generation the temperature difference increases. When the blood perfusion rate is quadrupled, from 0.006 sec^{-1} to 0.024 sec^{-1}, the temperature difference at the axis increases from 0.4 °C to 0.8 °C. When the metabolic heat generation rate is quadrupled from 2500 W/m^3 to 10000 W/m^3 the temperature difference increases by 0.05 °C. It can be seen that blood perfusion rate has much more impact on the surface temperature distribution than the metabolic heat generation rate. It can also be concluded that the surface temperature is more sensitive to the variations of the blood perfusion rate than to the metabolic heat generation rate.

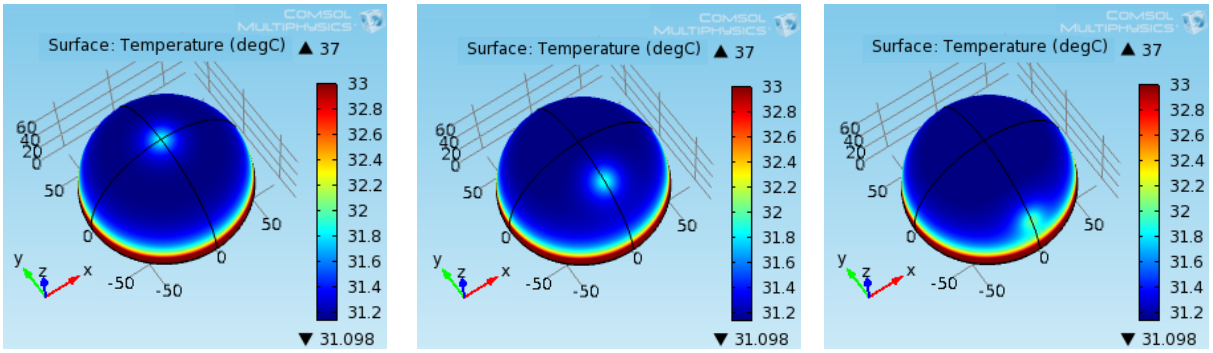

(a) (b) (c)

Figure 3.5: Surface temperature distribution for tumors with polar angles: (a) 0° (b) 30° (c) 60°.

3.3.2 Transient State Analysis

In this section the effect of the application of cooling load, also called thermostimulation, and the subsequent recovery phase (thermal response when the cooling load is removed), is analyzed. Factors affecting the magnitude of the thermal contrast during recovery phase are investigated.

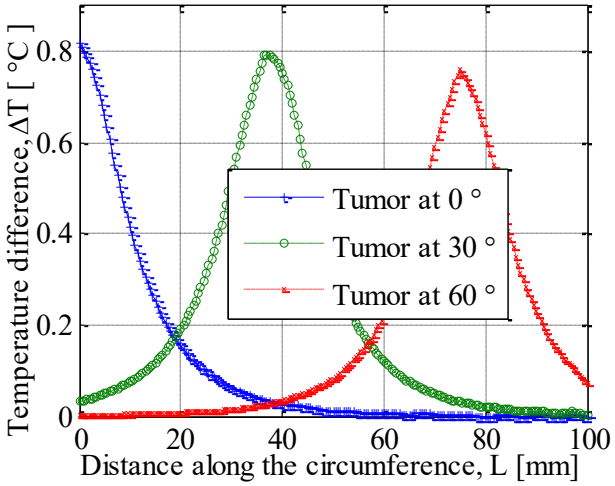

Figure 3.6: Surface temperature along the circumference for off-axis tumors

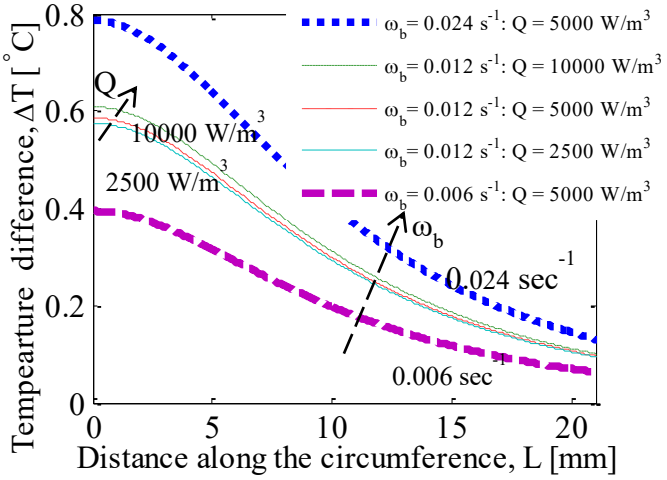

Figure 3.7: Variation in surface temperature distribution with varying blood perfusion rate and metabolic heat generation rate

Cooling Phase

Figure 3.8 shows the axial temperature profile during the cooling phase. The constant temperature boundary condition is applied for cooling and due to this the temperature at the surface is at 14 °C during cooling. As time progresses the temperature below the surface decreases with increasing cooling time. To obtain an estimate of the extent of the cooling, the cooling penetration depth has been defined as the maximum distance from the surface for which the drop in temperature is more than 0.3 °C. Figure 3.9 shows the variation in cooling penetration depth with time. As expected, the cooling depth increases with increasing cooling time.

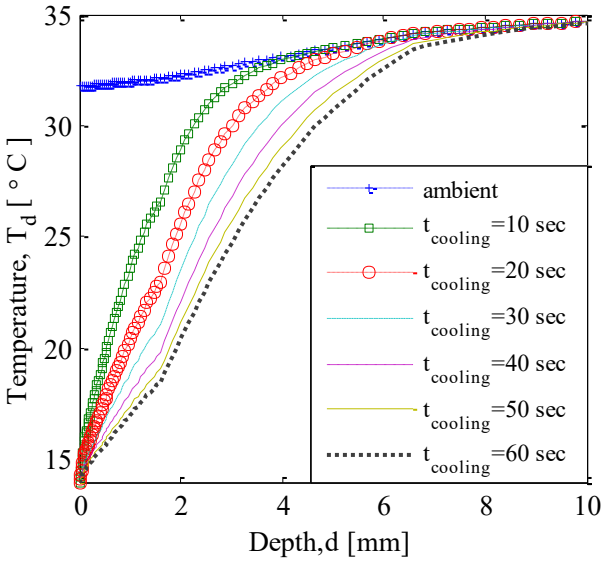

Figure 3.8: Temperature profile along the surface during cooling

Thermal recovery phase

Axial Temperature Profile: After the cooling load is removed, the temperature gradually increases and over time reaches the steady state condition. Figure 3.10 shows how the axial temperature changes after the cooling load is removed. It can be seen that, as time progresses, the temperature profile approaches the steady state condition (no cooling

load). The temperature of the tissue increases gradually after removing the cooling load. When the temperature profiles, just after removal of cooling and 50 seconds later, are compared, it is observed that the temperature of the region which is within 3 mm from the surface (towards the left of point (A)) experiences a decrease in temperature, whereas the deeper regions are still undergoing cooling. Similarly, when comparing temperature profiles at 50 seconds and 200 seconds, the region which is deeper than 6 mm is still undergoing cooling. Therefore it can be concluded that there is a time lag between removal of cooling load and rising of the temperature in the tissue and thus the cooling depth keeps on increasing even after removing the cooling load.

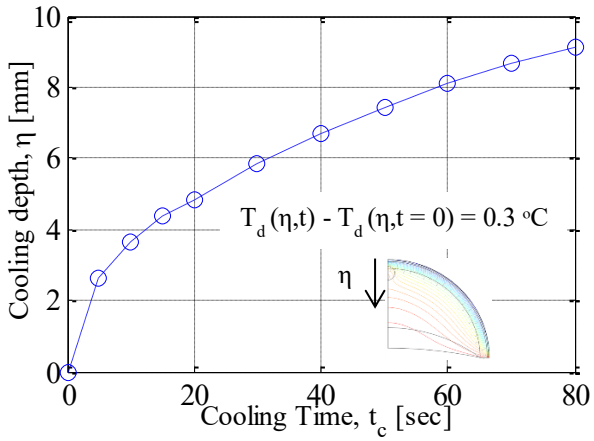

Figure 3.9: Cooling depth vs. cooling time

Recovery Profile: In figure 3.11 the surface temperature just above the tumor (on the axis) is plotted as a function of time during the thermal recovery phase for the normal and cancerous case. It should be noted that the plotted temperature is from the location which has the maximum temperature rise. The difference between the two profiles is indicated on the right axis. Constant temperature of 14 °C was applied during cooling, and therefore the recovery curve starts from 14 °C for both the cases. It can be seen that the difference between the two temperature profiles reaches a maximum of 0.9 °C after 10

minutes, and this time will be referred to as 'peak time'(t_p). The difference gradually stabilizes to 0.6 °C which is the steady state temperature difference. It can be seen that the temperature contrast increases by 0.3 °C due to the application of cooling load.

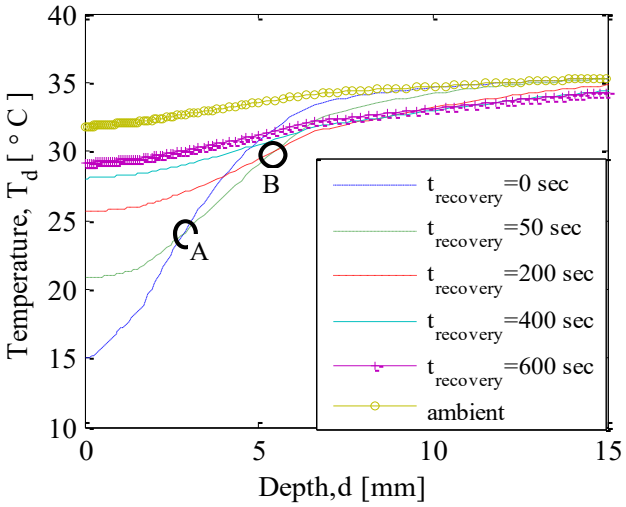

Figure 3.10: Temperature profile along the axis during recovery after 60 s of cooling

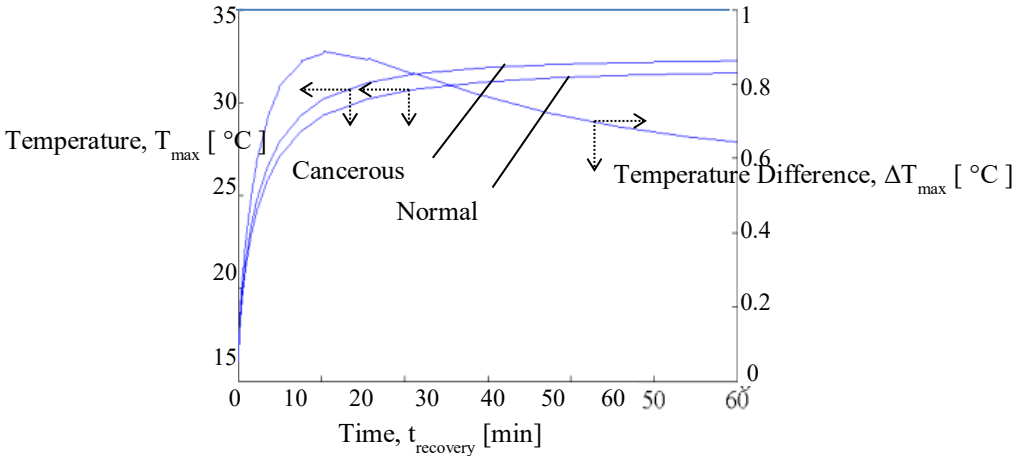

Figure 3.11: The effect of tumor on the temperature difference vs. time graph during recovery phase

Effect of cooling load: In this section the effect of cooling load on the thermal recovery profile is analyzed. Two cooling methods are considered: constant temperature cooling and convective cooling. When the cooling time, for constant temperature cooling, is increased from 10 seconds to 80 seconds the maximum temperature difference during

recovery, $\Delta T_{max,recovery}$, increases from 0.7 °C to 0.9 °C (figure 3.12). When the cooling temperature is reduced from 20 °C to 14 °C for the constant temperature cooling case the maximum temperature difference increases from 0.75 °C to 0.9 °C (figure 3.13). For the convective cooling situation the maximum temperature difference increased from 0.60 °C to 0.65 °C when cooling time was increased from 30 seconds to 120 seconds (figure 3.12). When the cooling temperature is decreased from 20 °C to 14 °C for the convective cooling case the maximum temperature difference increases from 0.60 °C to 0.62 °C (figure 3.13). The increase in maximum temperature difference is more for constant temperature cooling as compared to convective cooling.

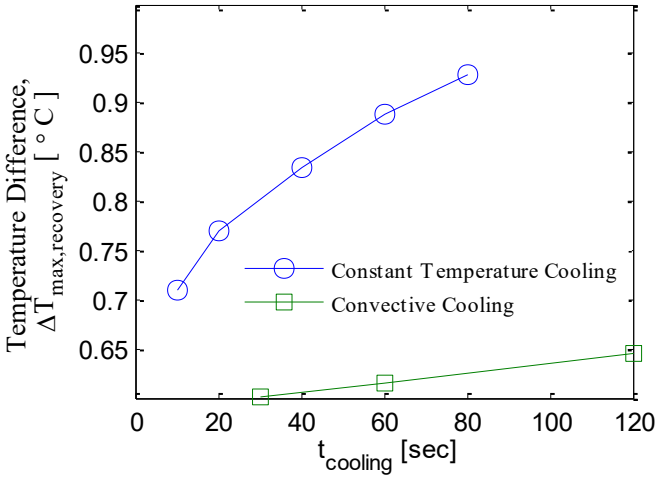

Figure 3.12: Effect of cooling time on the maximum temperature difference

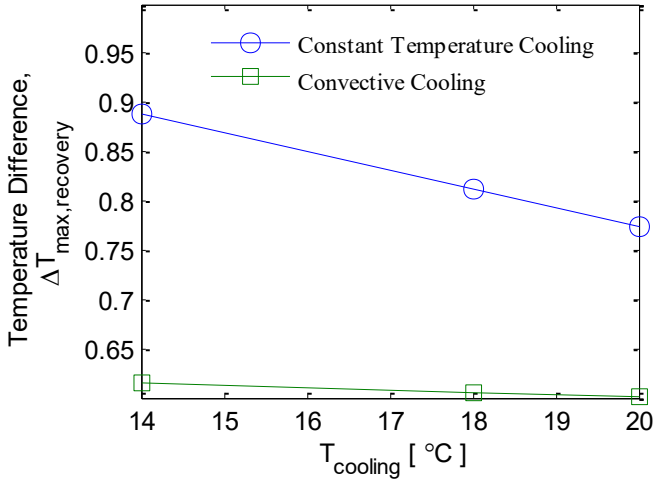

Figure 3.13: Effect of cooling temperature on the maximum temperature difference

3.3.3 Key Features to predict size and location of the tumor

As mentioned in section 3.3.1 there are two key features of the surface temperature profile relevant for predicting lesion properties: maximum temperature difference and half temperature difference length. By using these two features it is possible to estimate the location and size of the tumor. It should be noted that the blood

perfusion rate and metabolic heat generation rate are known quantities in the analysis. Further, only axisymmetric case was considered.

It was also observed that for off-axis tumors the polar angle of the tumor can be determined using surface temperature profile. Using this observation and the above mentioned features, it is possible to extend this analysis for a general case of off-axis tumors.

3.4 Conclusions

In the present work a 2D axisymmetric model of the breast was introduced and solved for temperature distribution under various conditions using FEM based commercial software COMSOL. The surface temperature distribution for various sizes and locations of axisymmetric tumors was analyzed. The behavior of off-axis tumors was analyzed next, and it was shown that the polar location of the tumor can be predicted using the surface temperature profile. The parametric analysis during steady state conditions predicts that the variation in surface temperature profile due to metabolic heat generation is negligible as compared to blood perfusion rate.

It is observed by means of transient analysis that the cooling depth increases even after removing the cooling load. The effect of cooling load on the recovery profile was analyzed and it was found that as the cooling time increases and cooling temperature decreases the highest temperature difference increases for both constant temperature cooling and convective cooling. Constant temperature cooling is far more effective than convective cooling.

Based on the steady state analysis two key features, maximum temperature difference and half temperature difference length were identified as data allowing to

estimate the location and size of the tumor from the surface temperature distribution. In this analysis metabolic heat generation and blood perfusion rate were assumed to be known quantities. Though the analysis was conducted for the axisymmetric case, it can be extended to off-axis tumors (section 3.3.1: 'Off-axis tumors') based on the observation that the polar angle of the tumor can be estimated using the surface temperature distribution.

Chapter 4

Inverse method for quantitative characterization of breast tumors from surface temperature data

The complete authorship of this work should be read as Rajeev Hatwar and Cila Herman. This work was published in International Journal of Hyperthermia (Hatwar and Herman 2017).

4.1 INTRODUCTION

Inverse problems are encountered in various fields of science and engineering, we will be dealing here with its application in bio-medicine. In the present study, tumor parameters are extracted from the surface temperature distribution, as the heat is generated within the body from the tumors and transported in all directions. In thermographic (Infrared) imaging a volume heat source (increased metabolic heat generation and blood perfusion in the malignant tumor is compared to normal heat generation in healthy tissue) is located within the body. We use the bioheat transfer equation here to model heat transfer processes inside human tissue, and compute surface temperature signatures which serve as input data for the inverse reconstruction algorithm. Then, based on the surface temperature profile, we estimated tumor parameters.

During the past few years, several research teams (Mital and Pidaparti 2008, Mitra and Balaji 2010, Bezerra *et al* 2013, Das and Mishra, 2013 and 2014) attempted to solve the inverse problem for breast cancer. Mital and Pidaparti (2008) simultaneously

estimated size, location and metabolic heat generation, and used Artificial Neural Network (ANN) and Genetic Algorithm (GA) methods on a multilayer, 2D model. Bezerra *et al* (2013) estimated thermal conductivity and blood perfusion rate using the Sequential Quadratic Programming method. They used a 3D surrogate geometry based on external breast prosthesis. Both these researchers (Mitra and Balaji (2010) and Bezerra *et al* (2013)) used a correlation for their analysis that related the diameter of the tumor with the metabolic heat generation rate. According to this correlation, larger tumors have lower metabolic heat generation rate. However, Gautherie (1980) observed that the metabolic heat generation rate was cancer-specific and case-specific and it was constant during tumor evolution. Based on his work, it can be concluded that the metabolic heat generation rate might not always be entirely dependent on the size of the tumor. Therefore, there is a need to relax this assumption inherent in the correlation used by Mitra and Balaji (2010) and Bezerra *et al* (2013).

Mitra and Balaji (2010) used the artificial neural network (ANN) method on a single tissue, 3D hemispherical model to simultaneously estimate size, location and metabolic heat generation of the lesion. It should be noted that they have used steady state data for their analysis. It will be shown in the present work that it is difficult to simultaneously estimate three tumor parameters (dimensions, location, metabolic heat generation rate or blood perfusion rate) with accuracy and uniquely, based on the steady state data alone. We will show that, for some situations, two different tumors can exhibit similar surface temperature signatures, and an inverse method based on steady state data alone can converge into incorrect solutions. The presence of noise and uncertainty coming from the clinical environment and during the acquisition of the surface

temperature can further add to the challenge. Therefore, inclusion of additional information in the form of transient response makes it possible to estimate the third parameter uniquely. The transient response is obtained after an application of cooling load to the surface and then recording the recovery profile. Das and Mishra (2013, 2014) estimated the size and location of tumor in a 2D rectangular domain, using the genetic algorithm and curve fitting method. They considered breast as a uniform tissue instead of a multilayer structure. In 2015, Das and Mishra extended their analysis to 3D hemispherical domain and used curve fitting method. All these researchers have based their analysis on steady state temperature data.

Based on the literature survey conducted, a need for an inverse reconstruction method exists that will allow us to simultaneously and uniquely estimate size, location and blood perfusion rate, a measure for the metabolic activity, of the tumor based on the surface temperature signature. In the present work we used, the Levenberg-Marquardt (LM) method (Ozisik and Orlande (2000)) to uniquely and simultaneously estimate the above mentioned parameters. We found that for this inverse analysis the steady state surface temperature was not sufficient to yield a unique solution, therefore, we added the transient data set to our inverse reconstruction algorithm. Transient data were generated by applying a cooling load and then recording the temperature as the tissue recovered (Pirtini Çetingül and Herman (2011), Cheng and Herman (2014)). It should be noted here that transient analysis has been used before (Deng and Liu 2000, Liu *et al* 2002) for inverse analysis, however it was limited to the estimation of the blood perfusion rate only. Kleinman and Roemer (1983) also used the transient analysis on a one-dimensional model to estimate the temperature distribution and blood perfusion rate beneath the

surface based on surface temperature data. Further, transient analysis was also used by Bhowmik and Repaka (2016) to estimate the geometric and thermophysical properties for melanoma. Although similar to our work there are major dissimilarities, among other things we have given an explanation for the need of transient analysis, have used initial guesses far away from the exact parameters, used a different optimization algorithm and have reduced computational time. Blood perfusion rate is a potential indicator of the increased cell activity in the tissue, which can be potentially related to the stage of the tumor (Gautherie (1980)). There are many variables involved in the accurate staging of the tumor and blood perfusion rate at best can be used an adjunct technique. Thus the transient version of the inverse method has a potential to aid in the staging of the tumor by estimating blood perfusion from the surface temperature signature.

The novelty in the present model is the combination of a more complex geometry, (which includes all the tissue layers with their thermophysical properties), incorporation of transient data and estimation of blood perfusion along with depth and size of tumor. One of the major advantages of the present inverse method over previously reported methods is that it uses transient data in addition to steady state data for the estimation of parameters, which resolves some issues encountered with the uniqueness of reconstruction based on steady state data alone. This additional set of input data improves the accuracy of the solution and can reduce the effect of noise in the input data therefore improving the robustness of the solution. The need for the transient analysis will be further justified in sections 4.3.2 and 4.3.3. Unlike some of the inverse methods used earlier (Mital and Pidaparti 2008, Mitra and Balaji 2010), this method is not statistical, therefore, it is more simple and intuitive. The progression of the solution can be

monitored, which is useful while accessing the performance and progress of the algorithm. Furthermore, our inverse method does not require test cases to train the algorithm like the statistical methods, which can prove to be an important advantage while applying this technique in clinical setting. The goal of our study was to develop inverse reconstruction software to support our portable infrared imaging system, therefore special attention was devoted to keeping the computational effort reasonable. The objective is to run the image, acquisition, processing and inverse reconstruction algorithms on a portable PC or laptop.

4.2 METHODOLOGY

The inverse reconstruction of tumor parameters based on surface temperature data involves several steps. In this study we use a computational phantom of the breast with the tumor to generate the surface temperature data for the testing of the reconstruction algorithm. In a clinical implementation these surface temperature data would be acquired by infrared imaging. The advantage of using a computational phantom to test the inverse reconstruction method is that the exact parameters of the tumor are known and this allows easy testing of the inverse reconstruction accuracy. The computational phantom also allows the flexibility to vary tumor properties in parametric studies. Once the inverse reconstruction method is extensively tested and validated, measurement data are used. We describe the mathematical model used to generate the computational phantom, as well as to solve the direct problem in Section 4.2.1. The direct problem involves calculation of the surface temperature distribution for a given set of system parameters during the iterative inverse reconstruction process. For solving the direct problem, FEM based commercial software COMSOL Multiphysics v 4.3 (2013) was used. The

Levenberg-Marquardt (LM) method was used to estimate the unknown tumor parameters using successive iterations and it is described in Section 4.2.2.

4.2.1 Mathematical model

Table 4.1: Thermophysical properties of the tissue layers in Equation (2.1)

		Thickness	Thermal conductivity	Density	Heat capacity	Blood perfusion rate	Metabolic heat generation
		Th Mm	k W/(m.K)	ρ kg/m^3	c J/(kg.K)	ω_b 10^{-4} m^3/s/m^3	Q W/m^3
1	Epidermis [a]	0.1	0.235	1200	3589	0	0
2	Papillary dermis[a]	0.7	0.445	1200	3300	2	368.1
3	Reticular dermis[a]	0.8	0.445	1200	3300	13	368.1
4	Fat	5[b]	0.21 [b]	930 [c]	2674 [a]	1.8 [b,d]	400 [b]
5	Gland	43.4[b]	0.48 [b,c]	1050 [c]	3770 [c]	5.4 [b,d]	700 [b]
6	Muscle	15[b]	0.48 [b]	1100 [c]	3800 [a]	8.1 [b,d]	700 [b]
7	Tumor	---	0.48 [b,c]	1050 [c]	3770 [c]	108 [b,d]	5000 [b]

[a] Pirtini Çetingül and Herman (2011)

[b] Ng and Sudharsan (2001)

[c] Amri *et al* (2011)

[d] Jiang *et al* (2011)

The system of seven partial differential equations (2.1.1) is solved, subject to boundary conditions (2.1.2 – 2.1.8) using the commercial software COMSOL Multiphysics v 4.3 (2013). A MATLAB code was developed for solving the inverse

problem. While solving the inverse problem in MATLAB, COMSOL was accessed to compute temperature distributions for a given set of input parameters updated by the inverse reconstruction algorithm. For the purpose of communication and control of COMSOL by means of MATLAB, the LiveLink for MATLAB was used. The PC computer system used to run the present model was equipped with an Intel core i-7 processor, with 3.4 GHz frequency and 32 GB RAM. A typical mesh generated for the computational domain contains 8,000 elements (figure 4.1 (a)). It takes about 6 seconds to solve the set of equations for steady state analysis and about 16 seconds for the transient analysis. Mesh sensitivity analysis was carried out to ensure that the change in temperature, due to further refinement of the mesh, was less than 0.1 %. The choice of the time step was governed by two factors, computational speed and accuracy. A smaller time step increases the accuracy but it also leads to increase in computational time. For the present case a time step of 2 seconds was taken as the temperature change was less than 0.1% after decreasing the time step. The steady state temperature distribution in the cancerous breast for the conditions described by equations (2.1-2.8), obtained using COMSOL, is shown in figure 4.1 (b).

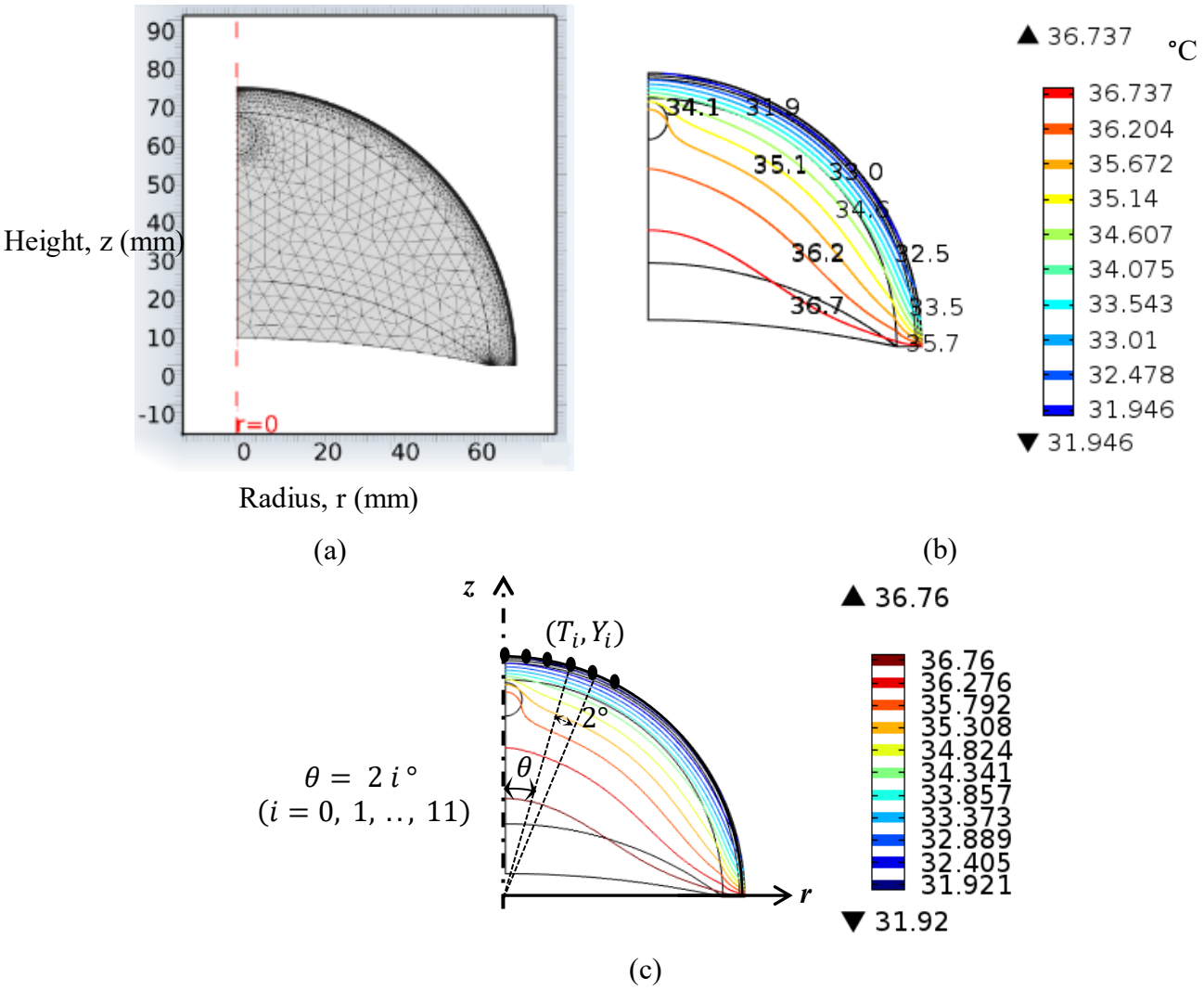

Figure 4.1: (a) Computational mesh, (b) computed temperature distribution in the cancerous breast and (c) coordinate system and surface data points used for the inverse reconstruction

4.2.2 Input data for the inverse problem: computational phantom

Input data for the inverse reconstruction algorithm are generated using the computational phantom in this study. In a clinical application computed surface temperature data (from the computational phantom) are replaced by measurement data obtained by means of infrared imaging. In the computational phantom, the tumor is

modeled in COMSOL for the exact set of tumor parameters R_e, D_e and ω_{b_e}. The exact set of tumor parameters for the steady state analysis (figure 1) is stored in the vector

$$\boldsymbol{E}_{ss} = \begin{bmatrix} R_e \\ D_e \end{bmatrix} \quad . \tag{4.1}$$

The transient analysis accounts for an additional unknown parameter ω_b, therefore the exact set of parameters for the transient case becomes

$$\boldsymbol{E}_{tr} = \begin{bmatrix} R_e \\ D_e \\ \omega_{b_e} \end{bmatrix}. \tag{4.2}$$

Computed surface temperature data, obtained solving the mathematical model described by equations (2.1-2.8) for tumor parameters from equations (4.1-4.2), at $I = 12$ points on the surface, corresponding to 12 angular locations (figure 4.1 (c))

$$\theta_i = 2\,i\,^\circ; \qquad i = 0, 1, 2, \dots, 11 \tag{4.3}$$

served as input values for the inverse reconstruction algorithm. Steady state temperature data computed using the COMSOL model, were stored in the input vector $\boldsymbol{Y_{ss}}$ as

$$\boldsymbol{Y}_{ss} = \begin{bmatrix} T(\theta_0 = 0°) \\ \vdots \\ T(\theta_i = 2i\,°) \\ \vdots \\ T(\theta_I = 22\,°) \end{bmatrix} \qquad i = 0, 1, 2, \dots, 11\,, \tag{4.4}$$

where $T(\theta_I = 2i\,°)$ represents the surface temperature at the polar angle $2i\,^\circ$ (figure 4.1 (c)).

The number of input data points in equation (4.4) was kept low, as a large number of data points would significantly increase computational effort and require advanced computational resources. The selected number of data points was determined by trial and error, and was guided by the required accuracy for the selected application. If necessary, the number of data points in a particular application can be increased to improve reconstruction accuracy. Further, the data points were distributed in the region where the temperature increase caused by the presence of the tumor is most pronounced, corresponding to the strongest measurement signal in a clinical application. In this study they were not distributed throughout the entire circumference, rather they were concentrated within a limited region (0-22° angle) relative to the *z* axis (figure 4.1 (c)).

For the transient analysis surface temperature data as a function of time was also collected during the thermal recovery phase at times t_j = 200s, 400s, 500s, 600s, 700s, 800s, 1000s. Only one surface point is considered to describe the time dependence of temperature, in order to strike a balance between the computational cost and accuracy. The selected point is located on the skin surface directly above the tumor ($\theta_0 = 0^o$), and this is the point that records the maximum temperature rise (Chanmugam *et al,* 2012). In the present work only a single point is taken to record the transient temperature. This was sufficient to get convergence for the transient case. Adding additional data points was increasing the size of the matrix, for each data point the rank of the matrix was increasing by 7, and therefore this was taxing on the computational resources. Furthermore there were problems with convergence after adding additional data points so we avoided adding additional points.

The vector containing the surface temperatures for the transient case consists of the Y_{ss}, as described by equation (4.4), followed by the transient data

$$\boldsymbol{Y}_{tr} = \begin{bmatrix} \boldsymbol{Y}_{ss} \\ T(\theta_0, t_1) \\ \vdots \\ T(\theta_0, t_k) \end{bmatrix} \tag{4.5}$$

where $T(\theta_0, t_j)$ represents the temperature data during thermal recovery at time t_j. The dimension of $\boldsymbol{Y}_{tr}$ is 19 × 1.

In clinical applications the measured steady state or time dependent temperature will be acquired by static or dynamic infrared imaging of the breast surface temperature. Typical thermal signatures were analyzed computationally by Chanmugam et al. (2012). They showed that the temperature rise can be more than 1 ºC for shallow and large tumors. For smaller and deeper tumors the temperature rise is low, but for the majority of cases analyzed by the authors it was more than 0.1 ºC. These results suggest that modern, miniature, low-cost IR imagers are suitable for clinical diagnostic applications. The infrared imager can be combined with a 3D imager, such as the Microsoft Kinect. As shown by Cheng (2015), mapping 2D temperature data onto a 3D surface mesh generated by Kinect increases measurement accuracy and should be considered for clinical implementation. The geometry of the breast is not hemi-spherical and the COMSOL model can be adjusted to accommodate the exact shape when data are available.

4.2.3 Inverse problem: overview

In this section we provide a general overview and rationale of the inverse reconstruction method used in our study, whereas details of the mathematical formulations of the inverse reconstruction method are introduced in Section 4.2.4. As

mentioned Section 4.1, the problem of extracting the model parameters (tumor location, dimensions and tumor properties R, D and ω_b, $\boldsymbol{E}_{ss}$ or $\boldsymbol{E}_{tr}$) from the observable data (measured or computed temperature distributions, $\boldsymbol{Y}_{ss}$ or $\boldsymbol{Y}_{tr}$ in the present study) is known as the inverse problem, and its application in heat transfer is known as the inverse heat transfer problem (IHTP). The measured or computed surface temperature distributions $\boldsymbol{Y}_{ss}$ or $\boldsymbol{Y}_{tr}$ (equations 4.4 and 4.5) as well as the initial guesses of the model parameters R, D and ω_b (their exact values are to be determined by inverse reconstruction) provide the input data.

IHTP problems are very sensitive to the changes in the input data to the model and therefore are classified as ill-posed problems (Ozisik and Orlande (2000)). To overcome the ill-posedness of the problem, regularization methods and other least square minimization methods are used. In the current work, the Levenberg-Marquardt (LM) method is implemented. In the LM method, the difference between experimental and calculated data is expressed in the form of the sum of squares S. The geometrical and thermophysical characteristics of the tumor, such as size, location and blood perfusion rate, R, D and ω_b, are adjusted iteratively, and the computed surface temperature response is compared to the measured or computed (using the phantom, Sections 4.2.1 and 4.2.2) temperature data to minimize S. In order to counter the ill-posed nature of the problem, the LM method uses a damping factor.

The LM method iteratively solves for the tumor parameters R, D and ω_b and computes surface temperature distributions for each iteration. The iterative process continues until the difference between measured and computed surface temperatures S falls below a certain value and satisfies the stopping criterion.

4.2.4 Inverse algorithm

The algorithm used to solve the inverse problem is illustrated in figures 4.2 and 4.3. The flowchart of the general algorithm is displayed in figure 4.2, and details of the LM regularization portion of the algorithm are provided in figure 4.3. Each block of the algorithm is identified by a letter and the blocks are referred to by figure number and letter in the text. For example, figure 4.2 (a) refers to block (a) in figure 4.2. It should be noted that the variables for steady state and transient state, though they have the same generic form, differ due to the presence of the additional parameter ω_b and additional transient data. These differences are described in the text and steady state and transient variables are referred to by their generic form, whenever admissible. For example, in figures 4.2 and 4.3 only the generic forms of these variables are used.

Input data, initial guesses and process variables

The algorithm begins with an initial guess for the set of unknown parameters R, D and ω_b stored in the vector $\boldsymbol{P}^0$ (figure 4.2 (c)) as

$$\boldsymbol{P}_{ss}^0 = \begin{bmatrix} R^0 \\ D^0 \end{bmatrix} \quad \text{for steady state (figure 4.2 (a)) and} \tag{4.6}$$

$$\boldsymbol{P}_{tr}^0 = \begin{bmatrix} R^0 \\ D^0 \\ {\omega_b}^0 \end{bmatrix} \quad \text{for the transient analysis (figure 4.2(b)).} \tag{4.7}$$

The algorithm proceeds from the initial guesses to improved estimates of unknown parameters iteratively, using LM method. The set of unknown parameters at the m^{th} iteration is represented by the vector $\boldsymbol{P}^m$ as

$$\boldsymbol{P}_{ss}^m = \begin{bmatrix} R^m \\ D^m \end{bmatrix} \quad \text{for steady state and} \tag{4.8}$$

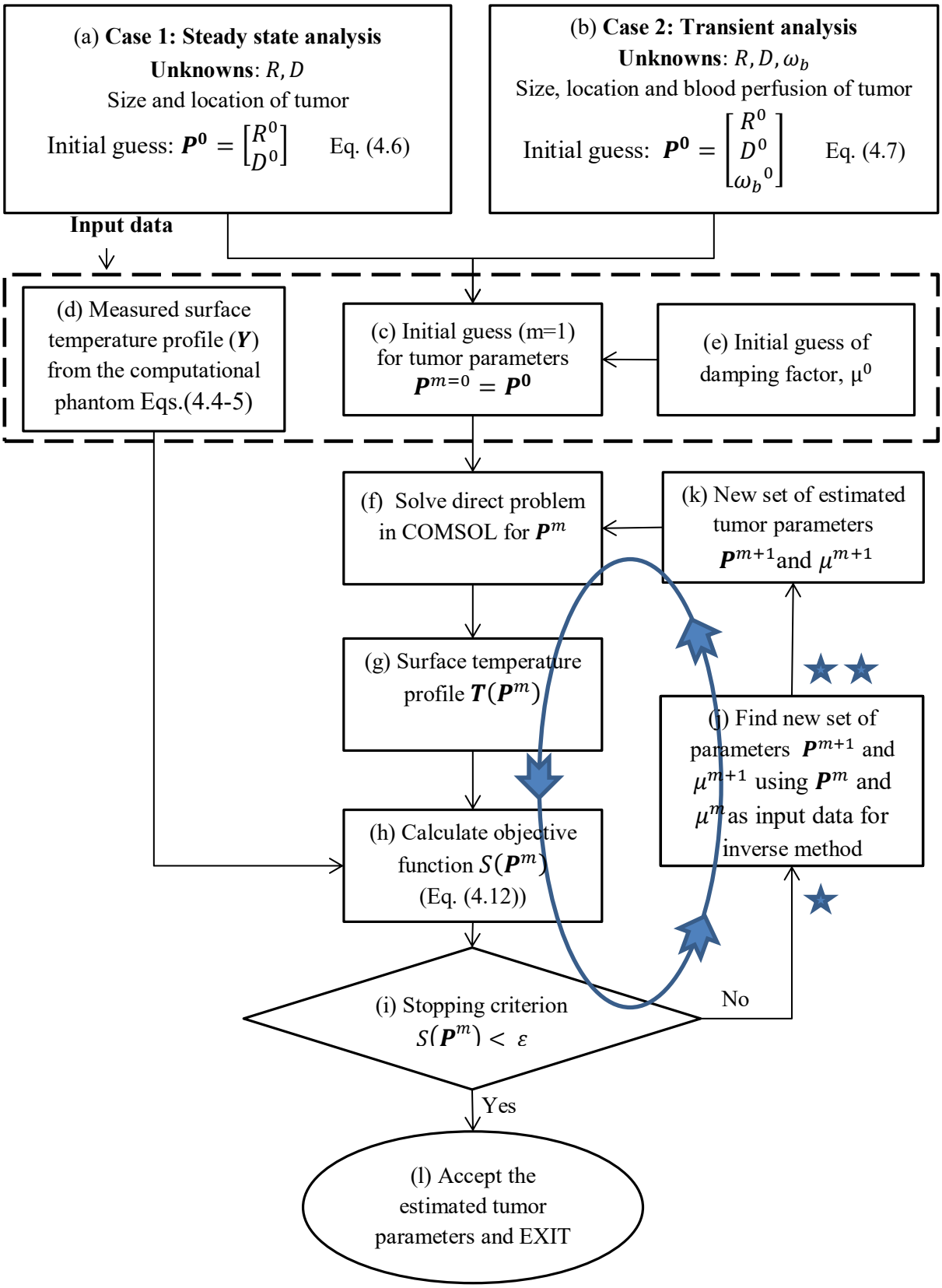

Figure 4.2: Flowchart of the inverse reconstruction algorithm

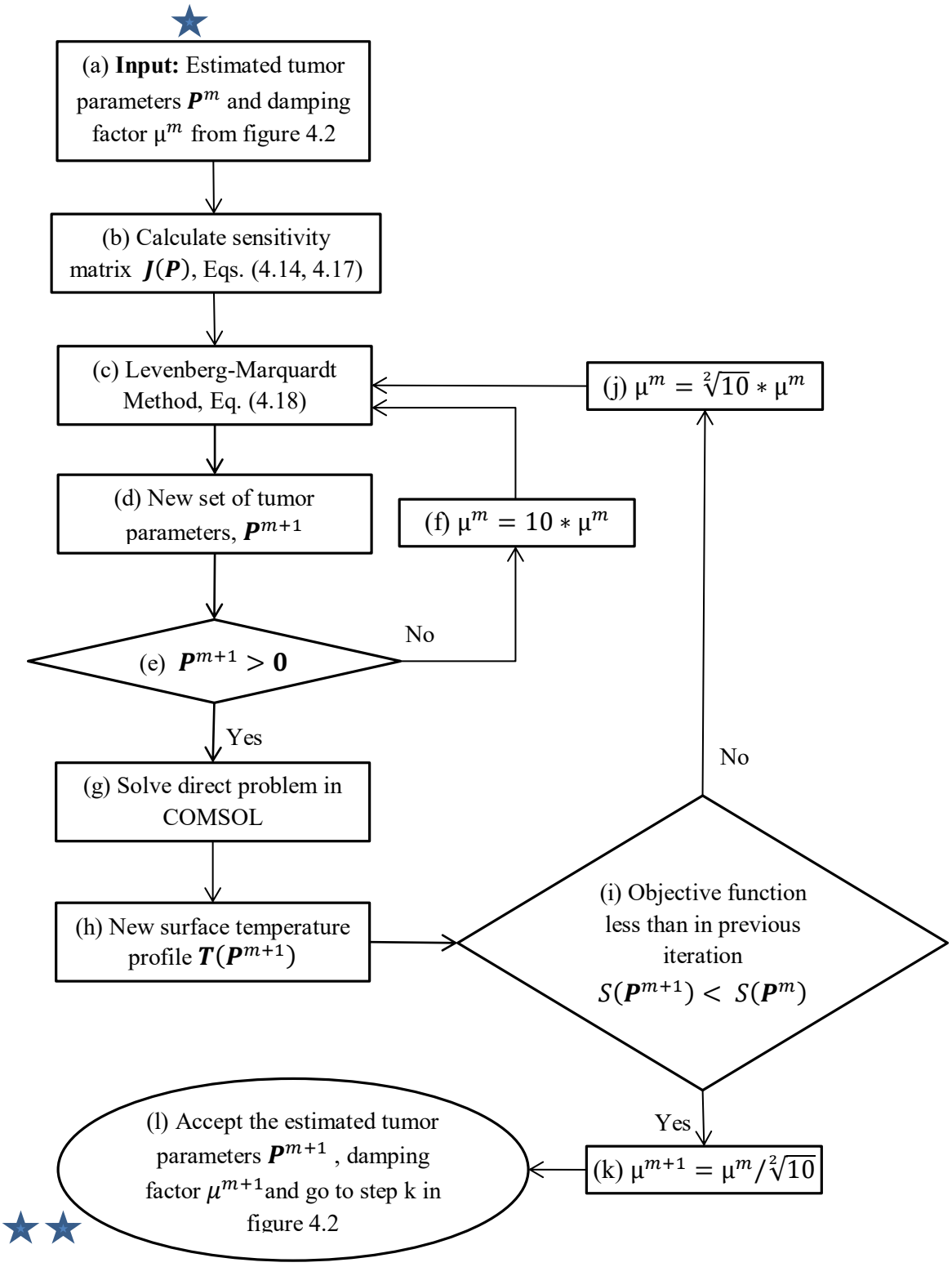

Figure 4.3: Flowchart describing block (j) in figure 4.2

$$\boldsymbol{P}_{tr}^{m} = \begin{bmatrix} R^m \\ D^m \\ {\omega_b}^m \end{bmatrix} \qquad \text{for transient analysis.} \tag{4.9}$$

The surface temperatures corresponding to the set of parameters $\boldsymbol{P}^m$ for the steady state analysis are stored in the vector $\boldsymbol{T}(\boldsymbol{P}^m)$ as

$$\boldsymbol{T}_{ss}(\boldsymbol{P}^m) = \begin{bmatrix} T(\theta_0 = 0°) \\ \vdots \\ T(\theta_i = 2i\,°) \\ \vdots \\ T(\theta_I = 22\,°) \end{bmatrix}. \qquad i = 0, 1, 2, \ldots, 11 \tag{4.10}$$

In transient analysis, $\boldsymbol{T}(\boldsymbol{P}^m)$ also contains surface temperature data obtained during the thermal recovery phase corresponding to $\theta = 0°$ at different times t_j (j = 1, 2, …. k), similar to the vector $\boldsymbol{Y}_{tr}$ described in section 4.2.2. $\boldsymbol{T}(\boldsymbol{P}^m)$ is described as

$$\boldsymbol{T}_{tr}(\boldsymbol{P}^m) = \begin{bmatrix} \boldsymbol{T}(ss) \\ T(\theta_0, t_1) \\ \vdots \\ T(\theta_0, t_k) \end{bmatrix}. \tag{4.11}$$

The measured temperature $\boldsymbol{Y}$, discussed in Section 4.2.2 (equations 4.4 and 4.5), is the second set of input data required by the algorithm (figure 4.2 (d)). The third input parameter used by the algorithm is the damping factor μ^0(figure 4.2 (e)). The value of μ^0 is taken to be μ^0= 0.1 for the steady state analysis with two unknowns and the initial guess is μ^0= 0.01 for transient analysis and the steady state analysis with three unknowns. The parameter μ^0 is used in the LM method and it is analogous to the relaxation factor. The role of μ^0 is explained in more detail in section 4.2.4.3.

The commercial finite element code COMSOL is used to solve the direct problem (figure 4.2 (f)) of evaluating the surface temperature profile $\boldsymbol{T}(\boldsymbol{P}^m)$ (figure 4.2 (g)) for each iteration m.

Main algorithm

The goal of the iterative procedure is to let $\boldsymbol{T} \rightarrow \boldsymbol{Y}$ and therefore $\boldsymbol{P}^m \rightarrow \boldsymbol{E}$. To this end we define the objective function $S(\boldsymbol{P}^m)$(figure 4.2 (h)), the sum of squared errors, as (Ozisik and Orlande (2000))

$$S(\boldsymbol{P}^m) = [\boldsymbol{Y} - \boldsymbol{T}(\boldsymbol{P}^m)]^T\,[\boldsymbol{Y} - \boldsymbol{T}(\boldsymbol{P}^m)] \quad . \tag{4.12}$$

$S(\boldsymbol{P}^m)$ is a measure of the difference between the measured/computed temperature profile $\boldsymbol{Y}$ and the one obtained during the inverse reconstruction process based on iteratively defined tumor parameters, $\boldsymbol{T}(\boldsymbol{P}^m)$ (figure 4.2 (g)). The form of the vectors $\boldsymbol{T}(\boldsymbol{P})$ and $\boldsymbol{Y}(\boldsymbol{P})$ is defined by equations (4.4), (4.8) and (4.10) for the steady state analysis and equations (4.5), (4.9) and (4.11) for the transient analysis. The set of tumor parameters $\boldsymbol{P}^m$ is accepted as the final estimate if the objective function, $S(\boldsymbol{P})$, falls below a pre-defined value ε as

$$S(\boldsymbol{P}^m) < \varepsilon = 10^{-5} \, . \tag{4.13}$$

Equation (4.13) is referred to as the stopping criterion (figure 4.2 (i)), and once it is met the algorithm stops (figure 4.2 (l)) with the accepted set of tumor parameters P^m. .

If the stopping criterion is not met, the set of parameters $\boldsymbol{P}^m$ is fed into the inverse method along with the current damping factor μ^m(figures 4.2 (j) and 4.3 (a)) to find the next estimate of the unknown parameters $\boldsymbol{P}^{m+1}$ and damping factor μ^{m+1} (figure 4.2 (k)). The next estimate (m+1) is fed into the direct problem (figure 4.2 (k) and (f)). This

iterative cycle continues until the stopping criterion is met and the set of parameters hence obtained is accepted as the final estimate (figure 4.2 (l)).

Improving the estimates: LM algorithm

The details of the algorithm used in the "inverse method" part of figure 4.2 (j) are illustrated in figure 4.3. The objective of this part, the LM algorithm, is to take a set of tumor parameters $\boldsymbol{P}^m$, either the initial guess or the improved values determined through the iterative process, as input (figure 4.3 (a)) and compute an improved estimate of tumor parameters $\boldsymbol{P}^{m+1}$ as the output (figure 4.3 (l)).

Based on the input parameters $\boldsymbol{P}^m$ and $\boldsymbol{T}(\boldsymbol{P}^m)$, the sensitivity matrix $\boldsymbol{J}(\boldsymbol{P}^m)$ is calculated first (figure 4.3 (b)). The sensitivity matrix accounts for the variation of surface temperature in response to the change of the tumor parameters R, D and ω_b. For the steady state analysis the sensitivity matrix is defined as

$$\boldsymbol{J}_{ss}(\boldsymbol{P}^m) = \left[\frac{\partial \boldsymbol{T}^{\mathrm{T}}(\boldsymbol{P}^m)}{\partial \boldsymbol{P}}\right] = \begin{bmatrix} \frac{\partial T_1}{\partial R} & \frac{\partial T_1}{\partial D} \\ \frac{\partial T_2}{\partial R} & \frac{\partial T_2}{\partial D} \\ \vdots & \vdots \\ \frac{\partial T_I}{\partial R} & \frac{\partial T_I}{\partial D} \end{bmatrix}, \tag{4.14}$$

where I is the total number of temperature measurements on the surface (12 in this study). In the sensitivity matrix an element located at ith column and jth row describes the variation of surface temperature at jth location with respect to parameter P_{i}. $\boldsymbol{J}_{ss}(\boldsymbol{P}^m)$ in equation (4.14) is a 12×2 matrix, as we have 2 unknown parameters, R and D, and 12 measurement points.

Individual elements of the sensitivity matrix are calculated using the approximation

$$\frac{\partial T_i}{\partial P_j} \approx \frac{\Delta T_i}{\Delta P_j} = \frac{\left(T_i(\boldsymbol{P}_{+j}) - T_i(\boldsymbol{P})\right)}{\Delta \boldsymbol{P}_j} \quad . \tag{4.15}$$

The term P_{+j} in equation (4.15) is defined as

$$\boldsymbol{P}_{ss+1} = \begin{bmatrix} \boldsymbol{R} + \Delta \boldsymbol{R} \\ \boldsymbol{D} \end{bmatrix} \text{ and } \boldsymbol{P}_{ss+2} = \begin{bmatrix} \boldsymbol{R} \\ \boldsymbol{D} + \Delta \boldsymbol{D} \end{bmatrix}$$

for the steady state analysis.

$\Delta \boldsymbol{P}$ in equation (4.15) is a pre-defined, fixed increment for the tumor parameters R and D, $\Delta \boldsymbol{P} =$ [0.2 mm, 0.2 mm] . The sensitivity matrix for the transient case is

$$\boldsymbol{J}_{tr}(\boldsymbol{P}^m) = \begin{bmatrix} \boldsymbol{B}(ss) \\ \boldsymbol{U}(\theta_0, t_1) \\ \vdots \\ \boldsymbol{U}(\theta_0, t_k) \end{bmatrix}, \tag{4.16}$$

where $\boldsymbol{B}(ss) = \begin{bmatrix} \frac{\partial T_1}{\partial R} & \frac{\partial T_1}{\partial D} & \frac{\partial T_1}{\partial \omega_b} \\ \frac{\partial T_2}{\partial R} & \frac{\partial T_2}{\partial D} & \frac{\partial T_2}{\partial \omega_b} \\ \vdots & \vdots & \vdots \\ \frac{\partial T_I}{\partial R} & \frac{\partial T_I}{\partial D} & \frac{\partial T_I}{\partial \omega_b} \end{bmatrix}$ and

$$\boldsymbol{U}(t_j) = \begin{bmatrix} \frac{\partial T_1(\theta_0)}{\partial R} & \frac{\partial T_1(\theta_0)}{\partial D} & \frac{\partial T_1(\theta_0)}{\partial \omega_b} \end{bmatrix}$$

for times t_j during thermal recovery t :{200s, 400s, 500s, 600s, 700s, 800s, 1000s }.

Elements of the sensitivity matrix for the transient situation are also determined using equation (4.15). For the transient case the term P_{+j} in equation (4.15) is defined as

$$\boldsymbol{P}_{tr+1} = \begin{bmatrix} \boldsymbol{R} + \Delta\boldsymbol{R} \\ \boldsymbol{D} \\ \boldsymbol{\omega_b} \end{bmatrix}, \boldsymbol{P}_{tr+2} = \begin{bmatrix} \boldsymbol{R} \\ \boldsymbol{D} + \Delta\boldsymbol{D} \\ \boldsymbol{\omega_b} \end{bmatrix} \text{ and } \boldsymbol{P}_{tr+3} = \begin{bmatrix} \boldsymbol{R} \\ \boldsymbol{D} \\ \boldsymbol{\omega_b} + \Delta\boldsymbol{\omega_b} \end{bmatrix} . \quad (4.17)$$

The dimensions of the sensitivity matrix $\boldsymbol{J}_{ss}(\boldsymbol{P}^m)$ are 3 × 19, larger than for steady state (equation (4.14)), because of the additional unknown parameter ω_b and the difference in the expressions for $\boldsymbol{T}(\boldsymbol{P})$ (equations (4.10) and (4.12)). Since the increment vector $\Delta\boldsymbol{P}$ for the transient case has an additional element accounting for ω_b, it takes the form $\Delta\boldsymbol{P}$ = [0.2 mm, 0.2 mm, 0.0001 ml/sec/ml]. Different values of $\Delta\boldsymbol{P}$ were tried and tested. The value used in the present work where giving the best results, in terms of convergence and computational time, and therefore were chosen.

After determining the sensitivity matrix, the LM method (figure 4.3 (c)) is used to calculate the next set of parameters $\boldsymbol{P}^{m+1}$ is (figure 4.3 (d))

$$\boldsymbol{P}^{m+1} = \boldsymbol{P}^m + \lfloor (\boldsymbol{J}^m)^{\mathrm{T}}\boldsymbol{J}^m + \mu^m\Omega^m \rfloor^{-1} (\boldsymbol{J}^m)^{\mathrm{T}}[\boldsymbol{Y} - \boldsymbol{T}(\boldsymbol{P}^m)] \quad (4.18)$$

where $\Omega^m = diag\lfloor (\boldsymbol{J}^m)^{\mathrm{T}}\boldsymbol{J}^m \rfloor$.

In equation (4.18) m represents the current iteration step and μ^m is the corresponding damping factor. As the damping factor is increased, the algorithm becomes more stable at the expense of speed. The damping factor controls the difference between $\boldsymbol{P}^m$ and probable$\boldsymbol{P}^{m+1}$; the larger μ^m is, the smaller will be the difference between tumor parameters in successive iterations, thereby making the algorithm slower. Furthermore, the term '*diag*' in equation (4.18) refers to a diagonal matrix comprised of the diagonal elements of the corresponding matrix.

The next set of parameters $\boldsymbol{P}^{m+1}$ hence obtained is checked (figure 4.3 (e)): if one of the parameters is negative, they are discarded and the LM method is used again

(figures 4.3 (c) and 4.3 (d)) after increasing damping factor μ by a factor of $\sqrt[3]{10}$ (figure 4.3 (f)). The resulting set of parameters is checked again (figure 4.3 (e)) and this cycle continues until the algorithm yields a set of realistic (positive) parameters. Based on the new set of parameters $\boldsymbol{P}^{m+1}$ the direct problem is solved (figure 4.3 (g, h)) and the corresponding objective function $S(\boldsymbol{P}^{m+1})$ (equation (4.14)) is calculated. This new parameter $\boldsymbol{P}^{m+1}$ is accepted only when the corresponding objective function $S(\boldsymbol{P}^{m+1})$ is less than the one associated with the previous input parameter set $\boldsymbol{P}^{m}$ (figure 4.3 (i))

$$S(\boldsymbol{P}^{m+1}) < S(\boldsymbol{P}^{m}) \ . \tag{4.19}$$

If this condition is met, the damping factor is decreased by a factor of $\sqrt[2]{10}$ (figure 4.3 (k)) and the new set of parameters $\boldsymbol{P}^{m+1}$ is accepted (figure 4.3 (l)). On the other hand if the objective function is larger, the set of parameters is discarded and the damping factor is increased by a factor of $\sqrt[2]{10}$ (figure 4.3 (j)). Then LM method is used again to obtain a new set of parameters (figure 4.3 (c)). This process continues until a set of parameters is obtained which is better than the set of parameters from the previous iteration, in terms of objective function (equation (4.12)).

4.3 RESULTS AND DISCUSSION

In Section 4.3.1 we introduce inverse reconstruction results for steady state analysis. We demonstrate that the steady state analysis has some inherent limitations, and we analyze these in Section 4.3.2. Finally, in Section 4.3.3, we show how to overcome these limitations by including transient temperature data in the inverse reconstruction algorithm.

In the present study only those tumors were considered which were capable of giving a detectable temperature rise on the skin surface. Figure 4.4 shows the temperature rise, at skin surface directly above the tumor, for different combinations of radius R, depth D and blood perfusion ω_b. The closer the tumor is to the surface and the larger its diameter is, the larger is the rise in the surface temperature.

4.3.1 Steady state analysis with two unknowns (R and D)

Tumor size (R, radius) and location (D, depth) are the unknown parameters in the inverse reconstruction method based on steady state surface temperature data. The thermophysical properties, thermal conductivity, density, heat capacity, blood perfusion rate and metabolic heat generation rate of the tumor are assumed to be known, and values used in our calculations are summarized in Table 4.1. A $D = 10$ mm deep tumor of $R = 5$ mm radius was modeled in FEM based commercial software COMSOL. Surface temperature distribution was computed using COMSOL and temperature data were then fed into the inverse reconstruction algorithm as measured temperatures $\boldsymbol{Y}$ and along with the initial guesses $\boldsymbol{P^0}$ and μ^0 for the unknown tumor parameters R and D and damping factor.

To examine the performance of our method, the inverse reconstruction algorithm was employed for three initial guesses $\boldsymbol{P}_{ss}^0$ (equation 4.6), labeled as cases 1, 2 and 3 in table 4.2. Figure 4.5 shows the progression of parameters R and D from the initial guesses to the exact values through the iteration process. The iterations shown in the abscissa of figure 4.5, represent the outer loop of the algorithm, displayed in figure 4.2. Each new iteration corresponds to a value of S smaller than in the previous iteration. Iterations corresponding to the inner loop of inverse method (figure 4.3), where the next best

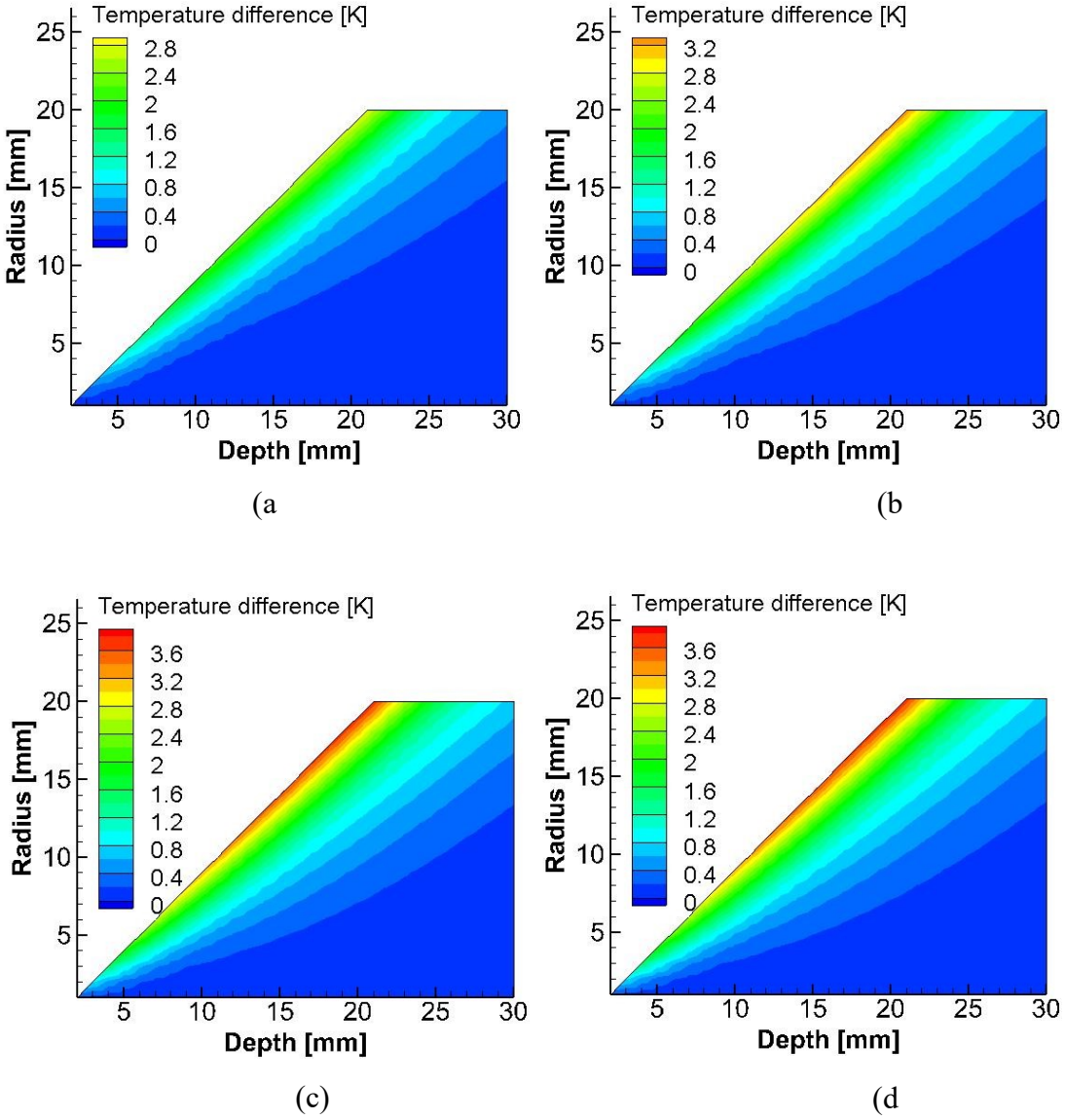

Figure 4.4: Temperature rise ΔT at a point directly above the tumor corresponding to $\theta_0 = 0^o$ as a function of tumor radius R and depth D for blood perfusion values (a) $\omega_b = 0.003$ $\mathrm{m}^3/\mathrm{s}/\mathrm{m}^3$, (b) $\omega_b = 0.006$ $\mathrm{m}^3/\mathrm{s}/\mathrm{m}^3$, (c) $\omega_b = 0.009$ $\mathrm{m}^3/\mathrm{s}/\mathrm{m}^3$ and (d) $\omega_b = 0.012$ $\mathrm{m}^3/\mathrm{s}/\mathrm{m}^3$.

parameter set $\boldsymbol{P}^{m+1}$ is estimated, are not shown. For example, for case 1, R and D started with an initial guess of 8 mm and 18 mm, respectively, and they converged to the exact values in 6 iterations (figures 4.5 (a) and (b)). The convergence trends are similar for cases 2 and 3. Case 1 took the least number of iterations to converge (7), while case 3

was the slowest to converge, within 13 iterations. Figure 4.5 (c) illustrates the variation of the objective function S during the iterative process for the three cases in table 4.2. The iterations stopped when the objective function reached a value that was less than the stopping criterion ε (10^{-5}). It is evident from these results that the solution converged to exact values within a reasonable number of iterations for very different initial guesses. Therefore we can conclude that the selected inverse reconstruction method based on steady state data is suitable for the reconstruction of the two geometrical parameters of the tumor.

4.3.2 Limitations of the steady state analysis

In section 4.3.1 steady state data were used to reconstruct two unknown tumor parameters D and R. In this section we add a third unknown parameter, the blood perfusion rate ω_b, to the set of unknown tumor parameters, and evaluate the feasibility of simultaneously reconstructing all three parameters from steady state data. The exact values of the tumor parameters for the steady state analysis and the three initial guesses are shown in Table 4.3. Figure 4.6 illustrates the progression of the parameters from the initial guess to the final solution. Final solutions along with the corresponding errors are shown in table 4.3. For all three cases, the iteratively computed solution progressed away from exact solution. Cases 1 and 2 exhibit large errors, especially for the estimates of ω_b, 83.3% and 40% respectively. For case 3 the error was smaller, with a maximum error of 7% for ω_b. The smaller error for case 3 can be attributed to the initial guess being very close to the exact solution.

This behavior of the inverse reconstruction algorithm can be explained by considering the results in figure 4.7, which compares the surface temperature profiles of

the three tumors. The temperature plotted in figure 4.7 is the temperature rise due to the presence of tumor. The temperature difference calculated by subtracting the surface temperature of the healthy breast from the temperature of the cancerous breast. One of the three surface temperature profiles in figure 4.7 correspond to the exact set of parameters (†) given in table 4.3. The remaining two show the converged, but incorrect, solutions of cases 1 and 2 marked by * in table 4.3. In spite of the marked difference in the tumor parameter values D, R and ω_b, the three tumors yield almost identical surface temperature profiles, close enough to satisfy the stopping criterion (equation 4.13). These results suggest that different combinations of D, R and ω_b can yield nearly identical thermal signatures, i.e. the thermal signatures of the tumor are not unique. Therefore, during the iterative revisions of the parameter set, the inverse algorithm converged to an incorrect solution. The reduction in surface temperature due to smaller tumor size for the final solution of case 1 is compensated by lower depth and a higher blood perfusion rate of the other tumors.

Table 4.2: Exact tumor parameters D and R and three sets of initial guesses (cases 1, 2 and 3) for the inverse problem with 2 unknowns (steady state analysis)

	Depth, D [mm]	Radius, R [mm]
Exact	**10**	**5**
Case 1	18	8
Case 2	21	11
Case 3	15	2

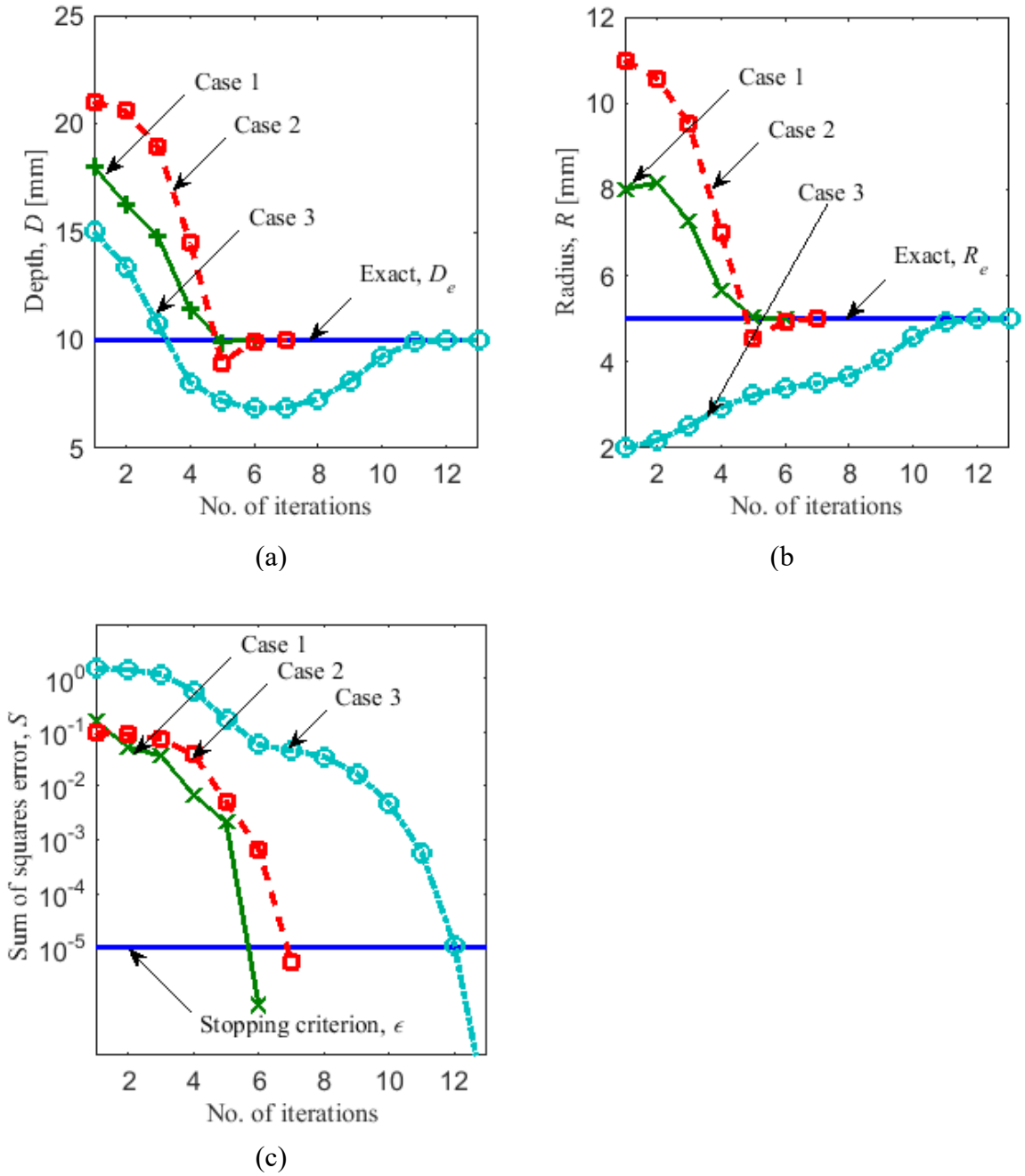

(a) (b

(c)

Figure 4.5: Evolution of (a) depth D and (b) radius R of the tumor and (c) error $S(\boldsymbol{P})$ versus the iteration number using steady state data for the three cases in table 4.2

Table 4.3: Exact parameter values and three sets of initial guesses for the inverse problem with 3 unknowns for steady state analysis. Temperature rise for sets of parameters marked by * is plotted in figure 4.7.

		Depth, D [mm]	Radius, R [mm]	Blood Perfusion rate, ω_b [$m^3/sec/m^3$]
	Exact *†	**11**	**7**	**0.003**
Case 1	**Initial**	**9**	**5**	**0.001**
	Final *	10.15	5.8	0.0055
	Error (%)	7.7	17.1	83.3
Case 2	**Initial**	**13**	**8**	**0.002**
	Final *	12	8.3	0.0018
	Error (%)	9.1	18.6	40
Case 3	**Initial**	**11.5**	**6.5**	**0.0025**
	Final	10.9	6.8	0.0032
	Error (%)	0.91	2.9	6.67

The analysis in section 4.3.1 demonstrates that, based on the steady state analysis, it was possible to estimate the location and the size of the tumor. However, the results in section 4.3.2 indicate that it is not possible to estimate the third parameter ω_b. When the blood perfusion rate is included along with size and location as unknown, the inverse

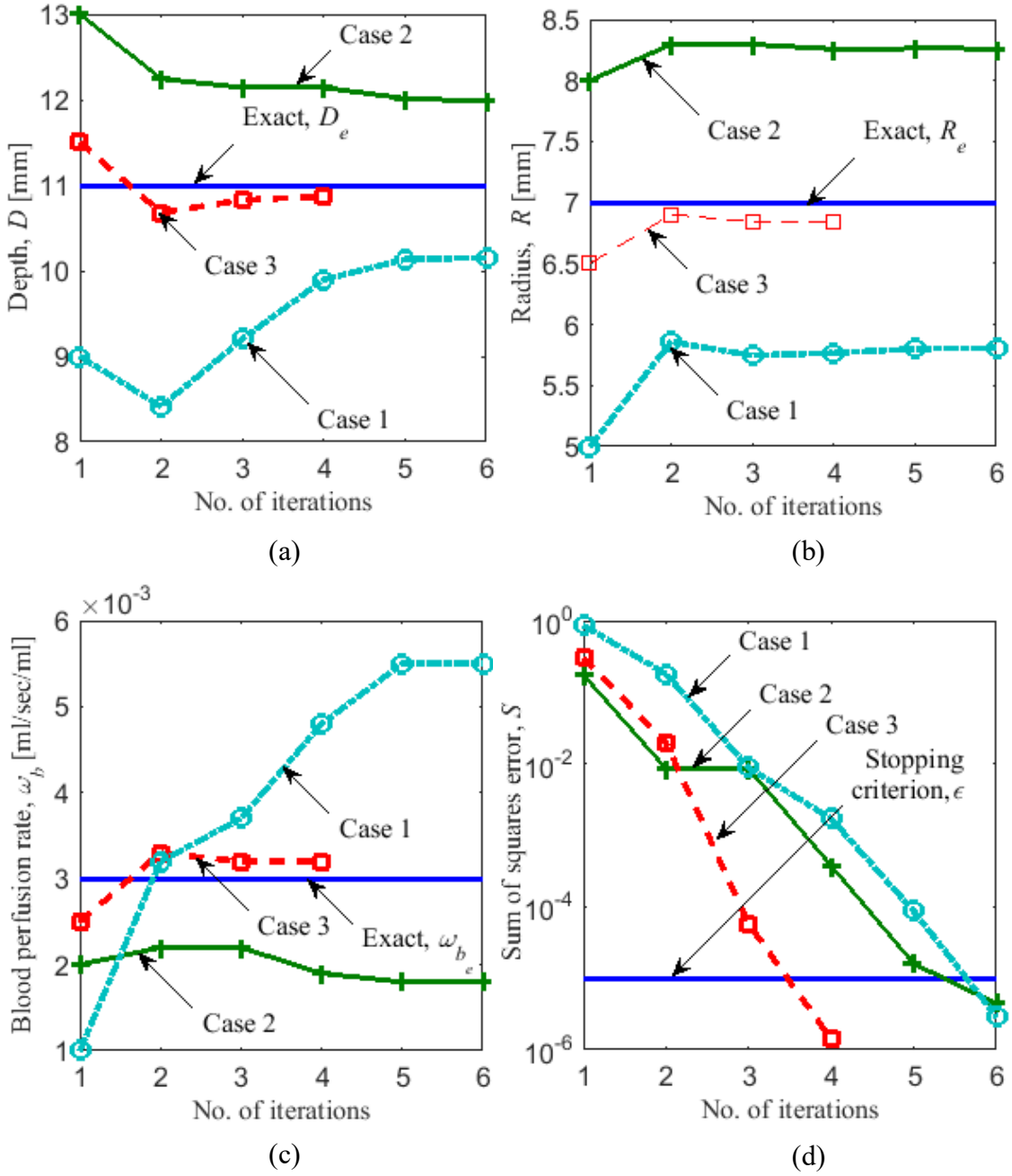

Figure 4.6: Evolution of (a) depth D (b) radius R (c) blood perfusion rate ω_b of the tumor and the (d) error $S(\boldsymbol{P})$ versus the number of iterations using steady state data for the three cases in table 4.3.

problem based on steady state analysis converges to the wrong solutions. Since different tumors yield almost identical surface temperature distributions, the inverse reconstruction

algorithm is unable to distinguish between them. This implies that the solution for this inverse problem with three unknowns is not unique, even though the algorithm yields a unique solution for two unknowns. In clinical applications, the presence of noise, can further accentuate the problem.

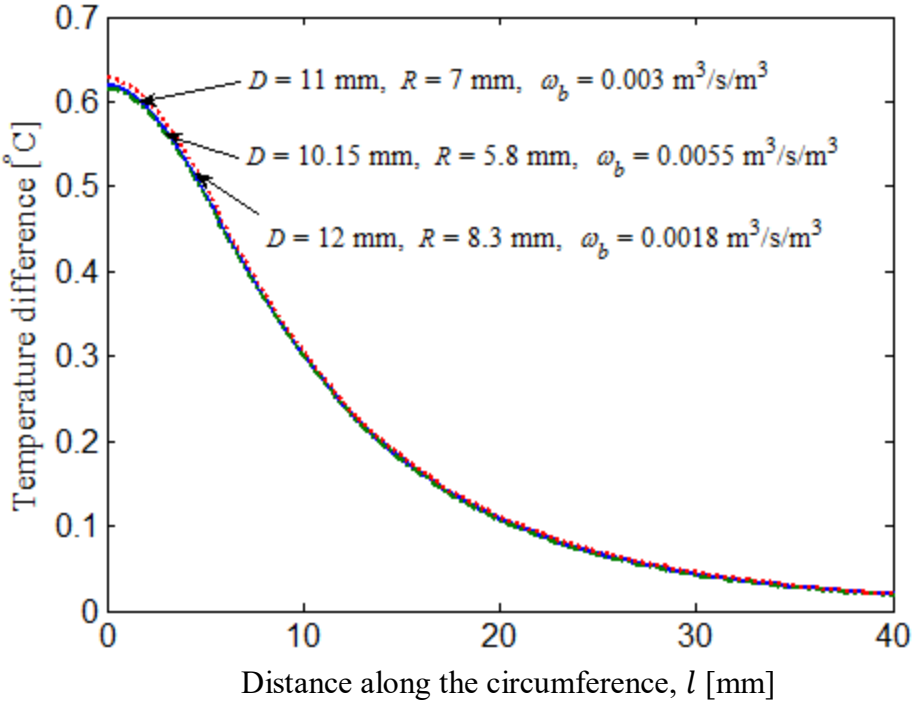

Figure 4.7: Surface temperature profiles for tumor parameters marked by * in table 2.3.3.

4.3.3 Solution: transient analysis

To overcome the non-uniqueness problem and solve this inverse problem in a robust manner, we incorporated the transient response in the input data. The transient response has been used in prior studies by Pirtini and Herman (2011) for melanoma detection, Cheng and Herman (2014) for the analysis of near surface lesions and Bhargava *et al.*(2014) for deep tissue injury. The imaging technique employed in these studies is known as dynamic infrared imaging, and it is explained in section 4.2.1 (equation 2.8). In

dynamic IR imaging a cooling load is applied on the surface for a certain amount of time. Then the cooling load is removed and the surface temperature is allowed to recover. The temperature measured during the thermal recovery process is used along with steady state temperature distribution to quantitatively assess lesions.

In order to compare surface temperatures generated by different tumors, first, the temperature of a cancerous breast was computed during the thermal recovery process, at a point located on the skin surface and on the axis, directly above the tumor. The reason for picking this particular point has been explained in section 4.2.2. Then the temperature of a healthy breast at the same location is subtracted from it, resulting in a temperature difference. In figure 4.8 this temperature difference is plotted against time, for the three tumors considered in the steady-state analysis. These are the same three tumors marked by "an asterisk" in table 4.3, which resulted in identical steady state surface temperature profiles (figure 4.7). It can be seen that the transient thermal recovery temperature profile is different for the three cases. Therefore the inverse reconstruction algorithm should not get trapped into incorrect solutions when transient data are included in the analysis. This approach makes it possible to estimate the blood perfusion rate along with the size and location of the tumor uniquely.

4.3.3.1 Transient analysis with three unknowns

To illustrate the use of transient response in inverse reconstruction we considered the same set of exact parameters $\boldsymbol{E}_{tr}$ (equation 4.2) and initial guesses $\boldsymbol{Y}_{tr}$ (equation 4.5) as for the steady state analysis (table 4.3) and added the transient data. A detailed description of the input parameters for the transient case is found in section 4.2.2. Figure 4.9 illustrates the progression of the solution from the initial guess to the converged

solution for D, R and ω_b. The error for each iteration is shown in figure 4.9 (d). The solution converged to the correct solution for all three initial guesses, with negligible errors (Table 4.4). Case 1 took the highest number of iterations to converge (34) and case 3 the least number of iterations (8). Since the blood perfusion rate is an indicator of the metabolic activity of the tumor, it can help estimate the stage of the tumor and therefore it is an important tumor parameter of interest in clinical applications. Further the use of additional set of input data improves the accuracy of the solution and can reduce the effect of noise in the input data therefore improving the robustness of the solution. In the transient analysis temperatures were recorded at intervals of more than 100 s and this makes sure that it is easily within the temporal resolution of IR cameras, which is less than a sec.

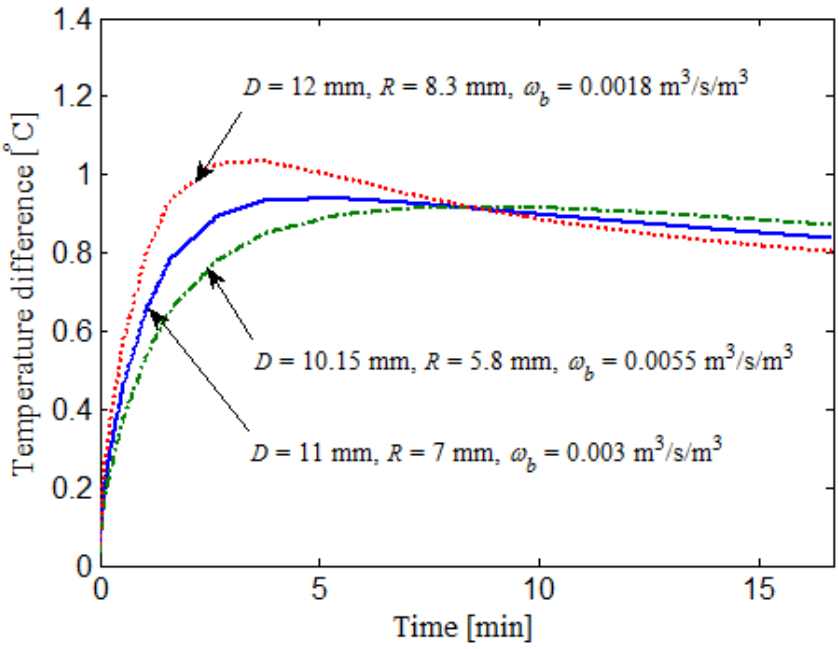

Figure 4.8: Thermal recovery temperature profile of a point directly above the tumor corresponding to θ_0. The tumors considered are the 3 tumors marked by * in table 4.3 and are also discussed in figure 4.7.

Several other cases were tried with different set of exact parameters and are listed in table 4.4. Different initial guesses were tried, including those which were far away from the exact parameters. The test cases considered here have tumors ranging from 12 mm to 30 mm in depth, 7 mm to 11 mm in radii and blood perfusion rate ranging from 0.003 1/s to 0.01 1/s. The error in the solution was low for near surface tumors and it increased with increasing depths. It was observed that tumors with 0.01 1/s blood perfusion rate and 11 mm radii gave errors of less than 1 % when they are within 20 mm from the body surface. Even though shallower tumors in Table 4.5 have blood perfusion rates lower than 0.01 1/s and hence lower rise in surface temperature (figure 4.4), they were giving low errors. Errors in blood perfusion rate were particularly large for deeper tumors, this can be explained by the fact that surface temperature becomes increasingly insensitive to the blood perfusion rates for deeper tissue layers (Kleinman and Roemer 1983). Further smaller tumors will be giving lower temperature signals, but it is the larger tumors which have been associated with lower survival (Carter *et al.* 1989). Different initial guesses were tried, including those which were far away from the exact parameters. The test cases dealt in here had tumors and then an estimate for their parameters was obtained. In the case of no tumor, it is expected that the algorithm will converge to a solution indicating no tumor. The solution will start from the initial guess for tumors and will eventually converge to zero radii and/or maximum depth and/or blood perfusion rate equal to the surrounding healthy tissue.

The ability gained by this novel approach to estimate the blood perfusion rate is very critical. MRI, mammography and other non-invasive modalities can identify the location and size of the tumor, but it is difficult to ascertain the level of malignancy of

the tumor based on these tumor parameters. The diagnosis of cancer might require multiple visits to the clinic, before a biopsy (definitive test), for determination of tumor malignancy. On the other hand, an estimate of blood perfusion rate can give an unequivocal indication of tumor malignancy, as there is a direct correlation between tumor growth rate and tumor malignancy. Therefore, this approach has the potential to reduce the time, cost and effort involved in tumor detection.

Even though this approach, in its present format, does not give accurate result for deeper tumors, it can be modified to give critical diagnostic and staging information. CT scans can be used to determine the location and size of the tumor and this information can then be potentially utilized to increase the accuracy of the blood perfusion rate estimation. Blood perfusion rate in turn can help in staging of the tumor, which is very critical in determining the cancer treatment strategy.

It should be noted that MRI can also be used to estimate blood perfusion. MRI can give the blood perfusion distribution within the tissue and it can prove beneficial for diagnosing and characterizing tumors. Thermography has an edge over MRI as it is much more economical and completely non-invasive. An MRI system is very expensive and requires a dedicated room or hardware (or large trailers for mobile systems) and a highly trained operator. A thermographic imaging system costs orders of magnitude less, is orders of magnitude smaller and can operated by existing clinical staff after basic training. It is suitable for screening and telemedicine applications. Additionally for MRI perfusion measurements, contrast agent has to be injected into the subject's body. Thermographic test can be 10 times cheaper and the equipment cost can be 100 times cheaper than MRI (Arora N *et al.* 2008).

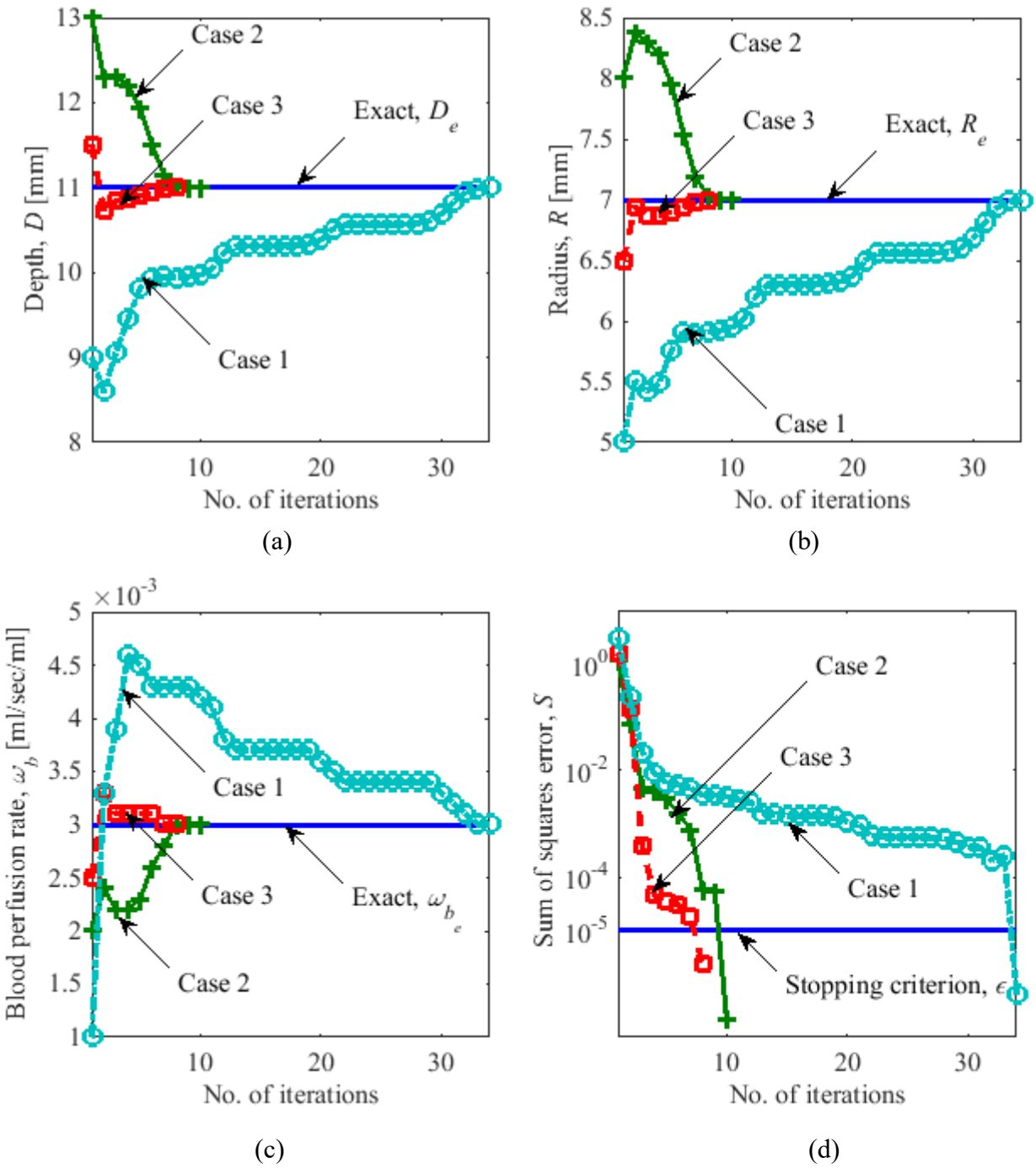

Figure 4.9: Evolution of (a) depth D (b) radius R (c) blood perfusion rate ω_b of the tumor and (d) error $S(\mathrm{P})$ vs the number of iterations using transient data for the three cases summarized in table 4.3.

Table 4.4: Exact parameter values and three sets of initial guesses for the inverse problem with three unknowns for transient analysis.

		Depth, D [mm]	Radius, R [mm]	Blood Perfusion rate, ω_b [$m^3/sec/m^3$]
	Exact	12	10	0.003
Case 1	**Initial**	10	8	0.002
	Final	12	10	0.003
	Error (%)	0.053	0.05	0
	Exact	13	10	0.004
Case 1	**Initial**	12	9	0.003
	Final	13	10	0.004
	Error (%)	0	0.001	0
Case 2	**Initial**	10	9	0.003
	Final	13	10	0.004
	Error (%)	0	0.009	0
Case 3	**Initial**	12	7	0.003
	Final	13	10	0.004
	Error (%)	0	0.015	0
Case 4	**Initial**	10	8	0.005
	Final	13	10	0.004
	Error (%)	0	0.008	0
	Exact	14	10	0.0045
Case 1	**Initial**	13	11	0.004
	Final	14	10	0.0045

	Error (%)	0.03	0.068	0
Case 2	**Initial**	12	9	0.003
	Final	14	10	0.0045
	Error (%)	0.022	0.082	0
Case 3	**Initial**	11	8	0.0035
	Final	14	10	0.0045
	Error (%)	0.02	0.073	0
Case 4	**Initial**	16	8	0.0025
	Final	14	10	0.0045
	Error (%)	0.014	0.055	0
Case 5	**Initial**	10	7	0.002
	Final	14	10	0.0045
	Error (%)	0.014	0.055	0
Case 6	**Initial**	8	4	0.001
	Final	14	10	0.0045
	Error (%)	0.021	0.074	0
Case 7	**Initial**	21	6	0.003
	Final	14	10	0.0045
	Error (%)	0.03	0.097	0
	Exact	16	11	0.0055
Case 1	**Initial**	14	9	0.002
	Final	16	11	0.0055
	Error (%)	0.002	0.014	0
Case 2	**Initial**	12	7	0.002
	Final	16	11	0.0055
	Error (%)	0.001	0.006	0

	Exact	15	11	0.01
Case 1	**Initial**	13	9	0.008
	Final	15	11	0.010
	Error (%)	0.013	0.035	0
Case 2	**Initial**	12	8	0.007
	Final	15	11	0.01
	Error (%)	0.001	0.006	0
Case 3	**Initial**	18	8	0.005
	Final	15	11	0.01
	Error (%)	0.015	0.042	0
	Exact	20	11	0.01
Case 1	**Initial**	22	9	0.007
	Final	20.02	10.90	0.0108
	Error (%)	0.1	0.91	8
	Exact	25	11	0.01
Case 1	**Initial**	23	9	0.008
	Final	25.07	10.53	0.015
	Error (%)	0.28	4.27	50
Case 2	**Initial**	20	9	0.007
	Final	25.10	10.50	0.0157
	Error (%)	0.4	4.54	57
	Exact	30	11	0.01
Case 1	**Initial**	28	9	0.008

	Final	29.71	10.15	0.0181
	Error (%)	0.97	7.73	81
Case 2	**Initial**	27	8	0.008
	Final	29.96	9.8	0.0319
	Error (%)	0.13	10.91	219
Case 3	**Initial**	26	7	0.007
	Final	29.59	9.51	0.0332
	Error (%)	1.37	13.55	232
Case 4	**Initial**	20	6	0.005
	Final	30.23	9.44	0.0637
	Error (%)	0.77	14.18	537

4.3.3.2 Noise analysis

The IR cameras available presently have temporal and spatial resolution of 10 mK and 0.05 mm respectively or better (Çetingül M P 2010), as mentioned in section 3.3.1. Although it should be noted that spatial resolution is not a property of the camera and for a certain sensor size it will depend on the distance of the camera from the object. The points on the body surface, at which the temperatures are measured (Figure 2.2 (c)), are at a distance of 5 mm from each other and the spatial resolution of the IR cameras, at 0.05 mm, is well above this, so they can easily capture the spatio-temperature variation.

For thermal resolution, an analysis has been done here to show the limitations when noise corresponding to 10 mK is present in temperature measurement. A random noise of 10 mK was generated in the temperature data using a MATLAB function. For the noise analysis the stopping criteria (equation 4.13) was relaxed by increasing ε to 5.10^{-4}. This particular stopping criteria was chosen based on multiple runs for different

cases and selecting an ε which will lead to convergence for maximum cases. The results hence generated have been tabulated in Table 4.5. The set of exact parameters have been taken from Table 4.4 and corresponding initial guesses are a subset of the cases investigated before in Table 4.4. It was made sure that the subset of the initial guesses had cases which were farther away from the exact set of parameters and therefore most challenging. As expected the errors associated with the final solution are larger here due to the presence of noise and a relaxed stopping criterion, as compared to the earlier case (Table 4.4). Here again the error increased with increasing depth of the tumor and the errors in blood perfusion estimates were particularly high for deep tumors.

4.3.4 Computational time

The time taken by this algorithm can vary from 10 min to 50 min depending on the number of iterations required for convergence. In general, the further the initial guess from the actual solution the larger the number of iterations will be as can be seen from figures 4.5 and 4.9. It takes around 75 seconds for one iteration loop as shown in the flowchart corresponding to the outer loop (figure 4.2), if the next set of parameters (figure 4.3 , block (d)) obtained using equation 4.18 is realistic (figure 4.3 , block (e)) and is a better estimate than the previous one (figure 4.3 , block (i)). If the estimate is unrealistic (figure 4.3, block (e)) it takes a couple of seconds to correct it and if it needs to be improved (figure 4.3, block (i)) it takes an extra 20 seconds for each loop.

4.3.5 Future work

Several improvements can be incorporated into the existing model in the future. First, the Levenberg-Marquardt algorithm can be modified to improve the robustness and speed. In the present work, only the last iteration parameters were saved and checked for

Table 4.5: Exact parameter values and three sets of initial guesses for the inverse problem with three unknowns for transient analysis. 10 mK noise, stopping criteria = 5e-4

		Depth, D [mm]	Radius, R [mm]	Blood Perfusion rate, ω_b [m^3/sec/m^3]
	Exact	**11**	**7**	**0.003**
Case 2	**Initial**	13	8	0.002
	Final	11.09	7.13	0.0029
	Error (%)	0.82	1.86	3.33
Case 3	**Initial**	11.5	6.5	0.0025
	Final	11.02	7	0.003
	Error (%)	0.18	0	0
	Exact	12	10	0.003
Case 1	**Initial**	10	8	0.002
	Final	11.97	9.97	0.003
	Error (%)	0.25	0.3	0
	Exact	13	10	0.004
Case 2	**Initial**	10	9	0.003
	Final	13.02	10	0.004
	Error (%)	0.15	0	0
Case 4	**Initial**	10	8	0.005
	Final	13	9.99	0.004

	Error (%)	0	0.1	0
	Exact	14	10	0.0045
Case 7	**Initial**	21	6	0.003
	Final	13.89	9.88	0.0046
	Error (%)	0.79	1.2	2.22
	Exact	16	11	0.0055
Case 1	**Initial**	14	9	0.002
	Final	16.01	8.91	1.82
	Error (%)	0.063	8.91	1.82
	Exact	15	11	0.01
Case 1	**Initial**	13	9	0.008
	Final	15.01	10.98	0.0102
	Error (%)	0.07	0.18	2
Case 2	**Initial**	12	8	0.007
	Final	14.99	10.98	0.0102
	Error (%)	0.07	0.18	2
Case 3	**Initial**	18	8	0.005
	Final	15.06	11.06	0.0098
	Error (%)	0.4	0.55	2
	Exact	20	11	0.01
Case 1	**Initial**	22	9	0.007

	Final	19.57	10.66	0.0101
	Error (%)	2.15	3.09	1
	Exact	25	11	0.01
Case 1	**Initial**	23	9	0.008
	Final	24.42	10	0.0155
	Error (%)	2.32	9.09	55
Case 2	**Initial**	20	9	0.007
	Final	24.57	10.3	0.0132
	Error (%)	1.72	6.37	32
	Exact	30	11	0.01
Case 1	**Initial**	28	9	0.008
	Final	27.3	9.4	0.0104
	Error (%)	9	14.55	4
Case 2	**Initial**	27	8	0.008
	Final	26.33	8.59	0.0116
	Error (%)	12.23	21.91	16
Case 3	**Initial**	26	7	0.007
	Final	26.89	8.54	0.0176
	Error (%)	10.37	22.36	76
Case 4	**Initial**	20	6	0.005
	Final	27.27	8.35	0.03
	Error (%)	9.1	24.09	174

improvement in the solution. This can be increased to two or three previous iterations, this might lead to increase in robustness of the algorithm. Further the placement of the data points on the surface and the time points during recovery phase can be varied to reduce the computational time. Second, a 3D model of the breast can be used to include tumors which are not centered along the axis. With the current version of COMSOL Livelink with MATLAB, it was not possible to iteratively change the location and dimension of tumor for a 3D model. So there is a need to use different software or to develop an indigenous code. Third, the variation in thermophysical properties with temperature can be included in the model to make it more accurate. For example, blood perfusion rate is dependent on temperature and due to application of cooling load there is going to be variations in temperature within the body tissue. Finally, a sensitivity analysis can be done to quantify the effect of uncertainties of the parameters involved.

4.4 CONCLUSIONS

In the present work we used an inverse reconstruction method, based on the Levenberg-Marquardt algorithm, to characterize a tumor based on the skin surface temperature. This method was applied for two different cases. The first case relied on steady state surface temperature data as input. Tumor location and size were the unknown parameters, and the thermophysical properties of the tumor and healthy tissue were considered to be known. In the second case transient data served as input along with steady state data, and the blood perfusion rate of the tumor was added to the unknown parameters. A multilayered 2D model of the breast was considered for the present analysis.

The first case, that uses the surface temperature profile at steady state, has some limitations. Though it can uniquely estimate size and location of the tumor based on steady state data, problem arises when an additional tumor parameter, blood perfusion rate, is added as an unknown. Noise in the input data can further accentuate the problem. In order to correctly and uniquely estimate the size, location and blood perfusion rate of the tumor simultaneously, we used transient analysis in the second case. For deeper tumors the solution seems to converge away from the exact set of parameters.

To summarize, addition of transient data with steady state data allows simultaneous estimation of blood perfusion rate, size and location of tumor, which is not possible with steady state data alone. Although this has limitations, but when combined with other modalities it can help in staging and treatment planning for cancer.

Chapter 5

CT Perfusion Imaging

The complete authorship of this work should be read as Rajeev Hatwar, Prof. Eleni Liapi and Prof. Robert Ivkov. The experiments were performed by Prof. Eleni Liapi.

5.1 INTRODUCTION

In computed X-ray tomography (CT) imaging, multiple images are taken at different angles to produce cross sectional images of the scanned object. A variation of this technique, CT perfusion imaging, allows the user to analyze the hemodynamics within the region of interest (Miles and Griffiths 2003, Kim *et al.* 2014). In this technique a contrast agent, which is opaque to x-rays, is injected intravenously. This is followed by a series of scans to trace the movement of the contrast agent within the target tissue. Images from these scans are then processed to obtain the information related to the flow of the contrast agent and thereby blood flow.

The knowledge of blood flow within a given tissue can prove beneficial for diagnostic purposes. Blood flow measurements can help in differentiating between normal and malignant tissue, further it can also give information about the necrotic regions present within a tumor (Miles *et al.* 2000, Miles 1999). The benefits of CT perfusion go beyond diagnosis as it can also be used for estimation of response to therapy and for treatment planning. Brain and liver are some of the most common applications of CT perfusion imaging. Interventional radiologists largely identify malignancy in a given liver tissue using the blood flow measurements of hepatic artery and portal vein, two

sources of blood supply for the liver (Pandharipande *et al.* 2005, Kim *et al.* 2014). Further, as seen in the previous section, blood perfusion is a dominant factor governing the temperature distribution within a tissue. Therefore, a precise knowledge of the blood perfusion distribution within a tissue is critical for modeling heat flow within the body tissue. All these factors make CT perfusion an important component for effective diagnosis and treatment planning.

There are different variations of CT scanners available commercially, some of the widely used scanners are listed in table 5.1.

Table 5.1 Commercially available CT scanners

Scanner	Name	Manufacturer
64- row multidetector CT scanner	VCT	GE Healthcare
4-MDCT scanner	Lightspeed Plus	GE Healthcare
16-MDCT scanner	LightSpeed	GE Healthcare
16-detector row scanner	Lightspeed 16	GE Medical Systems
Multi-detector row CT scanner	Sensation 16	Siemens medical solutions

X-ray CT enables non-invasive blood perfusion measurements, although imaging protocols and methods to calculate blood perfusion from acquired imaging data are still under development (Kim *et al.* 2014, Materne *et al.* 2000, Meier and Zierler 1954, Miles *et al.* 1991). The contrast concentration within a tissue increases as the blood brings the contrast material into the tissue. It subsequently decreases due to the removal of contrast

material from the tissue by venous outflow. Meier and Zierler have given a basic description of extracting blood perfusion and other perfusion parameters from the time varying contrast concentration in tissue (Meier and Zierler 1954). Over the time methods for calculating blood perfusion have evolved (Kim *et al.* 2014). Some of the most prevalent are the maximum slope method (Miles 1991, Miles *et al.*1991, Miles *et al.*1993), tracer kinetic method (Tofts *et al.*1999, Sourbron and Buckley 2011, 2013, Swinton *et al.*1970) and de-convolution method (Axel 1980, Axel 1983, Cuenod *et al.*2001).

The field of estimation of blood flow, volume using dye injection, indicator-dilution technique, started with Stewart (1897) and was further developed by Hamilton *et al.*(1932). During the later years there was confusion regarding this method and a detailed analysis of this was presented by Meier and Zierler (1954) and Zierler (1962).

Earlier studies used radio-isotopes as indicators (Sapirstein 1958, Zierler 1965) for blood flow estimation. Mathematical analysis of the flow of injected dye/contrast material in capillary beds has also been performed (Leonard and Jorgensen 1974, Borovetz *et al.* 1982, Lincoff *et al.* 1983). Fleming *et al.* used radiocolloid for estimating arterial and portal blood supplies for liver (Fleming *et al.* 1983). Mullani and Gould proposed a simple model for blood flow measurement where there is no venous outflow for some period before the start of recirculation (Mulani and Gould 1983). Patlak plot (Patlak *et al.* 1983 and Patlak and Blasberg 1985) was later developed which did not required compartmental models but required that concentration agent concentration has reached equilibrium within the tissue and plasma. This model has the flexibility to be used with homogenous as well as heterogeneous tissue and was applied to cerebral blood

flow by Patlak *et al.*. Rumberger *et al.* (1987) reported the calculations of the myocardial perfusion using contrast agent concentration curves obtained from CT scans and compared it with measurements from radiolabelled microspheres. Canine myocardial blood flow measurements were reported by Wolfkiel *et al.* (1987) and Gould *et al.* (1988) using radio-labeled microspheres and CT perfusion. Canine cerebral blood flow experiments were performed by Gobbel *et al.* (1993). Hattori *et al.* (1994) measured blood flow for superficial tumors. Cenic *et al.* (1999, 2000) developed a method for cerebral blood flow measurement and validated it against results obtained using microspheres. A kinetic based model was developed by Materne *et al.* (2000) for hepatic perfusion calculation and was validated using radiolabelled microspheres. Cuenod *et al.* (2001, 2002) used deconvolution method to calculate hepatic perfusion in rats. Wintermark *et al.* (2001) estimated cerebral blood flow by CT scans, using methods based on central volume principle (Meier and Zierler (1954)) and validated it against stable Xenon CT.

Peters *at al.* (1987) introduced a technique of measuring blood flow for an organ which was later extended by Miles (1991) to develop maximum slope method. Miles *et al.* (1994, 1995) applied this method for renal and pancreatic blood flow measurements. Miles *et al.* (1993) modified this technique to estimate blood flow in liver. Blomley *et al.* (1995) proposed a modification in maximum slope method for hepatic blood perfusion estimation. Maximum slope method was used by Bader *et al.* (1998) to assess the effect of liver transplantation on hepatic perfusion and by Koenig *et al.* (1998) for early detection of cerebral ischemic stroke.

The indicator-dilution technique has evolved into various methods which can be broadly classified as model-free and model based approaches. Maximum slope model is the widely used example of model-free approach. Tracer kinetic models, which come under deconvolution methods, are examples of model based approaches. These are described in the following sections.

In 1983 Axel developed a technique based on deconvolution to estimate blood flow related parameters (Axel 1983). In this technique the response to a quantum of injected dye contrast agent in the given tissue, response function, is defined with a set of unknown parameters. With the help of the characteristic of the contrast agent at the time of injection and the assumed response function, the concentration of the contrast agent in the tissue as a function of time is calculated and compared with actual experimental values. The unknown parameters in response function are selected on trial and error basis, until a close enough match is obtained. The hence obtained parameters are then used to obtain blood flow related parameters.

The method developed by Axel, deconvolution, is mathematically involved and require the users to have knowledge about the tissue structure to be able to make assumptions about the response function. The maximum slope method is relatively inexpensive computationally. It was developed by Miles in 1991, based on the work done by Peters *et al.*1987. Miles *et al.* were the first to apply the maximum slope method to the liver and validate it using dynamic colloid scintigraphy (Miles *et al.* 1993). This method assumes that contrast material is accumulating in the body tissue and there is no venous outflow in this period. It calculates the blood perfusion values using the maximum concentration values in arterial flow and maximum slope in the concentration of contrast

material in the tissue. This method was developed only for single blood supply organs, which was further extended to dual supply organ, liver, by Miles et. al. in 1993. Blomley *et al.* suggested modifications to the maximum slope method for liver in 1995.

Some of the other methods which had been employed by researchers are moments method, compartmental methods and Mullani-Gould formulation. Table 5.2 shows studies which have validated some of these methods primarily using microspheres and stable xenon washout.

Comparative study

Materne *et al.* proposed a version of tracer kinetic method for the liver perfusion, which was also compared using microspheres (Materne *et al.* 2000). The de-convolution method was first applied to liver by Cuenod *et al.* (2001). Maximum slope and tracer kinetic model are both based on dual input single compartment model, but are different. There have been studies comparing these methods by Kanda *et al.* in 2012.

Tracer kinetic models

It can be said that deconvolution method eventually evolved into tracer kinetic models. In these models the response function is defined with help of physiological parameters such as blood flow, blood volume, tissue permeability and amount of contrast agent extracted from the blood into the tissue (extraction fraction). The type and number of these unknown parameters varies within models, depending on the complexity of the model. The approach is to start with simplest model and check if this model is able to simulate the response as shown by experimental data (Sourbron and Buckley 2012). If the

match is satisfactory the model and the respective parameter values are accepted, otherwise a higher model with greater number of unknowns is tested.

Table 5.2 Validation studies for moments method, mullani-gould method, maximum slope method, deconvolution method and compartmental method.

Method	Validation	
Moments method	Microsphere measurements of regional cerebral perfusion in dogs	Gobbel *et al.* 1991 *Stroke*
	Comparison: Xenon washout studies in humans	Gobbel *et al.* 1993 *Am J Neuroradiol*
Mullani-Gould Formulation	Microspheres in canine myocardial studies	Wolfkliel *et al.* 1987 *Circulation*
		Rumberger *et al.*1987 *J Am Coll Cardiol*
		Gould *et al.*1988 Invest Radiol
Maximum Slope method*	Hepatic perfusion	Miles *et al.* 1993 *Radiol*
		Miles *et al.* 1994 *Invest Radiol*
		Miles *et al.* 1995 *Br J Radiol*
		Koenig *et al.* 1998 *Radiol*
		Blomley *et al.* 1993 *Invet. Radiol*
	Hepatic perfusion^{+}	Blomley *et al.* 1995 *J Comput Assist Tomgr*
Constrained Deconvolution method	Microspheres, rabbit cerebral Stable Xenon CT, Human cerebral	Cenic *et al.* 2000 *Am J Neuroradiol*
		Wintermark *et al.* 2001 Am J Neuroradiol
	Fluorescent microspheres, Canine cerebral	Nabavi *et al.* 1999 *J Comput Assist Tomogr*
Miscellaneous Compartmental methods	Radiolabeled microspheres/ Canine myocardial flow	Gould *et al.* 1988 *Invest Radiol*
	$H_2{}^{15}O$ PET Human cerebral	Gillard *et.al.* 2000 *Neurol Res*

Some of the widely used tracer kinetic models are distributed parameter model (DP), 2-compartment exchange model (2CXM), tissue-homogenity model (TH)(Sawada *et al.* 1989), adiabatic approximation to TH model (AATH) (Cenic *et al.* 2000 and Purdie *et al.* 2001), tissue uptake models (TU), compartmental uptake model (C-TU) (Pradel *et al.* 2003) and plug flow uptake model (P-TU) (St Lawrence *et al* 2000). An important factor to consider while choosing the model is the physiology of the tissue/organ. Certain models are suited for certain types of physiologies for example DP is widely used for liver (Petralia *et al.* 2011, Guyennon *et al.* 2010, Goresky *et al.* 1973), 2CXM for breast tumors (Cheong *et al.* 2004 and Brix *et al.* 2004).

Figures 5.1 and 5.2 illustrates the application of DP and AATH tracer kinetic models, respectively. Experiments were performed on white New Zealand rabbits were performed by Eleni Liapi. Data of the tissue concentration from artery, portal vein, spleen and healthy liver was collected from these experiments. DP and AATH model was applied to these data sets and the final set of parameters which gave the least errors and hence were accepted are given in figures 5.1 and 5.2.

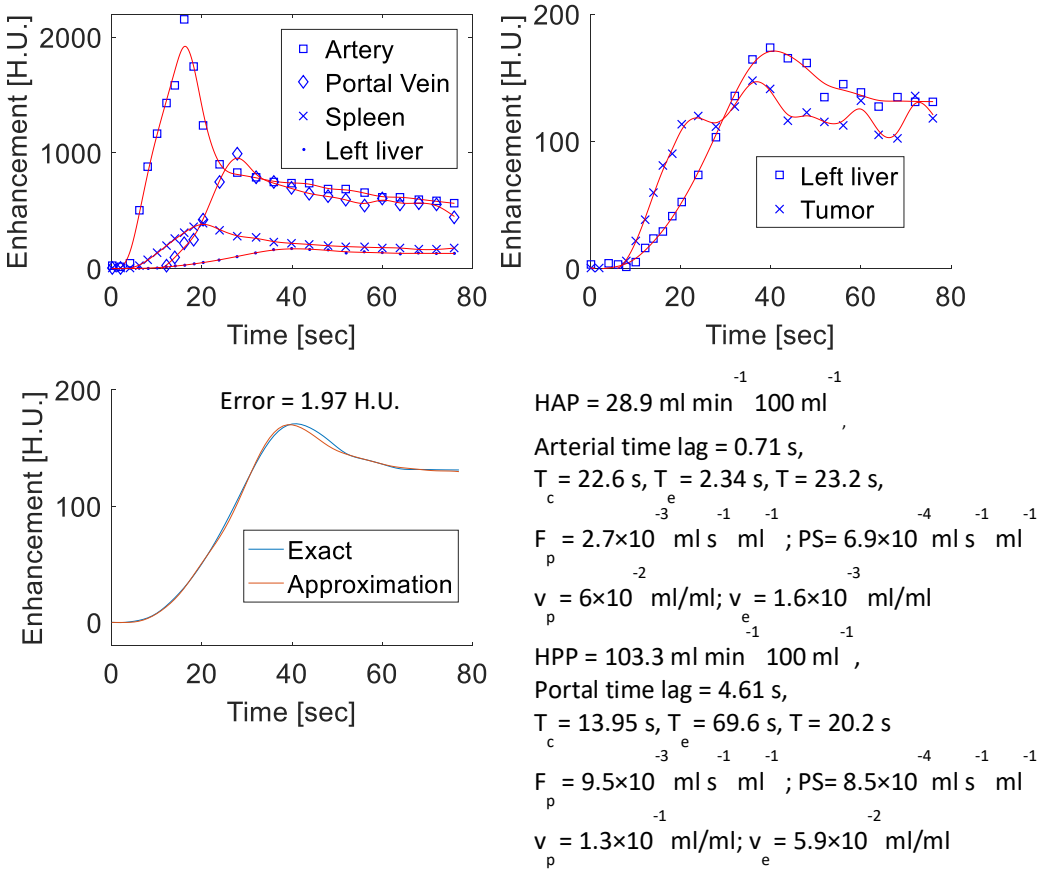

Figure 5.1: Set of parameters, plasma flow $F_{p,}$ permeability PS, plasma volume v_p, extracellular space volume v_e, for hepatic artery and portal vein in distributed parameter model for subject 10. These set of parameters give the liver concentration curve that is closest to the experimentally obtained data.

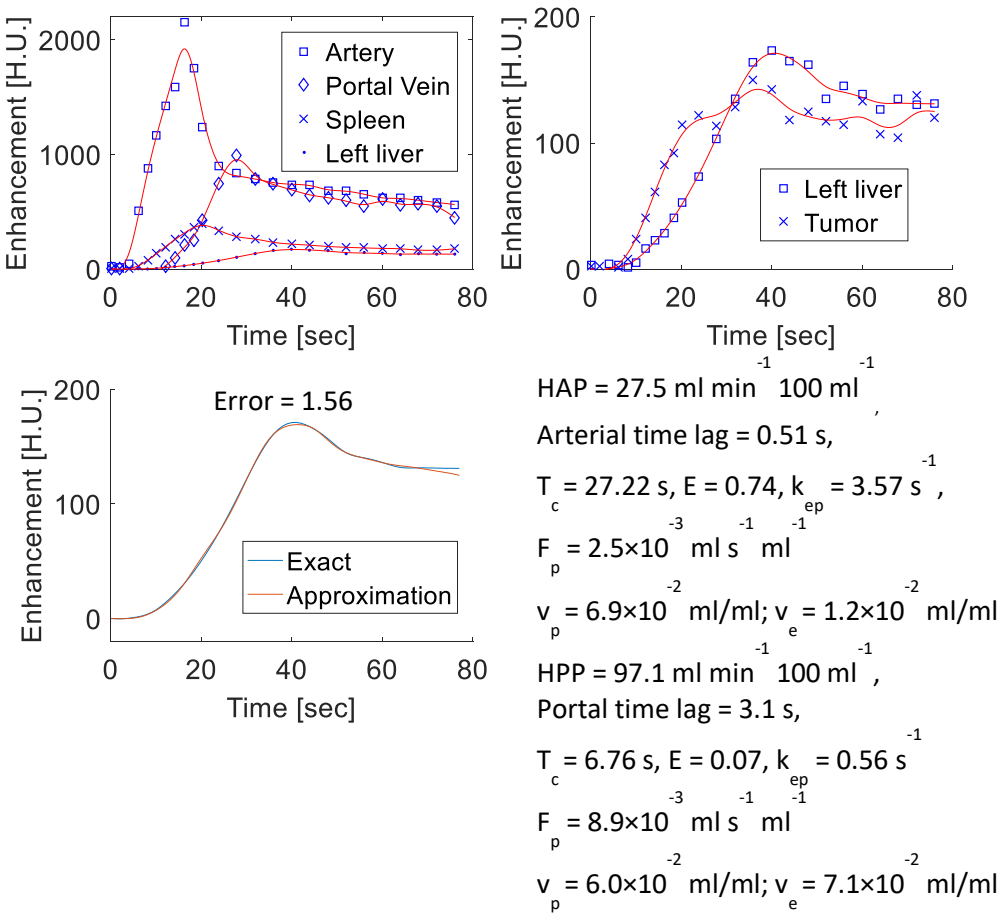

Figure 5.2: Set of parameters, plasma flow F_p, permeability PS, plasma volume v_p, extracellular space volume v_e, for hepatic artery and portal vein in adiabatic approximation model for subject 10. These set of parameters give the liver concentration curve that is closest to the experimentally obtained data.

5.2 Maximum Slope Model Assumption Discrepancy and Implications for Diagnosis of Hypervascular Liver Tumors with CT Perfusion

5.2.1 INTRODUCTION

For diagnostic radiologic imaging purposes, quantification of the blood flow within the healthy and tumorous liver is crucial for differentiation of the tumorous tissue from the healthy tissue, as well as evaluation of tumor response to therapy (Kim *et.al.* 2014). The liver is an organ with unique flow dynamics, related to its dual vascular supply from the portal vein and the hepatic artery (Bradley *et al.* 1945, O' Connor *et al.* 1988, Tygstrup *et al.*1962, Schenk *et al.* 1962) (figure 5.3). The hepatic artery supplies arterial blood to the liver, and accounts for approximately 25% of its blood flow, while the portal vein carries to the liver, venous blood drained from the spleen, gastrointestinal tract and its associated organs, supplying approximately 75% of its blood flow (Schenk *et al.* 1962). In contrast to liver, hypervascular primary and metastatic liver tumors are known to derive their vascular supply primarily from the hepatic artery, a well-known phenomenon and the basis of all intra-arterial therapies for these tumors (Liapi and Geschwind 2007, Cady and Oberfield 1974, Swinton *et al.* 1970).

Hepatic artery supplies blood to the liver from the cardio-pulmonary circulation. Liver also gets blood supply from the portal vein, which is in turn fed by mesenteric and splenic vein coming from gut and spleen respectively (Fleming *et al.* 1983). Therefore the blood arriving to the liver from the main circulation comes through hepatic artery first

and then through the portal vein en route spleen and gut. This time lag in the blood coming through the portal vein is exploited in the maximum slope method, to differentiate between the arterial and portal blood flow in the liver tissue.

CT perfusion is used by interventional radiologist to analyze the blood flow within the liver for diagnosing cancer (Kim *et.al.* 2014). The ratio of the blood supplies coming from hepatic artery and portal vein can be obtained from CT perfusion and therefore it can be used to differentiate between malignant and normal tissue. In CT perfusion a contrast agent, which is opaque to the X-rays, is injected intravenously and a series of CT scans are performed to trace the contrast agent within the body tissue. The contrast agent reaches the tissue through the feeding artery and is eventually drained out through the venous outflow. CT scan images give the variation of contrast agent concentration with time. As mentioned earlier, analysis of the CT scan images is required in order to obtain blood perfusion values and the maximum slope method has been used here for the analysis.

The maximum slope method assumes that the contrast material coming from the feeding artery accumulates inside the tissue, without any venous outflow. Therefore the slope of the tissue density curve (TDC), contrast agent concentration with time, gives the rate of intake of contrast material into the tissue. The TDC of the feeding artery gives the contrast concentration in the incoming blood flow to the tissue. By applying conservation of mass and equating the inflow of the contrast material to the rate of accumulation of contrast material in the tissue we get

$$F.c_{in}(t) = \frac{\Delta c(t)}{\Delta t}.V \tag{5.1}$$

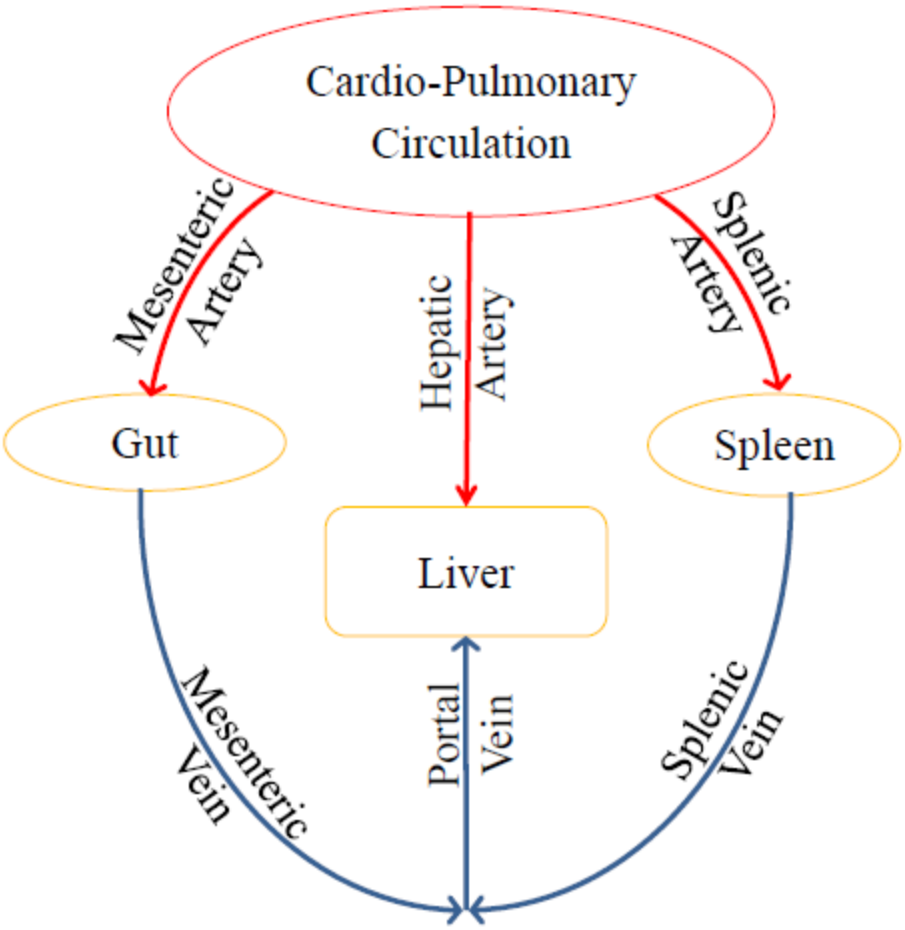

Figure 5.3. Illustration demonstrating blood circulation to the liver. Liver receives its blood supply from hepatic artery and portal vein. Blood arriving to the liver from the main circulation, first comes through the hepatic artery and after a time lag comes from the portal vein via the spleen and gut.

where $C_{in}(t)$ is the concentration of contrast material in the blood supply feeding the tissue at time t, F is the flow rate of the blood supply, $c(t)$ is the concentration of the contrast material of the tissue at time t and V is the volume of the tissue. To calculate the blood flow rate per unit volume of the tissue, the maximum slope of the liver TDC is divided by the maximum concentration (enhancement) in the arterial TDC. For this it has

to be ensured that only that portion of the TDC is analyzed where the no-venous outflow assumption is valid.

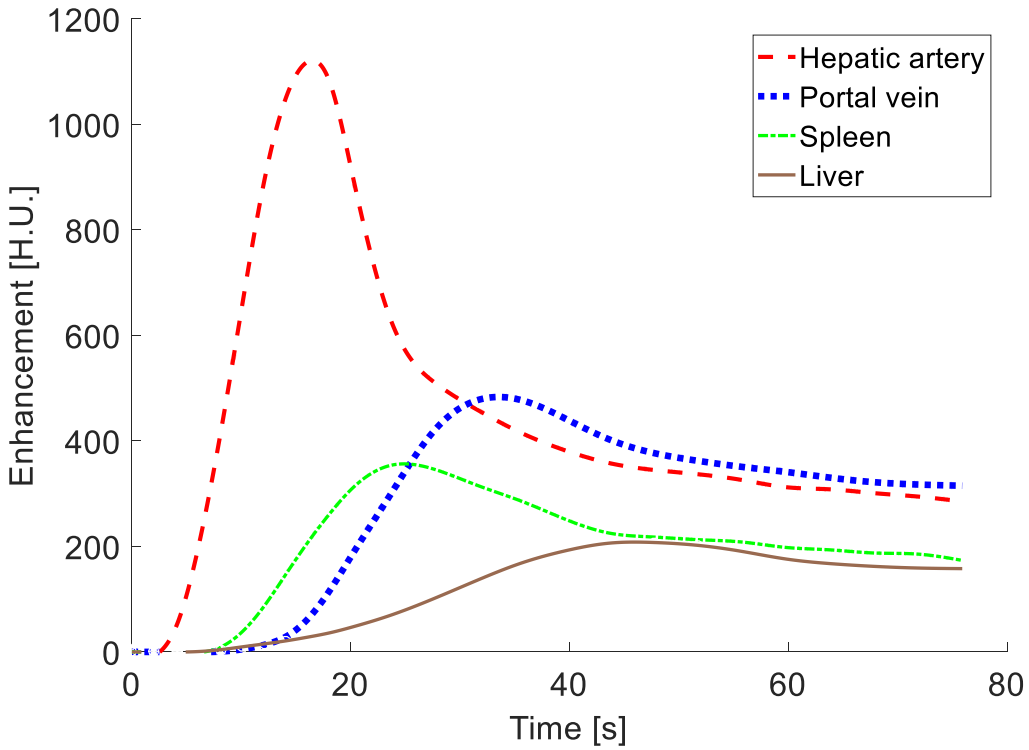

Figure 5.4 Typical tissue density curves (TDCs) for artery, portal vein, spleen and liver. The concentration of the contrast medium, enahancement, is given in terms of Hounsfield Units (H.U.). From the time of peak enhancement of the arterial, splenic and portal vein curves the sequence of the appearance of contrast material can be ascertained. These are representation of the TDCs and not actual data points.

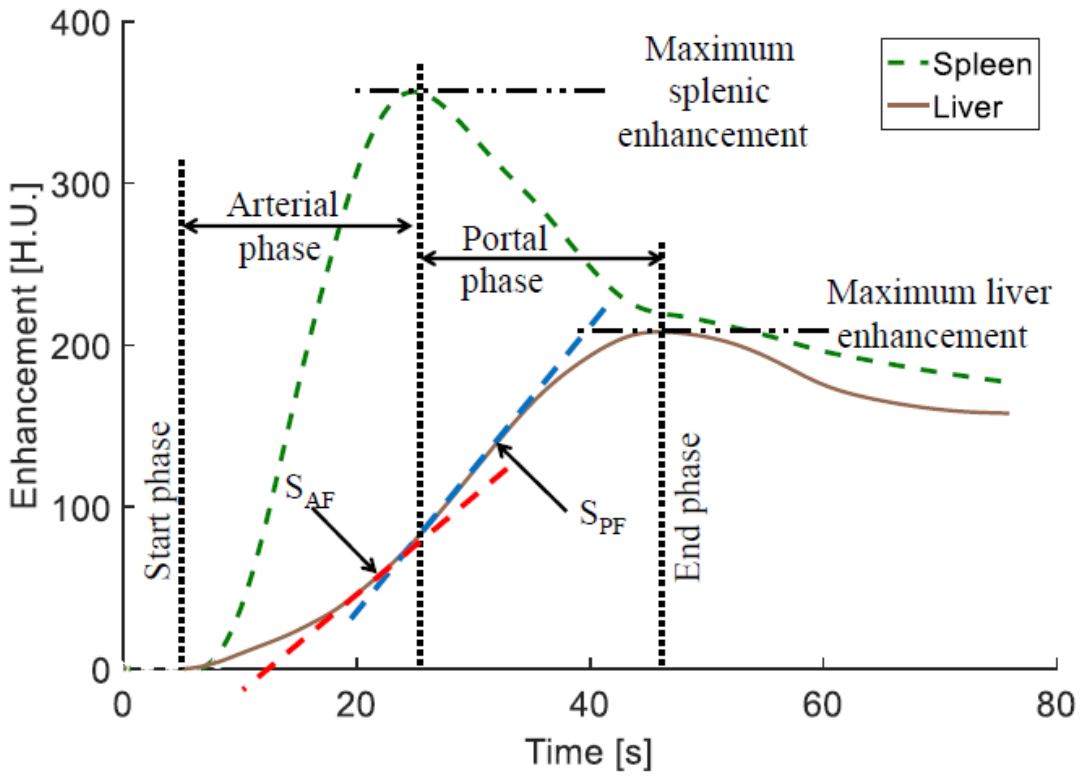

Figure 5.5. TDCs for liver and spleen, illustrating the arterial and portal phase, separated by the time of peak splenic enhancement, and the corresponding maximum slopes. Only that portion of the TDC is considered in maximum slope method which is after the start phase (SP) and the end phase (EP), defined by maximum enhancement values. These are representation of the TDCs and not actual data points.

As the liver receives its blood supply from two sources, the hepatic artery and hepatic portal vein, the maximum slope method needs to be modified to account for the dual-input. The contrast material coming from the main circulation comes directly to the liver through the hepatic artery, but it has to go through the spleen/gut in order to come through the portal vein (Fig 5.3). Therefore maximum slope method assumes that prior to the time of the splenic peak there is no contrast from other organs or tissues feeding the portal vein, thus up until this time, the liver is considered to be supplied with only arterial contrast. The time of maximal enhancement of spleen indicates the start of the portal

phase and the time of maximum tissue enhancement indicated the end of the portal phase. The bolus injection should be kept fast and short to avoid mixing of the two phases.

Figure 5.4 illustrates a typical TDC for liver tissue along with artery, portal vein and spleen. The TDC for liver is divided into two parts (Fig 5.5), first when the arterial supply dominates and the second when the portal blood supply dominates. The two parts are separated by the time of maximum splenic enhancement.

For hypervascular tumors, the time of maximal liver tissue enhancement may occur prior to or after the splenic maximal arterial enhancement. In the first case, we may then observe that the downward slope of the TDC of a tumor may occur before the spleen reaches its maximal enhancement, affecting therefore portal perfusion measurements. This anomaly was observed for some of the cases of hypervascular tumor, which lead to unreliable estimates of portal perfusion, while using maximum slope method. Other methods, such as tracer kinetic models, use the entire curve for the perfusion calculation and therefore do not have these problems. The aim of the present work was to evaluate the dual-input maximum slope method in calculating the hepatic arterial and portal perfusion of tumor in the VX2 rabbit liver model. We studied the TDC for 11 subjects (rabbits) and applied the dual-input maximum slope method for calculating the perfusion values. We specifically sought to examine whether the dual-input maximum slope method is able to calculate hepatic portal perfusion in cases of hypervascular hepatic tumors.

Material and Methods[1]

Adult New Zealand White rabbits were used in this study. All (n=11) weighed 3.5–4.2 kgs prior to imaging. Rabbits were housed in an Association for Assessment and Accreditation of Laboratory Animal Care (AAALAC)-accredited facility in compliance with the Guide for the Care and Use of Laboratory Animals (National Research Council 1996) and procedures were approved by the Johns Hopkins Institutional Animal Care and Use Committee (IACUC). Male and female white New Zealand rabbits were selected for their relevance to intra-arterial procedures and liver tumor imaging as part of our ongoing studies on liver cancer therapy. At designated time points, individual animals were randomly selected for inclusion in study cohorts at which point they underwent implantation of rabbit VX2 tumor in the liver for subsequent CT perfusion imaging. These experiments were performed by E. Liapi .

Animal Model And Tumor Implantation [1]

Each animal received tumor implantation in the left lobe of the liver as detailed in (Buijs *et al.* 2011, Lee *et al.* 2008). The tumors were allowed to grow in the rabbit livers for 13–15 days, after which time they were subsequently imaged (Yamamoto *et al.* 2006, Hong *et al.* 2005)

[1] The experiments were performed by E. Liapi and S. Mirpour

Wide-Array CT Perfusion Protocol [2]

For CT perfusion imaging, each rabbit was first sedated with intramuscular injection of ketamine and xylazine and subsequently scanned in a wide-array 320-clinical CT scanner (Aquillon ONE, Toshiba, Japan). The CT perfusion protocol included at least one non-contrast enhanced volume acquisition, followed by a series of contrast-enhanced CT acquisitions. Iso-osmolar contrast iodixanol (1.5 ml/kg, 320 mg I/ml-Visipaque, GE Healthcare Inc., Princeton, NJ) was injected intravenously at 1ml/sec via a 21G butterfly needle inserted in a marginal ear vein, followed by a saline flush of 7 ml at the same rate. The CT perfusion scanning parameters were: FOV=22cm, KV=120, mA=80, slice thickness=0.5mm, scan delay=6 sec. Total intermittent scanning time for each rabbit scan was 77 seconds. Wide-array CT scans were obtained every 2 sec for the first 25 seconds, and every 3 seconds thereafter and for an additional 42 seconds. Each scan takes 0.5 sec (one volume acquisition equals a single gantry rotation at a speed of 0.5 s per 360°rotation). A total of 27 acquisitions with 5,400 images were obtained during each CT perfusion study, which were subsequently transferred to a dedicated workstation for image reconstruction and analysis.

[2] The experiments were conducted by E. Liapi and S. Mirpour

Image reconstruction and analysis

Following CT acquisition, images were reconstructed with adaptive iterative dose reduction 3D (AIDR 3D; Toshiba Medical Systems, Japan), which is the manufacturer's commercial hybrid IR algorithm, combining reconstruction in the raw data and image space domains. The reconstruction filter (FC03), and the reconstructed section thickness (5 mm) were fixed for all studies.

Data was then exported to a dedicated workstation for image registration, using the manufacturer's commercial software program (Body Registration; Toshiba Medical System, Tochigi, Japan) that automatically corrects the spatially non-consistent position of each organ among the 27-image series of each study. The program adjusted the position of each organ three-dimensionally, i.e., proportionally along any axis and rotationally.

Maximum Slope Theory and Models

The maximum slope (MS) method has been used to calculate the arterial and portal perfusion. MS method assumes no-venous outflow in the tissue, therefore only that portion of the TDC is considered which is before the start of venous outflow (Fig. 5.5). In Aquilion ONE (Toshiba) the point of maximum enhancement is chosen as the point of the start of the venous outflow and defined as End Phase (EP). By definition, after EP the enhancement starts to decreases, which is only possible if the contrast material is leaving the tissue, signaling venous outflow. Further, a start phase (SP) is defined as the point where contrast material starts entering the tissue, signified by the start of contrast enhancement. A short and fast contrast bolus is administered to make sure the no-venous outflow assumption is valid.

In a single supply organ the maximum slope of the TDC between the SP and EP is calculated and divided by the peak enhancement of the supplying artery, to obtain the blood flow per unit volume, as given by the following equation.

$$\frac{F}{V} = \frac{max\left[\frac{d[c(t)]}{dt}\Big|_{t=SP}^{t=EP}\right]}{a(t)|max} \tag{5.2}$$

where F is the blood flow rate in the tissue, V is the tissue volume, SP is the start phase, EP is the end phase, SM is the time at which spleen attains maximum enhancement, $c(t)$ and $a(t)$ are the concentration of contrast medium in the tissue and artery at a time instant t .

With liver being a dual blood supply organ, fed by hepatic artery and portal vein, a different approach is used. The TDC can be, therefore, divided into two phases, the arterial phase, which is dominated by the arterial flow and the portal phase, which is dominated by the portal venous flow (Figure 5.5). These regions are separated at the point of maximum splenic enhancement (SM). The arterial and portal blood perfusion is given by the following equations:

$$\left(\frac{F}{V}\right)_A = \frac{max\left[\frac{d[c(t)]}{dt}\Big|_{t=SP}^{t=SM}\right]}{a(t)|max} \tag{5.3}$$

$$\left(\frac{F}{V}\right)_P = \frac{max\left[\frac{d[c(t)]}{dt}\Big|_{t=SM}^{t=EP}\right]}{p(t)|max} \tag{5.4}$$

where $\left(\frac{F}{V}\right)_A$ is the arterial blood flow rate per unit tissue volume, $\left(\frac{F}{V}\right)_P$ is the portal blood flow rate per unit tissue volume, SM is the time at which spleen attains maximum

enhancement, and $p(t)$ is the concentration of contrast medium in the portal vein at a time instant t .

By placing circular regions of interest (ROIs) over the aorta, the main portal vein, the right and left lobes of the liver, as well as over each entire tumor at the level of each longest axial diameter, TDC were derived. The size of each ROI was at least 1.0 cm^2 or larger, except for that in the portal vein and the aorta, which were set to cover their shortest axis at the level of the hepatic hilum (and with a diameter of 1.0 mm^2).

Perfusion was calculated by using: a) the dedicated commercial software, on a pixel by pixel basis, that uses the dual-input maximum slope model (Body Perfusion; Toshiba Medical System, Tochigi, Japan), and b) MATLAB Code (Mathworks, Natick MA). Flow measurements were expressed in mL per 100 mL per min. Arterial flow (AF), portal flow (PF) and perfusion index (PI) were calculated for tumor, left and right hepatic parenchyma.

A MATLAB (Mathworks, Natick MA) code was developed to implement the maximum slope method and calculate the perfusion values. After background subtraction, as described earlier, curve fitting was done for all the TDCs using 'smoothingspline' function in MATLAB. The fitted TDCs were discretized using a time step of 0.1 s for calculating maximum value or slope. The time corresponding to the maximum enhancement point for left/right liver and tumor ROI was taken as the EP point. For choosing the SP, we choose that point where the enhancement reached 10 % of the maximum enhancement in the corresponding TDC. The hepatic arterial perfusion (HPA) and hepatic portal perfusion (HPP) values were calculated using equation (5.3) and (5.4) respectively. The perfusion value hence obtained has '1/s' units, which is then changed to

'ml/(min.100ml)' by multiplying the perfusion value with 100*60 [ml. s/(min.100ml)]. The perfusion index was calculated using equation (5.5). The data was recorded and analyzed for 11 subjects.

$$HPI = \frac{HPA}{(HPA+HPP)} * 100 \quad (5.5)$$

Imaging analysis algorithm: ROIs

Images were processed in Toshiba CT scanner. The regions of interest (ROIs) were selected for the artery, portal vein, spleen, healthy liver (left/right) and tumor as shown in figure 5.6. The Toshiba software generated TDCs corresponding to these ROIs. CT scan comprised of 25 scans and therefore each of the six curves, corresponding to different ROIs, had 25 data which were recorded and used for the calculation of perfusion values. In order to remove the background noise the average of the first two points is subtracted from all the points.

Arterial and portal flow for tumor, left and right liver were calculated with the use of the commercial software (Body Perfusion, Toshiba) (Figure 5.7), as well as by extracting HU values from the TDC curves to MATLAB software (MathWorks, Natick, Massachusetts) and subsequently deriving perfusion values from the equation.

5.2.2 RESULTS

The maximum arterial and portal enhancement for 11 subjects is shown in Table 5.3. It also shows the SP and time to peak points of artery, portal vein and spleen. The SP of artery denotes the entering of contrast material in the artery and therefore starts the entire process. SP time of artery for different subjects varies, which makes the

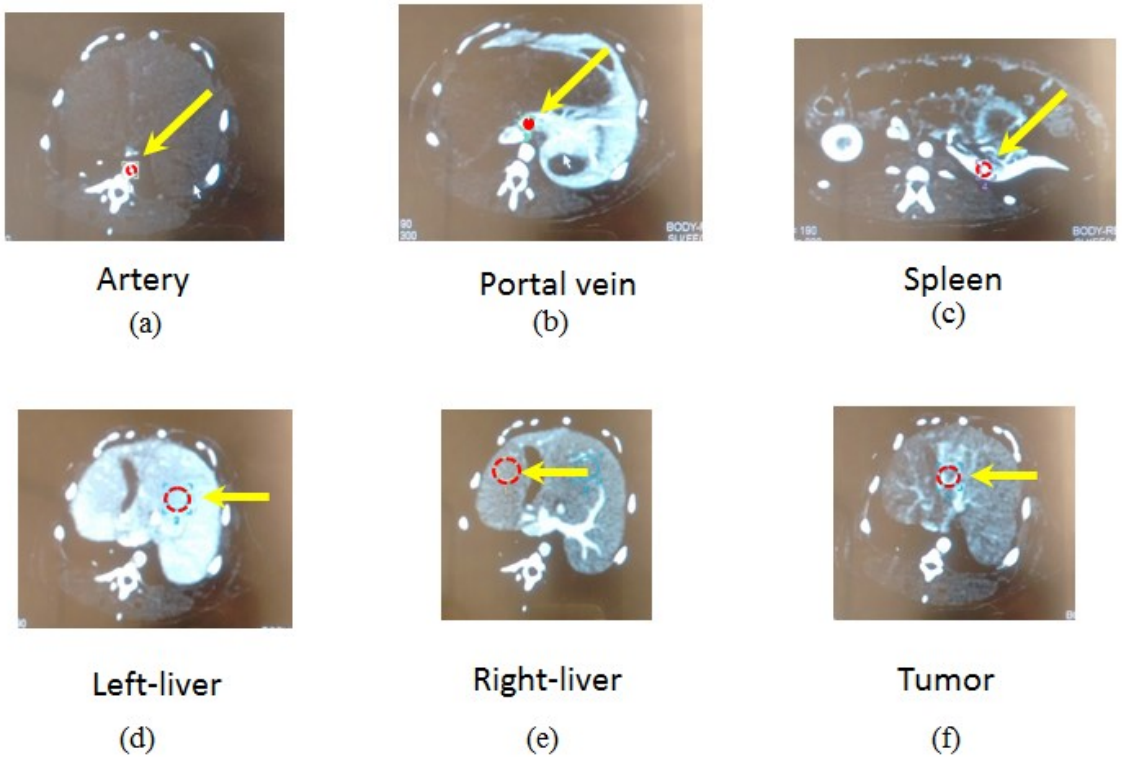

Figure 5.6. Regions of interest: (a) artery, (b) portal vein, (c) spleen, (d) left liver, (e) right liver and (f) tumor

comparison between subjects difficult. In order to normalize and therefore facilitate intra subject comparison all the time points have been subtracted by the SP time of artery. The normalized values are given in the last two columns of Table 5.3. Figure 5.8 shows the time of maximum enhancement for artery, portal vein and spleen for different subjects. The average values of the time of maximum enhancement, along with standard deviation, are shown in an insert.

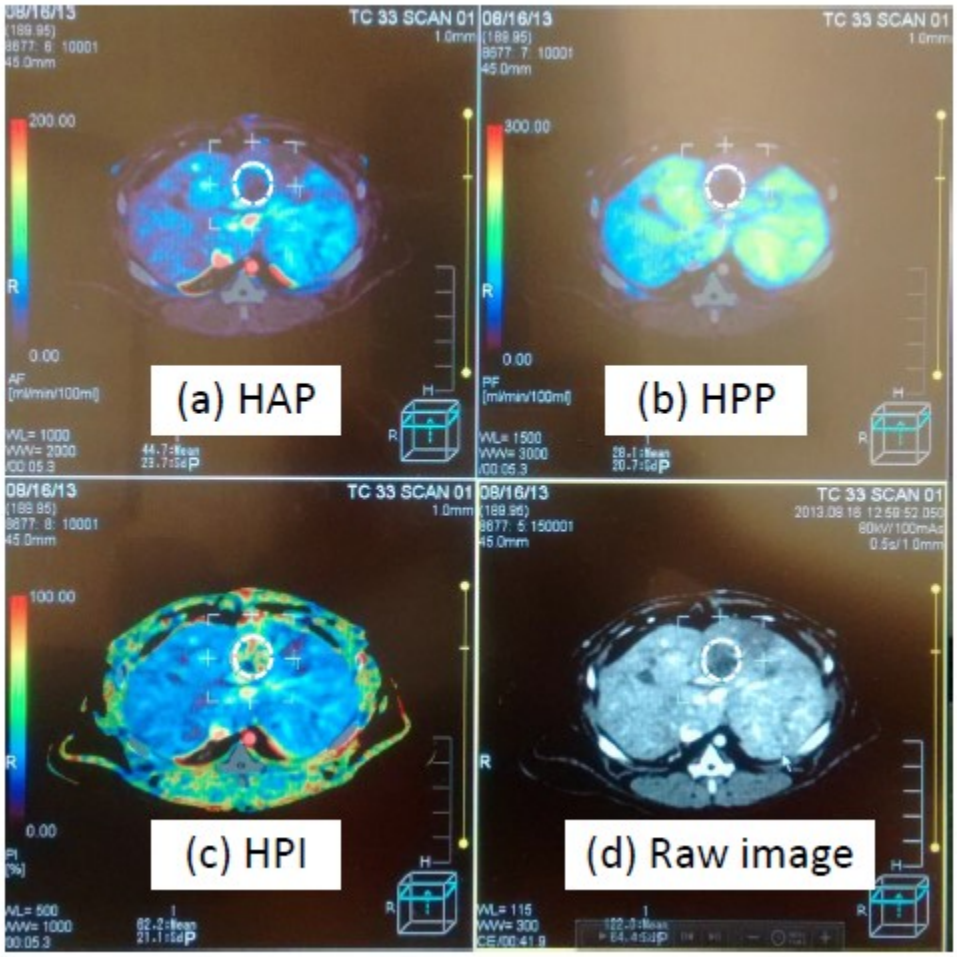

Figure 5.7. Color map for patient 33, with region of interest around a tumor, showing (a) Hepatic Arterial Perfusion (HAP), (b) Hepatic Portal Perfusion (HPP), (c) Hepatic Perfusion Index (HPI), and (d) raw/unprocessed image.

Table 5.3. The maximum enhancement of artery and portal vein. Start phase and time at maximum enhancement for artery, portal vein and spleen.

Patient No.	ROI	Maximum enhancement [H.U.]	Start Phase [s]	Maximum enhancement Time [s]	Normalized Start phase [s]	Normalized Maximum enhancement time [s]
10	Artery	1045.6	4.8	16.3	0	11.5
	Portal Vein	524	14.2	27.9	9.4	23.1
	Spleen		6.7	20.3	1.9	15.5
11	Artery	921.8	8.6	21.8	0	13.2
	Portal Vein	451.7	19.1	33.5	10.5	24.9
	Spleen		15.5	30.6	6.9	22
12	Artery	1121.2	5.2	16.5	0	11.3
	Portal Vein	483.2	15.4	33.5	10.2	28.3
	Spleen		10	24.9	4.8	19.7
14	Artery	903.4	5.3	17.9	0	12.6
	Portal Vein	407.4	16	31.2	10.7	25.9
	Spleen		10.9	24.6	5.6	19.3
15	Artery	968	4.9	15.1	0	10.2
	Portal Vein	369	15.8	27.4	10.9	22.5
	Spleen		9.3	21.8	4.4	16.9
20	Artery	961.9	2.1	11.6	0	9.5
	Portal Vein	529.7	9.1	21.1	7	19
	Spleen		4.6	17.1	2.5	15
23	Artery	1147	3	16	0	13
	Portal Vein	525.4	10.3	28.3	7.3	25.3
	Spleen		7.8	24.2	4.8	21.2
24	Artery	1358	5.6	17	0	11.4
	Portal Vein	514.8	15.7	26.3	10.1	20.7
	Spleen		10.5	26.2	4.9	20.6
33	Artery	2127	11.3	20.4	0	9.1
	Portal Vein	463.1	23.5	33.2	12.2	21.9
	Spleen		19.7	30.4	8.4	19.1
40	Artery	1210.5	4	13.8	0	9.8
	Portal Vein	352.1	12.5	24.6	8.5	20.6
	Spleen		6.5	17.7	2.5	13.7
41	Artery	1510.9	3.6	12.3	0	8.7
	Portal Vein	439.4	13.4	23.7	9.8	20.1
	Spleen		5.8	20.6	2.2	17

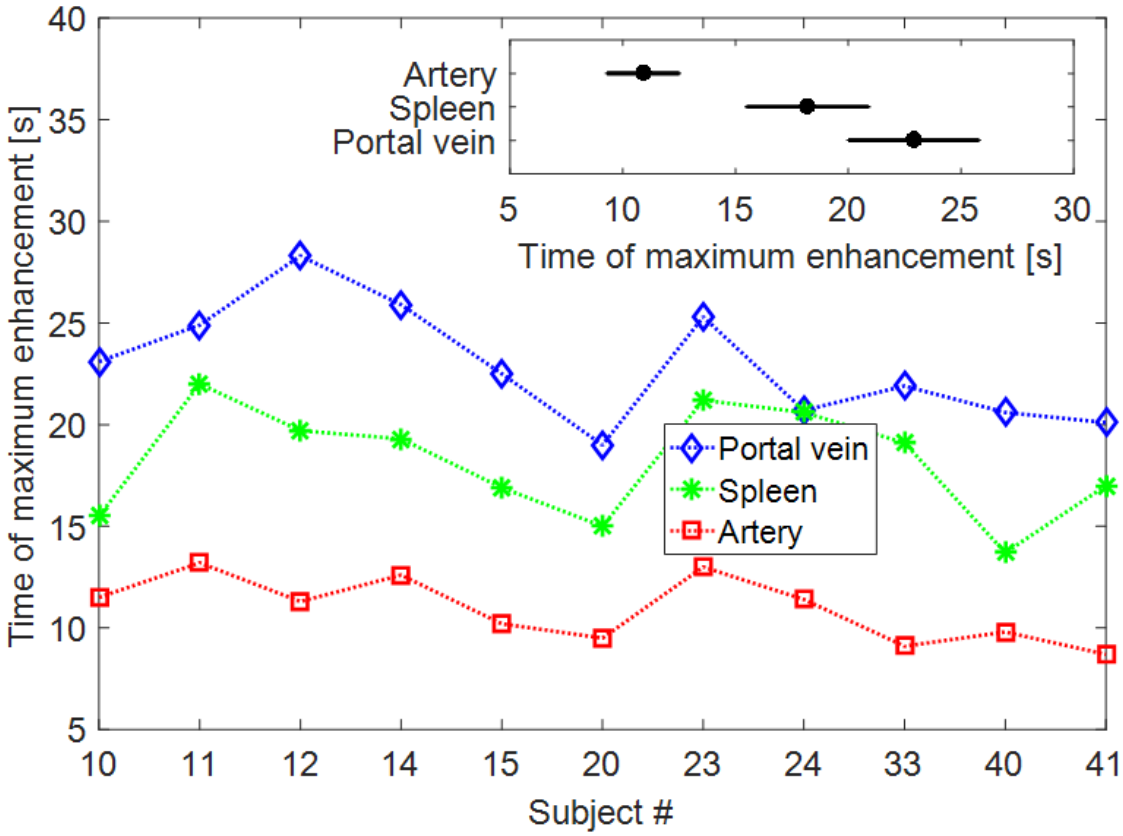

Figure 5.8. Time of maximum enhancement for artery, spleen and portal vein in 11 subjects. Figure insert shows the average time of maximum enhancement for artery, spleen and portal vein in 11 subjects. X-error bar denotes the standard deviation in average values. Artery attains maximum enhancement the earliest followed by spleen and portal vein.

Table 5.4. Time of start phase (SP), arterial maximum slope, portal maximum slope and end phase (EP) for left/right liver and tumor.

Patient No.	ROI	Start phase [s]	Arterial Slope [s]	Portal slope [s]	End Phase [s]		Normalized Start phase [s]	Normalized Arterial slope [s]	Normalized Portal Slope [s]	Normalized End phase [s]
10	Left Liver	12.6	20.3	30	40	7.8	15.5	25.2	35.2	12.6
	Right Liver	16.9	17.6	25.6	39.1	12.1	12.8	20.8	34.3	16.9
	Tumor	9.4	13.3	20.3	23.7	4.6	8.5	15.5	18.9	9.4
11	Left Liver	22	30.6	34.7	46.8	13.4	22	26.1	38.2	22
	Right Liver	25.7	29.9	30.6	45	17.1	21.3	22	36.4	25.7
	Tumor	13.4	19.7	na	29.5	4.8	11.1	na	20.9	13.4
12	Left Liver	14.8	24.9	31.9	39.6	9.6	19.7	26.7	34.4	14.8
	Right Liver	13.6	24.9	30.1	46	8.4	19.7	24.9	40.8	13.6
	Tumor	9.9	15.9	24.9	30.9	4.7	10.7	19.7	25.7	9.9
14	Left Liver	15.5	24.6	33	41.8	10.2	19.3	27.7	36.5	15.5
	Right Liver	15.2	24.6	29.8	43.8	9.9	19.3	24.5	38.5	15.2
	Tumor	9.7	12.2	24.6	25.3	4.4	6.9	19.3	20	9.7
15	Left Liver	17.8	21.8	30	39.4	12.9	16.9	25.1	34.5	17.8
	Right Liver	18.1	21.8	33	46.6	13.2	16.9	28.1	41.7	18.1
	Tumor	8.4	15.9	21.8	29.1	3.5	11	16.9	24.2	8.4
20	Left Liver	11.5	17.1	22	32.3	9.4	15	19.9	30.2	11.5
	Right Liver	13.2	17.1	23.8	34.3	11.1	15	21.7	32.2	13.2
	Tumor	5.2	12.4	17.1	17.6	3.1	10.3	15	15.5	5.2
23	Left Liver	17.5	24.2	26.3	40.6	14.5	21.2	23.3	37.6	17.5
	Right Liver	17.9	22.5	31.9	46.7	14.9	19.5	28.9	43.7	17.9
	Tumor	7.8	12.3	24.2	26.2	4.8	9.3	21.2	23.2	7.8
24	Left Liver	19.4	26.2	28.3	44.5	13.8	20.6	22.7	38.9	19.4
	Right Liver	20.2	25.4	34.1	42.9	14.6	19.8	28.5	37.3	20.2
	Tumor	11.1	13.2	26.2	30	5.5	7.6	20.6	24.4	11.1
33	Left Liver	26.3	30.4	35	48.1	15	19.1	23.7	36.8	26.3
	Right Liver	30.1	30.4	34.9	50.1	18.8	19.1	23.6	38.8	30.1
	Tumor	17.8	22.9	n.a.	30.3	6.5	11.6	na	19	17.8
40	Left Liver	14.4	17.5	26.4	39.8	10.4	13.5	22.4	35.8	14.4
	Right Liver	12.8	17.7	36.1	41.1	8.8	13.7	32.1	37.1	12.8
	Tumor	7.3	14.5	17.7	21.5	3.3	10.5	13.7	17.5	7.3
41	Left Liver	13.5	19.4	28.9	37	9.9	15.8	25.3	33.4	13.5
	Right Liver	13.8	20.6	24.1	37.9	10.2	17	20.5	34.3	13.8
	Tumor	7.7	11.1	na	19.8	4.1	7.5	na	16.2	7.7

Table 5.5. Perfusion value comparison: CT scanner vs. calculated values

Patient No.	ROI	Calculated HAP (ml/(min. 100ml))	Calculated HPP (ml/(min. 100ml))	Calculated HPI (%)	CT scanner similar ROI HAP (ml/(min. 100ml))	CT scanner similar ROI HPP (ml/(min. 100ml))	CT scanner similar ROI HPI (%)
10	Left Liver	33.6	92.2	26.7	50.7	128.6	28.2
	Right	34.9	162.7	17.6	50.3	158.5	24
	Tumor	57.2	68.6	45.5	85.2	55	61.7
11	Left	46.0	139.2	24.8	52.7	141.7	26.9
	Right	80.5	159.5	33.5	62.7	168.9	27
	Tumor	76.4	0.0	100.0	78.5	31.3	71.5
12	Left	36.2	100.4	26.5	57.2	104.6	36.4
	Right	41.4	109.7	27.4	54.9	131.5	29.5
	Tumor	84.3	27.9	75.1	115.8	40	75.5
14	Left	41.8	107.0	28.1	50.6	137.2	26.9
	Right	54.8	154.8	26.1	46.1	125.6	26.8
	Tumor	68.5	9.4	87.9	98	27	79.3
15	Left	40.0	126.8	24.0	31.8	168.1	15.9
	Right	29.5	112.1	20.8	24.2	144.9	14.4
	Tumor	47.9	23.8	66.8	51.3	47.2	54.8
20	Left	36.0	105.4	25.5	26.8	176.4	13.5
	Right	35.5	101.8	25.8	38.3	158.4	19.4
	Tumor	72.4	9.9	87.9	132.4	28.5	80.2
23	Left	57.2	143.7	28.5	60.4	166.4	26.7
	Right	47.6	94.4	33.5	47	140.6	25
	Tumor	57.0	21.0	73.1	73.9	31.8	74.7
24	Left	50.6	142.4	26.2	65.2	197	24.9
	Right	44.0	168.2	20.8	51.3	196.8	20.6
	Tumor	56.0	11.1	83.5	81.6	47.2	68.8
33	Left	19.2	127.6	13.1	69.1	192.6	26.4
	Right	17.1	135.8	11.2	44.4	134.8	24.8
	Tumor	21.1	0.0	100.0	44.7	28.1	62.2
40	Left	28.0	171.8	14.0	32.8	165.9	16.5
	Right	26.4	162.1	14.0	30.3	144	18.2
	Tumor	60.9	128.0	32.2	87.2	91.5	54.7
41	Left	30.3	103.8	22.6	73.6	137.5	34.7
	Right	17.9	113.1	13.7	47.5	154.4	23.4
	Tumor	49.0	0.0	100.0	114.1	28	79.4

The key points in the TDCs curves are the start/end phase and the point where the maximum arterial/portal slope is obtained. These points of left/right liver and tumor ROI for different time subjects are given in Table 5.4. Table 5.5 gives the perfusion values for left/right liver and tumor ROIs calculated using equations 5.3-5. The corresponding values obtained from the CT perfusion software Aquilon is also give in the table.

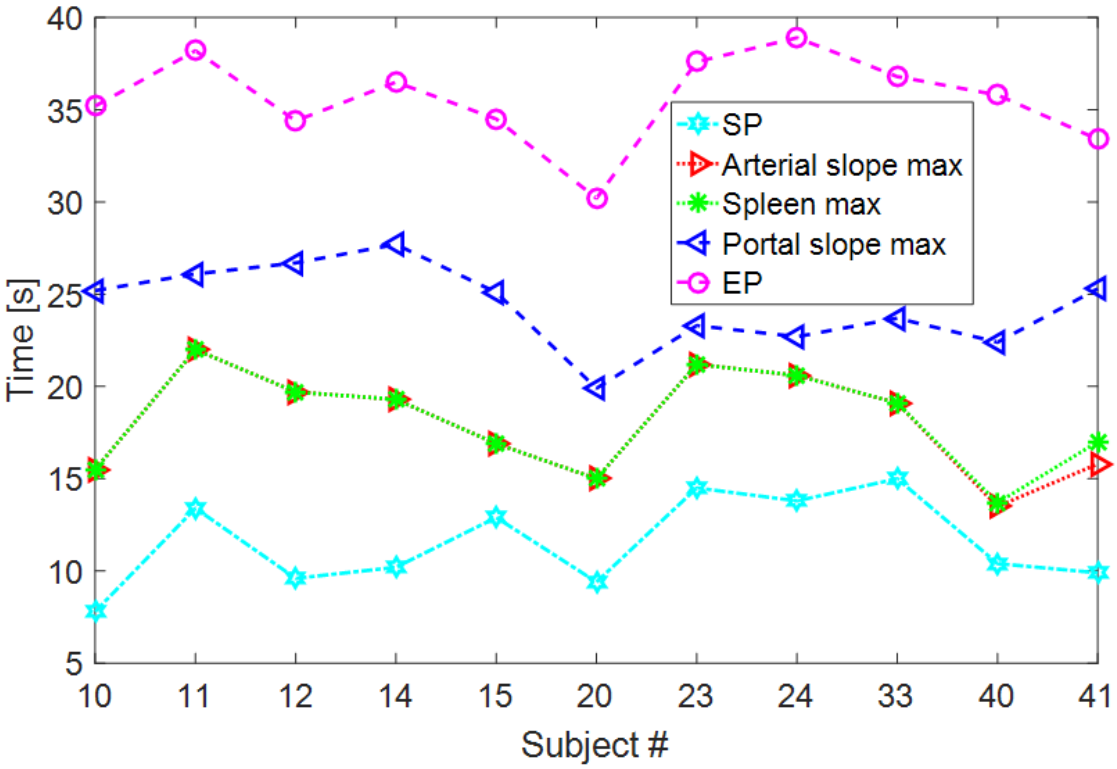

Figure 5.9. Time of start phase (SP), arterial maximum slope, portal maximum slope and end phase (EP) for healthy liver in 11 patients, along with the respective splenic maximum time. The portal phase has a larger duration than the arterial phase. The time of arterial maximum slope and splenic maximum is close.

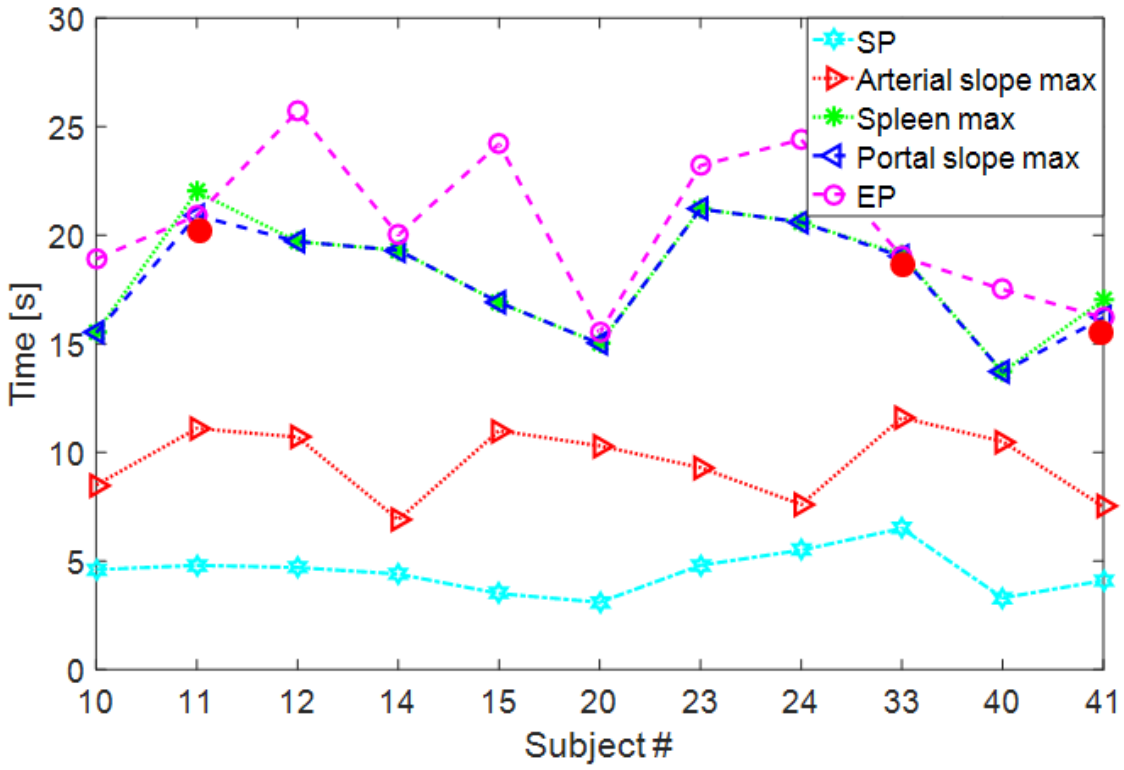

Figure 5.10. Time of start phase (SP), arterial maximum slope, portal maximum slope and end phase (EP) for tumor in 11 patients, along with the respective splenic maximum time. Note that for patients 11, 33 and 41 end phase points were before splenic maximum and therefore portal slope could not be calculated and has been marked fictitiously at corresponding end phase values by red circle. The duration of portal phase is much smaller than the arterial phase.

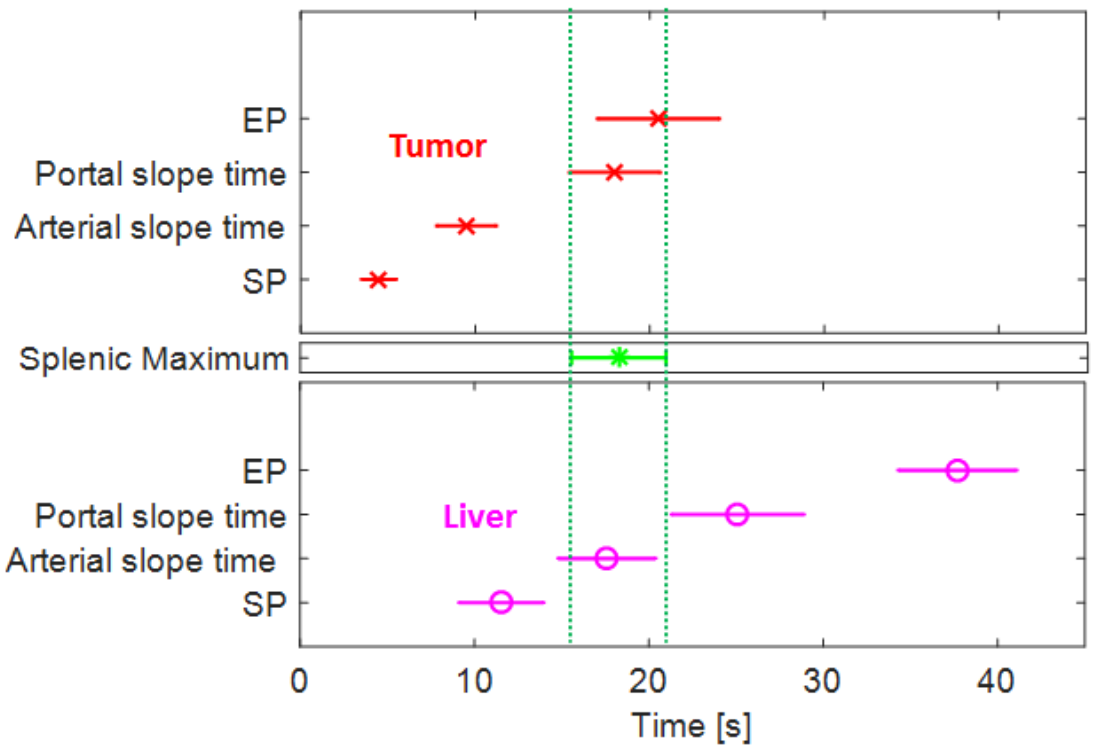

Figure 5.11. Average values of key time points for liver and tumor, along with standard deviation. Average time of maximum splenic enhancement is also shown. There is time difference between splenic maximum and EP/SP for healthy liver. For tumor, the EP region is overlapping the splenic maximum region, this might make it unfeasible to obtain portal phase if the EP point lies before the splenic maximum.

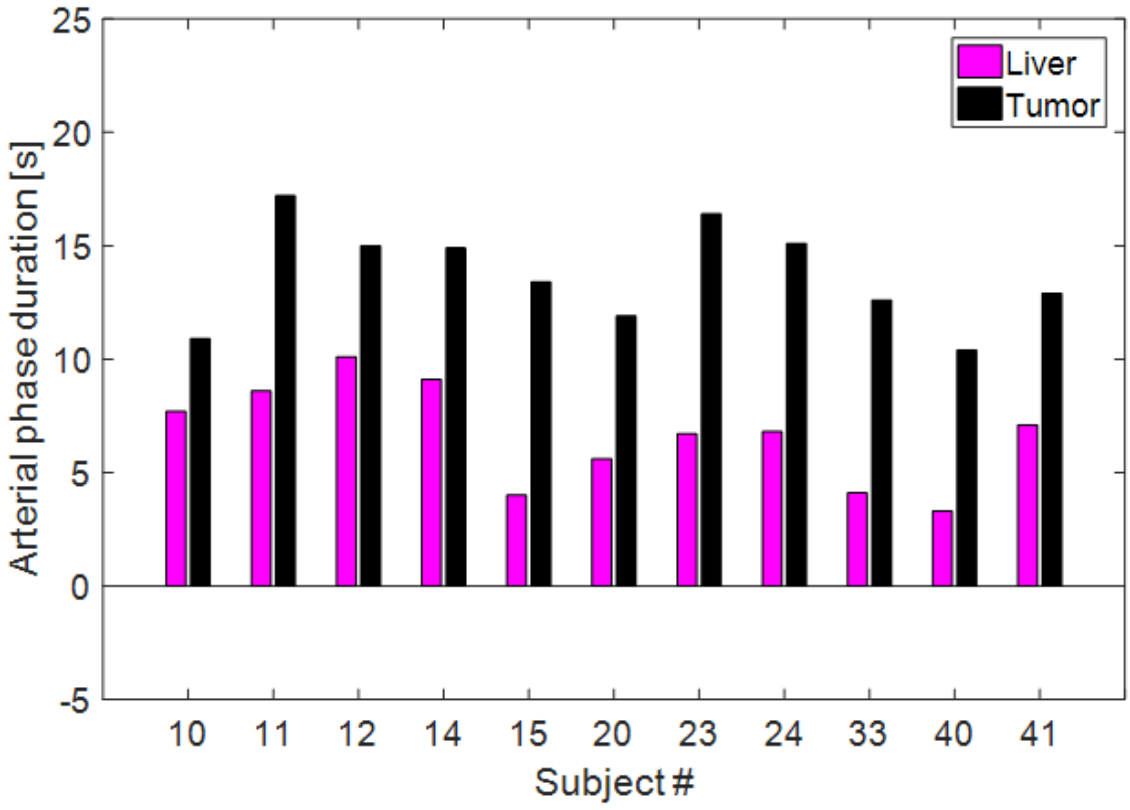

Figure 5.12. Arterial phase duration for healthy liver and tumor. Healthy liver have lower arterial phase duration than tumor. This result is expected as tumor has an early SP and is primarily fed by artery, in contrast with healthy liver which receives majority of its blood supply from the portal vein.

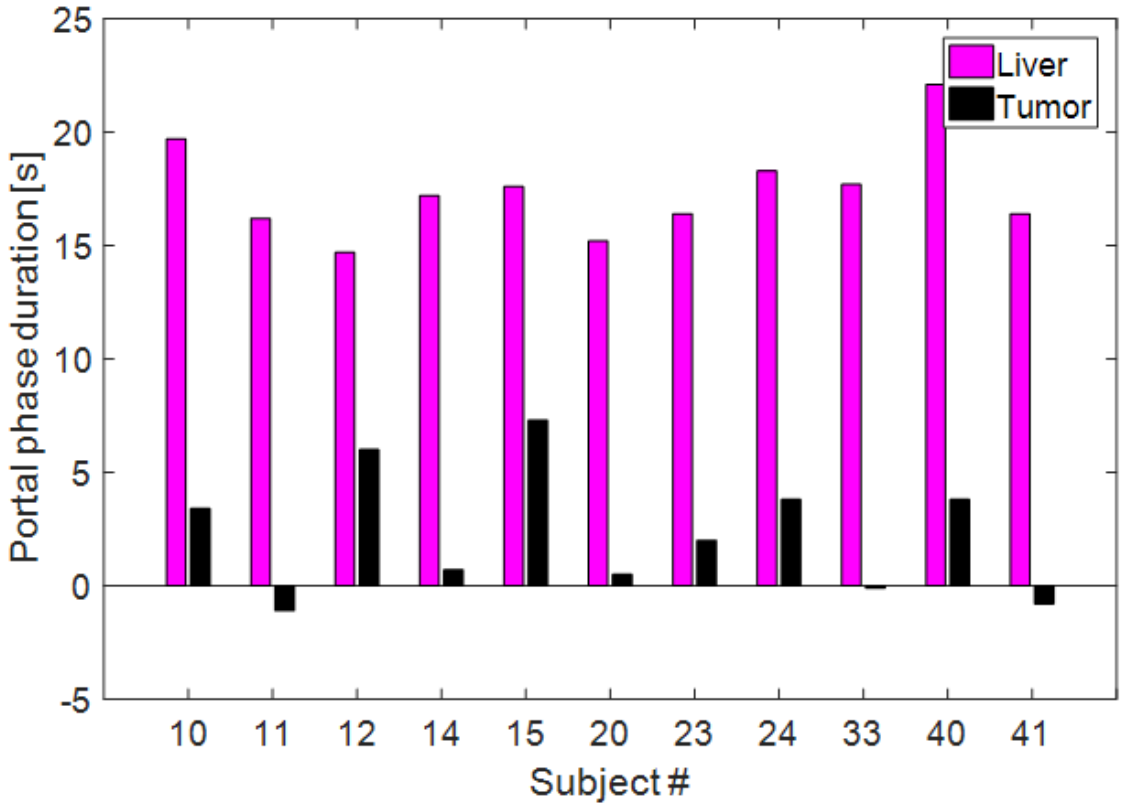

Figure 5.13. Portal phase duration for liver and tumor. Portal phase duration for tumor is very small and is non-existent for 3 (11, 14 and 41) out of the 11 subjects investigated. It can also be seen that the duration for liver is much larger than that of tumor, this is due to the fact that healthy liver has a late EP and receives majority of the blood supply from portal vein, whereas tumor gets the major portion of the blood supply from the tumor.

The TDC curves relevant to the MS method lie between the start phase and the end phase, signifying the start of the venous outflow. The start phase and the end phase of healthy liver in all 11 subjects are shown in Figure 5.9. As mentioned, earlier this main portion of the TDC curve is divided into arterial and portal phase by the time it takes for the spleen to attain maximum enhancement. Subsequently, the maximum slopes in the arterial and portal phases are calculated. The time corresponding to maximum arterial and

portal slope and splenic maximum enhancement is also illustrated in the same figure. Figure 5.10 illustrates these points corresponding to the tumorous region in the subjects. The average of these key time points for healthy and tumorous liver is illustrated in Figure 5.11, x-error bars represents the standard deviation. It can be seen that tumor starts earlier and ends earlier than healthy liver. The splenic maximum region is closer to the start phase for the healthy liver and to the end phase for tumor. The TDC curve from SP to EP for healthy liver is around 30 s and for tumor is around 20 s.

The arterial phase duration is greater for tumor as compared to a healthy liver as shown in Figure 5.12, on the other hand tumor has greater portal phase duration (Fig 5.13). For healthy liver the duration of arterial phase is greater than portal phase, whereas for tumorous region this is reversed. These results are expected as healthy liver gets majority of its blood supply from portal vein and tumor's blood supply is dominated by hepatic artery.

Figure 5.13 also illustrates the problem in using the maximum slope method to calculate the portal perfusion for tumor. Out of eleven subjects, three (11, 33 and 41) have a negative portal phase duration, this is due to the fact that for these cases the splenic maximum enhancement occurs after the end phase of the liver. By definition, portal slope can only be calculated from that portion of TDC which lies after the splenic maximum and before venous outflow (EP). Therefore, this demonstrates that it is not possible to obtain the portal perfusion values, using the MS method, for all cases.

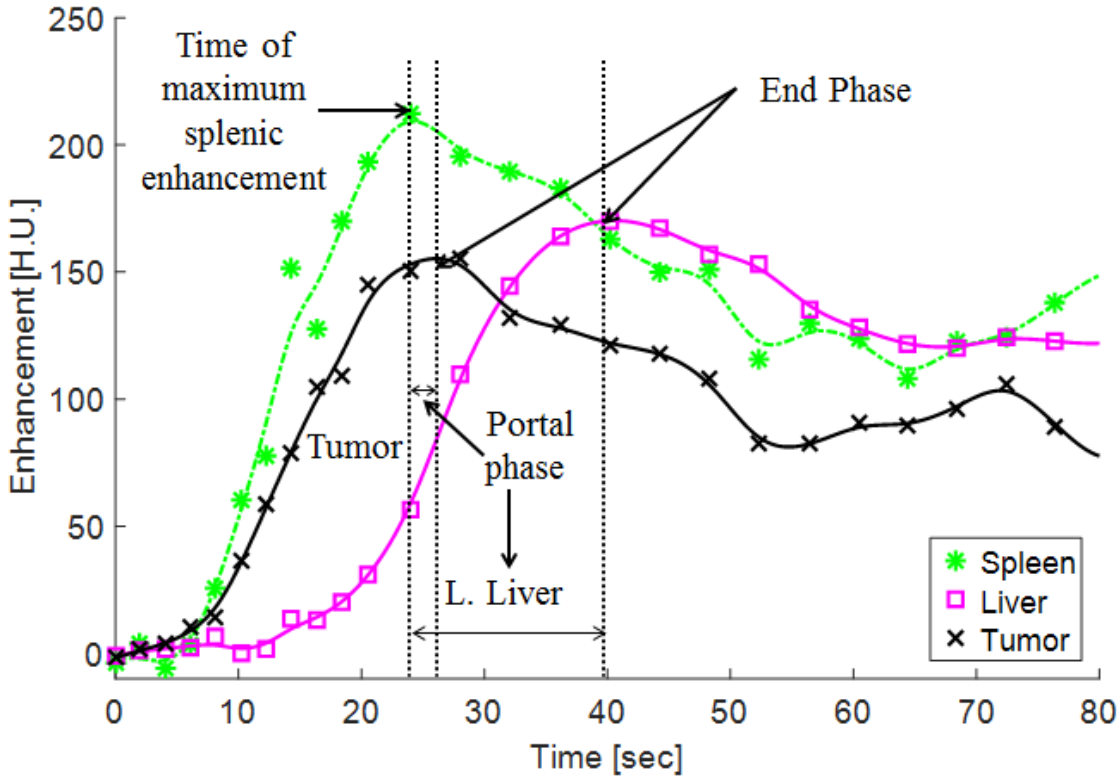

Figure 5.14. TDC for spleen, liver and tumor in subject 23. Time of maximum enhancement for spleen and end phase for liver and tumor has been marked by vertical dashed line. Portal phases for liver and tumor have been shown.

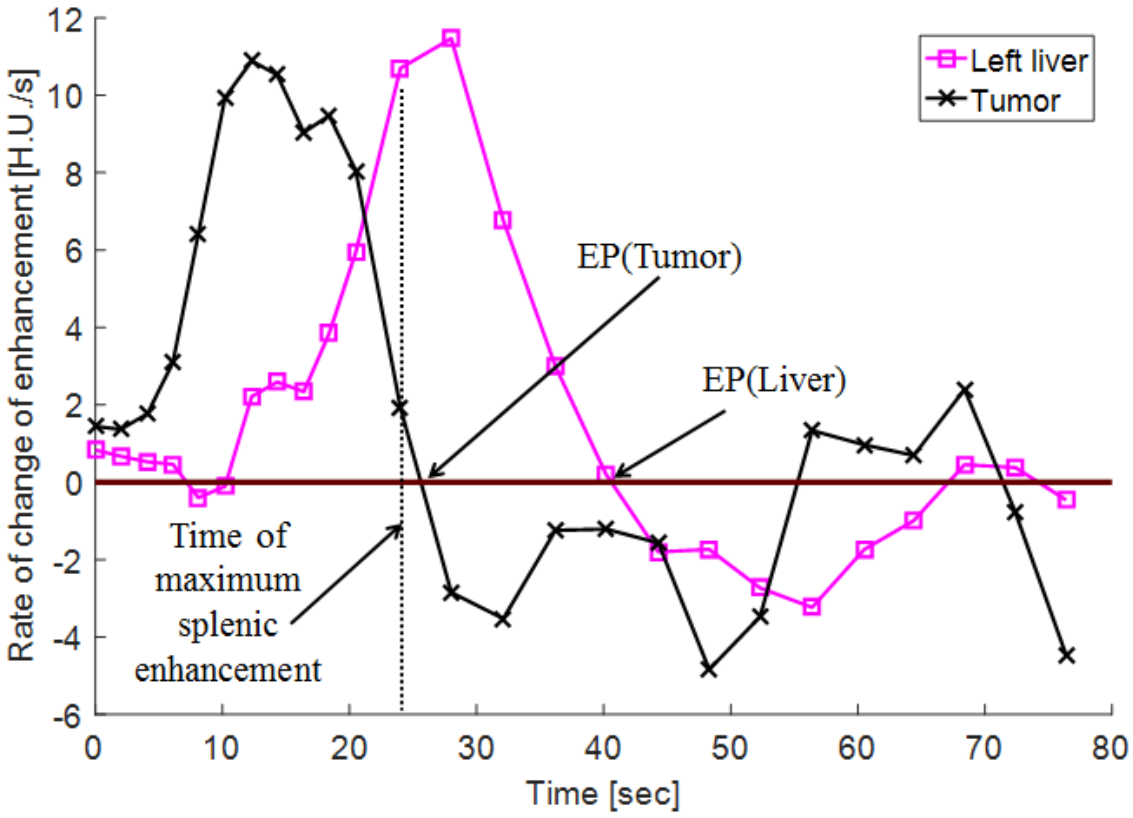

Figure 5.15. Rate of change of enhancement ($\frac{dc(t)}{dt}$), slope of the TDCs ($c(t)$), for liver and tumor in subject 23. The slope of a curve becomes zero as it reaches to its maximum. Therefore, the maximum for TDC can be clearly seen in this figure as the point where the rate of change of enhancement, slope of the TDC curve, crosses the zero line.

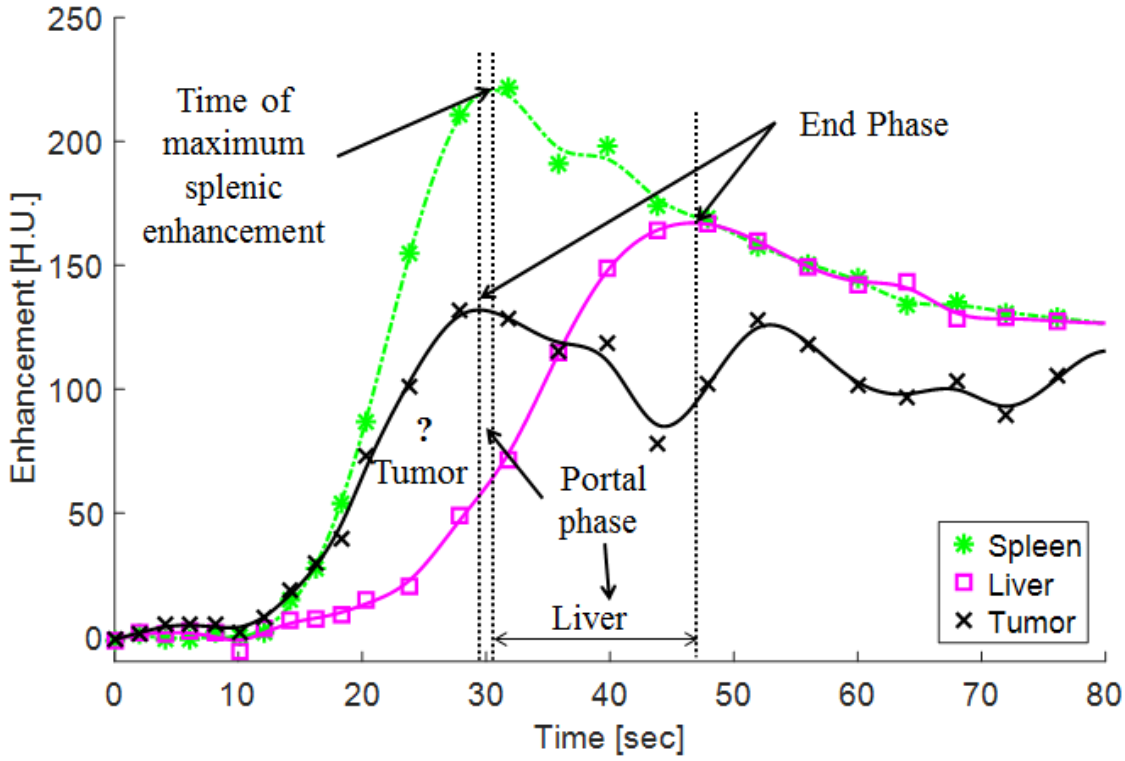

Figure 5.16. TDC for spleen, liver and tumor in subject 11. Tumor does not seem to have a portal phase as the spleen attains its maximum after the end phase of tumor. Spleen attains its maximum at 30.6 s and EP for tumor is 29.5 s.

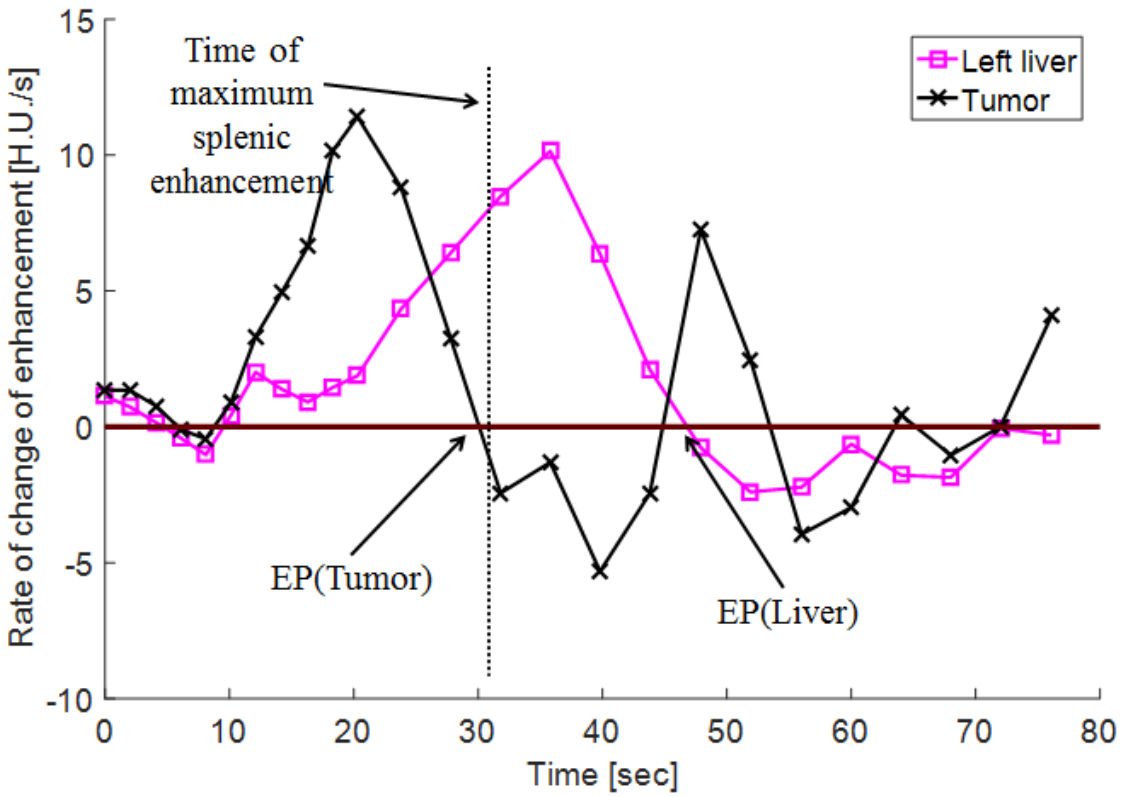

Figure 5.17. Rate of change of enhancement ($\frac{dc(t)}{dt}$), slope of TDCs ($c(t)$), for liver and tumor in subject 11. Under the no-venous outflow assumption rate of change of enhancement translates into the rate of intake of contrast medium inside the tissue. After the EP point of tumor at 29.6 s the rate drops below zero, indicating outflow of contrast medium from the tissue. As the splenic maximum occurs after the EP of tumor, there is no TDC left to calculate the portal slope without violating underlying assumption of the MS method.

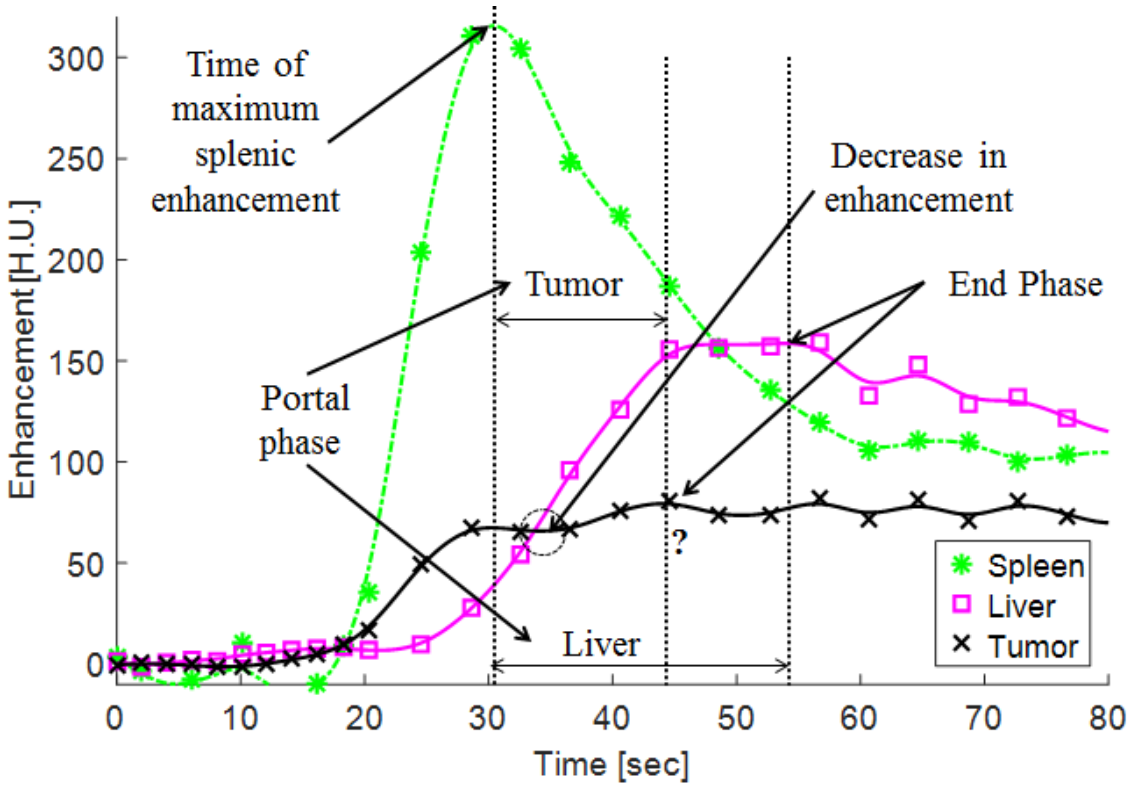

Figure 5.18. TDCs for spleen, liver and tumor in subject 33. The maximum enhancement of tumor (EP = 44 s) occurs after a dip in the TDC curve. A decrease in enhancement value signifies venous outflow and selecting EP after that violates the underlying assumption of maximum slope method. Therefore any maximum occurring after a dip in the TDC should be rejected and only that maximum point should be selected which occurs after a steady rise in the TDC.

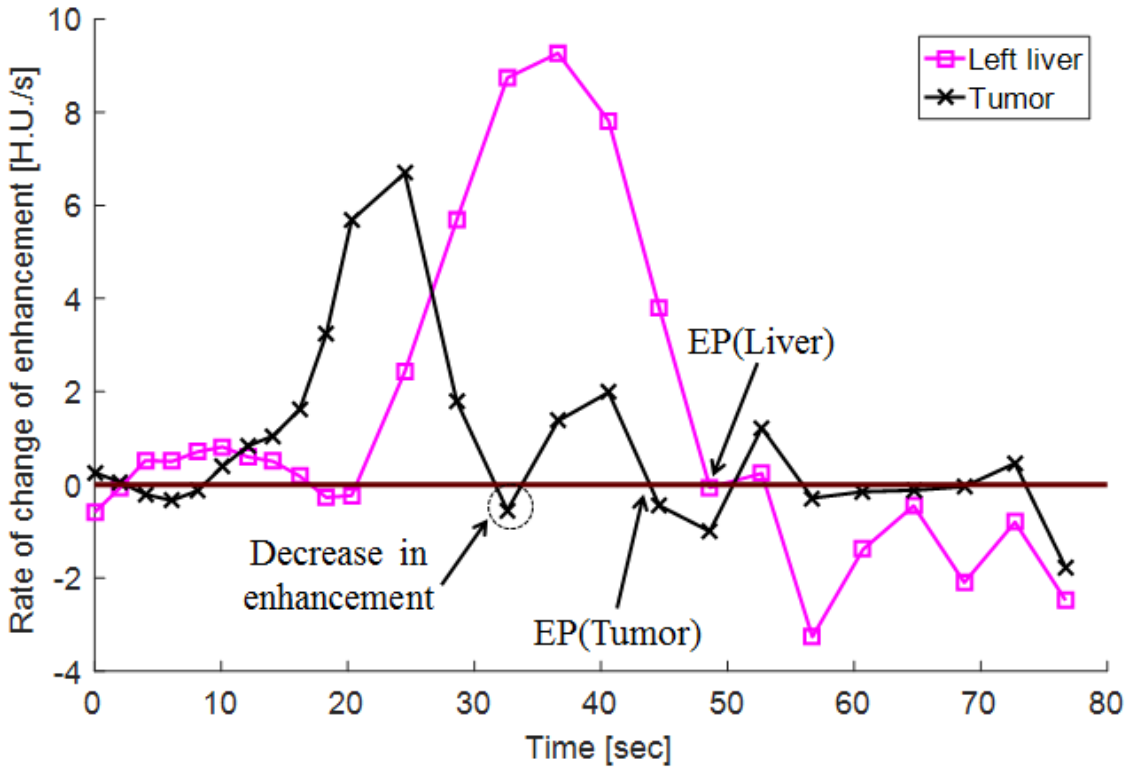

Figure 5.19. Rate of change of enhancement ($\frac{dc(t)}{dt}$), slope of TDCs ($c(t)$), for liver and tumor in subject 33. According to Figure 5.18 the tumor TDC is reaching maximum at 44 s. The rate of change of enhancement for tumor can be seen crossing the zero line at 44 s, but it also crosses the line before that at 30.3 s. The entry of this curve below the zero line is indicative of the start of venous outflow and hence it violates the underlying assumptions of the MS method.

Figure 5.14 illustrates the TDCs for healthy liver, tumor and spleen in subject 23. The tumor curve attains its maximum at 26 s and as discussed in the materials and method section this is taken as the end phase (EP) for tumor. Similarly left and right liver have EP points at 40.5 s and 46.5 s. For this subject all the EPs are after 24.1 s, splenic maximum, and therefore it is possible to calculate the portal perfusion for this case. The slopes of the left/right liver and tumor TDCs are plotted in figure 5.15. The slope of a curve becomes zero at its maximum and therefore the slope curve crosses the zero line at the corresponding EP points.

Table 5.3 and 5.4 shows the time of maximum enhancement for spleen and the end phase time for tumor. For the dual supply the maximum slope method to be applicable, the time of maximum splenic enhancement should be prior to the end phase of the tumor. This condition is satisfied for all but three subjects, 11, 33 and 41. There is another type of discrepancy which arises with subject 33. Although the end phase of the tumor in subject 33 is after the splenic maximum, the method of selection of end phase leads to violation of no-venous outflow assumption. The case of subject 11 and 33 has been analyzed in detail later in this section.

The TDCs for healthy liver and tumor in subject 11 are plotted separately in figure 5.16. The end phase of left and right liver occurs at 46.7 s and 45 s which is more than 13 s after the peak time of the spleen 30.5 s. The time between the splenic maximum and end phase is when the portal flow dominates and the maximum slope of the TDC curve is recorded here. In the case of tumor the end phase is at 29.6 s which is before the peak time of spleen. So for tumor it seems that by the time the portal flow starts to dominate the tumor TDC has gone beyond the maximum, signaling the start of the

venous outflow and hence the maximum slope model cannot be applied to find the hepatic portal flow for the tumor. Similar discrepancy is observed for subject #41.

Another type of discrepancy was observed in subject 33. The TDCs for spleen, liver and tumor are shown in figures 5.18. The slope for the left/right liver and tumor is illustrated in figure 5.19 and the key time points of the TDCs are shown in Table 5.3 and 5.4.

In this case although the end phase for the tumor occurs at 44 s, 13.5 s after the splenic maximum (30.5 s), the no-venous outflow assumption has been violated here. Figure 5.18 shows that soon after the splenic maximum, and therefore during the portal phase, a dip is observed in the enhancement values. The tumor TDC attains local maximum around 31 s and after that keeps on decreasing till 34 s. This becomes clearer in the Figure 5.19, where the slope of the curve goes below the zero line around 32 s. This shows that the contrast material has started to leave the tissue, making the no-venous outflow assumption invalid. The TDC for liver attains its global maximum at 44 s and the maximum portal slope is calculated at 39.25 s. The slope for portal slope was calculated where the no-venous outflow assumption was not valid.

5.2.3 DISCUSSION

As the healthy liver primarily gets its blood supply from the portal vein it has higher portal phase duration than tumor as seen in figure 5.12. On the other hand tumor is predominantly fed by hepatic artery and therefore it can be seen in figure 5.13 that tumors have higher arterial phase duration as compared to healthy liver.

It was observed that in some of the cases maximum splenic enhancement occurred after the end phase of tumor. This is something which is not expected according to the maximum slope method. There should ideally be a portion of tissue concentration curve after splenic maximum and before tumor maximum, which can be used to calculate maximum slope and hence blood perfusion rate. Under these circumstances the only possible estimate is that the tissue is receiving all its blood supply from hepatic artery, which does not seem to be plausible. Another problem which was observed here is the presence of local maxima in the tumor TDC curves, which occurred very early in the curves. By assumption inherent in the maximum slope model only the first maxima can be used as an end point, this can lead to ambiguity in some cases. One of the reasons behind these discrepancies is also that this method will benefit from more rigorous validation. There are also large variations present in blood perfusion values when evaluated using different methods. The solution to these discrepancies is to use other methods, tracer kinetic models, for evaluating blood perfusion values.

5.2.4 CONCLUSION

Maximum slope method was investigated to examine two anomalies present in the calculation of perfusion values. In the MS method the location of splenic maximum enhancement is crucial as it divides the arterial and portal phase. In some of the cases discussed in present work the splenic enhancement was occurring after the end point of the liver, due to which maximum slope method was unable to give an accurate HPP. Secondly, local minima was observed in the liver concentration curves which makes it difficult to accurately define the end phase of liver, which is again crucial for the calculation of perfusion values. Considering these limitations it is advisable to use other

methods for perfusion calculation where data accuracy is critical, such as while analyzing the heat transfer within the tissue. For other application it might be only necessary to check if the perfusion values are above a set cut-off, in such cases further work needs to be done to examine the accuracy of maximum slope method.

CHAPTER 6

OPTIMIZING TEMPORAL SAMPLINGS

The complete authorship of this work should be read as Rajeev Hatwar, Prof. Eleni Liapi and Prof. Robert Ivkov. The experiments were performed by Prof. Eleni Liapi. Optimization of temporal protocol was performed by Rajeev Hatwar under the guidance of his advisor, Prof. Robert Ivkov. The work also benefited from comments of Prof. Charles Meneveau.

6.1 INTRODUCTION

X-ray computer tomography (CT) involves exposure to radiations which can have an adverse effect on the body. The risk of cancer death associated with an abdominal scan is 12.5/10,000, which is comparable to the risk from a year of smoking (12/10,000) (Gray 1996). So there is a need to optimize the radiation dose, so as to get quality results without exposing subjects to more than necessary radiations.

There are three approaches to reduce the radiation dose during scanning. It can be reduced by decreasing tube current and tube voltage (Othman *et al.* 2016). Radiation dose is more sensitive to the tube voltage as compared to tube current, as it is proportional to tube voltage by power greater than 2 and "linearly related" to tube current. In the case of tube current noise increases with decreasing current, so there is a trade-off between image quality and radiation dose. Lastly, radiation dose can be reduced by decreasing the number of scans, decreasing the temporal samples.

Work has been done to optimize the number of samples needed to calculate various relevant parameters. To our knowledge all of them, have focused on analyzing equal time intervals (Ng *et al.* 2013, Kloska *et al.* 2010, Kamena *et al.* 2007, Goh *et al.* 2008, Kambadakone *et al.* 2011, Wiesmann *et al.* 2008, Wintermark *et al.* 2004, Ng *et al.* 2015, Bisdas *et al.* 2009) and they are retrospective studies. Table 6.1 gives the various methods which were used to calculate blood perfusion and the body tissue to which it was applied.

Table 6.1 Protocol optimization studies undertaken along with the respective methods and body tissue

	Method	Body tissue
Ng *et al.* 2013	Distributed Parameter model	Lung
Kloska *et al.* 2010	Maximum slope method	Head
Kamena *et al.* 2007	Deconvolution method	Head
Goh *et al.* 2008	Distributed parameter model	Colon/rectum
Kambadakone *et al.* 2011	Deconvolution method	Abdomen/Pelvis
Wiesmann *et al.* 2008	Deconvolution method	Head
Wintermark *et al.* 2004	Deconvolution method	Head
Ng *et al.* 2015	Distributed parameter model	Liver
Bisdas *et al.* 2009	Tracer kinetic model	Head/neck

Equal time intervals approach is justifiable for tracer kinetic models, like distributed parameter, which use the entire curve for the perfusion calculation. In case of

model-free approaches, like maximum slope method, the values are collected only at certain key points and not from the entire curve. Therefore some points on the curve are definitely more important than the other. Considering this, we have explored the possibility of using variable sample intervals in the present work.

Different methods have been employed to obtain an optimized protocol. The existing method of equal spaced time intervals is first analyzed. This is followed by a subject specific search for an optimized protocol for a fixed number of scans. All possible combinations of experimentally available temporal points are tried and tested against the full protocol by using a cost function, which comprises of different parameters related to perfusion. In order to obtain a common protocol, which can be applied to all the subjects, another set of calculations are performed in which all possible combinations are tried and the cost function comprises of all the subjects simultaneously. The results from these algorithms are tested against fixed interval case.

6.2 MATERIALS AND METHODS

Wide-array 320-slice clinical CT scanner, Aquilion ONE, from Toshiba Japan was used here. Twenty-eight adult male New Zealand white rabbits were used with VX2 liver tumor. Iso-osmolar contrast iodixanola was injected intravenously through a marginal ear vein at 1ml/sec. Contrast agent was injected intravenously and 25 scans conducted of 0.5 seconds each. The experiments were conducted by E. Liapi and S. Mirpour. Wide-array CT scans were obtained every 2 sec for the first 25 seconds, and every 3 seconds thereafter and for an additional 42 seconds.

For the retrospective study 11 subjects were considered and the analysis was done using them to find the optimized temporal protocol. This was followed by a

prospective study where the optimized protocol was applied on a new set of 17 subjects and then the accuracy of the optimized protocol was tested.

Several different protocols were tested during optimization and are described later in this section. The cost function used for the optimization process calculates the percentage error in HAP, HPP and HPI for the healthy liver (equations 6.1-3) and takes average of all them (equation 6.4).

$$\Delta HAP = 100 \times \left| \frac{HAP_{n\ samples} - HAP_{gold\ standard}}{HAP_{gold\ standard}} \right| \quad (6.1)$$

$$\Delta HPP = 100 \times \left| \frac{HPP_{n\ samples} - HPP_{gold\ standard}}{HPP_{gold\ standard}} \right| \quad (6.2)$$

$$\Delta HPI = 100 \times \left| \frac{HPI_{n\ samples} - HPI_{gold\ standard}}{HPI_{gold\ standard}} \right| \quad (6.3)$$

$$Cost\ function = Avg.error = {}^{(\Delta HAP + \Delta HPP + \Delta HPI)}\Big/_{3} \quad (6.4)$$

The cost function used here had equal weightage for HPI, HAP and HPP. Since HPI includes HAP and HPP (Equation 5.5), this combination inherently gives more weightage to hepatic perfusion index, which is useful for interventional radiologist.

All the tissue density curves are standardized by fixing the starting point to the beginning of the appearance of contrast agent in the arterial curve. To calculate the starting point first the background noise is subtracted from the curves. For this the first two points are used to calculate average background noise which is subtracted from the respective curves. Then the starting of the arterial curve is decided using a cut-off of 100

H.U. The tissue density curve with all 25 experimental data points is used for generating a fitted curve. In the present work 'smoothing spline' function is used for curve fitting. These curves are shifted so that all of them begin at arterial start time.

In the case of equally spaced time intervals, data points at an interval of 0.5 s are extracted from the fitted and standardized curve, starting at 0 s and ending at 40 s, and this is assumed to be the gold standard for calculating error. The end phase in the standardized curves were occurring within 40 s and therefore points after this were not included. For comparative analysis data points are extracted at an interval of 1 s, 2 s, 3 s, 4 s, 5 s, 6 s, 8 s and 10 s. 'Smoothing spline' fitting is used for curve fitting with these points. These fitted curves are used for calculating the perfusion related parameters.

For the case of variably spaced time interval, data at the following time points, which is based on existing protocol, are extracted from the fitted and standardized curves:

0 s, 2 s, 4 s, 6 s, 8 s, 10 s, 12 s, 14 s, 16 s, 18 s, 20 s, 24 s, 28 s, 32 s, 36 s and 40 s.

The data points hence obtained are used subsequently for all analysis related to variably spaced time intervals. The fitted curve based on these 16 points is used to calculate the gold standard values for all the relevant parameters. All possible combinations of 4 to 16 time points are chosen out of these data points, followed by 'smoothing spline' curve fitting. The best possible combination for a given number of time points is selected which gives the lowest cost function. First this optimization is carried out individually for all the subjects, to get a protocol customized according to each subject. The protocol obtained through this process gives the smallest cost function for the corresponding subject. Subsequently, it is extended to obtain a protocol which gives the lowest average cost

function across all subjects, and is common to all the subjects. Once a common protocol is obtained using the retrospective analysis, it is applied to prospective data.

In the retrospective study the temporal samples before 40 s are chosen. The maximum slope method does not use the points once the maximum of tissue has reached. In all the subjects studied this point was before 40 s. Different combinations of protocols are tested against a gold standard to check the variation in the cost function.

6.3 RESULTS AND DISCUSSION

Figure 6.1 shows the deviation of the hepatic arterial perfusion with increase in the time interval between different temporal samples. The x axis represents the actual values, obtained using the gold standard of 0.5 seconds interval. HAP for different time intervals is plotted on the y axis. A line corresponding to an exact match is plotted on each of the subplots. The further the points are from this line the poorer is the approximation. As the time interval is increasing the points are moving further away from the straight line. There is an over prediction as the sample interval increases. Similar trends are observed for other parameters: hepatic portal perfusion, hepatic perfusion index, maximum arterial contrast, maximum portal vein contrast, arterial maximum slope and the portal maximum slope.

Table 6.2 shows the percentage error for each subject for different lengths of time intervals ranging from 0.5 seconds (83 scans), gold standard, to 10 seconds (7 scans). Error has been calculated by averaging the errors (cost function) in HAP, HPP and HPI for healthy liver regions. The error gradually increased with the increase in the length of time intervals, though the increase in error varied for different patients. The error with 10 seconds time interval varied from around 14 % to 46 % within different subjects. Figure

6.2 shows the pictorial representation of table 6.2. It can be seen that the errors decrease with increasing number of scans. The variability in the error among different subjects can be clearly seen in the figure.

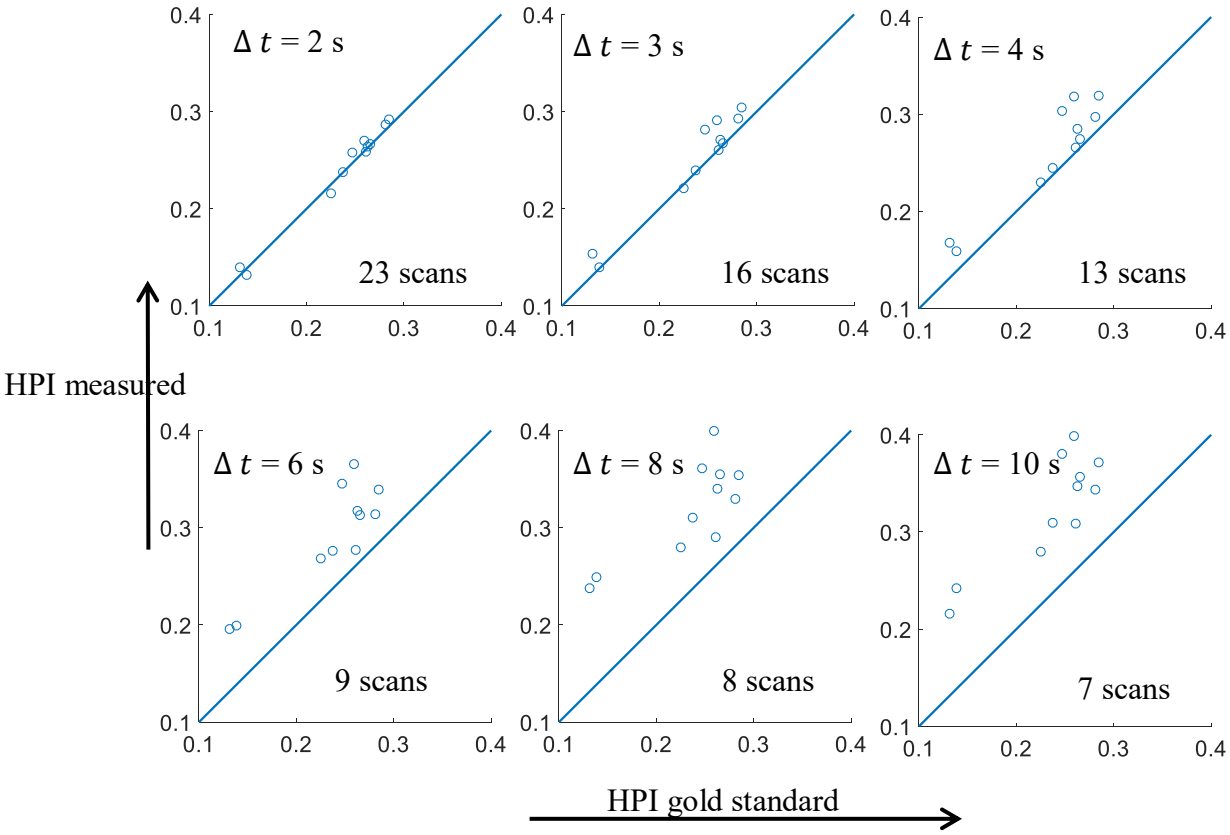

Figure 6.1: The effect of increasing time intervals, for equally spaced time interval, on the computation of HPI for different subjects has been shown here. Note that only the healthy liver tissue was considered here. The HPI for the gold standard case of 0.5 s time interval is given on the horizontal axis and other are plotted on the vertical axis. HPI estimation deteriorates with increasing time intervals and for most of the cases it is over predicting the value of HPI.

Table 6.2: Error for different subjects with equally spaced temporal samples for retrospective cases

Time intervals	10	8	6	5	4	3	2	1	0.5
Number of samples	5	6	7	9	11	14	21	41	81
Total samples	7	8	9	11	13	16	23	43	83
Subject Tag									
10	28.92	28.45	15.03	10.76	5.70	2.63	1.32	0.19	0
11	38.89	34.11	30.08	24.99	17.63	10.72	3.30	0.31	0
12	24.27	22.75	16.10	12.93	6.57	2.38	0.41	0.05	0
14	18.04	14.23	9.68	7.92	4.58	3.44	1.68	0.23	0
15	23.32	24.98	14.40	10.64	5.38	1.87	0.28	0.55	0
20	40.63	44.14	33.41	26.83	18.16	9.64	3.32	0.16	0
23	21.84	20.79	14.00	11.49	9.24	5.45	2.07	0.11	0
24	13.76	12.17	5.92	3.61	1.56	0.58	0.67	0.08	0
33	43.36	57.13	34.64	27.73	19.72	11.96	4.50	0.35	0
40	46.17	52.23	28.61	15.23	11.93	8.63	7.10	1.57	0
41	17.80	18.53	14.47	6.96	1.89	2.79	3.44	0.93	0

Average	28.82	29.95	19.67	14.46	9.31	5.46	2.55	0.41	0

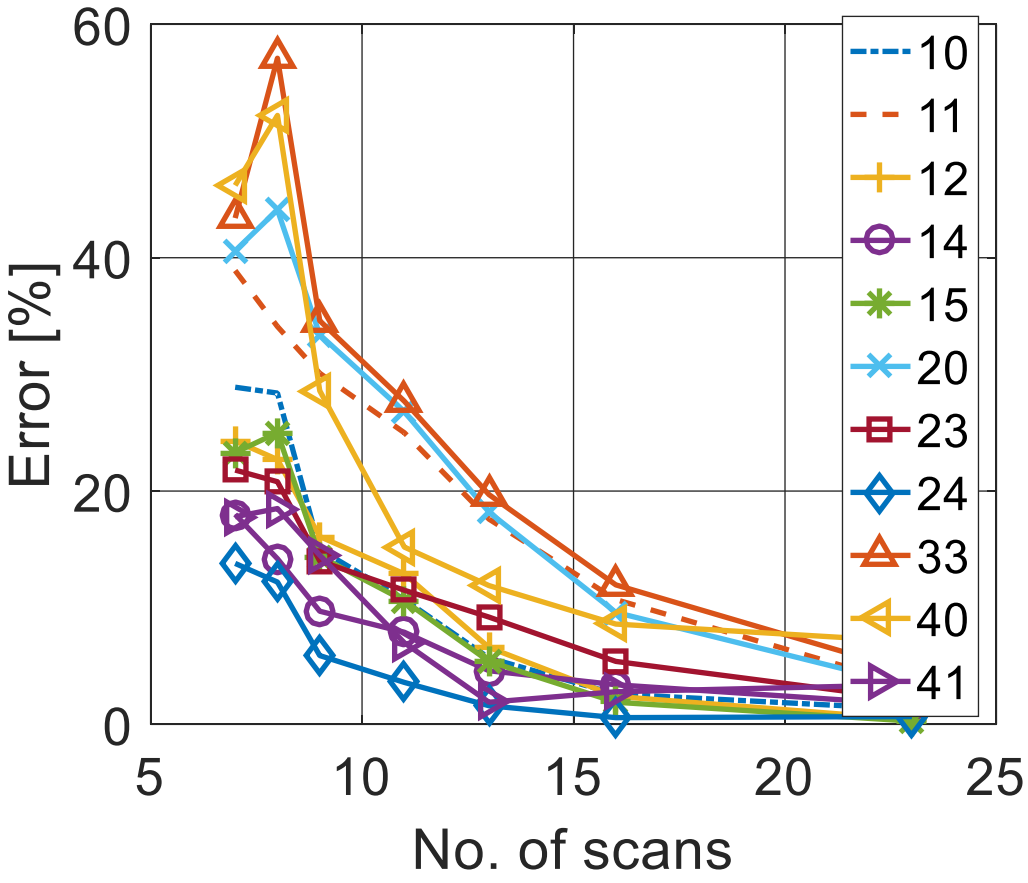

Figure 6.2: Variation of error in calculation of perfusion values for different subjects as a function of number of scans. Here equal duration of time intervals was used. Error decreases as the number of scans increases. The error calculated here is based on the average error in HPA, HPP and HPI values for healthy liver.

The results from the subject specific study, where different combinations of temporal protocols were tried for individual subjects, are presented in table 6.3 and illustrated in figure 6.3. Errors obtained from the abbreviated protocol for individual subjects have been plotted against the number of scans in figure 6.3. The total number of

scans was varied from 6 scans to 18 scans and the errors decreased as the number of scans increased. The errors for all the subjects and number of scans considered here were lower than 2.5 %.

Table 6.3: Error for different subjects with variable time intervals. Here the protocol was obtained separately for different subjects

Free samples	4	5	6	7	8	9	10	11	12	13	14	15	16
Total samples	6	7	8	9	10	11	12	13	14	15	16	17	18
Subject													
1	1.10	0.18	0.55	0.13	0.11	0.05	0.04	0.06	0.08	0.06	0.03	0.02	0
2	0.66	2.01	1.47	1.35	1.64	1.60	0.91	0.56	0.21	0.02	0.06	0.13	0
3	1.52	0.80	0.36	0.08	0.20	0.07	0.06	0.06	0.06	0.03	0.02	0.04	0
4	0.47	0.31	0.19	0.36	0.36	0.24	0.25	0.29	0.16	0.02	0.03	0.05	0
5	0.41	0.13	0.17	0.09	0.05	0.03	0.04	0.03	0.09	0.08	0.05	0.04	0
6	0.92	0.73	0.43	0.37	0.14	0.23	0.07	0.09	0.03	0.02	0.04	0.05	0
7	0.84	0.32	0.24	0.06	0.05	0.16	0.16	0.11	0.07	0.04	0.09	0.05	0
8	0.70	0.11	0.11	0.05	0.03	0.26	0.15	0.02	0.02	0.01	0.01	0.03	0
9	1.12	0.44	0.31	0.28	0.47	0.61	0.15	0.14	0.06	0.03	0.07	0.12	0
10	2.18	0.75	0.74	0.14	0.09	0.06	0.07	0.04	0.03	0.01	0.07	0.06	0
11	0.14	0.06	0.06	0.13	0.05	0.02	0.03	0.21	0.09	0.02	0.04	0.01	0
average	0.91	0.53	0.42	0.28	0.29	0.30	0.18	0.15	0.08	0.03	0.05	0.05	0.00

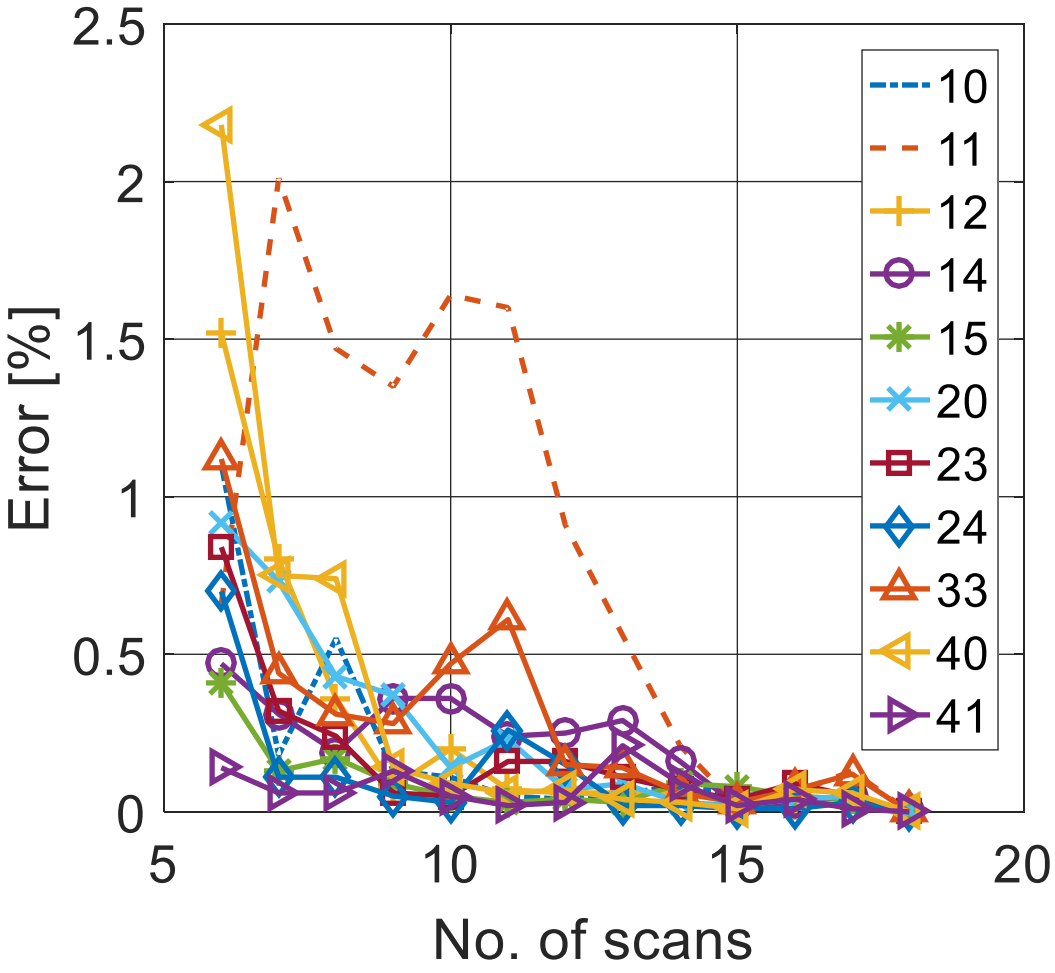

Figure 6.3: Variation of error in calculation of perfusion values for different subjects as a function of number of scans. Here variable duration of time intervals was used. For a given number of scans all possible combinations of available temporal scans were tried for each of the subjects separately, and therefore the protocol obtained are different for all the subjects. Error decreases as the number of scans increases. The error calculated here is based on the average error in HPA, HPP and HPI values for healthy region. Note that the errors obtained here are lower than the one obtained from the previous case of fixed interval.

Figure 6.4 is a pictorial representation of the best 50 combinations of temporal samples for a given number of free samples in the case of Subject 1 (10). The samples were arranged in the increasing order of cost function. On the y-axis different combinations are shown, with best combination at the top. The horizontal axis, x-axis, represents the time since the start of the arterial phase. The constituents temporal samples of a particular combination are marked in blue color and the samples which are left behind are kept as yellow. Some of the temporal samples were more frequently present in the best 50 cases than others. The most frequent temporal samples occurred at 12 s, 24 s and 28 s.

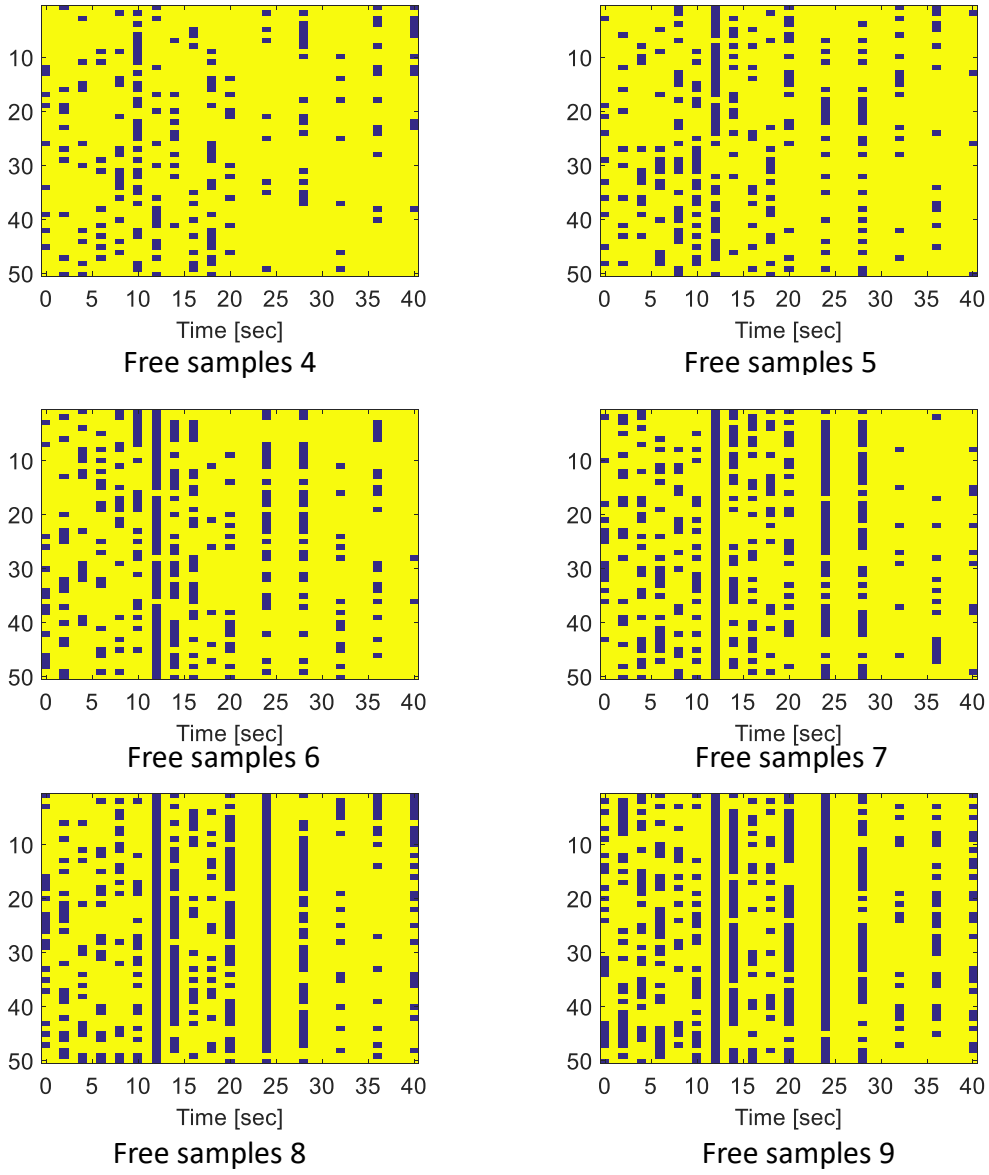

Figure 6.4: Optimized best 50 cases of subject 10 for variable spaced intervals. All possible combinations of temporal samples were tried for a given number of temporal samples and the best 50 cases have been shown pictorially in these plots. Horizontal axis represents the temporal samples and the vertical axis shows the best 50 cases in with decreasing order of rank with the best 50 cases in with decreasing order of rank with the best case at the top.

The tissue density curves of artery, portal vein, spleen and healthy liver for subject 1 (10) are shown in figure 6.5. Curves for artery, portal vein and spleen are plotted on the left y-axis. For clarity, liver curve is plotted on the right y-axis. Different temporal points along with their serial numbers are shown at the bottom of the figure. Further, time points corresponding to arterial and portal slope calculation and end points are marked by black circles. The significance of temporal samples at 12 s, 24 s and 28 s can be seen in this figure. It should be noted here that these time points are from the start of the arterial curve as described in the methods section. The maximum of the arterial curve occurs at around 12 s. The portal slope maximum and the maximum of the liver occurs around 24 s and 28 s. These instances are important in the calculation of perfusion values and hence are prominently occurring in the best cases.

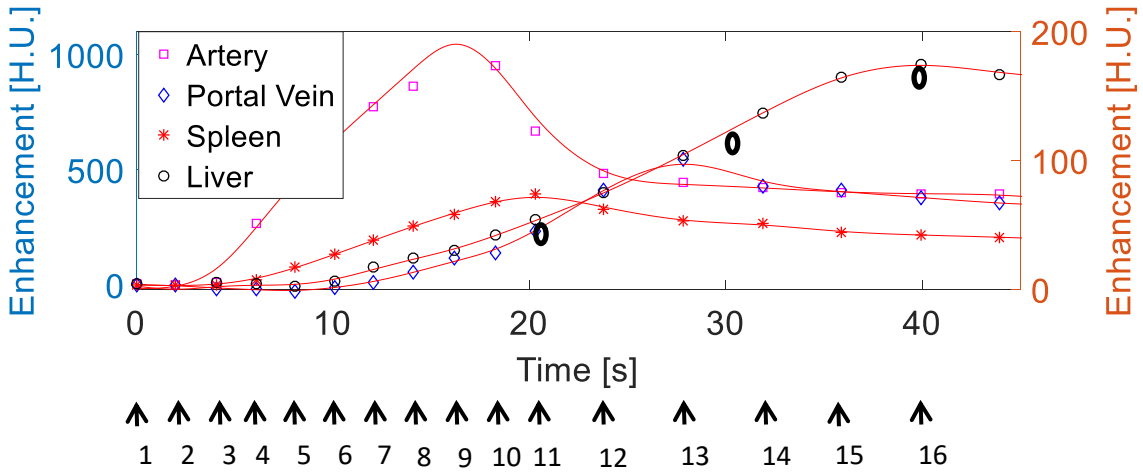

Figure 6.5: Tissue density curves of artery, portal vein, spleen and liver for subject # 10.Arterial, portal vein and splenic curves are plotted on the left y-axis. A separate right y-axis is used for plotting liver curve. Different temporal time points can be seen in the figure.

The optimized protocol, which is common across all the subjects, is shown in figure 6.6 and table 6.4. It can be seen that in the optimized protocols 10 s, 12 s and 28 s are present in all the cases with different number of free samples. These are the times around which maximum in the artery and portal maximum slope is observed, and therefore these time points are so prominently occurring in the optimized protocol. As can be seen clearly in figure 6.6 the time points after 10 s are more important than the once occurring before it. In the optimized protocols only one of the time points before 10 s are chosen till the number of free samples are less than or equal to 9. The selection of these time points, occurring before 10 s is scattered as compared to the occurrence of time points after 10 s.

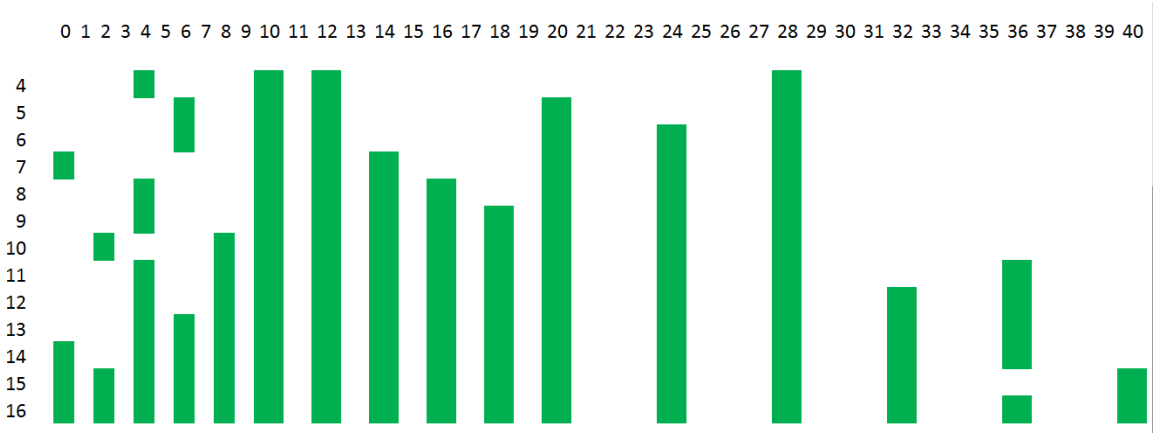

Figure 6.6: Optimized common temporal samples for a set number of free samples. Horizontal axis shows the time duration from the start of the arterial phase and the vertical axis shows the number of free sample being used.

Table 6.4: Optimized common temporal protocols for a set number of free samples. This is based on retrospective data

Free samples	Optimized temporal protocols															
4	4	10	12	28												
5	6	10	12	20	28											
6	6	10	12	20	24	28										
7	0	10	12	14	20	24	28									
8	4	10	12	14	16	20	24	28								
9	4	10	12	14	16	18	20	24	28							
10	2	8	10	12	14	16	18	20	24	28						
11	4	8	10	12	14	16	18	20	24	28	36					
12	4	8	10	12	14	16	18	20	24	28	32	36				
13	4	6	8	10	12	14	16	18	20	24	28	32	36			
14	0	4	6	8	10	12	14	16	18	20	24	28	32	36		
15	0	2	4	6	8	10	12	14	16	18	20	24	28	32	40	
16	0	2	4	6	8	10	12	14	16	18	20	24	28	32	36	40

Figure 6.7 shows the results for the cases when a common protocol was selected for all the subjects, for a given number of time points. These values have been tabulated in table 6.5. The errors reduce with increasing number of scans and are greater than the ones obtained using subject specific protocol. Errors are throughout below 20 % and for more than 10 scans they are below 10 %.

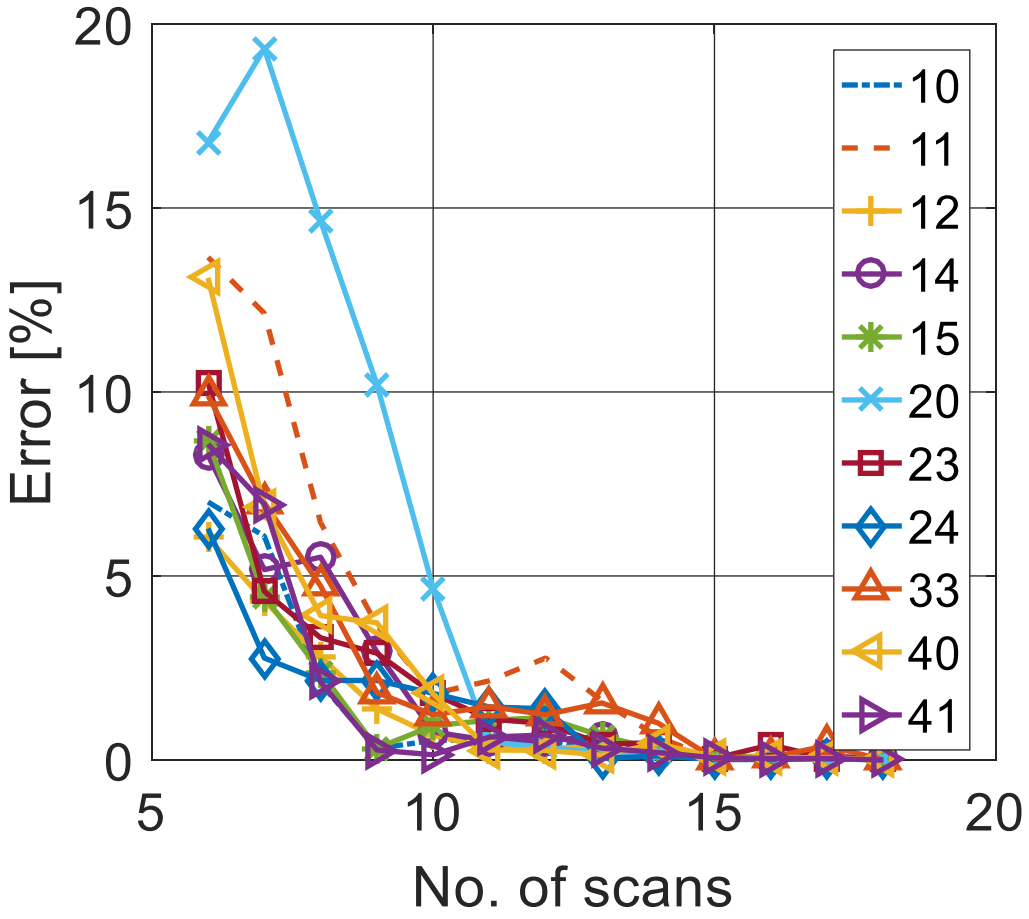

Figure 6.7: Variation of error in calculation of perfusion values for different subjects as a function of number of scans. Here, variable duration of time intervals were used. For a given number of scans all possible combinations of available temporal scans were tried for all the subjects simultaneously and therefore common protocol was used for all the subjects for a given number of scans. Error decreases as the number of scans increases. The error calculated here is based on the average error in HPA, HPP and HPI values for healthy region.

Table 6.5: Error for different subjects with variable time intervals. Here the protocol was obtained simultaneously for all the subjects, and hence a common protocol was used for all the subjects.

Total samples	6	7	8	9	10	11	12	13	14	15	16	17	18
Free samples	4	5	6	7	8	9	10	11	12	13	14	15	16
Subjects													
1	7.01	6.08	2.08	0.31	.53	.54	.53	.21	.20	.06	.08	.06	0
2	13.7	12.1	6.45	3.67	1.8	2.2	2.8	1.6	.62	.02	.11	.13	0
3	6.05	4.32	2.80	1.39	.67	0.31	0.30	.39	.13	.03	.02	.05	0
4	8.28	5.17	5.51	2.94	.76	0.53	0.54	.63	.18	.02	.05	.13	0
5	8.67	4.45	2.39	0.32	.93	1.08	1.15	.65	.28	.08	.10	.05	0
6	16.79	19.3	14.6	10.2	4.7	0.49	0.34	.20	.19	.03	.06	.05	0
7	10.26	4.58	3.32	2.90	1.80	1.11	0.99	.43	.47	.04	.41	.05	0
8	6.29	2.77	2.16	2.16	1.81	1.44	1.39	.04	.11	.01	.01	.03	0
9	9.90	6.99	4.73	1.83	1.23	1.45	1.23	1.5	1.0	.03	.07	.39	0
10	13.10	6.85	3.92	3.73	1.80	0.27	0.26	.13	.45	.07	.07	.06	0
11	8.58	6.95	2.12	0.27	0.14	0.62	0.68	.32	.20	.06	.04	.04	0
average	9.87	7.24	4.56	2.70	1.47	0.91	0.92	.56	.35	.04	.09	.09	0

The comparison between the equally spaced time intervals and variable spaced time interval is given in figure 6.9. The variable spaced time intervals case has both the

subject specific protocol and common protocol for all the subjects. The lowest error is observed for the variable spaced time intervals case with subject specific protocol, which is expected as here the protocols are tailored for individual subjects. The errors corresponding to the equal spaced interval case were the highest, as all the times were given equal weightage and the protocol was common for all the subjects. For the case of variable spaced time intervals with common protocol, for all the subjects, the errors were expectedly higher than the case with subject specific protocol but lower than the equally spaced time interval case. With a total of 7 scans the equally spaced time interval gave an error of almost 30%, which came down below 10 % when variable spaced time interval was used with subject specific protocol. The error further went down below 1 % for the variable interval case with subject specific protocol, although this cannot be used as subjects will have variations among themselves and a common protocol based on all the subjects will have to be used instead. There was a clear reduction in the error with the use of variable spaced intervals over the fixed interval case.

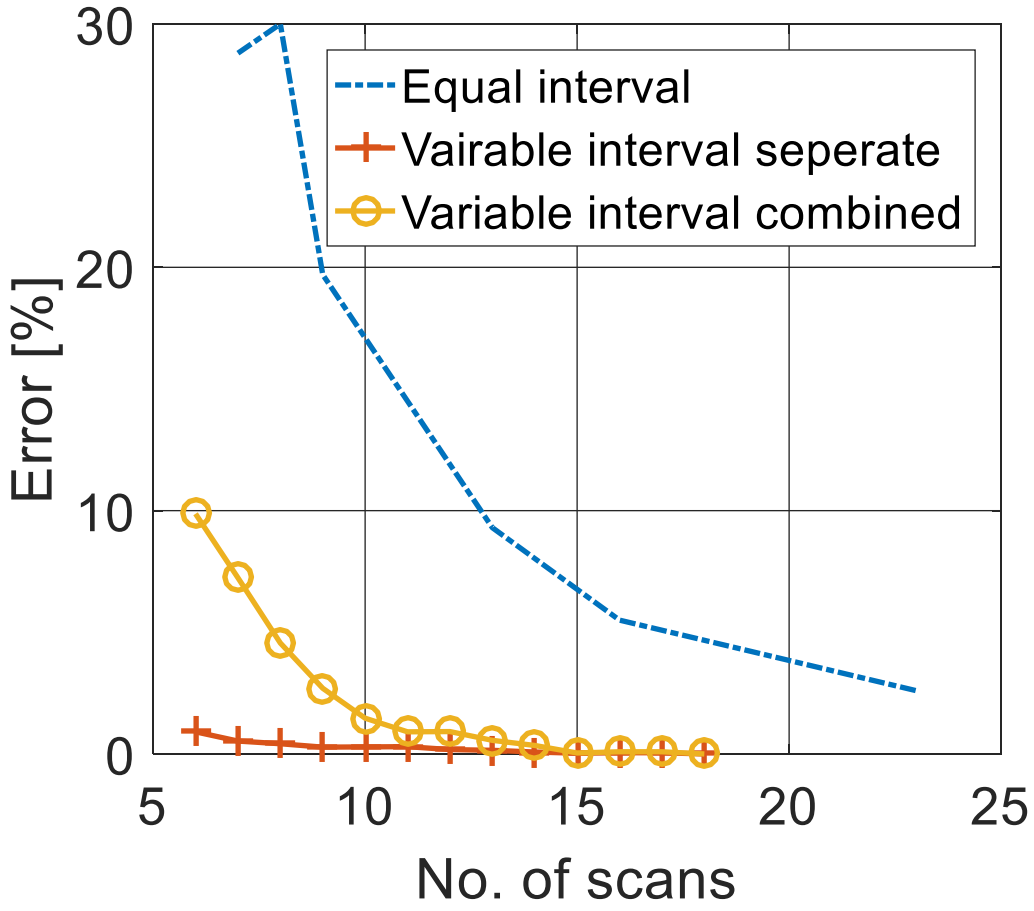

Figure 6.8: Comparison of fixed time interval protocol and variable time interval protocol. Individual subjects with variable time intervals were optimized to give separate protocols and their average error are plotted against the fixed time interval case. Further a combined protocol is obtained using all the subjects with variable time intervals. It can be seen that the variable time interval protocol is better than the fixed interval case as it gives lower error. The least error is obtained by the subject specific case but for practical reasons, a combined protocol is required which also gives lower errors as compared to the equally spaced intervals.

The optimized protocol obtained using the retrospective data was applied to the prospective data. The errors hence obtained are given in table 6.6.

Table 6.7 and 6.8 gives the HPI for healthy and tumorous liver respectively, obtained from different number of scans. The gold standard being 18 scans was used to calculate the true value of HPI, which was in turn used to estimate diagnostic capabilities for the reduced number of scans. For comparison similar analysis was done for the prospective data using equally spaced intervals (Table 6.9 and 6.10). As the number of scans reduced the value of HPI deviated from the actual values. In order to estimate the diagnostic capability for the cases of reduced scans a cut-off off for HPI was needed. For the present case 37% cut-off was chosen based on the HPI index observed for healthy human livers. Based on this false positives and false negatives were calculated for equally and variably spaced time interval case and have been tabulated in Table 6.11. False positives decreased with an increase of number of scans. Equally spaced time interval case had high false positives as compared to variable spaced time interval cases. For the latter case false positives were observed only when the total number of scans were less than or equal to 8, and that for only one case each for 7 and 8 scans. False negatives were observed only when the number of scans was 6 for the case of variably spaced time interval case. Therefore it can be concluded that the variably spaced time interval case gives better outcome than the equally spaced time interval case. Further the number of scans was reduced from 25 to 9 which translate into radiation dose reduction from 165 mGy to 59 mGy.

Additional analysis

It can be seen from Table 6.7 that for some of the cases HPI is relatively high for a healthy liver. There is a potential of user related differences in perfusion calculation. To highlight this point and to achieve better results, a second reading was done for cases 8, 9

and 12. The results are shown in Table 6.12-14. It can be seen that HPI for these cases is much closer to expected values of healthy liver. The errors for these cases are also less as compared to errors in Table 6.13. The reason for the reduction of errors is that the optimized protocol was obtained for a healthy liver which has HPI values around 0.3 and therefore it is a better suited for cases which have HPI values close to 0.3. The analysis done earlier in Table 6.11 is repeated here with new set of data and is given in Table 6.15. The results are similar to the once obtained earlier, for 9 or more scans there are no false negatives and only one false positive out of 15 subjects.

6.4 CONCLUSION

Here the number of scans required in CT perfusion, were reduced to limit the radiation dose exposure. CT perfusion data was collected from scans performed on 11 rabbits for the retrospective study. Different combinations of variable spaced time intervals were tested against equally spaced time intervals. Errors in the calculation of HPA, HPP and HPI were considerably reduced when variable spaced time intervals were used as compared to equal spaced time interval. These optimized protocols were applied to prospective data set of 15 rabbits. The number of scans were reduced to 9 scans, as against to 25 scans in the original protocol, with satisfactory diagnostic capabilities. Only one false negative was obtained when the number of scans was further reduced to 7. The optimized protocol hence developed has the potential to reduce the radiation dose from 165 mGy to 59 mGy.

Table 6.6: Error for different subjects, from prospective data set, with the common, optimized protocol obtained from the retrospective data. Here the protocol was obtained simultaneously for all the subjects, and hence a common protocol was used for all the subjects.

Free samples	4	5	6	7	8	9	10	11	12	13	14	15	16
Total samples	6	7	8	9	10	11	12	13	14	15	16	17	18
Subject													
1	14.5	6.92	6.69	5.86	3	0.7	0.1	0.4	0.4	0.1	0.1	.04	0
2	29.9	12.4	13.4	20	11	6.1	1.4	2.7	2.9	3.2	2.7	0.1	0
3	21.1	35.7	17.3	10.17	6.1	3.8	0.5	0.6	0.6	0.2	.05	.06	0
4	7.28	6.38	3.60	3.11	2.1	1.7	1.7	.14	.15	.00	.03	.01	0
5	10.8	9.14	5.24	8.56	5.7	2.3	1.1	1.1	0.9	0.3	.05	.47	0
6	243.	51.2	51.1	39.25	41	42	37	37	56	62	61	36	0
7	--	--	--	--	--	--	--	--	--	--	--	--	-
8	39.7	8.02	8.19	3.71	1.65	0.70	0.7	.15	0.4	0.1	0.12	0.1	0
9	76.4	5.48	6.38	3.57	0.81	1.26	.14	1.5	.92	.06	0.13	.45	0
10	13.4	17.8	17.3	7.50	1.30	2.08	2.4	4.9	1.1	0.1	0.17	1.1	0
11	16.1	2.81	3.35	4.55	1.71	0.97	.05	0.5	0.5	0.0	0.03	.03	0
12	--	--	--	--	--	--	--	--	--	--	--	--	--
13	2.40	10.7	4.72	3.58	1.83	0.84	.74	.33	.05	.02	0.01	.02	0
14	16.2	6.31	5.74	3.65	1.20	0.44	0.4	0.1	.16	.02	0.02	.06	0
15	27.5	13.6	7.53	7.77	4.02	2.26	.47	.36	.71	.23	0.11	.10	0
16	14.8	2.82	4.00	4.52	0.52	0.56	.47	.21	.20	.04	0.03	.40	0
17	13.0	5.15	6.24	7.38	8.00	8.54	8.7	.49	.70	.13	0.22	.97	0

Table 6.7: HPI of healthy liver for prospective data set. This is based on the optimized protocol with variable spaced time intervals.

Free samples	4	5	6	7	8	9	10	11	12	13	14	15	16
Total samples	6	7	8	9	10	11	12	13	14	15	16	17	18
Subject													
1	0.29	0.34	0.34	0.33	0.32	0.31	0.31	0.31	0.31	0.31	0.31	0.31	0.31
2	0.26	0.18	0.19	0.23	0.21	0.19	0.17	0.19	0.19	0.19	0.17	0.18	0.18
3	0.34	0.50	0.40	0.43	0.40	0.39	0.38	0.38	0.38	0.38	0.38	0.38	0.38
4	0.32	0.37	0.37	0.36	0.36	0.36	0.36	0.35	0.35	0.35	0.35	0.35	0.35
5	0.36	0.36	0.34	0.36	0.34	0.33	0.33	0.33	0.33	0.32	0.32	0.32	0.32
6	0.47	1.00	1.00	1.00	1.00	1.00	1.00	1.00	0.83	0.82	0.82	1.00	0.92
7	0.25	0.54	0.71	0.90	0.92	0.94	0.95	1.00	1.00	1.00	1.00	1.00	1.00
8	0.32	0.49	0.46	0.49	0.50	0.51	0.51	0.51	0.50	0.51	0.51	0.51	0.51
9	0.31	0.56	0.56	0.57	0.59	0.60	0.59	0.58	0.59	0.59	0.59	0.59	0.59
10	0.24	0.27	0.21	0.24	0.25	0.25	0.25	0.27	0.25	0.26	0.26	0.26	0.26
11	0.28	0.30	0.29	0.29	0.31	0.30	0.31	0.31	0.31	0.31	0.31	0.31	0.31
12	0.38	0.39	0.45	0.44	0.45	0.45	0.45	0.73	0.83	0.83	0.83	1.00	1.00
13	0.35	0.38	0.37	0.36	0.36	0.36	0.36	0.36	0.36	0.36	0.36	0.36	0.36
14	0.28	0.35	0.34	0.33	0.33	0.32	0.32	0.32	0.32	0.32	0.32	0.32	0.32
15	0.27	0.23	0.21	0.22	0.20	0.20	0.19	0.20	0.20	0.19	0.19	0.19	0.19
16	0.28	0.33	0.32	0.32	0.34	0.34	0.34	0.34	0.34	0.34	0.34	0.34	0.34
17	0.20	0.21	0.21	0.20	0.20	0.20	0.20	0.22	0.23	0.23	0.23	0.23	0.23

Table 6.8: HPI of tumor for prospective data set.

Total samples	6	7	8	9	10	11	12	13	14	15	16	17	18
Free samples	4	5	6	7	8	9	10	11	12	13	14	15	16
Subject													
1	0.50	0.51	0.51	0.46	0.49	0.48	0.49	0.49	0.49	0.49	0.49	0.49	0.49
2	0.74	0.43	0.42	0.60	0.67	0.67	0.59	0.62	0.61	0.61	0.60	0.60	0.60
3	0.34	0.42	0.43	0.44	0.49	0.50	0.55	0.50	0.51	0.51	0.62	0.61	0.62
4	0.44	0.53	0.52	0.52	0.53	0.53	0.53	0.53	0.53	0.53	0.53	0.53	0.53
5	0.57	0.48	0.49	0.49	0.50	0.50	0.47	0.48	0.48	0.50	0.48	0.48	0.48
6	1.00	0.97	0.90	0.94	0.93	0.93	0.91	0.93	0.74	0.74	0.73	0.98	0.79
7	0.78	0.47	0.43	0.57	0.54	0.54	0.57	0.99	0.84	0.83	0.82	1.00	1.00
8	1.00	1.00	1.00	1.00	1.00	1.00	1.00	1.00	0.68	0.72	0.69	0.68	0.69
9	1.00	1.00	1.00	1.00	1.00	1.00	1.00	0.90	0.94	0.94	0.94	0.90	0.86
10	0.74	0.74	0.82	0.73	0.75	0.73	0.70	0.75	0.72	0.74	0.73	0.73	0.72
11	0.67	0.69	0.74	0.63	0.66	0.55	0.58	0.59	0.59	0.61	0.59	0.59	0.59
12	0.83	1.00	1.00	1.00	1.00	1.00	1.00	1.00	1.00	1.00	1.00	1.00	1.00
13	0.69	0.69	0.70	0.69	0.72	0.73	0.74	0.72	0.72	0.72	0.72	0.72	0.72
14	0.68	0.74	0.75	0.71	0.71	0.69	0.70	0.70	0.72	0.70	0.71	0.70	0.43
15	0.68	0.60	0.66	0.57	0.64	0.61	0.56	0.59	0.51	0.56	0.52	0.52	0.52
16	0.38	0.43	0.39	0.40	0.41	0.41	0.41	0.42	0.42	0.42	0.42	0.42	0.42
17	0.95	0.78	0.47	0.46	0.45	0.44	0.44	0.54	0.55	0.54	0.54	0.54	0.54

Table 6.9: HPI of healthy liver for prospective data set. This is based on the equally spaced time intervals.

Time intervals	10	8	6	5	4	3	2	1	0.5
Total samples	7	8	9	11	13	16	23	43	83
Subject									
1	0.40	0.37	0.35	0.34	0.33	0.32	0.30	0.29	0.29
2	0.32	0.30	0.30	0.25	0.23	0.19	0.17	0.17	0.17
3	0.57	0.49	0.42	0.43	0.40	0.38	0.37	0.37	0.36
4	0.47	0.47	0.42	0.40	0.37	0.35	0.34	0.34	0.34
5	0.44	0.43	0.39	0.38	0.36	0.33	0.31	0.29	0.29
6	1.00	1.00	1.00	1.00	1.00	1.00	0.87	0.80	0.80
7	1.00	1.00	1.00	1.00	1.00	1.00	1.00	1.00	1.00
8	0.53	0.53	0.48	0.47	0.47	0.49	0.52	0.53	0.53
9	0.52	0.49	0.52	0.53	0.55	0.58	0.59	0.56	0.56
10	0.32	0.30	0.27	0.25	0.23	0.24	0.25	0.28	0.29
11	0.37	0.39	0.34	0.33	0.33	0.32	0.30	0.30	0.30
12	0.88	1.00	0.65	1.00	1.00	1.00	1.00	1.00	1.00
13	0.46	0.46	0.41	0.37	0.37	0.36	0.36	0.36	0.36
14	0.38	0.36	0.34	0.34	0.34	0.33	0.32	0.33	0.33
15	0.35	0.34	0.28	0.26	0.22	0.20	0.19	0.19	0.19
16	0.37	0.34	0.33	0.33	0.33	0.33	0.34	0.36	0.36
17	0.27	0.28	0.24	0.24	0.24	0.23	0.22	0.21	0.21

Table 6.10: HPI of tumor for prospective data set. This is based on the equally spaced time intervals.

Time intervals	10	8	6	5	4	3	2	1	0.5
Total samples	7	8	9	11	13	16	23	43	83
Subject									
1	0.55	0.51	0.49	0.48	0.48	0.48	0.49	0.50	0.51
2	0.61	0.66	0.58	0.56	0.56	0.58	0.62	0.60	0.58
3	0.54	0.65	0.62	0.64	0.63	0.61	0.59	0.59	0.59
4	0.60	0.60	0.56	0.55	0.54	0.53	0.52	0.52	0.52
5	0.57	0.54	0.49	0.50	0.48	0.49	0.48	0.48	0.48
6	1.00	1.00	0.84	0.92	0.89	0.85	0.75	0.69	0.68
7	1.00	1.00	0.78	1.00	1.00	1.00	1.00	1.00	1.00
8	0.90	0.93	1.00	1.00	0.84	0.71	0.62	0.60	0.60
9	1.00	1.00	1.00	0.89	0.88	0.87	0.88	0.82	0.82
10	0.66	0.73	0.85	0.82	0.77	0.73	0.69	0.69	0.70
11	0.62	0.71	0.77	0.72	0.76	0.66	0.56	0.52	0.51
12	1.00	1.00	1.00	1.00	1.00	1.00	0.93	0.76	0.72
13	0.77	0.84	0.77	0.69	0.70	0.70	0.65	0.62	0.60
14	0.66	0.65	0.66	0.64	0.54	0.56	0.41	0.42	0.41
15	0.61	0.55	0.61	0.58	0.54	0.56	0.51	0.48	0.48
16	0.41	0.47	0.43	0.48	0.47	0.43	0.39	0.39	0.39
17	0.89	1.00	1.00	1.00	0.72	0.58	0.49	0.47	0.45

Table 6.11: False +ve/-ve for healthy and tumorous region using equal and variable spaced time interval for prospective analysis

	Equal spaced time interval				Variably spaced time interval			
	Healthy		Tumor		Healthy		Tumor	
No. of Scans	False +ve	False -ve	False +ve	False -ve	False +ve	False -ve	False +ve	False -ve
6	--	--	--	--	0	4	0	0
7	8	0	0	0	1	0	0	0
8	6	0	0	0	1	0	0	0
9	4	0	0	0	0	0	0	0
10	--	--	--	--	0	0	0	0
11	4	0	0	0	0	0	0	0
12	--	--	--	--	0	0	0	0
13	1	0	0	0	0	0	0	0
14	--	--	--	--	0	0	0	0
15	--	--	--	--	0	0	0	0
16	1	0	0	0	0	0	0	0
17	--	--	--	--	0	0	0	0
18	--	--	--	--	0	0	0	0
23	0	0	0	0	--	--	--	--
43	0	0	0	0	--	--	--	--

Table 6.12: Errors in healthy liver case, from prospective data set. Here new set of data points has been taken for subjects 8, 9 and 12. Cases 6 and 7 have been removed here.

Free Samples	4	5	6	7	8	9	10	11	12	13	14	15	16
Total samples	6	7	8	9	10	11	12	13	14	15	16	17	18
Subject													
1	14.5	6.92	6.69	5.86	3.0	.69	.12	.38	.45	.07	.07	.04	0
2	29.9	12.4	13.4	20.0	11	6.1	1.5	2.7	2.9	3.2	2.7	.13	0
3	21.1	35.6	17.3	10.2	6.1	3.8	.48	.64	.65	.25	.05	.06	0
4	7.28	6.38	3.60	3.1	2.1	1.7	1.7	.14	.15	.00	.03	.01	0
5	10.8	9.14	5.24	8.6	5.7	2.3	1.1	1.1	.94	.30	.05	.47	0
8	21.6	9.24	6.63	5.8	3.4	.59	.20	.57	.58	.11	.06	.04	0
9	23.5	18.6	11.5	6.2	.51	2.9	1.4	.56	1.4	.02	.08	.09	0
10	13.5	17.8	17.3	7.5	1.3	2.1	2.4	4.9	1.1	.09	.17	1.1	0
11	16.1	2.81	3.35	4.6	1.7	.97	.05	.52	.48	.00	.03	.03	0
12	4.77	8.78	11.7	7.7	2.3	2.1	1.7	.60	.69	.03	.14	.06	0
13	2.40	10.7	4.7	3.6	1.8	.84	.74	.33	.05	.02	.01	.02	0
14	16.2	6.31	5.7	3.7	1.2	.44	.41	.11	.16	.02	.02	.06	0
15	27.5	13.6	7.5	7.8	4.0	2.3	.47	.36	.71	.23	.11	.10	0
16	14.9	2.8	4.0	4.5	.52	.56	.47	.21	.20	.04	.03	.40	0
17	13.0	5.2	6.2	7.4	8.0	8.5	8.7	0.49	0.70	0.13	0.22	0.97	0

Table 6.13: HPI of healthy liver for prospective data set with variable spaced time intervals. Here new set of data points has been taken for subjects 8, 9 and 12. Cases 6 and 7 have been removed here.

Free samples	4	5	6	7	8	9	10	11	12	13	14	15	16
Total samples	6	7	8	9	10	11	12	13	14	15	16	17	18
Subject													
1	0.29	0.34	0.34	0.33	0.32	0.31	0.31	0.31	0.31	0.31	0.31	0.31	0.31
2	0.26	0.18	0.19	0.23	0.21	0.19	0.17	0.19	0.19	0.19	0.17	0.18	0.18
3	0.34	0.50	0.40	0.43	0.40	0.39	0.38	0.38	0.38	0.38	0.38	0.38	0.38
4	0.32	0.37	0.37	0.36	0.36	0.36	0.36	0.35	0.35	0.35	0.35	0.35	0.35
5	0.36	0.36	0.34	0.36	0.34	0.33	0.33	0.33	0.33	0.32	0.32	0.32	0.32
8	0.30	0.38	0.37	0.36	0.38	0.37	0.37	0.37	0.37	0.37	0.37	0.37	0.37
9	0.32	0.46	0.43	0.42	0.44	0.45	0.44	0.43	0.43	0.43	0.43	0.43	0.43
10	0.24	0.27	0.21	0.24	0.25	0.25	0.25	0.27	0.25	0.26	0.26	0.26	0.26
11	0.28	0.30	0.29	0.29	0.31	0.30	0.31	0.31	0.31	0.31	0.31	0.31	0.31
12	0.28	0.33	0.34	0.33	0.31	0.31	0.31	0.30	0.30	0.30	0.30	0.30	0.30
13	0.35	0.38	0.37	0.36	0.36	0.36	0.36	0.36	0.36	0.36	0.36	0.36	0.36
14	0.28	0.35	0.34	0.33	0.33	0.32	0.32	0.32	0.32	0.32	0.32	0.32	0.32
15	0.27	0.23	0.21	0.22	0.20	0.20	0.19	0.20	0.20	0.19	0.19	0.19	0.19
16	0.28	0.33	0.32	0.32	0.34	0.34	0.34	0.34	0.34	0.34	0.34	0.34	0.34
17	0.20	0.21	0.21	0.20	0.20	0.20	0.20	0.22	0.23	0.23	0.23	0.23	0.23

Table 6.14: HPI of tumor for prospective data set applying variable spaced time interval. Here new set of data points has been taken for subjects 8, 9 and 12. Cases 6 and 7 have been removed here.

Total samples	6	7	8	9	10	11	12	13	14	15	16	17	18
Free samples	4	5	6	7	8	9	10	11	12	13	14	15	16
Subject													
1	0.50	0.51	0.51	0.46	0.49	0.48	0.49	0.49	0.49	0.49	0.49	0.49	0.49
2	0.74	0.43	0.42	0.60	0.67	0.67	0.59	0.62	0.61	0.61	0.60	0.60	0.60
3	0.34	0.42	0.43	0.44	0.49	0.50	0.55	0.50	0.51	0.51	0.62	0.61	0.62
4	0.44	0.53	0.52	0.52	0.53	0.53	0.53	0.53	0.53	0.53	0.53	0.53	0.53
5	0.57	0.48	0.49	0.49	0.50	0.50	0.47	0.48	0.48	0.50	0.48	0.48	0.48
8	1.00	1.00	0.99	0.94	0.92	0.86	0.85	0.86	0.87	0.87	0.86	0.86	0.86
9	1.00	1.00	1.00	1.00	1.00	1.00	1.00	0.99	0.82	0.83	0.82	0.91	0.89
10	0.74	0.74	0.82	0.73	0.75	0.73	0.70	0.75	0.72	0.74	0.73	0.73	0.72
11	0.67	0.69	0.74	0.63	0.66	0.55	0.58	0.59	0.59	0.61	0.59	0.59	0.59
12	0.55	0.55	0.57	0.66	0.68	0.68	0.67	0.67	0.67	0.67	0.67	0.67	0.67
13	0.69	0.69	0.70	0.69	0.72	0.73	0.74	0.72	0.72	0.72	0.72	0.72	0.72
14	0.68	0.74	0.75	0.71	0.71	0.69	0.70	0.70	0.72	0.70	0.71	0.70	0.43
15	0.68	0.60	0.66	0.57	0.64	0.61	0.56	0.59	0.51	0.56	0.52	0.52	0.52
16	0.38	0.43	0.39	0.40	0.41	0.41	0.41	0.42	0.42	0.42	0.42	0.42	0.42
17	0.95	0.78	0.47	0.46	0.45	0.44	0.44	0.54	0.55	0.54	0.54	0.54	0.54

Table 6.15: False +ve/-ve for healthy and tumorous region using variable spaced time interval for prospective analysis. Here new set of data points has been taken for subjects 8, 9 and 12. Cases 6 and 7 have been removed here.

	Variably spaced time interval			
	Healthy		Tumor	
Number Of Scans	False +ve	False -ve	False +ve	False -ve
6	0	2	0	1
7	2	0	0	0
8	2	0	0	0
9	0	0	0	0
10	1	0	0	0
11	1	0	0	0
12	0	0	0	0
13	1	0	0	0
14	1	0	0	0
15	0	0	0	0
16	0	0	0	0
17	0	0	0	0
18	0	0	0	0

Chapter 7

Effect of Discontinuities and Penetrations on the Shielding Efficacy of High Temperature Superconducting Magnetic Shields

The complete authorship of this work should be read as Rajeev Hatwar, Dr. Jozef Kvitkovic, Prof. Cila Herman and Dr. Sastry Pamidi. Rajeev Hatwar performed the experiments and analysis in the guidance of Dr. Jozef Kvikovic and Dr. Sastry Pamidi. The experimental setup was developed by Dr. Jozef Kvitkovic and Dr. Sastry Pamidi. This work was published in IOP conference series: Materials science and engineering (Hatwar *et al.* 2015).

7.1 INTRODUCTION

There are some materials in nature that experience zero electrical resistances below certain temperature. Such materials are called superconductors and the threshold temperature is known as critical temperature (T_c). They are classified based on their critical temperature as low and high temperature superconductors. When the critical temperature is below 134 K and above 20 K they are known as high temperature

superconductors and when the critical temperatures are below 20 K they are referred to as low temperature superconductors. Due to the zero electrical resistance of these materials they are capable of carrying much higher current then conventional cables (Figure 7.1). Some of the applications of superconductors are in powerful superconducting magnets (magnetic resonance imaging, nuclear magnetic resonance and maglev train), magnetic shielding, transmission/distribution of power and electric motors/generators.

Sensitive electronic equipment such as superconducting quantum interface device (SQUIDS) in magneto-encephalography (Pizella *et al.* 2001) and other medical applications require high level of magnetic shielding to protect them from spurious magnetic fields. Further, devices that generate strong magnetic fields also need to be shielded in order to contain their magnetic fields and ensure proper functioning of other instruments in their vicinity. Although ferromagnetic materials are normally used for AC magnetic shielding applications, the magnetic shielding provided by them is limited to frequencies above 1 kHz (Pavese *et al.* 1998). High temperature superconducting (HTS) materials such as $YBa_2Cu_3O_7$ (YBCO) have been demonstrated to be suitable for shielding both for DC and AC magnetic fields (Fagnard *et al.* 2009, Fagnard *et al.* 2012). Second generation (2G) HTS have been successfully developed on commercial level with excellent superconducting and mechanical properties. Long lengths of 2G HTS are being produced at various widths up to 45 mm (AMSC). Figure 7.2 shows how the effect of hole on the magnetic shield, encasing a sensitive equipment, and how a mask over the hole can mitigate the effect of the hole.

Figure 7.1. Conventional electrical cables and superconducting cables used in accelerators at CERN (Wikimedia 2017)

Various studies have been done in the past on magnetic shields made of superconducting bulk material and tapes. Kvitkovic *et al.* have studied the effect of the geometry, operating temperature, and interlayer separation on magnetic shielding efficacy of shields made of 2G HTS (Kvitkovic *et al.* 2009, Kvitkovic *et al.* 2015, Kvitkovic *et al.* 2011, Kvitkovic *et al.*2013). Fabrication of large practical shields require many sections of HTS and magnetic shields needed for large high power density machines will need to allow access to power feedthroughs and sensor wiring. Aging and mechanical stresses will also lead to spots of degraded superconducting properties (Kim *et al.* 2011, Yuan *et al.* 2011). So far the effects of discontinuities and penetrations in

magnetic shields on their performance have not been studied. Therefore it is important to quantify the effect of discontinuities on shielding efficacy of HTS magnetic shields and potential solutions to mitigate the negative effects of the penetrations and discontinuities.

The present work focuses on understanding the effect of a circular hole on the magnetic shielding efficacy of a 2G HTS shield. This chapter presents the results of the experimental studies of the shielding factor at variable amplitudes and frequencies of external magnetic field on the shields with and without an opening and a simple method to mitigate the negative effects of an opening.

7.2 EXPERIMENTAL SETUP

A helical copper magnet (Pamidi *et al.* 2012) (figure 7.3) was used to generate a transverse external AC magnetic field. Magnetic shields were kept in a uniform AC magnetic field, which was perpendicular to the surface of the shields. The external magnetic field, B_{ext}, was calculated based on the current supplied to the magnet and the previously measured magnet constant. Internal magnetic field, B_{int}, was measured using a calibrated Hall Probe placed inside the magnetic shield, at mid distance between the two parallel rectangular sheets and at the centre of the rectangular plates as shown in Figure 7.4.

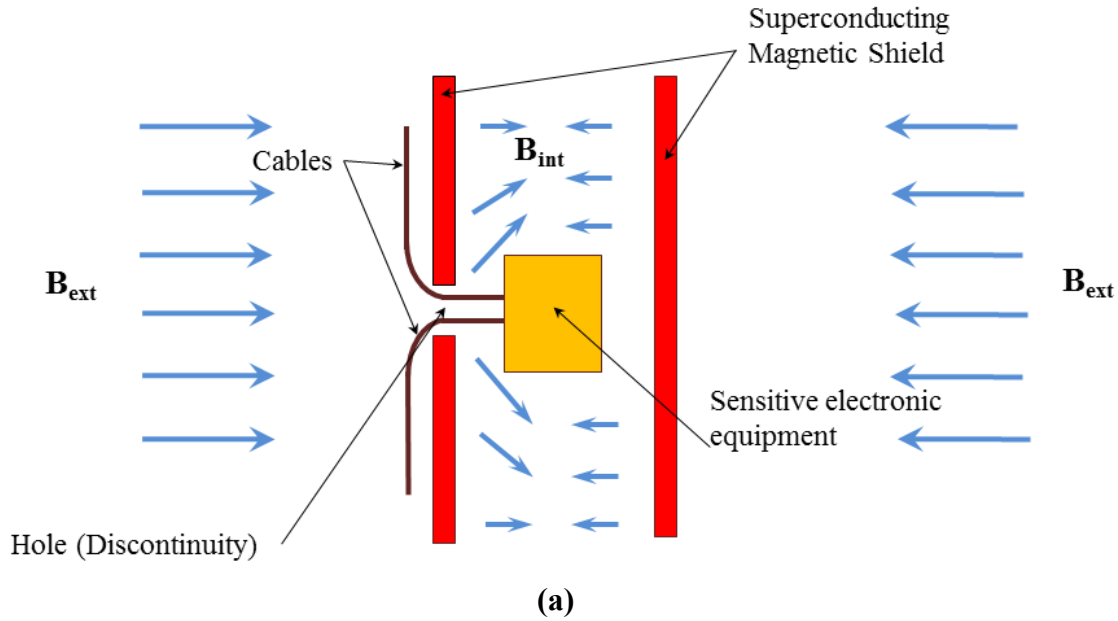

(a)

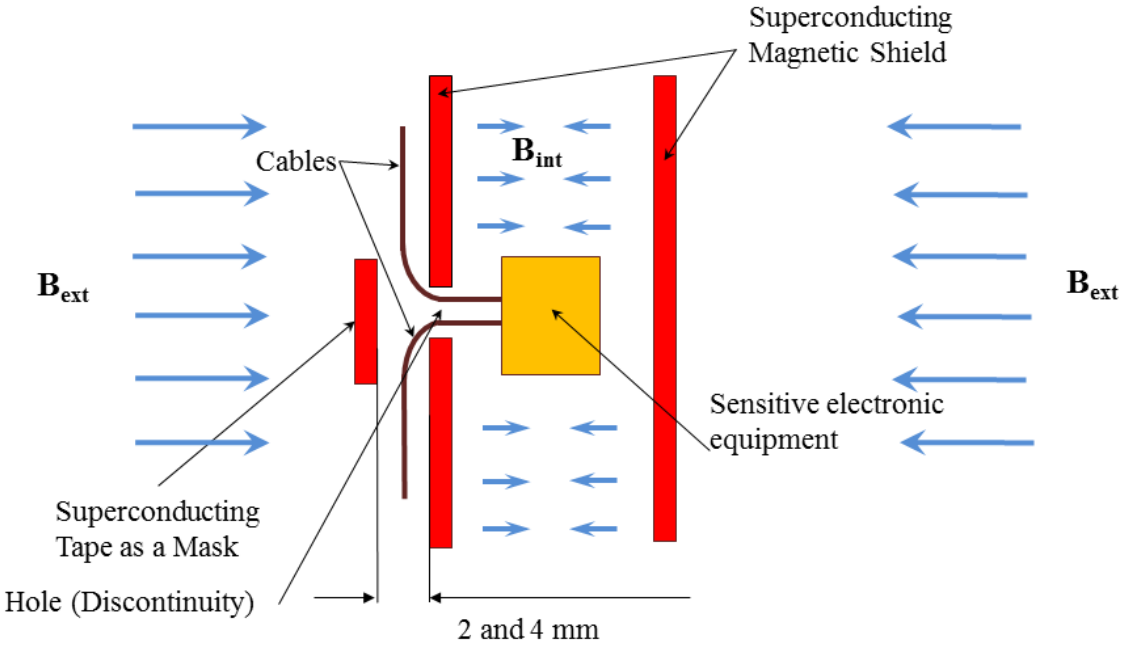

(b)

Figure 7.2 (a) Effect of a hole in the superconducting layer on the magnetic field. (b) Use of masking layer to mitigate the effect of hole in the magnetic shield.

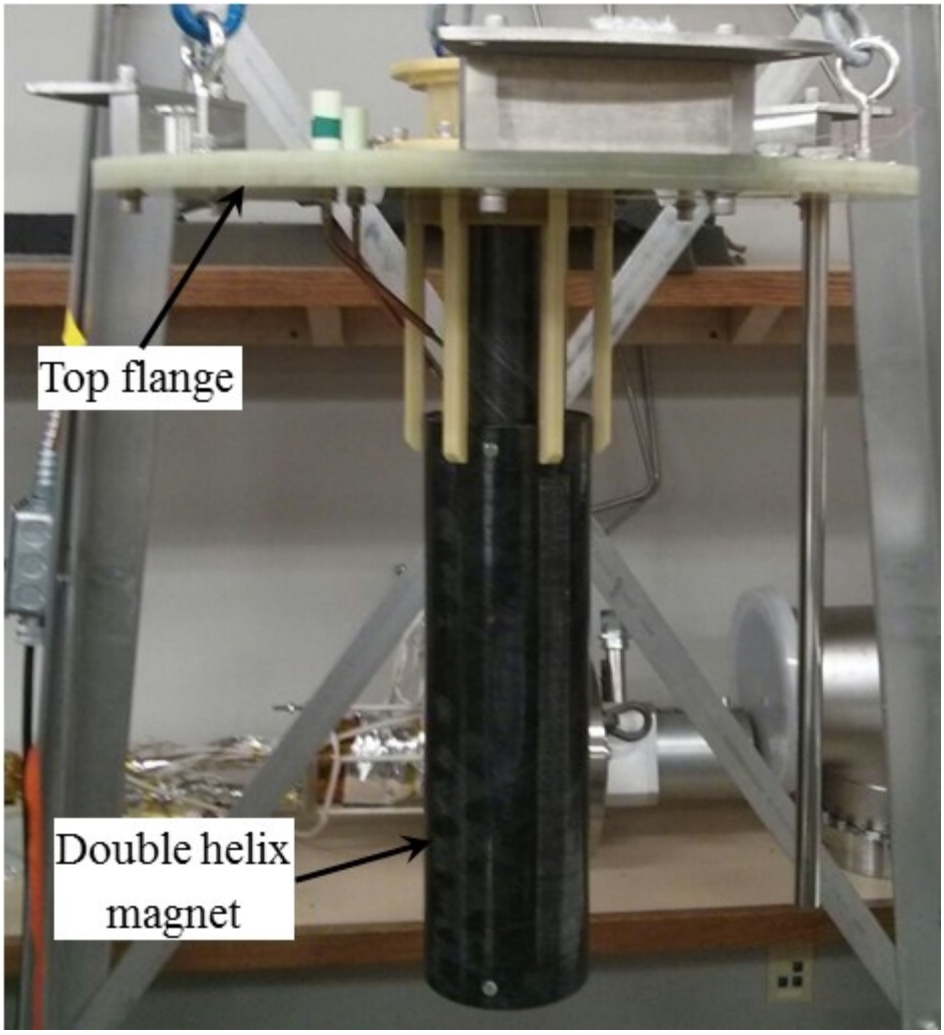

Figure 7.3. Double helix magnet used to generate external magnetic field.

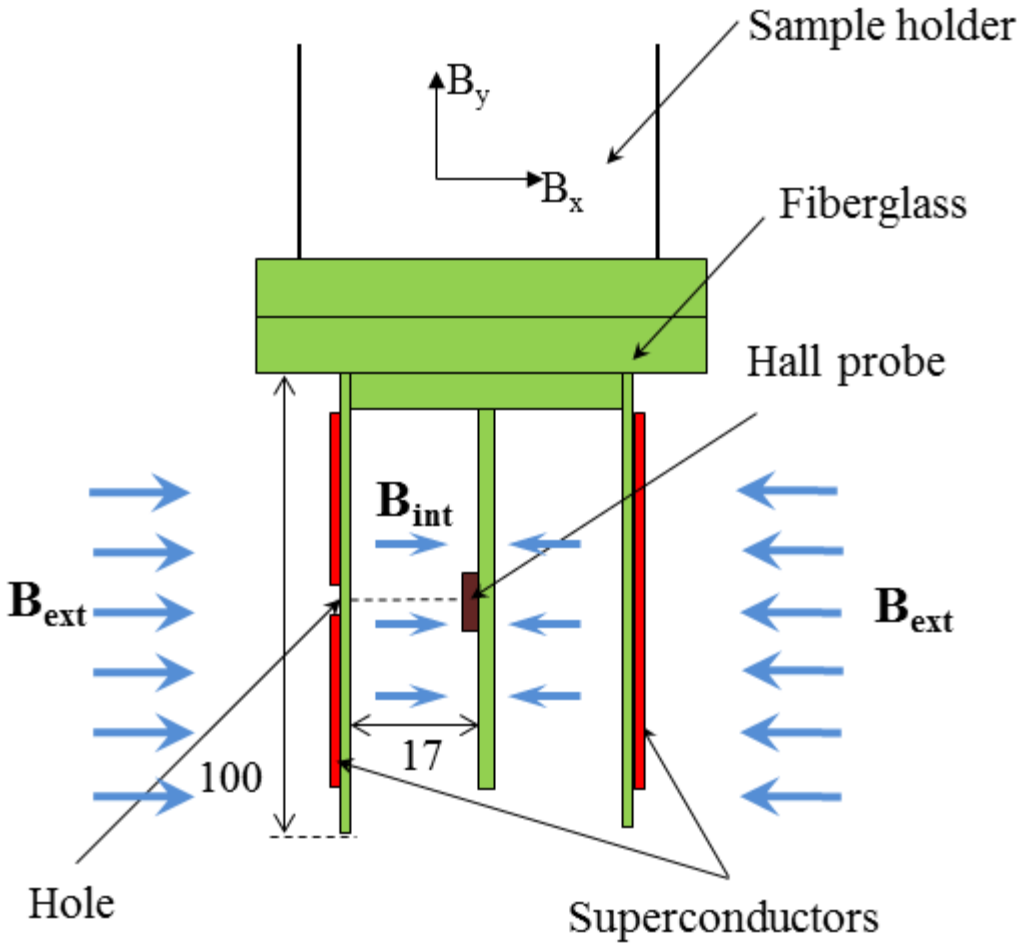

Figure 7.4. A schematic of the experimental setup and position of the hole. All dimensions are in mm.

The dimensions of the rectangular plates are 60 mm × 100 mm and the distance between the two parallel sheets is 38 mm. The support structure for the magnetic shield is made of G-10 plates. Three layers of YBCO tapes are attached onto the G-10 plates using cryogenic Kapton adhesive tape. Each layer consists of three pieces of 45 mm wide 2G HTS superconducting tape, manufactured by American Superconductor Corporation. The setup with parallel superconducting layers was mounted on a sample holder as shown in figure 7.5. The holes were drilled at the centre of the shield, at the same height as the Hall

probe Figure 7.4. The size of the hole was varied with diameter of 1 mm, 3 mm, 6 mm and 12 mm to study the effect of the size of discontinuities and penetrations on the shielding effect. A 45 mm × 45 mm section of the HTS tape is placed on top of the 12 mm hole to mask the opening, with a G-10 fiberglass piece in between them. The distance between the mask and the shield was varied at 2 mm and 4 mm, for two different configurations as shown in Figure 7.2.

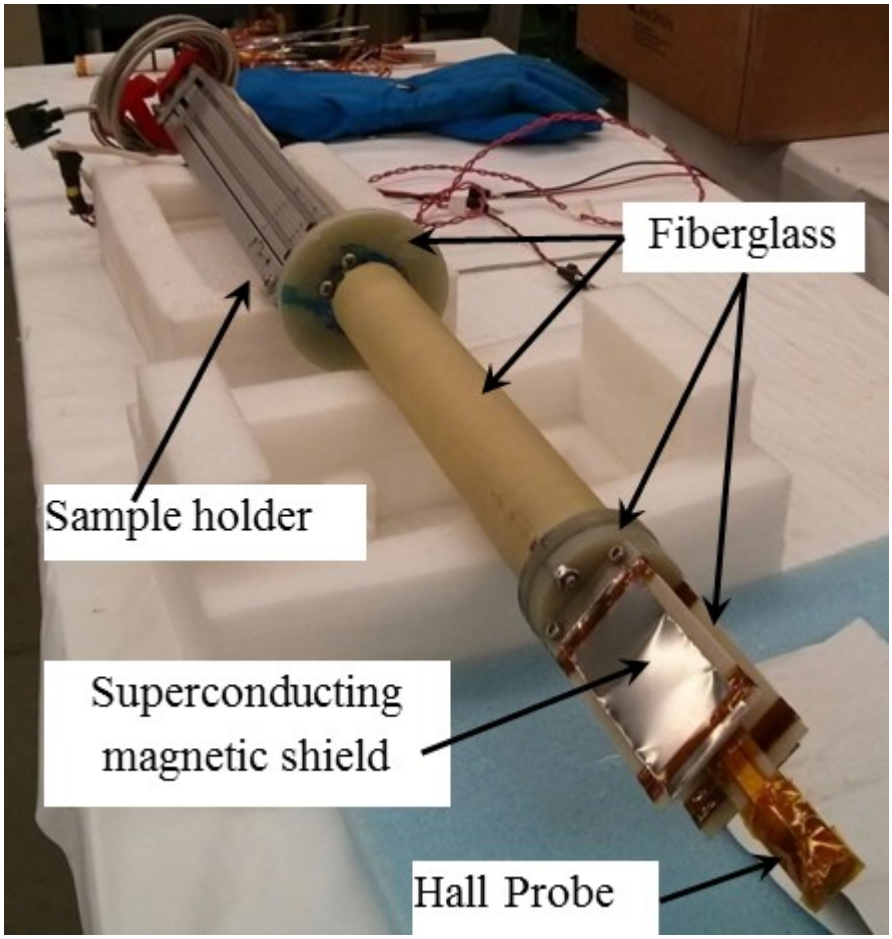

Figure 7.5 Sample holder, which has the parallel super conducting layers, is used to place these layers inside the helical magnet and liquid nitrogen.

Shielding factor, SF, is a measure of the effectiveness of the magnetic shield and it is expressed as:

$$SF\ (\%) = 100 \times \frac{B_{ext} - B_{int}}{B_{ext}}$$

The frequency of magnetic field was varied from 20 Hz to 400 Hz. The experimental setup was maintained at 77 K by immersing in a liquid nitrogen bath (Figure 7.6 -7). All magnetic field magnitudes are expressed in rms values. The block diagram for the instrumentation is shown in figure 7.8. Details of the experimental setup are described elsewhere (Kvitkovic *et al.* 2013).

Figure 7.6 Sample holder along with superconducting plates placed inside the helical magnet and immersed in liquid nitrogen filled dewar flask.

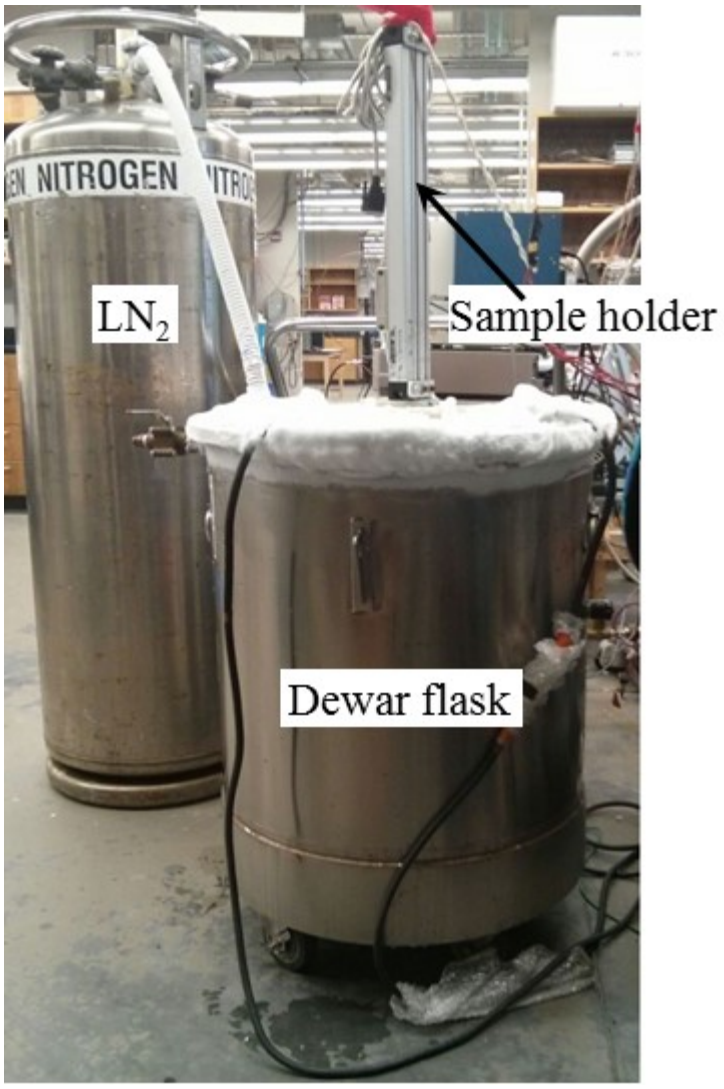

Figure 7.7. Dewar flask being filled with liquid nitrogen from a liquid nitrogen cylinder. Moisture in the surrounding air condenses and turns into ice on the top of the flask.

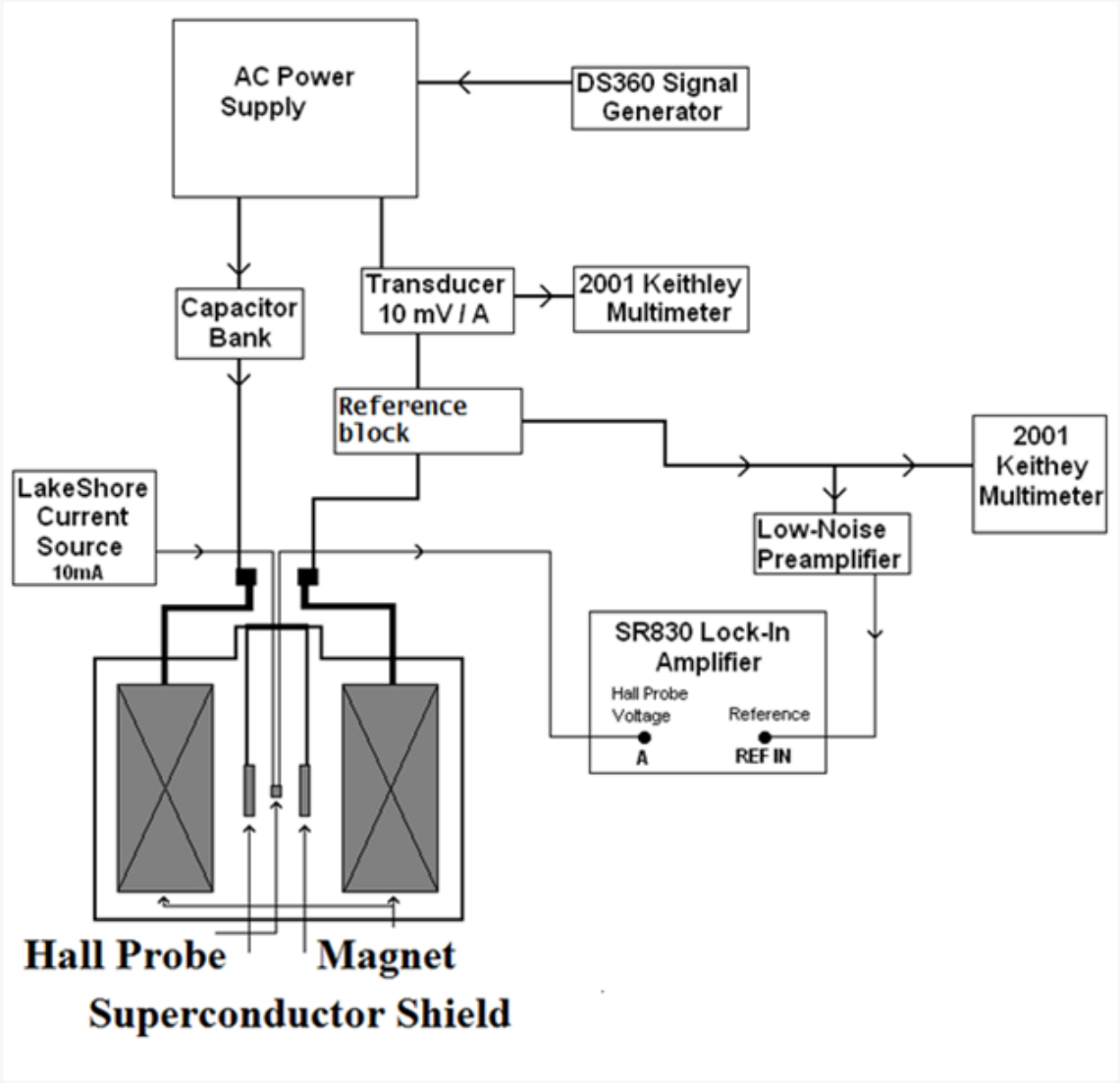

Figure 7.8. Block diagram of the instrumentation used in the magnetic shielding experiment is shown here.

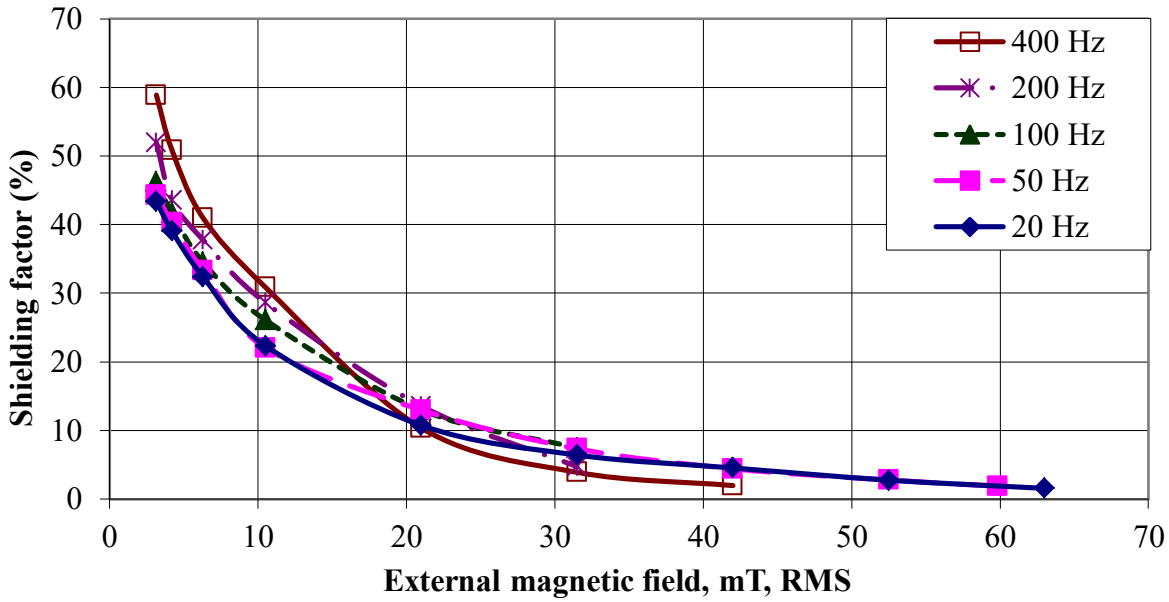

Figure 7.9 Variation of shielding factor with external magnetic field for 3 layer shield with no holes.

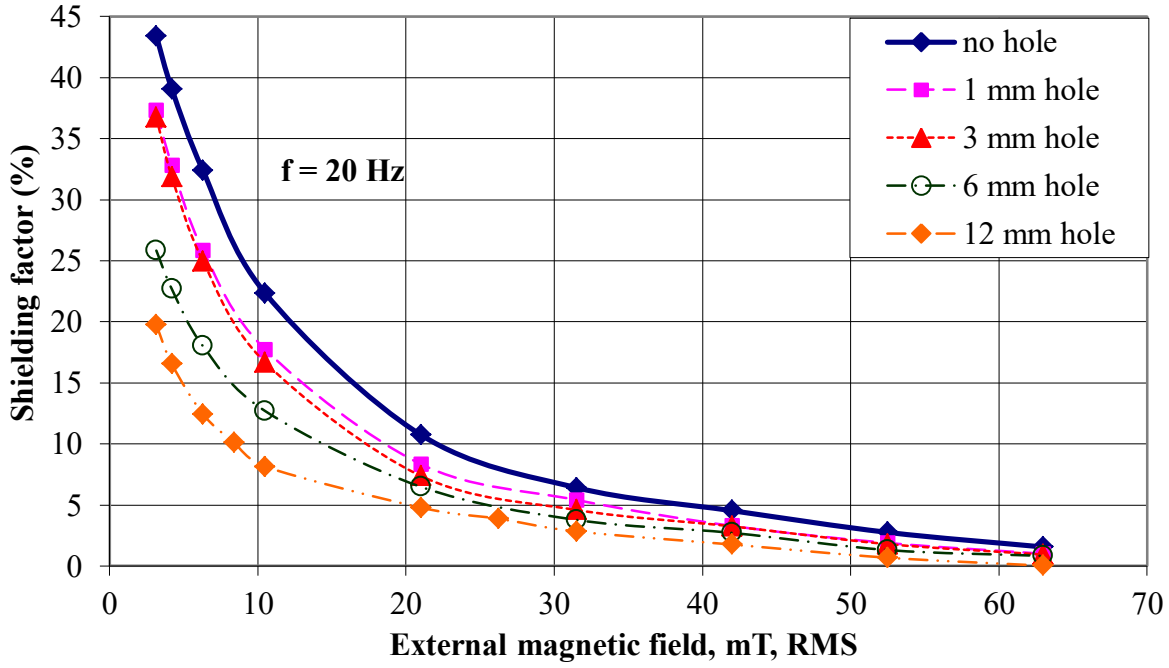

Figure 7.10 Variation of shielding factor with external magnetic field at 20 Hz for different sizes of holes.

7.3 RESULTS AND DISCUSSION

The variation of shielding factor of the shield without any opening with B_{ext} for different frequencies is shown in Figure 7.9. It can be seen that for lower B_{ext}, shielding factor increases with increasing frequency. The shielding factor decreases as the B_{ext} increases. Shielding factor at 20 Hz goes down from 44 % to 1.5 % as the B_{ext} increases from 2.5 mT to 63 mT. Similar trend is observed for other frequencies. This can be explained by the fact that the critical current, I_c, decreases with increasing B_{ext} which leads to a lower shielding factor. So for high B_{ext}, the shielding factor for higher frequency is lower. The shielding factor at 31.5 mT for various frequencies is in the range of 4 to 7%.

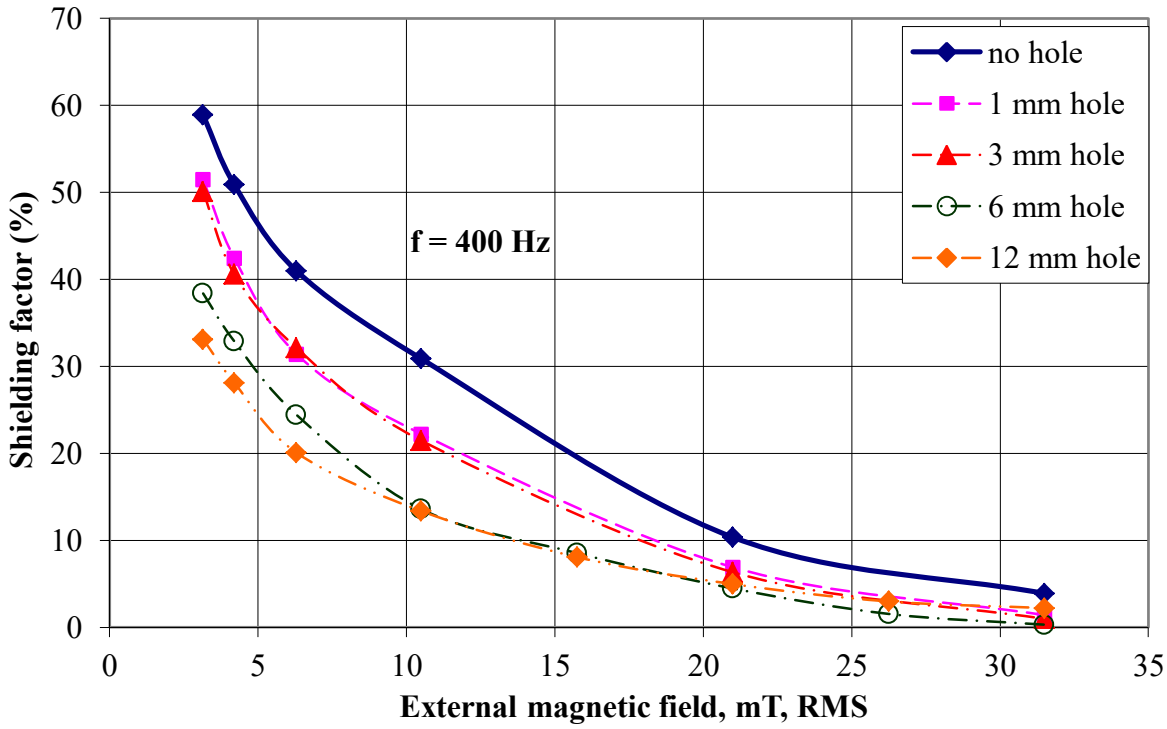

Figure 7.11 Variation of shielding factor with external magnetic field at 400 Hz for different sizes of holes.

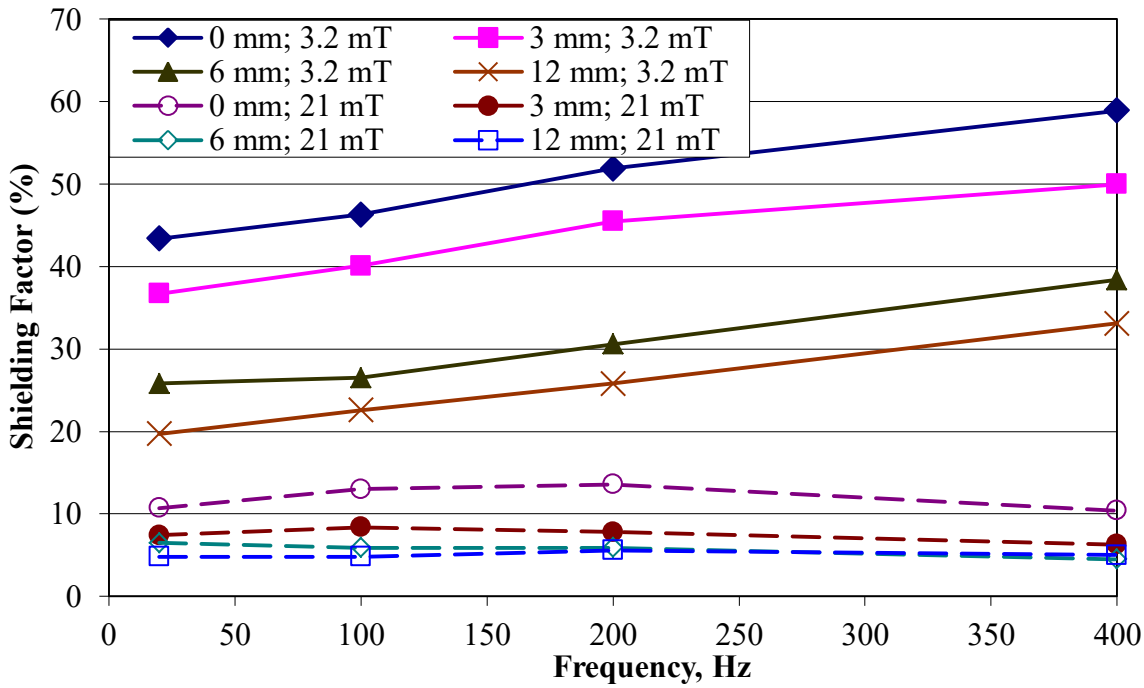

Figure 7.12 Shielding factor vs frequency for 3 layer shield. Hole diameter is the parameter and external magnetic field magnitude of 3.2 mT and 21 mT.

Figure 7.10 shows the variation in the shielding factor with B_{ext} at 20 Hz for different sizes of holes. Similar to the case of a shield with no opening, the shielding factor for the shield with a hole decreases with increasing B_{ext}. Further, it can be seen that the shielding factor decreases with increasing hole size. For B_{ext} of 2.5 mT, the shielding factor is 44 % with no hole and 37.5 %, 25.5 % and 22 % for 1 mm, 6 mm and 12 mm hole size, respectively. The effect of hole size gradually diminishes as B_{ext} increases. There is a decrease of shielding factor from 10.7 % to 4. 8 % as the hole size increases from no hole to 12 mm hole at 21 mT. At 63 mT this reduction in shielding factor is from 1.5 % to 0.03 %. Similar trend is observed for 400 Hz as shown in Figure 7.11. The frequency dependence of the shielding factor at different applied magnetic field amplitudes for

different hole sizes is depicted in Figures 7.12 and 7.13. It can be seen that at lower B_{ext}, the dependence of shielding factor on frequency is high and as B_{ext} increases the effect of frequency diminishes to a small value.

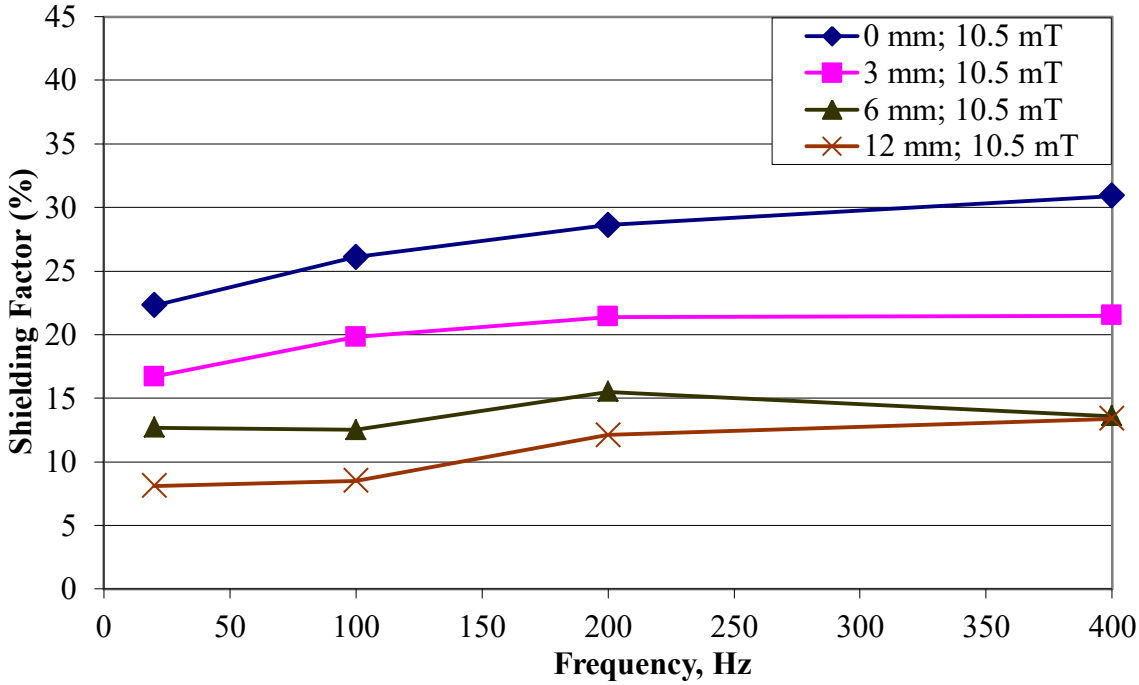

Figure 7.13. Shielding factor vs frequency. Hole diameter is the parameter and applied magnetic field magnitude is 10.5 mT.

In order to assess ways to mitigate the effect of the hole, a piece of superconducting tape of smaller dimension (45 x 45 mm^2) was used as a mask for the opening. The mask was placed at a distance of 2 mm or 4 mm in front of the 12 mm hole. The effect of the mask layer on the shielding factor at 20 Hz is shown in figure 7.14. Both the configurations were able to successfully compensate for the 12 mm hole. The shielding factor at 10.5 mT increased from 8.14 % to 27.48 % with the addition of the mask at a distance of 4 mm. This was higher than 22 %, the shielding factor obtained with a sheet without any

hole. When the mask was placed at 2 mm the shielding factor further increased to 35%. So the mask not only compensated for the effect of the hole, but also enhanced the shielding. Similar behavior is observed at 400 Hz as shown in Figure 7.15. Figures 7.16 and 7.17 show the effect of the mask layer, covering the 12 mm hole, on the shielding factor at different B_{ext} for frequencies ranging from 20 to 400 Hz. It can be seen that at lower B_{ext} (3.2 mT), although the shielding factor improves with the mask, it is unable to compensate fully. Whereas for B_{ext} > 7 mT the shielding factors recover completely with the use of the mask and is above the curve representing a sheet without any hole.

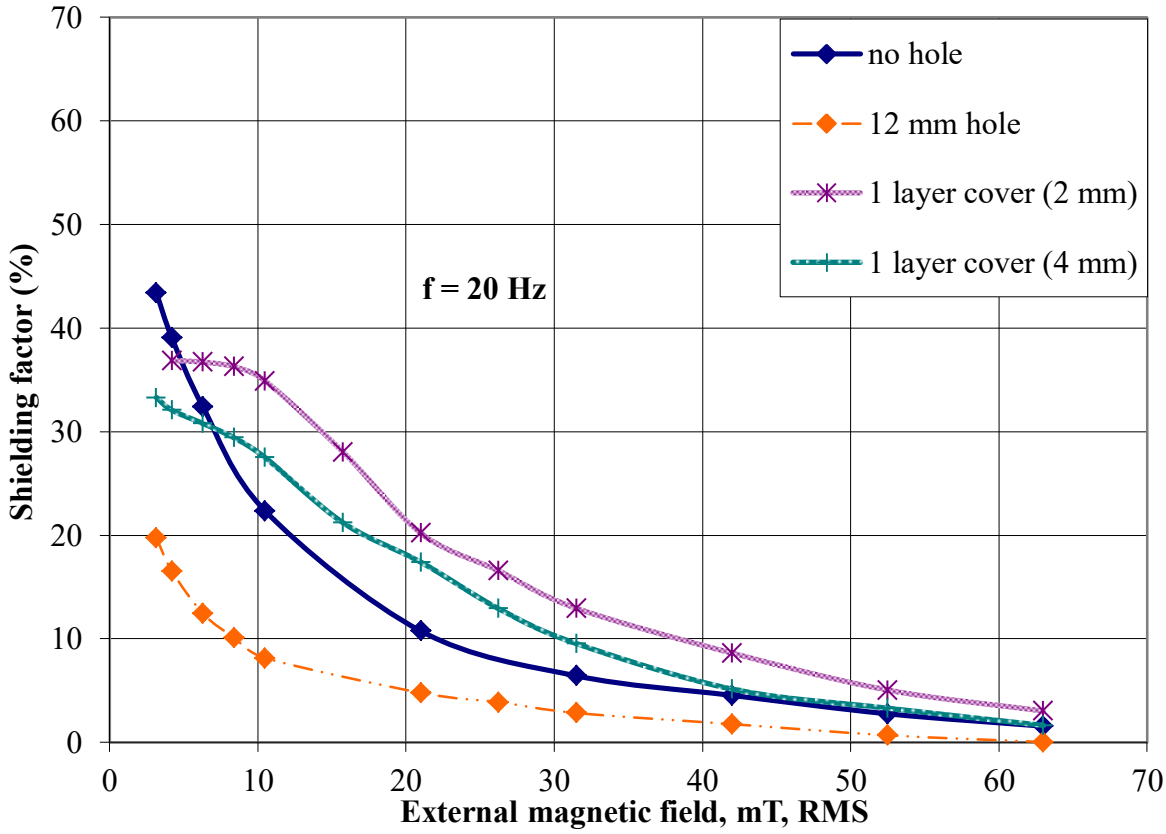

Figure 7.14. Effect of the mask placed at a distance of 2 mm and 4 mm from the 12 mm hole at 20 Hz.

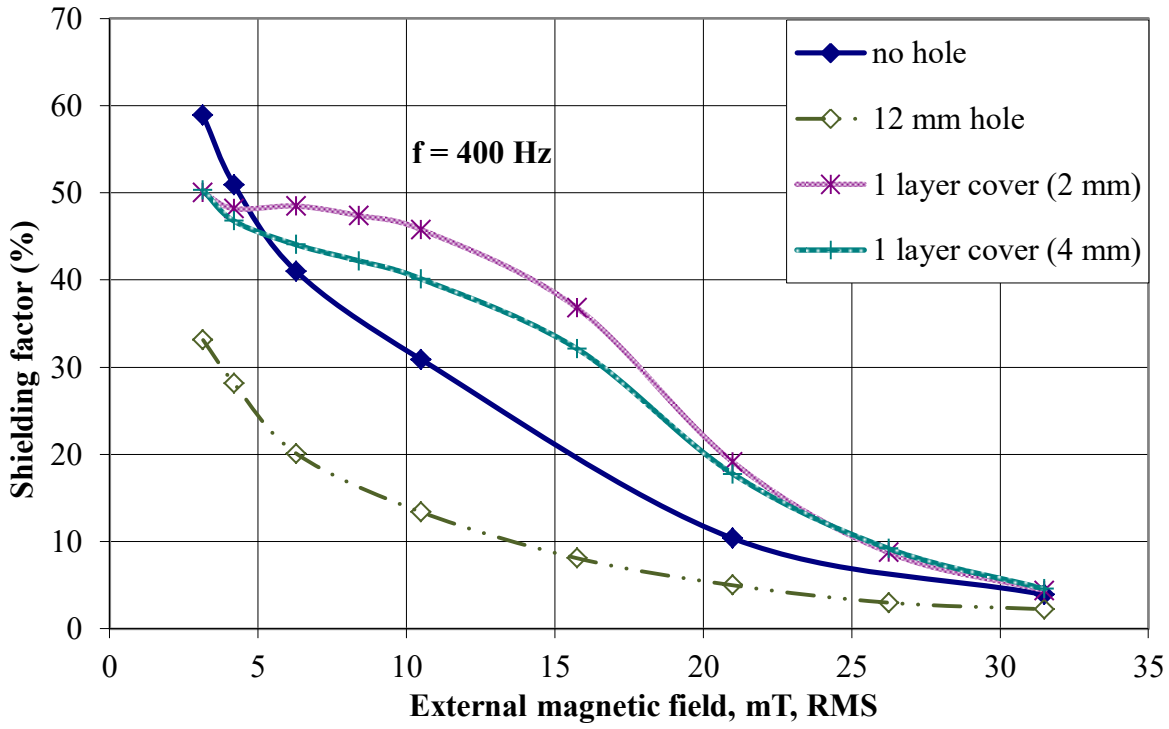

Figure 7.15. Effect of the mask placed at a distance of 2 mm and 4 mm from the 12 mm hole at 400 Hz.

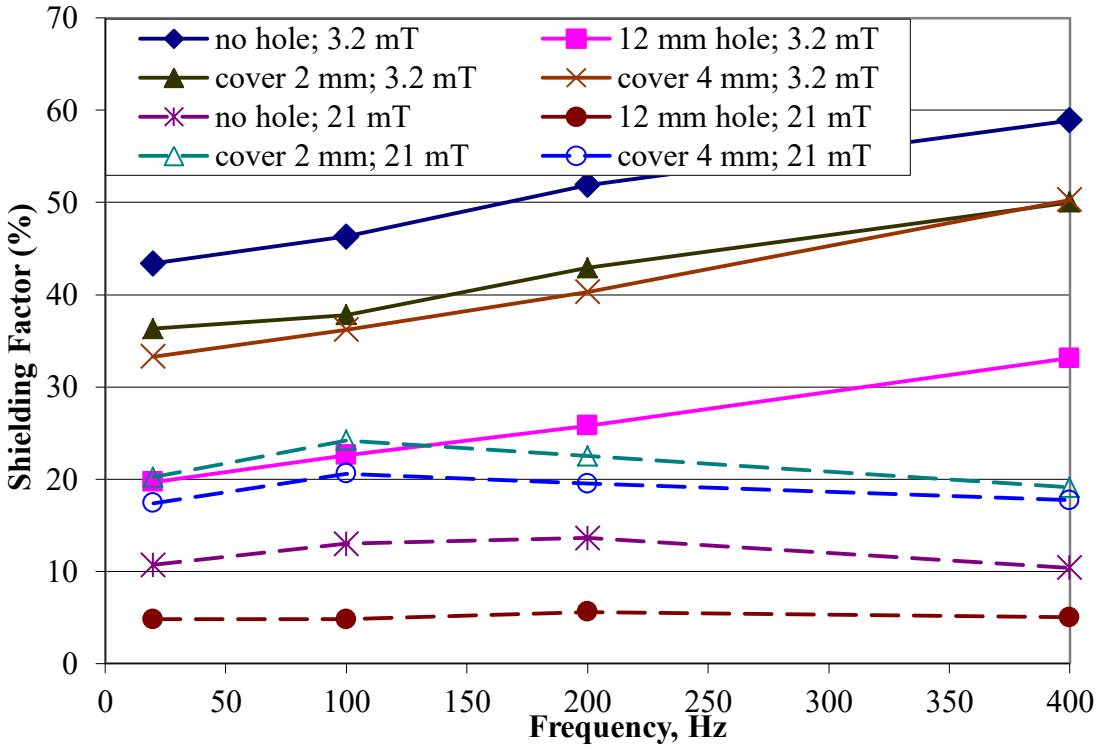

Figure 7.16. Effect of the mask placed at a distance of 2 mm and 4 mm from the 12 mm hole for 3.2 mT and 21 mT of applied external magnetic fields.

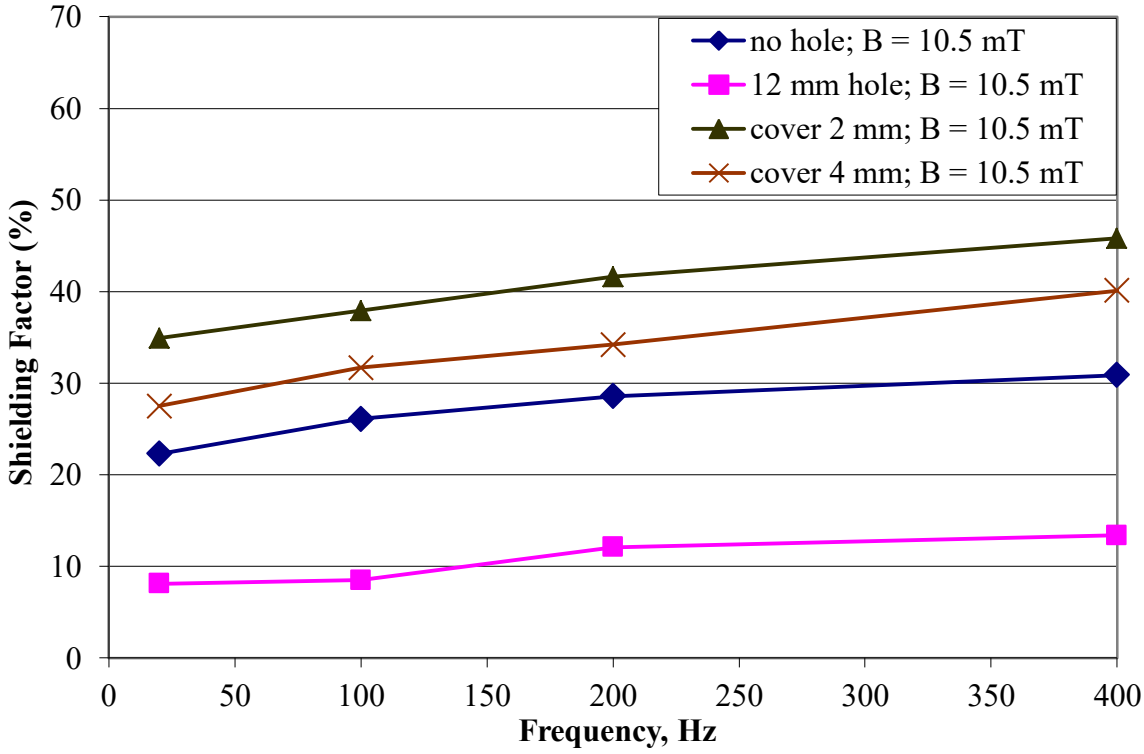

Figure 7.17. Effect of the mask placed at a distance of 2 mm and 4 mm from the 12 mm hole for 10.5 mT of applied external magnetic field.

7.4 CONCLUSION

The effect of discontinuities, such as penetration necessary for pipes and cables, in superconducting magnetic shields fabricated from 2G HTS tapes on the shielding efficacy is studied with the goal finding ways to mitigate the negative effects. It was shown that the decrease in the shielding factor caused by a penetration can be mitigated using a superconducting mask to cover the hole at certain distance.

The shielding factor showed a strong dependence on the magnitude and frequency of the external magnetic field. Shielding factor decreases with increasing external magnetic field and increases with increasing frequency. The discontinuity in the superconducting

shields caused by a hole leads to a drop in shielding factor and the extent of the drop increases with increasing hole size. A superconducting mask is shown to mitigate the negative effect and provides a simple method to manage the need for access to the magnetically shielded space for electrical and signal cables and other piping. Further work is needed to optimize the dimension and location of the mask layer to enable fabrication of practical superconducting shields for large volumes that require penetrations.

Chapter 8

Summary

8.1 INTRODUCTION

In the thesis the concepts of heat and mass transfer were applied to the biological tissue. The characterization of breast tumor was made possible by the application of the bio heat transfer equation to the breast tissue. The temperature distribution within the tissue was obtained using the bio heat transfer equation and the inverse problem of estimating tumor parameters was solved using an algorithm based on Levenberg-Marquardt method. Further, concepts of mass transfer were used for the diagnosis of liver cancer in rabbit livers. CT perfusion allows us to obtain the variation of the concentration distribution of injected dye within the tissue of a subject. Maximum slope method is then employed to get an estimate of the blood flow within the body tissue based on the dye concentration. Maximum slope method is one of the many methods available for calculating blood perfusion. In the present work the short comings of this method for some cases were discussed. An analysis was done to reduce the number of scans required in CT perfusion and thereby reduce the radiation dose involved. Finally, some experiments were performed to estimate the shielding efficacy of superconducting material. Superconducting materials needs to be maintained at very low temperatures and this makes these experiments critical from the heat transfer point of view.

8.2 BREAST CANCER ANALYSIS AND CHARACTERIZATION

A multilayered breast cancer model was developed in COMSOL, which uses bio heat transfer equation for computing temperature distribution. A steady state analysis was carried out using a two dimensional breast model by varying different tumor size, location, metabolic heat generation rate, blood perfusion rate for axisymmetric tumor. Maximum temperature rise and the half temperature difference length are the two important factors which can be used to associate the temperature profile with tumor size and location. The variation of surface temperature profile with metabolic heat generation rate is negligible as compared to blood perfusion rate. Off-axis tumors were analyzed for three dimensional model and it was observed that the polar location of the tumor can be estimated based on the surface temperature profile. Transient analysis was also conducted were the effect of cooling load and time on the recovery temperature was examined. It was observed that increase in cooling time and decrease in cooling temperature leads to an increase in temperature contrast between the normal and cancerous skin temperature. It was also observed that constant temperature cooling is more effective that convective cooling.

This analysis was extended to solve the inverse problem of characterizing tumor based on the surface temperature profile. COMSOL was used to develop a multi layered two dimensional breast model to calculate the temperature distribution for a given set of parameters. This model enabled us to calculate the surface temperature profile for a given set of tumor parameters. This model was then linked with MATLAB using LiveLink, which was used to write the code for the inverse algorithm which was based on Levenberg-Marquadt method. It was observed that steady state data alone is sufficient

only when the number of unknown variables are two, size and location when a third unknown parameter is added in the form of blood perfusion rate steady state data does not give unique solution. In order to solve this problem a transient data, in the form of recovery temperature, after the application of a cooling load, is added which allows the simultaneous estimation of three unknown parameters. The additional information related to blood perfusion is critical as it gives important insight into the nature of the tumor. In general, malignant tumors have substantially higher blood perfusion rate that benign tumors and hence it can be used to differentiate between these two.

8.3 CT PERFUSION

CT perfusion was used to calculate blood perfusion rate within liver tumor of rabbits. Maximum slope method was used in the present work for this purpose. In this section we first highlighted the limitations of maximum slope method. The time at which the concentration of the contrast agent in the spleen peaks is crucial for this method. It divides the liver concentration curve into arterial and portal phase, the two sources of blood supply to the liver tissue. For certain cases the splenic maximum was occurring after the end point of the liver curve because of which it was not possible to get an accurate measure of the blood perfusion for those cases. Further there were cases for which local maxima was occurring in the liver curve, which made it difficult to get an exact location of the end point of the liver. The end point location is crucial for the blood perfusion estimation in maximum slope method.

In the sixth chapter we worked on the optimization of the temporal protocol to reduce the number of scans. Variable time interval approach was used in the present work

in contrast with prevalent fixed time interval case. There was a considerable amount of reduction in the errors with variable time interval case as compared to the fixed time interval cases. Further it was observed that the diagnostic capabilities of the scans were satisfactory even with 9 scans, which were obtained using the optimizing algorithm, as compared to the original protocol of 25 scans. Even when the number of scans was further reduced to 7 there were no false negative and only one false positive. This approach has the potential to reduce the number of scans to a third.

8.4 SUPERCONDUCTING SHIELDS

Experiments were performed using superconducting tapes, YBCO, to calculate the effects of hole on the shielding efficacy. The shielding effect of the superconducting tape showed deterioration with an increase in the size of the hole. When a superconducting mask was used to cover the hole shielding efficacy of the superconducting tapes was restored. Typical power devices need penetrations for power and signal cabling and the penetrations create discontinuities in HTS shields. Hence it is important to assess the effect of the necessary discontinuities on the efficacy of the shields and the design modifications necessary to accommodate the penetrations. Further, the operation of superconducting devices requires very low temperature and the inherent high thermal gradients involved makes proper insulation extremely important. Therefore the working of superconducting materials is also important from the heat transfer point of view.

8.5 FUTURE WORK

A number of improvements that can be made in the projects undertaken in the present work. A more realistic, 3D model of the breast can be developed which can

incorporate off-axis tumors. The Levenberg-Marquardt algorithm used here can be improved to construct more robust algorithm. A sensitivity analysis can be conducted to estimate the effect of variation in thermophysical properties. Here the tumors were considered to be homogeneous, they can be modeled instead with a necrotic core. Instead of relying only on dynamic cooling, different types of cooling/heating load can be applied here.

In the CT perfusion section the temporal optimization can be performed for methods other than maximum slope method. This will enable us to choose a method which needs the least number of scans for diagnostic purposes. The effect of reduction of number of scans on the deterioration of the quality of registration and thereby perfusion calculation, can be studied.

Bibliography

Amri A, Saidane A, Pulko S. Thermal analysis of a three-dimensional breast model with embedded tumour using the transmission line matrix (TLM) method. Computers in Biology and Medicine. 2011;41(2):76-86.

Anbar M, Milescu L, Grenn MW, Zamani K, Marino MT. Study of skin hemodynamics with fast dynamic area telethermometry (DAT). InEngineering in Medicine and Biology Society, 1997. Proceedings of the 19th Annual International Conference of the IEEE 1997 (Vol. 2, pp. 644-648). IEEE.

Arora N, Martins D, Ruggerio D, Tousimis E, Swistel AJ, Osborne MP, Simmons RM. Effectiveness of a noninvasive digital infrared thermal imaging system in the detection of breast cancer. The American Journal of Surgery. 2008;196(4):523-6.

Axel L. Cerebral blood flow determination by rapid-sequence computed tomography: theoretical analysis. Radiology. 1980;137(3):679-86.

Axel L. Tissue mean transit time from dynamic computed tomography by a simple deconvolution technique. Investigative radiology. 1983 Jan 1;18(1):94-9.

AMSC [online]. Available from: http://www.amsc.com/[Accessed 1 July 2017]

Bader TR, Herneth AM, Blaicher W, Steininger R, Mühlbacher F, Lechner G, Grabenwöger F. Hepatic perfusion after liver transplantation: noninvasive measurement with dynamic single-section CT. Radiology. 1998;209(1):129-34.

Berrington de González A, Reeves G. Mammographic screening before age 50 years in the UK: comparison of the radiation risks with the mortality benefits. British journal of cancer. 2005;93(5):590.

Bhargava A, Chanmugam A, Herman C. Heat transfer model for deep tissue injury: a step towards an early thermographic diagnostic capability. Diagnostic pathology. 2014;9(1):36.

Blomley MJ, Coulden R, Bufkin C, Lipton MJ, Dawson P. Contrast bolus dynamic computed tomography for the measurement of solid organ perfusion. Investigative radiology.1993;28:72-7.

Bradley SE, Ingelfinger FJ, Bradley GP, Curry JJ. The estimation of hepatic blood flow in man. Journal of Clinical Investigation. 1945;24(6):890.

Blomley MJ, Coulden R, Dawson P, Kormano M, Donlan P, Bufkin C, Lipton MJ. Liver perfusion studied with ultrafast CT. Journal of computer assisted tomography. 1995;19(3):424-33.

Bhatia V, Bhatia R, Dhindsa S, Dhindsa M. Imaging of the vulnerable plaque: new modalities. Southern medical journal. 2003;96(11):1142-8.

Bergman TL, Lavine AS, Incropera FP and Dewitt DP. Fundamentals of heat and mass transfer.John Wiley & Sons; 2011.

Bisdas S, Foo CZ, Thng CH, Vogl TJ, San Koh T. Optimization of perfusion CT protocol for imaging of extracranial head and neck tumors. Journal of digital imaging. 2009;22(5):437-48.

Bezerra LA, Oliveira MM, Rolim TL, Conci A, Santos FG, Lyra PR, Lima RC. Estimation of breast tumor thermal properties using infrared images. Signal Processing. 2013;93(10):2851-63.

Borovetz HS, Inskeep WH, Lincoff AM, Hardesty RL. Role of longitudinal diffusion in the extravascular pulmonary space on parameter estimates derived from data of multiple indicator dilution. Physics in medicine and biology. 1982;27(6):819.

Bleyer A, Welch HG. Effect of three decades of screening mammography on breast-cancer incidence. New England Journal of Medicine. 2012;367(21):1998-2005.

Buijs M, Vossen JA, Geschwind JF, Salibi N, Pan L, Ventura VP, Liapi E, Lee KH, Kamel IR. Quantitative proton MR spectroscopy as a biomarker of tumor necrosis in the rabbit VX2 liver tumor. Journal of Vascular and Interventional Radiology. 2011;22(8):1175-80.

Bronzino JD, editor. Medical devices and systems. CRC Press; 2006.

Bhowmik A, Repaka R. Estimation of growth features and thermophysical properties of melanoma within 3-D human skin using genetic algorithm and simulated annealing. International Journal of Heat and Mass Transfer. 2016;98:81-95

Brix G, Kiessling F, Lucht R, Darai S, Wasser K, Delorme S, Griebel J. Microcirculation and microvasculature in breast tumors: pharmacokinetic analysis of dynamic MR image series. Magnetic resonance in medicine. 2004;52(2):420-9.

Cady B, Oberfield RA. Arterial infusion chemotherapy of hepatoma. Surgery, gynecology & obstetrics. 1974;138(3):381-4.

Carter CL, Allen C, Henson DE. Relation of tumor size, lymph node status, and survival in 24,740 breast cancer cases. Cancer. 1989;63(1):181-7.

Cenic A, Nabavi DG, Craen RA, Gelb AW, Lee TY. Dynamic CT measurement of cerebral blood flow: a validation study. American Journal of Neuroradiology. 1999;20(1):63-73.

Cenic A, Nabavi DG, Craen RA, Gelb AW, Lee TY. A CT method to measure hemodynamics in brain tumors: validation and application of cerebral blood flow maps. American Journal of Neuroradiology. 2000;21(3):462-70.

Cuenod CA, Leconte I, Siauve N, Frouin F, Dromain C, Clément O, Frija G. Deconvolution technique for measuring tissue perfusion by dynamic CT: application to normal and metastatic liver. Academic radiology. 2002;9(1):S205-11.

Cuenod CA, Leconte I, Siauve N, Resten A, Dromain C, Poulet B, Frouin F, Clément O, Frija G. Early changes in liver perfusion caused by occult metastases in rats: detection with quantitative CT. Radiology. 2001;218(2):556-61.

Çetingül MP, Herman C. Quantification of the thermal signature of a melanoma lesion. International Journal of Thermal Sciences. 2011;50(4):421-31.

Cheng TY, Herman C. Analysis of skin cooling for quantitative dynamic infrared imaging of near-surface lesions. International Journal of Thermal Sciences. 2014;86:175-88.

COMSOL Multiphysics, 2011, Version 4.2, Comsol Inc.

Çetingül MP, Herman C. A heat transfer model of skin tissue for the detection of lesions: sensitivity analysis. Physics in Medicine and Biology. 2010;55(19):5933.

Çetingül MP. Using high resolution infrared imaging to detect melanoma and dysplastic nevi. PhD Dissertation Johns Hopkins University. 2010

Clark AT, Mangat JS, Tay SS, King Y, Monk CJ, White PA, Ewan PW. Facial thermography is a sensitive and specific method for assessing food challenge outcome. Allergy. 2007;62(7):744-9.

Corvi A, Innocenti B, Mencucci R. Thermography used for analysis and comparison of different cataract surgery procedures based on phacoemulsification. Physiological measurement. 2006;27(4):371.

Chanmugam A, Hatwar R, Herman C. Thermal analysis of cancerous breast model. InInternational Mechanical Engineering Congress and Exposition:[proceedings]/International Mechanical Engineering Congress and Exposition. International Mechanical Engineering Congress and Exposition 2012 (Vol. 2012, p. 134). NIH Public Access.

Das K, Mishra SC. Estimation of tumor characteristics in a breast tissue with known skin surface temperature. Journal of Thermal Biology. 2013;38(6):311-7.

Das K, Mishra SC. Non-invasive estimation of size and location of a tumor in a human breast using a curve fitting technique. International Communications in Heat and Mass Transfer. 2014;56:63-70.

Das K, Mishra SC. Simultaneous estimation of size, radial and angular locations of a malignant tumor in a 3-D human breast–A numerical study. Journal of thermal biology. 2015;52:147-56.

Deng ZS, Liu J. Parametric studies on the phase shift method to measure the blood perfusion of biological bodies. Medical engineering & physics. 2000;22(10):693-702.

Dixon JM, editor. ABC of breast diseases. John Wiley & Sons; 2009.

Elmore JG, Barton MB, Moceri VM, Polk S, Arena PJ, Fletcher SW. Ten-year risk of false positive screening mammograms and clinical breast examinations. New England Journal of Medicine. 1998;338(16):1089-96.

Fleming JS, Ackery DM, Walmsley BH, Karran SJ. Scintigraphic estimation of arterial and portal blood supplies to the liver. Journal of nuclear medicine: official publication, Society of Nuclear Medicine. 1983;24(12):1108-13.

Fletcher SW, Elmore JG. Mammographic screening for breast cancer. New England Journal of Medicine. 2003;348(17):1672-80.

Fagnard JF, Denis S, Lousberg G, Dirickx M, Ausloos M, Vanderheyden B, Vanderbemden P. DC and AC shielding properties of bulk high-Tc superconducting tubes. IEEE Transactions on Applied Superconductivity. 2009;19(3):2905-8.

Fagnard JF, Elschner S, Hobl A, Bock J, Vanderheyden B, Vanderbemden P. Magnetic shielding properties of a superconducting hollow cylinder containing slits: modelling and experiment. Superconductor Science and Technology. 2012;25(10):104006.

Gautherie M, Gros CM. Breast thermography and cancer risk prediction. Cancer. 1980;45(1):51-6.

Gautherie M. Thermopathology of breast cancer: measurement and analysis of in vivo temperature and blood flow. Annals of the New York Academy of Sciences. 1980;335(1):383-415.

Gillard JH, Minhas PS, Hayball MP, Bearcroft PW, Antoun NM, Freer CE, Mathews JC, Miles KA, Pickard JD. Assessment of quantitative computed tomographic cerebral perfusion imaging with H2150 positron emission tomography. Neurological research. 2000;22(5):457-64.

Gøtzsche PC, Nielsen M. Screening for breast cancer with mammography. Cochrane Database Syst Rev. 2009;4(1).

Gould RG, Lipton MJ, Mcnamara MT, Sievers RE, Koshold S, Higgins CB. Measurement of Regional: Myocardial Blood Flow in Dogs by Ultrafast CT. Investigative radiology. 1988;23(5):348-53.

Guyennon A, Mihaila M, Palma J, Lombard-Bohas C, Chayvialle JA, Pilleul F. Perfusion characterization of liver metastases from endocrine tumors: computed tomography perfusion. World journal of radiology. 2010;2(11):449.

Goresky CA, Bach GG, Nadeau BE. On the uptake of materials by the intact liver. The transport and net removal of galactose. Journal of Clinical Investigation. 1973;52(5):991.

Gobbel GT, Cann CE, Fike JR. Comparison of xenon-enhanced CT with ultrafast CT for measurement of regional cerebral blood flow. American journal of neuroradiology. 1993;14(3):543-50.

Gobbel GT, Cann CE, Fike JR. Measurement of regional cerebral blood flow using ultrafast computed tomography. Theoretical aspects. Stroke. 1991;22(6):768-71.

Gray JE. Safety (risk) of diagnostic radiology exposures. Chapter. 1996;4:15.

Goh V, Liaw J, Bartram CI, Halligan S. Effect of temporal interval between scan acquisitions on quantitative vascular parameters in colorectal cancer: implications for helical volumetric perfusion CT techniques. American Journal of Roentgenology. 2008;191(6):W288-92.

Hong K, Kobeiter H, Georgiades CS, Torbenson MS, Geschwind JF. Effects of the type of embolization particles on carboplatin concentration in liver tumors after transcatheter arterial chemoembolization in a rabbit model of liver cancer. Journal of vascular and interventional radiology. 2005;16(12):1711-7.

Hammer C, Fanning A, Crowe J. Overview of breast cancer staging and surgical treatment options. Cleveland Clinic journal of medicine. 2008;75(1):S10.

Hatwar R, Herman C. Inverse method for quantitative characterisation of breast tumours from surface temperature data. International Journal of Hyperthermia. 2017:1-7.

Hatwar R, Kvitkovic J, Herman C, Pamidi S. Effect of Discontinuities and Penetrations on the Shielding Efficacy of High Temperature Superconducting Magnetic Shields. InIOP Conference Series: Materials Science and Engineering 2015 (Vol. 102, No. 1, p. 012012). IOP Publishing..

Hattori H, Miyoshi T, Okada J, Yoshikawa K, Arimizu N, Hattori N. Tumor blood flow measured using dynamic computed tomography. Investigative radiology. 1994;29(10):873-6.

Herman C. Emerging technologies for the detection of melanoma: achieving better outcomes. Clinical, cosmetic and investigational dermatology. 2012;5:195.

Harvey JA, Herman CR, Pinkerton JV. Short-term cessation of hormone replacement therapy and improvement of mammographic specificity. Journal of the National Cancer Institute. 1997;89(21):1623-5.

Hoekstra P. Quantitive digital thermology: 21st century imaging systems. InOAND Conference 2001.

Head JF, Lipari CA, Elliott RL. Comparison of mammography and breast infrared imaging: sensitivity, specificity, false negatives, false positives, positive predictive value and negative predictive value. In[Engineering in Medicine and Biology, 1999. 21st Annual Conference and the 1999 Annual Fall Meetring of the Biomedical

Engineering Society] BMES/EMBS Conference, 1999. Proceedings of the First Joint 1999 Oct (Vol. 2, pp. 1116-vol). IEEE.

Hamilton WF, Moore JW, Kinsman JM, Spurling RG. Studies on the circulation. American Journal of Physiology--Legacy Content. 1932;99(3):534-51.

Isard HJ. Other imaging techniques. Cancer. 1984 Feb 1;53(S3):658-64.

Jiang L, Zhan W, Loew MH. Modeling static and dynamic thermography of the human breast under elastic deformation. Physics in medicine and biology. 2010;56(1):187.

Jackson VP, Hendrick RE, Feig SA, Kopans DB. Imaging of the radiographically dense breast. Radiology. 1993;188(2):297-301.

Jørgensen KJ, Gøtzsche PC. Overdiagnosis in publicly organised mammography screening programmes: systematic review of incidence trends. Bmj. 2009;339:b2587.

Jiang LJ, Ng EY, Yeo AC, Wu S, Pan F, Yau WY, Chen JH, Yang Y. A perspective on medical infrared imaging. Journal of medical engineering & technology. 2005;29(6):257-67.

Kvitkovic J, Voccio J, Pamidi SV. Shielding of AC magnetic fields by coils and sheets of superconducting tapes. IEEE Transactions on Applied Superconductivity. 2009;19(3):3577-80.

Kanda T, Yoshikawa T, Ohno Y, Kanata N, Koyama H, Takenaka D, Sugimura K. CT hepatic perfusion measurement: comparison of three analytic methods. European journal of radiology. 2012;81(9):2075-9.

Kvitkovic J, Pamidi S, Voccio J. Shielding AC magnetic fields using commercial YBa2Cu3O7-coated conductor tapes. Superconductor Science and Technology. 2009;22(12):125009.

Kvitkovic J, Davis D, Zhang M, Pamidi S. Magnetic shielding characteristics of second generation high temperature superconductors at variable temperatures obtained by cryogenic helium gas circulation. IEEE Transactions on Applied Superconductivity. 2015;25(3):1-4.

Kvitkovic J, Patil P, Pamidi SV, Voccio J. Characterization of 2G superconductor magnetic shields at 40–77 K. IEEE Transactions on Applied Superconductivity. 2011;21(3):1477-80.

Kvitkovic J, Davis D, Zhang M, Pamidi S. Influence of interlayer separation on magnetic shielding properties of 2G HTS sheets made of 46 mm wide RABiTS tape. IEEE Transactions on Applied Superconductivity. 2013;23(3):8200605-.

Kim JH, Kim CH, Iyyani G, Kvitkovic J, Pamidi S. Transport AC loss measurements in superconducting coils. IEEE Transactions on Applied Superconductivity. 2011;21(3):3269-72.

Kloska SP, Fischer T, Sauerland C, Buerke B, Dziewas R, Fischbach R, Heindel W. Increasing sampling interval in cerebral perfusion CT: limitation for the maximum slope model. Academic radiology. 2010;17(1):61-6.

Kämena A, Streitparth F, Grieser C, Lehmkuhl L, Jamil B, Wojtal K, Ricke J, Pech M. Dynamic perfusion CT: optimizing the temporal resolution for the calculation of perfusion CT parameters in stroke patients. European journal of radiology. 2007;64(1):111-8.

Kambadakone AR, Sharma A, Catalano OA, Hahn PF, Sahani DV. Protocol modifications for CT perfusion (CTp) examinations of abdomen-pelvic tumors:

impact on radiation dose and data processing time. European radiology. 2011;21(6):1293-300.

Keyserlingk JR, Ahlgren PD, Yu E, Belliveau N. Infrared Imaging of the Breast: Initial Reappraisal Using High-Resolution Digital Technology in 100 Successive Cases of Stage I and II Breast Cancer. The Breast Journal. 1998;4(4):245-51.

Keyserlingk JR, Ahlgren PD, Yu E, Belliveau N, Yassa M. Functional infrared imaging of the breast. IEEE Engineering in Medicine and Biology Magazine. 2000;19(3):30-41.

Kennedy DA, Lee T, Seely D. A comparative review of thermography as a breast cancer screening technique. Integrative cancer therapies. 2009;8(1):9-16.

Koenig M, Klotz E, Luka B, Venderink DJ, Spittler JF, Heuser L. Perfusion CT of the brain: diagnostic approach for early detection of ischemic stroke. Radiology. 1998;209(1):85-93.

Kleinman AM, Roemer RB. A direct substitution, equation error technique for solving the thermographic tomography problem. Journal of biomechanical engineering. 1983;105(3):237-43.

Kim SH, Kamaya A, Willmann JK. CT perfusion of the liver: principles and applications in oncology. Radiology. 2014;272(2):322-44.

Law J, Faulkner K, Young KC. Risk factors for induction of breast cancer by X-rays and their implications for breast screening. The British journal of radiology. 2007;80(952):261-6.

Lawson RN. Thermography a new tool in the investigation of breast lesions. Can. Med. Assoc. J.. 1957;13:517-24.

Lawson RN, Chughtai MS. Breast cancer and body temperature. Canadian Medical Association Journal. 1963;88(2):68.

Lawson RN. A new infrared imaging device. Canadian Medical Association Journal. 1958;79(5):402.

Liu J, Zhou YX, Deng ZS. Sinusoidal heating method to noninvasively measure tissue perfusion. IEEE transactions on biomedical engineering. 2002;49(8):867-77.

Leonard EF, Jørgensen SB. The analysis of convection and diffusion in capillary beds. Annual review of biophysics and bioengineering. 1974;3(1):293-339.

Lincoff AM, Borovetz HS, Inskeep WH. Characterisation of the unsteady transport of labelled species in permeable capillaries: role of convective dispersion. Physics in medicine and biology. 1983;28(11):1191.

Liapi E, Geschwind JF. Transcatheter and ablative therapeutic approaches for solid malignancies. Journal of Clinical Oncology. 2007;25(8):978-86.

Lee KH, Liapi E, Vossen JA, Buijs M, Ventura VP, Georgiades C, Hong K, Kamel I, Torbenson MS, Geschwind JF. Distribution of iron oxide–containing Embosphere particles after transcatheter arterial embolization in an animal model of liver cancer: evaluation with MR imaging and implication for therapy. Journal of Vascular and Interventional Radiology. 2008;19(10):1490-6.

Lawson R. Implications of surface temperatures in the diagnosis of breast cancer. Canadian Medical Association Journal. 1956;75(4):309.

Materne R, Van Beers BE, Smith AM, Leconte I, Jamart J, Dehoux JP, Keyeux A, Horsmans Y. Non-invasive quantification of liver perfusion with dynamic computed

tomography and a dual-input one-compartmental model. Clinical Science. 2000;99(6):517-25.

Mullani NA, Gould KL. First-pass measurements of regional blood flow with external detectors. Journal of Nuclear Medicine. 1983;24(7):577-81.

Meier P, Zierler KL. On the theory of the indicator-dilution method for measurement of blood flow and volume. Journal of applied physiology. 1954;6(12):731-44.

Miles KA, Hayball M, Dixon AK. Colour perfusion imaging: a new application of computed tomography. The Lancet. 1991;337(8742):643-5.

Miles KA. Measurement of tissue perfusion by dynamic computed tomography. The British journal of radiology. 1991;64(761):409-12.

Miles KA, Hayball MP, Dixon AK. Functional images of hepatic perfusion obtained with dynamic CT. Radiology. 1993;188(2):405-11.

Mital M, Pidaparti RM. Breast tumor simulation and parameters estimation using evolutionary algorithms. Modelling and simulation in engineering. 2008;2008:4.

Mitra S, Balaji C. A neural network based estimation of tumour parameters from a breast thermogram. International Journal of Heat and Mass Transfer. 2010;53(21):4714-27.

Miles KA, Hayball MP, Dixon AK. Functional imaging of changes in human intrarenal perfusion using quantitative dynamic computed tomography. Investigative radiology. 1994;29(10):911-4.

Miles KA, Hayball MP, Dixon AK. Measurement of human pancreatic perfusion using dynamic computed tomography with perfusion imaging. The British journal of radiology. 1995;68(809):471-5.

Miles KA, Griffiths MR. Perfusion CT: a worthwhile enhancement?. The British journal of radiology. 2003;76(904):220-31.

Miles KA, Charnsangavej C, Lee FT, Fishman EK, Horton K, Lee TY. Application of CT in the investigation of angiogenesis in oncology. Academic radiology. 2000;7(10):840-50.

Miles KA. Tumour angiogenesis and its relation to contrast enhancement on computed tomography: a review. European journal of radiology. 1999;30(3):198-205.

Ng EK. A review of thermography as promising non-invasive detection modality for breast tumor. International Journal of Thermal Sciences. 2009;48(5):849-59.

Ng CS, Hobbs BP, Wei W, Anderson EF, Herron DH, Yao JC, Chandler AG. Effect on perfusion values of sampling interval of computed tomographic perfusion acquisitions in neuroendocrine liver metastases and normal liver. Journal of computer assisted tomography. 2015;39(3):373-82.

Ng CS, Chandler AG, Wei W, Anderson EF, Herron DH, Kurzrock R, Charnsangavej C. Effect of sampling frequency on perfusion values in perfusion CT of lung tumors. American Journal of Roentgenology. 2013;200(2):W155-62.

National Research Council. Guide for the Care and Use of Laboratory Animals, National Academy Press, Washington, DC (1996)

"National Cancer Institute":http://www.cancer.gov (2012)

Nagasawa A, Okada H. Thermal recovery. In: Atsumi K (Ed): Medical Thermography. Tokyo: University of Tokyo Press; 1973. p. 151-165.

Ng EY, Fok SC. A framework for early discovery of breast tumor using thermography with artificial neural network. The Breast Journal. 2003;9(4):341-3.

Ng EY, Chen Y, Ung LN. Computerized breast thermography: study of image segmentation and temperature cyclic variations. Journal of medical engineering & technology. 2001;25(1):12-6.

Ng EY, Kee EC. Advanced integrated technique in breast cancer thermography. Journal of medical engineering & technology. 2008;32(2):103-14.

Ng EY, Sudharsan NM. An improved three-dimensional direct numerical modelling and thermal analysis of a female breast with tumour. Proceedings of the Institution of Mechanical Engineers, Part H: Journal of Engineering in Medicine. 2001;215(1):25-37.

Ng EY, Sudharsan NM. An improved three-dimensional direct numerical modelling and thermal analysis of a female breast with tumour. Proceedings of the Institution of Mechanical Engineers, Part H: Journal of Engineering in Medicine. 2001;215(1):25-37.

Nabavi DG, Cenic A, Dool J, Smith RM, Espinosa F, Craen RA, Gelb AW, Lee TY. Quantitative assessment of cerebral hemodynamics using CT: stability, accuracy, and precision studies in dogs. Journal of computer assisted tomography. 1999;23(4):506-15.

Othman AE, Afat S, Brockmann MA, Nikoubashman O, Brockmann C, Nikolaou K, Wiesmann M. Radiation dose reduction in perfusion CT imaging of the brain: a review of the literature. Journal of Neuroradiology. 2016;43(1):1-5.

O'Connor MK, MacMathuna P, Keeling PW. Hepatic arterial and portal venous components of liver blood flow: a dynamic scintigraphic study. Journal of nuclear medicine. 1988;29(4):466-72.

Osman MM, Afify EM. Thermal modeling of the normal woman's breast. Journal of biomechanical engineering. 1984;106:123.

Osman MM, Afify EM. Thermal modeling of the malignant woman's breast. Journal of biomechanical engineering. 1988;110:269.

Ohashi Y, Uchida I. Applying dynamic thermography in the diagnosis of breast cancer. IEEE Engineering in Medicine and Biology Magazine. 2000;19(3):42-51.

Ozisik MN, Orlande H Inverse heat transfer: fundamentals and applications. CRC Press; 2000.

Osako T, Iwase T, Takahashi K, Iijima K, Miyagi Y, Nishimura S, Tada K, Makita M, Akiyama F, Sakamoto G, Kasumi F. Diagnostic mammography and ultrasonography for palpable and nonpalpable breast cancer in women aged 30 to 39 years. Breast Cancer. 2007;14(3):255-9.

Okada Y, Kawamata T, Kawashima A, Hori T. Intraoperative application of thermography in extracranial-intracranial bypass surgery. Operative Neurosurgery. 2007 Apr 1;60(suppl_4):ONS-362.

Pizzella V, Della Penna S, Del Gratta C, Romani GL. SQUID systems for biomagnetic imaging. Superconductor Science and Technology. 2001;14(7):R79.

Pavese F Handbook of Applied Superconductivity (Bristol: Institute of Physics) 1998 p 1461

Pamidi S, Kvitkovic J, Trociewitz U, Ishmael S, Meinke R, Stelzer G. A novel magnet for AC loss measurements on 2G superconductor rings and coils in axial and radial magnetic fields. IEEE Transactions on Applied Superconductivity. 2012;22(3):9003004-.

Pandharipande PV, Krinsky GA, Rusinek H, Lee VS. Perfusion imaging of the liver: current challenges and future goals. Radiology. 2005;234(3):661-73.

Purdie TG, Henderson E, Lee TY. Functional CT imaging of angiogenesis in rabbit VX2 soft-tissue tumour. Physics in medicine and biology. 2001;46(12):3161.

Pradel C, Siauve N, Bruneteau G, Clement O, De Bazelaire C, Frouin F, Wedge SR, Tessier JL, Robert PH, Frija G, Cuenod CA. Reduced capillary perfusion and permeability in human tumour xenografts treated with the VEGF signalling inhibitor ZD4190: an in vivo assessment using dynamic MR imaging and macromolecular contrast media. Magnetic resonance imaging. 2003;21(8):845-51.

Petralia G, Fazio N, Bonello L, D'andrea G, Radice D, Bellomi M. Perfusion computed tomography in patients with hepatocellular carcinoma treated with thalidomide: initial experience. Journal of computer assisted tomography. 2011;35(2):195-201.

Patlak CS, Blasberg RG, Fenstermacher JD. Graphical evaluation of blood-to-brain transfer constants from multiple-time uptake data. Journal of Cerebral Blood Flow & Metabolism. 1983;3(1):1-7.

Pennes HH. Analysis of tissue and arterial blood temperatures in the resting human forearm. Journal of applied physiology. 1948;1(2):93-122.

Pizzella V, Della Penna S, Del Gratta C, Romani GL. SQUID systems for biomagnetic imaging. Superconductor Science and Technology. 2001;14(7):R79.

Rumberger JA, Feiring AJ, Lipton MJ, Higgins CB, Ell SR, Marcus ML. Use of ultrafast computed tomography to quantitate regional myocardial perfusion: a preliminary report. Journal of the American College of Cardiology. 1987;9(1):59-69.

Rosenberg RD, Hunt WC, Williamson MR, Gilliland FD, Wiest PW, Kelsey CA, Key CR, Linver MN. Effects of age, breast density, ethnicity, and estrogen replacement therapy on screening mammographic sensitivity and cancer stage at diagnosis: review of 183,134 screening mammograms in Albuquerque, New Mexico. Radiology. 1998;209(2):511-8.

Siegel RL, Miller KD, Jemal A. Cancer statistics, 2016. CA: a cancer journal for clinicians. 2016;66(1):7-30.

Sledge GW. Screening for Breast Cancer: Is the Picture Changing ? Clinical Breast Cancer. 2009; 9(4): 212

Sudharsan NM, Ng EY, Teh SL. Surface temperature distribution of a breast with and without tumour. Computer methods in biomechanics and biomedical engineering. 1999;2(3):187-99.

Sapirstein LA. Regional blood flow by fractional distribution of indicators. American Journal of Physiology--Legacy Content. 1958;193(1):161-8.

Sudharsan NM, Ng EY. Parametric optimization for tumour identification: bioheat equation using ANOVA and the Taguchi method. Proceedings of the Institution of Mechanical Engineers, Part H: Journal of Engineering in Medicine. 2000;214(5):505-12.

Sawada YA, Patlak CS, Blasberg RG. Kinetic analysis of cerebrovascular transport based on indicator diffusion technique. American Journal of Physiology-Heart and Circulatory Physiology. 1989;256(3):H794-812.

St Lawrence KS, Frank JA, McLaughlin AC. Effect of restricted water exchange on cerebral blood flow values calculated with arterial spin tagging: a theoretical investigation. Magnetic resonance in medicine. 2000;44(3):440-9.

Schenk Jr WG, McDonald JC, McDonald K, Drapanas T. Direct measurement of hepatic blood flow in surgical patients: with related observations on hepatic flow dynamics in experimental animals. Annals of surgery. 1962;156(3):463.

Swinton sr NW, Caddy B, Nahra KS, Watkins jr E. Arterial infusion chemotherapy of liver metastases arising from rectal and colonic cancer. Proceedings of the Royal Society of Medicine. 1970;63(Suppl 1):21.

Saxena AK, Willital GH. Infrared thermography: experience from a decade of pediatric imaging. European journal of pediatrics. 2008;167(7):757-64.

Sourbron SP, Buckley DL. Classic models for dynamic contrast-enhanced MRI. NMR in biomedicine. 2013;26(8):1004-27.

Sourbron SP, Buckley DL. On the scope and interpretation of the Tofts models for DCE-MRI. Magnetic resonance in medicine. 2011;66(3):735-45.

Stewart GN. Researches on the circulation time and on the influences which affect it. The Journal of physiology. 1897;22(3):159-83.

Sobti A, Sobti P, Keith LG. Screening and diagnostic mammograms: why the gold standard does not shine more brightly. International journal of fertility and women's medicine. 2005;50(5 Pt 1):199-206.

Tygstrup N, Winkler K, Mellemgaard K, Andreassen M. Determination of the hepatic arterial blood flow and oxygen supply in man by clamping the hepatic artery during surgery. Journal of Clinical Investigation. 1962;41(3):447.

Tofts PS, Brix G, Buckley DL, Evelhoch JL, Henderson E, Knopp MV, Larsson HB, Lee TY, Mayr NA, Parker GJ, Port RE. Estimating kinetic parameters from dynamic contrast-enhanced T 1-weighted MRI of a diffusable tracer: standardized quantities and symbols. Journal of magnetic resonance imaging. 1999;10(3):223-32.

Wiesmann M, Berg S, Bohner G, Klingebiel R, Schöpf V, Stoeckelhuber BM, Yousry I, Linn J, Missler U. Dose reduction in dynamic perfusion CT of the brain: effects of the scan frequency on measurements of cerebral blood flow, cerebral blood volume, and mean transit time. European radiology. 2008;18(12):2967.

Wintermark M, Smith WS, Ko NU, Quist M, Schnyder P, Dillon WP. Dynamic perfusion CT: optimizing the temporal resolution and contrast volume for calculation of perfusion CT parameters in stroke patients. American Journal of Neuroradiology. 2004;25(5):720-9.

Wolfkiel CJ, Ferguson JL, Chomka EV, Law WR, Labin IN, Tenzer ML, Booker M, Brundage BH. Measurement of myocardial blood flow by ultrafast computed tomography. Circulation. 1987;76(6):1262-73.

Wintermark M, Maeder PP, Thiran JP, Schnyder P, Meuli RA. Quantitative assessment of regional cerebral blood flows by perfusion CT: A critical review of the underlying theoretical models. European Radiology. 2001; 11(7), 1220-1230.

Wikimedia Commons contributors, "File:CERN-cables-p1030764.jpg," Wikimedia Commons, the free media repository, https://commons.wikimedia.org/w/index.php?title=File:CERN-cables-p1030764.jpg&oldid=245894618 (accessed June 30, 2017).

Yamamoto A, Imai S, Kobatake M, Yamashita T, Tamada T, Umetani K. Evaluation of tris-acryl gelatin microsphere embolization with monochromatic X rays: comparison with polyvinyl alcohol particles. Journal of vascular and interventional radiology. 2006;17(11):1797-802.

Yuan W, Coombs TA, Kim JH, Han Kim C, Kvitkovic J, Pamidi S. Measurements and calculations of transport AC loss in second generation high temperature superconducting pancake coils. Journal of Applied Physics.;110(11):113906.

Zierler KL. Theoretical basis of indicator-dilution methods for measuring flow and volume. Circulation Research. 1962;10(3):393-407.

Zierler KL. Equations for measuring blood flow by external monitoring of radioisotopes. Circulation research. 1965;16(4):309-21.

Vita

Rajeev Hatwar was born on October 13, 1986 in Bhopal, India. He received his Bachelors of Technology degree in Mechanical Engineering from Indian Institute of Technology (IIT) Bombay (Mumbai), India in 2004. He worked as a derivative trader in Futures First and as a senior research fellow in IIT Bombay after his bachelors. He came to US in 2011 to pursue graduate studies in Mechanical Engineering. He got his M.Sc degree in Mechanical engineering from Johns Hopkins University, Baltimore, Maryland in 2013 and completed his doctoral study in 2017.